Preparation of mixed metal oxide catalysts for VOC total oxidation

Parag M. Shah

Submitted in fulfilment of the requirements for the degree of PhD

APPENDIX 1 - STATEMENTS AND DECLARATIONS TO BE SIGNED BY THE CANDIDATE AND INCLUDED IN THE THESIS

STATEMENT 1

This thesis is being submitted in partial fulfilment of the requirements for the degree of ... (insert PhD, MD, MPhil, etc., as appropriate)

Signed……………………………………………….

Date……………………………………………….

STATEMENT 2

This work has not been submitted in substance for any other degree or award at this or any other university or place of learning, nor is it being submitted concurrently for any other degree or award (outside of any formal collaboration agreement between the University and a partner organisation)

Signed……………………………………………….

Date……………………………………………….

STATEMENT 3

I hereby give consent for my thesis, if accepted, to be available in the University's Open Access repository (or, where approved, to be available in the University's library and for inter-library loan), and for the title and summary to be made available to outside organisations, subject to the expiry of a University-approved bar on access if applicable.

Signed……………………………………………….

Date……………………………………………….

DECLARATION

This thesis is the result of my own independent work, except where otherwise stated, and the views expressed are my own. Other sources are acknowledged by explicit references. The thesis has not been edited by a third party beyond what is permitted by Cardiff University's Use of Third Party Editors by Research Degree Students Procedure.

Signed……………………………………………….

Date……………………………………………….

WORD COUNT…………………………………..

(Excluding summary, acknowledgements, declarations, contents pages, appendices, tables, diagrams and figures, references, bibliography, footnotes and endnotes)

I.   Acknowledgments

Firstly, I would like to thank my supervisor, Professor Stuart Taylor for providing me the opportunity to undertake a PhD under his guidance. Thank you for being there through the highs and lows during the three years and support along the way. I am also forever grateful to Cardiff University for providing funding for the project.

I would also like to thank the many staff members who kept the project flowing. Thank you to Dr. Tom Davies for his help with the electron microscopy and Dr. David Morgan for his assistance with the XPS. A big thank you to the team in the chemistry workshop and technical staff for all their support with the various reactors across the lab. I would like to thank all postdocs, past and present, for their help no matter how large the problem was. This project would have been impossible without all your help.

I am also indebted to all the project students who helped me throughout the project. It was a pleasure to train you all and was a great experience. Particular thanks to Andy Day, Joe Burnett, Lara Reustch, Kieran Aggett, John Turner and Aoife Taylor for their contribution to this project.

Next, I would like to thank all the PhD students who put up with me in the CCI for the past five years and thankful to everyone who made me feel welcome from day one as a young bachelor's project student. The office, labs and pubs would have been boring without all of you. So, thank you for all the cups of teas, coffees, beers and morale throughout the project. Particular thanks to Luke, Simon and DM for being there since day 1. Another thanks have to given to Nia, for helping me set up the reactors and putting up with my nagging over the past 3 years. To the rest of the 'Rigade' keep the vortex flowing without me and good luck to all of you.

I would also like to thank everyone I have met in Cardiff throughout my time here. From everyone who I have lived with over the years or spent time in the pub with it was a pleasure. Especially to Nick and Roddy for providing company at the cricket. A big thanks to Kokos for being my second home and the Cardiff University Cricket Club, especially the 'Saturday Saucers' for providing me constant entertainment throughout the years.

Finally thanks to all my friends and family back in London and across the world. In particular to my parents, your support pushed me when times were tough. I owe you both a lot.

II. Abstract

The preparation, characterisation and total oxidation of VOCs, propane and naphthalene, over ceria-zirconia, ceria-manganese and iron-manganese mixed metal oxide catalysts were investigated. Ceria-zirconia mixed metal oxides were prepared using a mechanochemical method from nitrate and carbonate precursors. Addition of low concentrations of zirconia into ceria produced the most active ceria-zirconia mixed metal oxide catalysts. Ceria-zirconia mixed metal oxides produced from nitrates were more active for naphthalene total oxidation, and the catalysts prepared from carbonates were more active for propane. The higher activity of the ceria-zirconia mixed metal oxides was ascribed to higher surface area, lower reduction temperatures and higher relative concentration of surface oxygen defects, when compared to the parent oxides.

Ceria-manganese mixed metal oxides with higher concentrations of manganese produced the most active VOC total oxidation catalysts. The optimal way to produce ceria-manganese mixed metal oxide catalysts were co-precipitation which were washed with 2 l of water. The presence of large crystallites of Mn_2O_3, higher surface area and lower reduction temperatures led to the high VOC total oxidation activity over these catalysts. Along with this, phase separation between ceria and manganese oxide crystallites led to an increase in activity.

The preparation of iron-manganese mixed metal oxides was optimised using co-precipitation. $Fe_{0.50}Mn_{0.50}O_x$ prepared using ammonium hydroxide and calcined at 500 °C produced the most active propane total oxidation catalyst of the study. However, no synergy between iron oxide and manganese oxide for naphthalene total oxidation was observed over these catalysts. The high activity of the $Fe_{0.50}Mn_{0.50}O_x$ sample was attributed to the presence of bulk and surface $Mn_3O_4,$ which was noted to be more active than Mn_2O_3 in the iron-manganese mixed metal oxide catalysts. These catalysts also had large manganese oxide crystallites and no bulk or surface contaminants from sodium or potassium which also led to the high activity.

III. Publication list

Contents

1 Introduction

1.1 Introduction to Catalysis

The first human civilisations took advantage of catalysts without specifically knowing it, during production of alcohol, bread and other food products. The term 'catalytic force' was coined by J.J Berzelius in 1835, in which he was describing materials which could accelerate the rate of a reaction whilst remaining unaffected during the reaction [1]. This occurs by the catalyst effecting the kinetics of a reaction and with the thermodynamics of the reaction unaltered. This occurs by providing the reaction with an alternative reaction pathway, which has a lower activation energy. The molecules form bonds with the catalyst, which provides this lower energy pathway, which then react on the catalyst then the final product desorbs from the catalyst, leaving it unaffected, Figure 1-1 .
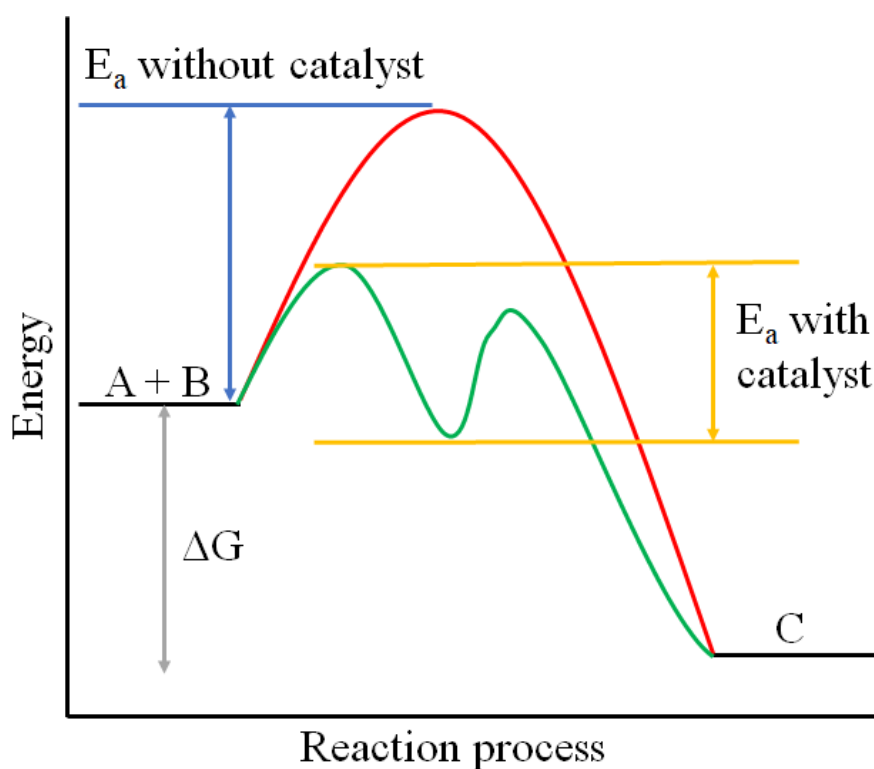
Figure 1-1: An energy level diagram of an uncatalysed and catalysed reaction

Catalysis has allowed for reactions which were previously very difficult to undertake to be carried out at more manageable conditions or allowed for reduction of costs due to lower energy requirements needed to carry out these reactions. This has led to a significant growth in the catalysis sector, with hundreds of thousands of articles, reports and books published since Berzeluis' initial finding. Industrially catalysis provides around 85-90 % of products in the chemical industry and around 80 % of all manufactured products require a catalyst at some point in their manufacture [2]. Overall catalysts are

estimated to be responsible for generation of $3.5 trillion in 2002 with this number rising every year since [3]. Therefore, catalysts are integral to daily life with the modern lifestyle impossible without them.

Catalysts are split into three categories: heterogeneous, homogeneous and biological. Heterogeneous catalysts are in a different phase to the reactants, and are normally in the form of solids which react with gas or liquid phase mixtures. Homogeneous catalysts are in the same phase as the reactants and are typically in the liquid phase. Homogeneous catalysts can be more active or selective than heterogeneous catalysts. However, they are not as robust to changes in conditions and are harder to remove from the reaction solution. Biological catalysts are normally formed of large macromolecule structures, such as enzymes. These are very active for specific reactions, however, only under certain conditions, with slight variations causing significant loss of activity and deactivation.

1.2 Introduction to Volatile Organic Compounds

1.2.1 Classification of VOCs

Volatile organic compounds (VOCs) are identified by a range of characteristics. The USA's Environmental Protection Agency describe VOCs as:

'A large group of organic chemicals that include any compound of carbon excluding carbon monoxide, carbon dioxide, carbonic acid, metallic carbides or carbonates, and ammonium carbonate' [4]. The EU define VOCs as 'any organic compound having a vapour pressure of 0.01 kPa or more at 20 °C [5].' This means the definition of VOCs is very broad and can include many different types of organic molecules, and they can be from a range of sources.

The two major sources of VOCs emissions occur either from nature, biogenic, or produced from man-made activities, anthropogenic. Biogenic sources are out of human control and are released from forests, swamps, animal, insects and volcanic activity. Biogenic VOCs account for ~75 % of total VOC emission in the USA [4] with an estimated 1,150,000,000,000 kg of VOCs emitted from natural sources [6]. Most of the biogenic VOC emissions comes from plants using VOCs to communicate or self-repair, with isoporene and monoterpene accounting for most of these biogenic VOC emissions [6,7].

Anthropogenic activities, such as large-scale chemical or petroleum refining, or smaller scale petrol stations, dry cleaning produce VOCs. VOCs are also produced at a domestic scale from a large range of sources including solvents, cleaning materials, cooking and from insulating materials [8]. However, the largest source of VOC production arises from

products or by-products of hydrocarbon oxidation. Due to advancement in catalytic technologies and legislation, such as the Gothenberg Protocol [9], VOC emissions are decreasing year upon year [4]. However, the global human population is continuously growing and modernising. This means the energy and structural requirements are increasing year upon year too. Therefore to make sure anthropogenic emissions of VOCs are controlled and limited, increased development of technologies, including catalysis is needed.

1.2.2 Propane as a VOC

Propane is a simple three carbon linear hydrocarbon which is normally in the gas phase. However, due to the nature of the molecule it can be easily compressed and liquified allowing for increased concentrations of propane can be used as a transportation fuel. The majority of propane production comes from by-products of oil and petrochemical refining [10]. Due to the low price of propane it is normally sent for further refinement or dehydrogenation into propene. However, currently there is a move away from traditional fossil fuels which had led to an increase in the use of liquified propane gas (LPG), which is propane mixed with other short chain hydrocarbons such as butane.

Over 2.4 million barrels of LPG were consumed in the US each day in 2012 [11] with this number projected to increase yearly [10]. Most of the increased propane use has been in internal combustion engines. However, LPG can also be used in large or small scale energy production. LPG can burn more efficiently than other fuels [12]. However, due to the increase in use of propane. Higher concentrations of unburnt propane are being emitted due to inefficiencies in the combustion process. This is leading to increased emission of the VOC [13].

Propane is a non-toxic VOC, however, when inhaled it can act as a mild asphyxiant. Propane can lead to suffocation if the concentrations increase above 10 % [14]. Due to the flammable nature of propane, high concentrations of propane can also become a potential fire hazard. The major reason to abate propane from the atmosphere is its increased effect on global warming. It has a global warming potential 3.3 times greater than that of carbon dioxide [15], and can stay in the atmosphere for long periods of time [16]. Therefore, it is essential to remove or reduce emissions of propane.

1.2.3 Naphthalene as a VOC

Naphthalene is the simplest polycyclic aromatic hydrocarbon and is present in the solid phase at room temperature. However it's extremely volatile and can sublime at relatively low temperatures. Naphthalene is normally obtained from heavy petroleum fractions

during fractional distillation, or from coal tar distillation [17]. Industrially naphthalene, is used as a feedstock for phthalic anhydride or insecticide production. Domestically naphthalene-based products were used in mothballs and other fumigants. However, due to the potential mutagenic and carcinogenic nature of naphthalene, its use in domestic settings has been slowly phased out.

Naphthalene is emitted during incomplete combustion of diesel [18], coal [19] and wood burning [20]. Diesel is still a common fuel for vehicles, and coal is regularly used in power plants across the developing world, significant concentrations of naphthalene are emitted, and potentially will be for many years to come. Naphthalene causes a whole range of environmental effects, which will be discussed below in section 1.3, and therefore needs to be abated from the atmosphere.

1.3 Environmental Effects of VOCs

1.3.1 Effects on ozone

VOC emissions can affect ozone concentrations in both ground (troposphere) and upper atmosphere (stratosphere) levels. Ground level ozone is a key component of photochemical smog [21] and changing concentrations in the stratosphere will lead to formation of the ozone hole, as seen in areas in Australia [22]. Both reactions occur *via* different mechanisms. Ground level ozone formation occurs by a combination of VOCs, nitrogen oxides, oxygen and sunlight:

$$NO_2 + h\upsilon \rightarrow NO + O$$
$$R - CH_3 + 2\ NO + 2\ O_2 \rightarrow RCHO + 2\ NO_2 + H_2O$$
$$O + O_2 \rightarrow O_3$$
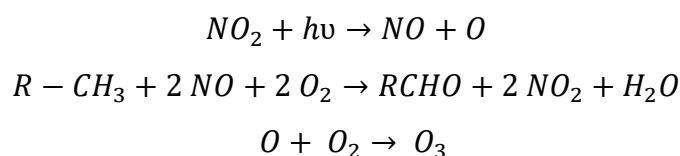
Ground level ozone causes problems for human health, such as breathing problems and tissue injury. With concentrations of ground level ozone increasing year upon year, this has led to increased cases of respiratory problems, which may cause a loss of billions in dollars of productivity and required healthcare [23]. It is also a pathogen in plant-life, making its presence significantly damaging for all land living life [22].

Ozone is naturally present in the upper atmosphere and helps protect the earth's surface from the harmful UV radiation emitted from the sun. However, if a VOC is present in the upper atmosphere, it can act as a catalyst for ozone depletion following the mechanism below [24]:

$$X + O_3 \rightarrow XO + O_2$$
$$XO + O_3 \rightarrow X$$
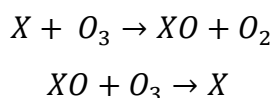
This reaction is more pronounced in chlorine containing compounds, however, it is noted to occur in aromatic VOCs [25]. Due to the breaking down of the ozone layer in the upper atmosphere, increased levels of UV radiation will enter the earth's atmosphere. This will lead to increased exposure to UV radiation to humans causing higher cases of sunburn and skin cancer. The increased levels of UV radiation will also effect surface concentrations of ozone too. With the ground level ozone formation mechanism requiring a source of radiation, the increased UV radiation will allow this reaction to occur more freely, thus leading to more ground level ozone [26]. With both reactions occurring via the presence of a VOC, it is essential that emissions of VOCs are reduced.

1.3.2 Formation of nitrogen oxides
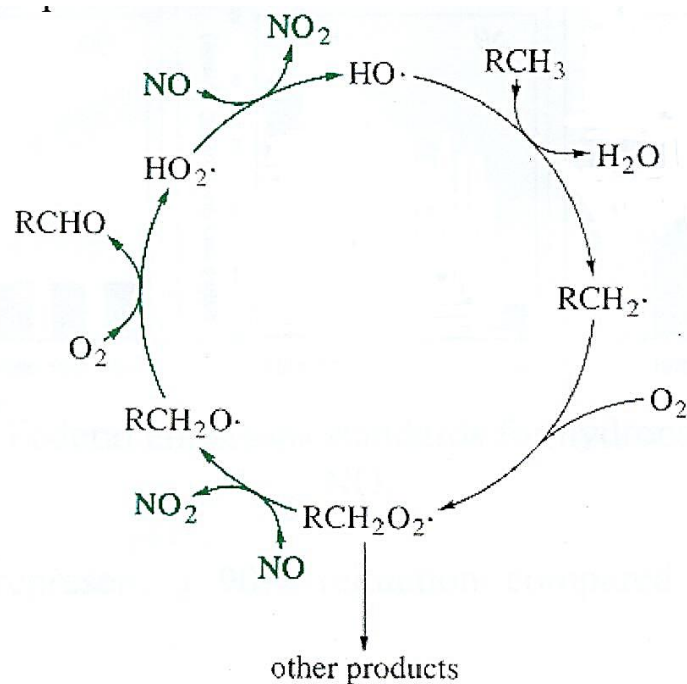
Figure 1-2: Formation cycle of compounds which contribute to smog formation from reactions of VOCs, nitrogen oxides and oxygen [27]

Nitrogen oxides are formed of nitrogen species with any number of oxygen atoms bound to it. The formation of nitrous oxides is shown in Figure 1-2, and involves several different species including VOCs. These nitrogen oxide species contribute to ground level ozone formation, along with smog, therefore it is essential to stop formation. Nitrogen oxides also have a secondary effect on the environment, which also causes significant harm, in the form of acid rain. Nitrogen oxides can react with water vapour in air and form nitric and nitrous acid, following the equations below [28]:

$$4NO_2 + O_2 + 2H_2O \rightarrow 4HNO_3$$
$$4NO + O_2 + 2H_2O \rightarrow 4HNO_2$$
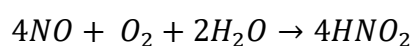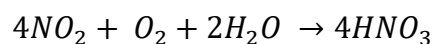
These acids then lower the pH of the rain, causing the formation of acid rain. Acid rain can cause significant damage to stone structures via erosion and weathering. It can also acidify soil and water causing problems for plant and aquatic life. This will cause problems in the ecosystem which in turn will affect food and water supplies for human consumption. Therefore to reduce the effects of acid rain and increased levels of smog, VOCs emissions need to be reduced.

1.3.3 Formation of particulate matter and soot

Particulate matter is a combination of solid particles and liquid droplets found in air. It is defined by its size in micrometres ranging from coarse to ultrafine particulates [29]. The majority of particulate matter occurs naturally from sand, dust and biogenic sources [30]. However, soot is the main particulate matter emitted from anthropogenic activities and occurs during VOC combustion. Soot, a mass of impure carbon particles, is formed during incomplete combustion of organic compounds, when the C/O ratio is below 0.5 [31]. However, soot can be formed at either higher or lower C/O ratios depending on the nature of the VOC being combusted [32]. Diesel engines convert 10-20 % of its fuel into soot [32], with a portion of it arising from poly aromatic hydrocarbons [33].

Soot formation from poly aromatic hydrocarbons can occur *via* two pathways. Either the poly aromatic hydrocarbon can condense and polymerise around an existing aromatic structure. Or the aromatic hydrocarbon can fragment and condense with other smaller linear or branched hydrocarbons to form soot. However, the fragmentation route is significantly slower than the condensation route [31]. Both condensation reactions occur during reactions with water vapour in the atmosphere. Other gas phase molecules, such as sulfur oxides, nitrogen oxides along with ammonium based molecules can also allow these processes to occur [34].

Soot is a major component of smog and can affect the environment in this manner [35]. Also due to the other impurities present in soot, it can lead to damage, or acidification of water supplies, which can significantly harm aquatic life and ecosystems [36]. High levels of soot inhalation or exposure can cause a range of health problems. Soot inhalation can affect both the cardiovascular and respiratory systems. It also reported to be carcinogenic due to its toxic nature at high concentrations [37]. Therefore to keep these environmental and health problems to a minimum, VOC emissions and especially those coming from poly aromatic hydrocarbons, such as naphthalene, need to be significantly reduced.

1.3.4 Greenhouse effect

As mentioned previously, some VOCs have a much higher global warming potential than carbon dioxide. Along with this, VOCs can remain stable in the upper atmosphere for significantly longer periods of time compared to carbon dioxide. Therefore, with higher and higher concentrations of pollutants including VOCs in the atmosphere, this will lead to increased effects of global warming. This will cause an increase in the greenhouse effect which will then lead to an increase in the surface temperature. The increase in surface temperature will lead to more VOCs being evaporated into the higher atmosphere making the greenhouse effect worse. This will become a continuous cycle leading to very high surface temperatures which will effect all forms of life. Therefore the reduction in VOC emissions will be required.

1.4 Current Methods of Removing VOCs

1.4.1 Thermal oxidation

Thermal oxidation, or incineration, is the simplest way to remove VOCs from exhaust or waste streams [38], it is oxidation over a very hot flame. It can be used for a variety of VOCs, making this technique very flexible. Depending on the VOC being destroyed, the main products are carbon dioxide and water. As mentioned above, carbon dioxide has less of an impact on the environment compared to emission of the original VOCs.

However, this simplicity and flexibility comes with its own disadvantages. It is very expensive to run a thermal incinerator. High temperatures are required to combust many VOCs therefore some incinerators have to run above 1000 °C. Most of the energy required to run a VOC incineration plant will come from fossil fuels, therefore adding to the greenhouse gases emitted during this process. The conditions in the incineration have to be carefully managed otherwise harmful by-products may also be formed. These by-products arise from reactions between impurities from the VOC, the VOC itself or air. By-products such as dioxins, nitrogen oxides and soot can be emitted. Therefore due to these factors other VOC abatement technologies have been researched.

1.4.2 Absorption methods

Absorption methods involve the VOC absorbing into a suitable liquid. Due to different types of VOCs available, a range of absorbents can be used including toluene [39], water [40] or silicone oil [41,42]. The absorbent is then treated using oxidation agents, heated, biological agents or centrifuged to remove the VOC contaminant. Like incineration, this method has been commercialised. A key advantage of this method is the potential recuperation of the VOC which can be purified and used in further chemical processes.

Any production of potential by-products is reduced in this process therefore making the process more environmentally friendly compared to incineration.

However, due to the specific conditions required to use this method for singular VOC abatement, this will make it difficult to abate mixtures of VOCs from waste streams. Also due to the multiple step process required to regenerate the absorbent, this will complicate the process leading to increased costs and time required for this method. Some VOC contaminants can't be removed from the absorbent. If the absorbent needs to be constantly replaced, this will increase the costs required for the method from waste management and absorbent replacement.

1.4.3 Adsorption methods

Adsorption methods comprise of the VOC contaminant to be adsorbed onto a solid material. The adsorbate is then heat treated to remove the VOC, sometimes regenerated and then used for adsorption again. Zeolites [43] and activated carbon [44] based materials are normally used for adsorption. This is due to the porous structure and very high surface area associated with these materials, which allow for maximum adsorption to occur on the surface. Like absorption methods, different materials characteristics are needed for different VOCs. However, this method can be used for both gas and liquid phase reactions, which increases the variety of this method compared to the absorption method.

As seen from the absorption, the disadvantage of this method are the multiple steps required to remove VOCs from the adsorbent. This will add to the costs and time required for this method. Also the regenerative process normally requires high temperatures and harsh oxidising environments. This affects the adsorbing properties of the material, resulting in less VOC contaminants being adsorbed on the material upon successive uses. After multiple uses the material will then become nonviable for adsorption use and will have to be deposed of, increasing costs and time required for changing the material.

1.4.4 Catalytic oxidation

An alternative method to the above methods is catalytic oxidation of VOCs. This method uses a similar set up to the thermal incineration, however the VOC containing gas stream is passed over a catalyst bed rather than a heated flame. As seen in section 1.1, addition of a catalyst reduces the activation energy and total energy required for the reaction. This means the temperature required to oxidise the VOCs will be significantly reduced compared to the non-catalysed thermal oxidation reactions. This will lead to decrease in energy requirement of the process leading to a decrease in costs too [45]. The presence

of the catalyst will also increase the selectivity of the reaction leading to decreased formation of by-products. The reduction in by-products will also occur from the lower temperature of the reaction.

Catalytic oxidation is also very flexible compared to the adsorption and absorption methods. Only one step is required for catalytic oxidation of VOCs making the process much simpler. Also due to the higher selectivity of the catalyst, only one catalyst bed will be required if a range of VOCs are being abated. Adsorption and absorption methods may require a range of materials to be used to abate the mixture of VOCs, which adds to the complexity of these methods compared to the catalytic oxidation. Also catalytic oxidation can remove VOCs from a large range of concentrations whereas the other methods are normally limited to concentrations above 1 % [38].

VOC total oxidation catalysts can be formed from a range of materials which will be discussed in the section below.

1.5 VOC total oxidation catalysts

1.5.1 Supported nanoparticles on metal oxides

Currently supported noble metal oxides make up ~75 % of VOC total oxidation catalysts [46]. These catalysts are based on either platinum, palladium, silver and gold nanoparticles which can be alloyed with other closely related metals [47]. The nanoparticles are then deposited on metal oxide based supports. The supports are categorised on their activity during the oxidation reactions and are characterised as inert, silica or alumina, or reducible, ceria, iron oxides or manganese oxides. Platinum and palladium based catalysts are the most commonly used oxidation catalyst and have been intensely studied since the 1970's [48].

High activity of noble metal catalysts is reported for a wide range of VOC total oxidation reactions. Platinum is noted to be more active than palladium for a range of VOC total oxidation reactions. The higher activity is attributed to the small nanoparticles of the noble metal, which lead to increased dispersion of the metals and more active sites for VOC total oxidation [49,50]. The particle side can also effect the redox mechanism, oxygen binding on the nanoparticle and the reaction pathway that occurs over the nanoparticle [51]. Other factors, such as the precursor used to prepared the catalyst, potential poisoning and nature of the support also significantly affect noble metal catalysts [51].

However, this increased activity comes at a cost both economically and chemically. Due to the rarity of the noble metals this means the price of the metals are significantly more

expensive compared to the transition metal oxide catalysts. Even though only small amounts of noble metals are supported on the catalysts (typically between 0.1-5 %), the price is higher compared to the transition metal oxide alternatives. Due to the smaller quantities of active sites in noble metal oxide catalysts compared to transition metals they are more susceptible to deactivation [52]. Deactivation of noble metal catalysts can arise from a range of sources and occur instantaneously or over a long period of time [53]. Small species such as chlorine [52–54] and sulfur [55,56], present in the precursor or in the reactant feed, can significantly affect noble based catalysts. Chlorine causes the redispersion of noble metal nanoparticles and changes the oxidation state of platinum, making it less effective as a VOC total oxidation catalyst [52]. Sulfur and other small molecules can bind irreversibly with platinum and palladium nanoparticles leading to inhibition of the active site on noble metal catalysts. As mentioned above, particle size of the noble metal can affect the VOC total oxidation activity of a catalyst. Thermal degradation can affect the size of the nanoparticle by sintering the particle leading to loss of active phase or crystallisation of the material. This is determined by the melting point of the noble metal, and with most VOC total oxidation reactions occurring at high temperatures, this will cause thermal degradation to occur [57].

To counteract the high cost of the components and deactivation occurring in the supported noble metal catalysts, a shift toward noble metals alloyed with transition metals has been occurring. Vanadium and ceria alloyed with platinum is reported to increase naphthalene [58] and methane [59] total oxidation activity respectively. Cobalt has been used to enhance both gold [60] and platinum [61] catalysts for VOC total oxidation reactions. Along with increased activity, addition of transition metals can decrease the effects of sulphur poisoning on noble metal catalysts [62].

Recent discoveries report that metal oxide catalysts can have higher VOC total oxidation activity compared to supported noble metals. Manganese oxides had significantly higher ethyl acetate and hexane total oxidation activity compared to supported platinum catalysts [63]. The increased thermal stability of metal oxide catalysts, resistance to poisons and lower cost of transition metal oxide catalysts has led to increased research on these materials.

1.5.2 Metal oxide catalysts

1.5.2.1 Ceria

Cerium is the most abundant rare earth metal with bastnaesite and monazite as its main ores [49]. Cerium can be easily oxidised to produce cerium dioxide (or ceria) [64], which

has a cubic fluorite structure with Fm3m space group [65]. Ceria is used in a wide range of industrial applications, including solid oxide fuel cells, removal of sulfur oxides from gaseous streams, treatment of liquid waste, photocatalytic water splitting and water gas shift reactions [65–67]. Ceria is most prevalently used in oxidation reactions and three-way catalysts for vehicle emission control [68,69]. Ceria based materials have been extensively investigated over the past 20 years, with a number of publications a year increasing from under 500 to over 2000 a year between 1994-2015 [66]. This is due to ceria's ability to change between Ce^{4+} and Ce^{3+} oxidation states and form non-stochiometric CeO_{2-x}. This forms defect sites on the surface of the lattice, which forms active sites and oxygen defect sites. Ceria has a high melting point, making it resistant to thermal degradation and increasing the stability of the material during VOC total oxidation reactions, Table 1-1.

Table 1-1: Selected studies of ceria for VOC total oxidation reactions

VOC	Preparation Method	Concentration of VOC / %	GHSV / h^{-1}	T_{50} / °C	Ref.
Benzene	Citric acid	0.17	60,000	526	[70]
Toluene	Co-precipitation	0.70	7,600	600	[71]
	Citric acid	0.17	60,000	380	[70]
	Sol-gel	0.10	200,000	245	[72]
	Commercial sample	0.70	7,600	210	[73]
	Hydrothermal	0.05	22,500	220	[74]
Chlorobenzene	Sol-gel	0.10	15,000	-	[75]
Naphthalene	Co-precipitation	0.01	60,000	275	[76]
	Urea	0.01	60,000	175	[76]
	Nano-casting with KIT-6	0.045	50,000	225	[77]
	Combustion with ethyl glycol	0.045	45,000	200	[78]
Trichloroethylene	Thermal decomposition of nitrate salts	0.01	15,000	150	[79]
Propane	Modified co-precipitation	1.00	-	-	[80]
	Hydrothermal	0.20	30,000	-	[81]
Formaldehyde	Co-precipitation	0.05	21,000	250	[82]
	Co-precipitation	0.058	30,000	250	[83]
Methanol	Reverse nano-emulsion	0.50	-	340	[84]
	Commercial sample	0.70	7,600	260	[73]

Methane	Polyol based annealing	1.00	4,000	-	[85]
	Co-precipitation	1.00	34,000	672	[86]
Acetone	Reverse nano-emulsion	0.50	-	325	[84]

The method used to prepare ceria has a significant effect on its activity for VOC total oxidation. The preparation method used to synthesise the ceria, will affect the surface area and crystallite size of the material. Both of these effects are reported to have the greatest influence on ceria for VOC total oxidation [72]. These factors are also affected by the calcination temperature used to prepare the ceria, along with other variables. The nature of the VOC also has a significant effect on the activity of ceria for total oxidation. Ceria is noted to have poor performance for total oxidation of VOCs containing chlorine species [66]. Also as seen in Table 1-1, ceria has low propane total oxidation activity. This may have arisen from the method used to prepare the ceria, which produced ceria with low surface area.

1.5.2.2 Zirconia

Table 1-2: Selected studies of zirconia for VOC total oxidation reactions

VOC	Preparation Method	Concentration of VOC / %	GHSV / h^{-1}	T_{50} / °C	Ref.
Toluene	Commercial	0.07	-	500	[87]
	Commercial	0.10	30,000	275	[88]
	Silica-nanosphere	0.40	-	450	[89]
Propene	Co-precipitation	2.30	40,000	-	[90]
Methane	Co-precipitation	1.00	-	550	[91]
	Urea hydrolysis	2.00		700	[92]
Chloromethane	Co-precipitation	1.00	-	450	[91]
Dichloromethane	Commercial	0.10	30,000	350	[88]
Trichloroethylene	Commercial	0.10	30,000	400	[88]
Formaldehyde	Hydrothermal	-	52,000	277	[93]

Zirconium is a transition metal, which has seen increased use in recent years. It is primarily mined from zircon ore. Many of the zirconium containing ores are contaminated with an array of other transition metals with hafnium is the most common contaminant [94]. Zirconium can be easily oxidised into zirconium dioxide (or zirconia). Zirconia has three polymorphs, monoclinic, tetragonal and cubic, which are dependent on the temperature used to prepare the zirconia [95]. Zirconia has a number of commercial uses, however its main uses are in refractories, ceramics and advanced ceramics and catalysts [96]. The percentage of zirconia used for catalysts rose from 6 % to 12 % between 2002-

2005, and this number has been rising ever since. Industrially, zirconia is used to upgrade hydrocarbons with functional groups [97,98].

Like ceria, zirconia can also form oxygen defect sites. The defects arise from paramagnetic F-centres, which can excite and activate surface oxygen species [99]. The ability to activate oxygen, and thermal stability of zirconia, has lead to an increase in studying the material for oxidation reactions. It is mainly used to support noble metal nanoparticles, however, zirconia is also noted to be active for VOC total oxidation, Table 1-2. Zirconia has poor activity for naphthalene total oxidation when prepared using urea and co-precipitation [100]. However, rather than a pure metal oxide catalyst, zirconia is added to another metal oxide to enhance the catalytic activity of the material. This will be mentioned in later sections of this chapter.

1.5.2.3 Manganese oxides

Table 1-3: Selected studies of manganese oxides for VOC total oxidation reactions

VOC	Preparation Method	Concentration of VOC / %	GHSV / h^{-1}	T_{50} / °C	Ref.
Ethylene	Solution combustion	0.10	19,100	225	[101]
Propylene	Solution combustion	0.10	19,100	200	[101]
Naphthalene	Thermal decomposition of nitrates	0.045	75,000	210	[102]
Toluene	Solution combustion	0.10	19,100	210	[101]
	Hydrothermal	0.10	32,000	210	[103]
	Urea-nitrate combustion	0.06	-	240	[104]
	Hydrothermal	0.05	22,500	210	[105]
	Co-precipitation	0.10	20,000	175	[106]
	Citrate	1.00	-	210	[107]
	Calcination of commercial materials	0.10	-	250	[108]
Propane	Decomposition with acids	0.80	-	240	[109]
Ethanol	Urea-nitrate combustion	0.16	-	220	[104]
	Reflux	0.40	16,000	150	[110]
	Citrate	1.00	-	200	[107]
Ethyl acetate	Urea-nitrate combustion	0.18	-	240	[104]

Acetaldehyde	Reflux	0.40	16,000	195	[110]
Ethyl acetate	Citrate	1.00	-	252	[107]
Methane	Co-precipitation	1.00	36,000	350	[111]
Benzene	Oxalic acid	0.01	-	200	[112]

Manganese is an abundant material and can be easily oxidised. This is shown by thirty known manganese containing ores reported across the globe [113]. Manganese is stable in many oxidation states, however, the most common oxides are MnO, MnO_2, Mn_2O_3 and Mn_3O_4. Industrially a majority of manganese consumption occurs by the steel industry and upgrading ferroalloys [114]. It is also used for a number of other applications, including electronics and batteries, along with agriculture uses [115]. Manganese oxides are catalytically active for a wide range of reactions, including: alcohol decomposition, partial and total oxidation, reduction, decomposition of sulphur species, and can act as adsorption materials [116]. It is reported than manganese oxides are the most promising metal oxide for total oxidation of short-chain VOCs [38], due to their low toxicity and cost of the catalytic material. This is seen in the range of different VOCs oxidised over manganese oxide catalysts, Table 1-3.

The VOC total oxidation performance of manganese oxides depend on the surface area, preparation method and oxidation state [25]. The oxidation state of manganese is reported to have a significant effect on naphthalene total oxidation activity [102], with Mn_2O_3 reported to be the most active phase. The oxidation state of manganese also affects toluene total oxidation, with Mn_3O_4 reported to be the manganese oxide phase with the highest activity [108]. Manganese's ability to remain stable at a number of oxidation states allows for defect site formation, which leads to increased defect sites, oxygen mobility and vacancies [63].

1.5.2.4 Iron oxides

Iron is one of the most abundant and cheapest materials available for chemical uses. Iron is commonly found in hematite, goethite and jarosite ores on the earth's surface [117], and over 3,000 million tonnes of iron ore is extracted each year [118]. Iron can be easily oxidised, and like manganese, it can be stable in a range of oxidation states. Iron oxides are normally found in the FeO, Fe_3O_4 or Fe_2O_3 phases, depending on the oxidation state of the iron. Like many of the transition metals, iron has a variety of uses. It is the main component of steel, found in pigments for paints, adsorbents for water and gas production along with a range of other uses [119]. Iron oxides are a vital part of the catalyst industry with many large-scale processes using the material. Ammonia production, water gas shift and Fischer-Tropsch reactions all use either iron oxides as bulk catalysts or for supports

for nanoparticles [119,120]. Iron compounds are one of the first oxidation catalysts reported in the literature. Aqueous oxidation of tartaric acid was conducted over iron [121] and since then a number of water treatment catalysts have been developed based on iron materials [122]. The use of iron oxides for gas phase VOC total oxidation is not that common, compared to other metal oxides, however, examples are shown in Table 1-4.

Table 1-4: Selected studies of iron oxides for VOC total oxidation reactions

VOC	Preparation Method	Concentration of VOC / %	GHSV / h^{-1}	T_{50} / $°C$	Ref.
Ethanol	Citrate	1.00	-	260	[107]
	Co-precipitation	1.00	-	180	[123]
Ethyl acetate	Citrate	1.00	-	290	[107]
Toluene	Citrate	1.00	-	260	[107]
	Nanocasting	0.10	30,000	185	[124]
Acetone	Co-precipitation	0.70	7,600	200	[125]
Propane	Nanocasting	0.80	20,000	305	[124]
	Co-precipitation	2.00	-	400	[123]
	Co-precipitation	0.50	15,000	-	[126]
Naphthalene	Co-precipitation	0.01	60,000	300	[76]
Methanol	Co-precipitation	0.70	7,600	280	[127]
Methane	Co-precipiation	1.50	-	460	[128]

The surface area and morphology affects the VOC total oxidation activity of iron oxides. The morphology of the iron oxide affected the surface and oxygen defects, along with its reducibility, which was a significant factor for toluene total oxidation over iron oxides [124]. However, for a number of VOC total oxidation reactions, iron has poor activity, although, iron has shown some promise as an additive to other metal oxide catalysts. This will be discussed in a later section of this chapter.

1.5.3 Mixed metal oxides

1.5.3.1 Ceria-zirconia mixed metal oxides

Ceria has appreciable activity for a variety of VOC total oxidation reactions, section 1.5.2.1, however it has some limitations. It has noticeable thermal resistance, however, over extended periods of time ceria can sinter leading to a decrease in surface area, oxygen storage capacity and overall catalytic activity [129]. Addition of a secondary metal into the ceria lattice minimises these effects by stabilising the surface area and crystallite size. Zirconia can incorporate into the cubic fluorite structure of ceria [130]. This will lead to increased surface defect sites on the ceria-zirconia oxide lattice. This will lead to an increase surface oxygen species, leading to an increase in oxidation activity. This is observed by decrease in surface reduction temperatures when 20 %

zirconia is added into the ceria lattice [87]. Addition of zirconia into ceria has been shown to increase the thermal stability and increase the oxygen storage capacities compared to pure ceria [131,132]. Along with these, the surface area of ceria-zirconia mixed metal oxides is reported to increase compared to the pure metal oxides [133,134]. Industrially ceria-zirconia mixed metal oxides have been exclusively used for oxidation catalysts. In particular it has helped the development of three-way catalysts for catalytic convertors [132,135]. With all these factors considered, ceria-zirconia mixed metal oxide catalysts have shown appreciable activity for VOC total oxidation reactions, as shown in Table 1-5.

Table 1-5: Selected studies of ceria-zirconia mixed metal oxides for VOC total oxidation reactions

VOC	Preparation Method	Optimum Ce:Zr ratio	Concentration of VOC / %	GHSV / h^{-1}	T_{50} / °C	Ref.
Propane	Citric acid	$Ce_{0.33}Zr_{0.67}O_x$	0.08	60,000	540	[136]
Naphthalene	Urea	$Ce_{0.75}Zr_{0.25}O_x$	0.02	-	225	[137]
	Urea	$Ce_{0.99}Zr_{0.01}O_x$	0.01	135,000	210	[100]
	Co-precipitation	$Ce_{0.99}Zr_{0.01}O_x$	0.01	135,000	210	[100]
Methane	Co-precipitation	$Ce_{0.83}Zr_{0.17}O_x$	1.00	20,000	600	[138]
	Urea	$Ce_{0.75}Zr_{0.25}O_x$	2.00	-	525	[92]
Toluene	Co-precipitation	$Ce_{0.50}Zr_{0.50}O_x$	-	12,000	240	[139]
	Co-precipitation	$Ce_{0.94}Zr_{0.06}O_x$	-	-	330	[87]
	Commercial	$Ce_{0.80}Zr_{0.20}O_x$	0.10	30,000	205	[88]
1,2-Dichloroethane	Commercial	$Ce_{0.50}Zr_{0.50}O_x$	0.10	30,000	295	[140]
	Commercial	$Ce_{0.50}Zr_{0.50}O_x$	0.10	30,000	295	[88]
Trichloroethylene	Commercial	$Ce_{0.15}Zr_{0.85}O_x$	0.10	30,000	385	[140]
	Commercial	$Ce_{0.15}Zr_{0.85}O_x$	0.10	30,000	385	[88]
Hexane	Commercial	$Ce_{0.80}Zr_{0.20}O_x$	0.10	30,000	250	[140]
Ethyl acetate	Hydrothermal	$Ce_{0.70}Zr_{0.30}O_x$	1.21	335	325	[141]

Addition of zirconia into the ceria decreased the T_{50} temperature, the temperature at which 50 % of the VOC concentration has been removed, for many of the VOC total oxidation reactions, when compared to the parent oxide. The optimal ceria-zirconia ratio changes depending on the VOC oxidised. However, many of the reactions have increased activity over ceria-zirconia mixed metal oxides which are ceria rich. Phase separation causing the formation of bulk zirconia phases are reported to be inactive for naphthalene total oxidation reactions [100]. Increased activity in doped ceria was also ascribed to increased surface oxygen species and defects [142].

1.5.3.2 Ceria-manganese mixed metal oxides

Along with zirconia, ceria has also been doped with first row transition metals. Addition of copper and iron oxides into the ceria lattice led to increased naphthalene [142] and soot [143] total oxidation compared to the parent ceria. However manganese as a dopant has shown the most promise for ceria. Addition of manganese into the ceria causes migration of lattice oxygen, leading to increased surface oxygen for total oxidation reactions [66,67]. The combination of ceria and manganese can also stabilise the active surface oxygen, leading to increased amounts of oxygen available for total oxidation reactions [144,145]. The ceria can also stabilise higher oxidation states of manganese, which are reported to have higher VOC total oxidation activity [146]. Ceria-manganese mixed metal oxides have shown high activity for total oxidation of small molecules (CO and NO) [83,146–148]. Along with this ceria-manganese mixed metal oxides have been used for wet VOC total oxidation. Ceria-manganese mixed metal oxides were highly active for aqueous phase phenol total oxidation due to electron rich surface activating adsorbed oxygen [105,149]. Along with aqueous phase VOC total oxidation, ceria-manganese mixed metal oxides have also shown high total oxidation activity for a range of gas phase VOCs, Table 1-6.

Table 1-6: Selected studies of ceria-manganese mixed metal oxides for VOC total oxidation reactions

VOC	Preparation Method	Optimum Ce:Mn ratio	Concentration of VOC / %	GHSV / h^{-1}	T_{50} / °C	Ref.
Toluene	Hydrothermal	$Ce_{0.15}Mn_{0.85}O_x$	0.10	32,000	160	[103]
	Hydrothermal	$Ce_{0.40}Mn_{0.60}O_x$	0.05	22,500	190	[74]
	Combustion	$Ce_{0.50}Mn_{0.50}O_x$	0.06	-	235	[104]
	Co-precipitation	$Ce_{0.25}Mn_{0.75}O_x$	0.10	60,000	220	[150]
Benzene	Co-precipitation	$Ce_{0.25}Mn_{0.75}O_x$	0.10	60,000	180	[150]
Chlorobenzene	Sol-gel	$Ce_{0.14}Mn_{0.86}O_x$	0.10	15,000	200	[151]
	Co-precipitation	$Ce_{0.25}Mn_{0.75}O_x$	0.10	60,000	315	[150]
Hexane	Co-precipitation	$Ce_{0.50}Mn_{0.50}O_x$	0.20	80	210	[152]
Propane	Nanocasting	$Ce_{0.60}Mn_{0.40}O_x$	-	10,000	232	[80]
Methane	Citric acid	$Ce_{0.40}Mn_{0.60}O_x$	1.00	60,000	460	[153]
Formaldehyde	Co-precipitation	$Ce_{0.20}Mn_{0.80}O_x$	0.058	30,000	100	[83]
	Modified co-precipitation	$Ce_{0.50}Mn_{0.50}O_x$	0.058	21,000	80	[82]
Ethanol	Combustion	$Ce_{0.50}Mn_{0.50}O_x$	0.16	-	175	[104]
Ethyl acetate	Combustion	$Ce_{0.50}Mn_{0.50}O_x$	0.18	-	200	[104]
Acetic acid	Combustion	$Ce_{0.50}Mn_{0.50}O_x$	0.14	-	210	[104]

O-xylene	Co-precipitation	$Ce_{0.25}Mn_{0.75}O_x$	0.10	60,000	250	[150]

The majority of the ceria-manganese mixed metal oxides active for VOC total oxidation are manganese rich. This was due to the phase segregation of manganese oxides [104], and increased oxygen vacancies observed in the manganese rich mixed metal oxides [103]. Synergy between the two metal oxides have been noted for toluene and benzene total oxidation. With both ceria [154] and manganese oxides [102] noted to be active for naphthalene total oxidation, it can be assumed that synergy between the two metals will be observed for naphthalene and propane total oxidation.

1.5.3.3 Iron-manganese mixed metal oxides

Along with being a dopant, manganese oxides have also had additional metals doped into the lattice to improve the total oxidation activity of the material. Addition of first row transition metals into manganese oxide led to an increase in activity for a range of reactions. Copper-manganese mixed metal oxides reported to have increased total oxidation of naphthalene [155], benzene [156,157] and CO [158] compared to the parent oxide. Cobalt is reported to be an extremely active metal for a range of reactions including propane total oxidation [159]. Addition of manganese into the cobalt led to an increase in activity for a range of VOC total oxidation reactions [109,111,160]. Increased activity of the manganese containing mixed metal oxides were attributed to formation of solid solutions and changing of redox properties of the parent oxide upon addition of the second oxide [158,160].

Table 1-7: Selected studies of iron-manganese mixed metal oxides for VOC total oxidation reaction

VOC	Preparation Method	Optimum Fe:Mn ratio	Concentration of VOC / %	GHSV / h^{-1}	T_{50} / $°C$	Ref.
Acetone	Co-precipitation	$Fe_{0.50}Mn_{0.50}O_x$	-	-	125	[161]
Trichloroethylene	Co-precipitation	$Fe_{0.40}Mn_{0.60}O_x$	-	-	200	[161]
Ethanol	Citrate	$Fe_{0.25}Mn_{0.75}O_x$	1.00	-	230	[107]
	Co-precipitation	$Fe_{0.50}Mn_{0.50}O_x$	1.00	15,000	180	[123]
Toluene	Citrate	$Fe_{0.25}Mn_{0.75}O_x$	1.00	-	280	[107]
Propane	Co-precipitation	$Fe_{0.50}Mn_{0.50}O_x$	2.00	15,000	300	[123]

Iron has also been used as a dopant for cobalt based catalysts. Improvement to cobalt oxide from iron dopants is noted for methanol [162], ethanol [163] and CO [164] total oxidation. Along with synergy between other first row transition metals, both iron oxide and manganese oxide have shown synergy for a range of reactions. Iron-manganese

mixed metal oxides showed synergy for olefin conversion [165] and dehydrogenation reactions [166]. Along with this, iron-manganese mixed metal oxides also showed appreciable activity for propane and propene partial oxidation [167]. Iron-manganese mixed metal oxides have been noted to be active for soot total oxidation [168], along with a handful of VOC total oxidation reactions, .

Increased catalyst activity occurs due to smaller iron ions replacing the manganese in the lattice of the mixed metal oxide. This leads to defect formation leading to increased oxygen vacancies on the surface, which changes the redox activity of the surface [107].

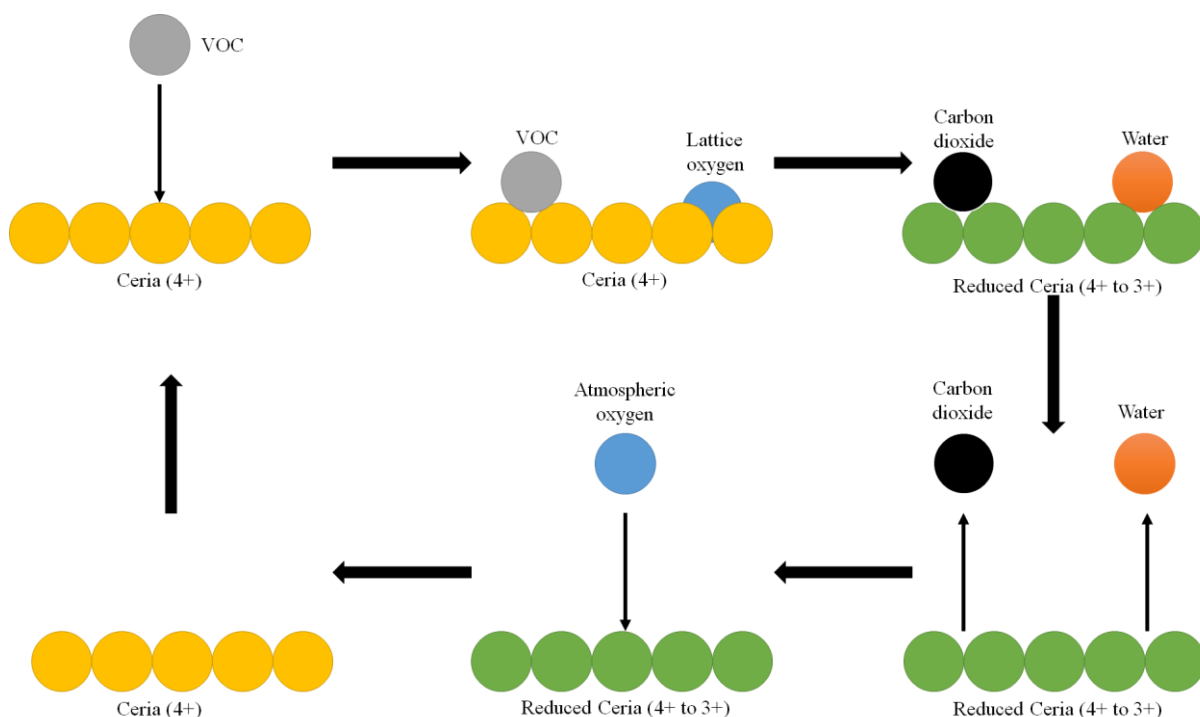## 1.6 Mechanism of total oxidation

Figure 1-3: Mars-van Krevelen mechanism using an example catalyst (ceria) for VOC total oxidation

The Mars-van Krevelen mechanism [169] is the reported reaction pathway for both propane [170] and naphthalene total oxidation [137], on copper-ceria mixed metal oxides supported on alumina and ceria-zirconia respectively. The reaction follows the scheme in Figure 1-3 and starts with adsorption of the VOC onto the catalyst surface. The VOC then becomes oxidised by lattice oxygen into carbon dioxide and water. These products will then desorb off the surface leaving the surface of the metal oxide reduced. Then an oxygen molecule from the reaction mixture will adsorb onto the surface to reoxidise the surface and allow the reaction to occur again. This mechanism will occur quicker if the surface is unstable from defect sites or oxygen vacancies which allows the recycling of oxygen to occur at a faster rate.

1.7 Project Aims

The main aim of this project is to produce catalysts which are highly active and selective for naphthalene and propane total oxidation. To achieve this, the catalysts must perform both reactions at as low a temperature possible and for extended periods of time. Three catalyst systems will be investigated for both reactions, ceria-zirconia, ceria-manganese and iron-manganese mixed metal oxides.

Catalysts can be prepared using a variety of different methods, with each method effecting the total oxidation activity of the catalyst, as seen in the various summary tables in this chapter. Therefore we hope to optimise the preparation method used for each of the three catalyst systems and understand the important catalyst features controlling the total oxidation reactions.

Along with the investigation of catalytic activity, the catalysts will be characterised using a wide range of bulk and surface methods. The aim of this it to study the effects of addition of metal oxide dopants into the parent oxide and to correlate any factors with the propane or naphthalene total oxidation activities.

1.8 References

[1]   J.. Berzelius, Quelques Idées sur une nouvelle Force agissant dans les Combinaisons des Corps Organiques, Ann. Chim. (1836).

[2]   G.J. Hutchings, C.R.A. Catlow, C. Hardacre, M.G. Davidson, Catalysis making the world a better place: satellite meeting, Philos. Trans. R. Soc. A Math. Phys. Eng. Sci. 374 (2016) 20150358. doi:10.1098/rsta.2015.0358.

[3]   D. Filmore, Catalysts Rising, Ind. Facts Fig. (2002) 33.

[4]   U.S. Environmental Protection Agency, Volatile Organic Compounds Emissions, Rep. Environ. (2011).

[5]   COUNCIL DIRECTIVE 1999/13/EC of 11 March 1999 on the limitation of emissions of volatile organic compounds due to the use of organic solvents in certain activities and installations, Off. J. Eur. Communities. (1999).

[6]   A. Guenther, C. Nicholas Hewitt, E. David, R. Fall, G. Chris, G. Tom, H. Peter, L. Klinger, L. Manuel, W.A. Mckay, P. Tom, B. Scholes, R. Steinbrecher, R. Tallamraju, J. Taylor, P. Zimmerman, A global model of natural volatile organic compound emissions s Raja the balance Triangle changes in the atmospheric accumulation rates of greenhouse Triangle Several inventories of natural and Exposure Assessment global scales have been two classes Fores, J. Geophys. Res. 100 (1995) 8873–8892. doi:10.1029/94JD02950.

[7]   J. Kesselmeier, M. Staudt, Biogenic Volatile Organic Compounds (VOC): An Overview on Emission, Physiology and Ecology, J. Atmos. Chem. 33 (1999) 23–88. doi:10.1023/A:1006127516791.

[8]   S. Scirè, L.F. Liotta, Supported gold catalysts for the total oxidation of volatile organic compounds, Appl. Catal. B Environ. 125 (2012) 222–246. doi:10.1016/j.apcatb.2012.05.047.

[9]   The Swedish NGO Secretariat on Acid Rain, The CAFE Programme & the Thematic Strategy on Air Pollution, (2006) 1–8. http://ec.europa.eu/environment/archives/cafe/.

[10] M. Sloan, 2016 Propane Market Outlook, (2016). www.icfi.com.

[11] http://www.theglobaleconomy.com/rankings/lpg_consumption/, (n.d.). http://www.theglobaleconomy.com/rankings/lpg_consumption/ (accessed July 28, 2017).

[12] V.R. Choudhary, G.M. Deshmukh, D.P. Mishra, Kinetics of the complete combustion of dilute propane and toluene over iron-doped ZrO2 catalyst, Energy and Fuels. 19 (2005) 54–63. doi:10.1021/ef0498871.

[13] A.S. Ramadhas, Alternative fuels for transportation, 6th ed., CRC Press, 2011.

[14] C.A. Fonseca, D.S. Auerbach, R. V. Suarez, The forensic investigation of propane gas asphyxiation, Am. J. Forensic Med. Pathol. 23 (2002) 167–169. doi:10.1097/00000433-200206000-00011.

[15] M.O. McLinden, J.S. Brown, R. Brignoli, A.F. Kazakov, P.A. Domanski, Limited options for low-global-warming-potential refrigerants, Nat. Commun. 8 (2017) 1–9. doi:10.1038/ncomms14476.

[16] T. V. Choudhary, S. Banerjee, V.R. Choudhary, Catalysts for combustion of methane and lower alkanes, Appl. Catal. A Gen. 234 (2002) 1–23. doi:10.1016/S0926-860X(02)00231-4.

[17] World Health Organization, WHO guidelines for indoor air quality: selected pollutants, WHO Regional Office for Europe, 2010. doi:10.1186/2041-1480-2-S2-I1.

[18] M.M. Rhead, R.D. Pemberton, Sources of naphthalene in diesel exhaust emissions, Energy and Fuels. 10 (1996) 837–843. doi:10.1021/ef9502261.

[19] A.M. Mastral, M.S. Callén, T. García, Polycyclic aromatic hydrocarbons and organic matter associated to particulate matter emitted from atmospheric fluidized bed coal combustion, Environ. Sci. Technol. 33 (1999) 3177–3184. doi:10.1021/es990241a.

[20] N.R. Khalili, P.A. Scheff, T.M. Holsen, PAH source fingerprints for coke ovens, diesel and, gasoline engines, highway tunnels, and wood combustion emissions, Atmos. Environ. 29 (1995) 533–542. doi:10.1016/1352-2310(94)00275-P.

[21] J. Duan, J. Tan, L. Yang, S. Wu, J. Hao, Concentration, sources and ozone formation potential of volatile organic compounds (VOCs) during ozone episode in Beijing, Atmos. Res. 88 (2008) 25–35. doi:10.1016/j.atmosres.2007.09.004.

[22] A.D. Cortese, Clearing the air, Environ. Sci. Technol. 24 (1990) 442–8. doi:10.1016/s0262-4079(19)30210-6.

[23] M. Lippmann, Health Effects Of Ozone A Critical Review, J. Air Pollut. Control Assoc. 39 (1989) 672–695. doi:10.1080/08940630.1989.10466554.

[24] H.J.T. Bloemen, J. Burn, Chemistry and Analysis of Volatile Organic Compounds in the Environment, 2nd ed., Springer, 1995.

[25] M.S. Kamal, S.A. Razzak, M.M. Hossain, Catalytic oxidation of volatile organic compounds (VOCs) - A review, Atmos. Environ. 140 (2016) 117–134. doi:10.1016/j.atmosenv.2016.05.031.

[26] K.R. Solomon, X. Tang, S.R. Wilson, P. Zanis, A.F. Bais, Changes in tropospheric composition and air quality due to stratospheric ozone depletionThis article is published as part of the United Nations Environmental Programme: Environmental effects of ozone depletion and its interactions with climate change: 200, Photochem. Photobiol. Sci. 2 (2003) 62. doi:10.1039/b211086e.

[27] B.J. Finlayson-Pitts, J.N. Pitts, Atmospheric chemistry of tropospheric ozone formation: Scientific and regulatory implications, Air Waste. 43 (1993) 1091–1100. doi:10.1080/1073161X.1993.10467187.

[28] F. Parungo, C. Nagamoto, R. Madel, A Study of the Mechanisms of Acid Rain Formation, J. Atmos. Sci. 44 (1987) 3162–3174.

[29] M.J. Kleeman, J.J. Schauer, G.R. Cass, Size and Composition Distribution of Fine

Particulate Matter Emitted from Motor Vehicles, Environ. Sci. Technol. 34 (2000) 1132–1142.

[30] R. Giere, X. Querol, Solid Particulate Matter in the Atmosphere, (2010) 215–222.

[31] R.C. Flagan, J.H. Seinfield, Fundamentals of air pollution engineering, 1st ed., Prentice-Hall Inc., 1988.

[32] H. Bockhorn, Soot Formation in Combustion Processes (Review), Combust. Explos. Shock Waves. 41 (1994) 1–303. doi:10.1007/s10573-005-0083-2.

[33] M.M. Maricq, An examination of soot composition in premixed hydrocarbon flames via laser ablation particle mass spectrometry, J. Aerosol Sci. 40 (2009) 844–857. doi:10.1016/j.jaerosci.2009.07.001.

[34] C. Seigneur, Current status of air quality models for particulate matter, J. Air Waste Manag. Assoc. 51 (2001) 1508–1521. doi:10.1080/10473289.2001.10464383.

[35] W.H. Su, Q.P. Zhang, W.Z. Song, C. Luo, Y.F. Siu, Problems of soot pollution and environmental effects in northern china, Aerosol Sci. Technol. 10 (1989) 231–235. doi:10.1080/02786828908959261.

[36] E.M. Winkler, Dust and Acid Rain, Distribution. 6 (1976) 295–302.

[37] R. Niranjan, A.K. Thakur, The toxicological mechanisms of environmental soot (black carbon) and carbon black: Focus on Oxidative stress and inflammatory pathways, Front. Immunol. 8 (2017) 1–20. doi:10.3389/fimmu.2017.00763.

[38] T. Garcia, B. Solsona, S.H. Taylor, Handbook of Advanced Methods and Processes in Oxidation Catalysis: From Laboratory to Industry, 1st ed., Imperial College Press, 2014.

[39] F. Heymes, P. Manno-Demoustier, F. Charbit, J.L. Fanlo, P. Moulin, A new efficient absorption liquid to treat exhaust air loaded with toluene, Chem. Eng. J. 115 (2006) 225–231. doi:10.1016/j.cej.2005.10.011.

[40] Y.S. Chen, H.S. Liu, Absorption of VOCs in a rotating packed bed, Ind. Eng. Chem. Res. 41 (2002) 1583–1588. doi:10.1021/ie010752h.

[41] E. Dumont, G. Darracq, A. Couvert, C. Couriol, A. Amrane, D. Thomas, Y. Andrès, P. Le Cloirec, VOC absorption in a countercurrent packed-bed column using water/silicone oil mixtures: Influence of silicone oil volume fraction, Chem. Eng. J. 168 (2011) 241–248. doi:10.1016/j.cej.2010.12.073.

[42] E. Dumont, G. Darracq, A. Couvert, C. Couriol, A. Amrane, D. Thomas, Y. Andrès, P. Le Cloirec, Hydrophobic VOC absorption in two-phase partitioning bioreactors; influence of silicone oil volume fraction on absorber diameter, Chem. Eng. Sci. 71 (2012) 146–152. doi:10.1016/j.ces.2011.12.017.

[43] P.A. Mangrulkar, S.P. Kamble, J. Meshram, S.S. Rayalu, Adsorption of phenol and o-chlorophenol by mesoporous MCM-41, J. Hazard. Mater. 160 (2008) 414–421. doi:10.1016/j.jhazmat.2008.03.013.

[44] G. Busca, S. Berardinelli, C. Resini, L. Arrighi, Technologies for the removal of phenol from fluid streams: A short review of recent developments, J. Hazard. Mater. 160 (2008) 265–288. doi:10.1016/j.jhazmat.2008.03.045.

[45] D.R. Van Der Vaart, W.M. Vatavuk, A.H. Wehe, The Estimation of Thermal and Catalytic Incinerators for the Control of VOCs, J. Air Waste Manag. Assoc. 41 (1991) 497–501. doi:10.1080/10473289.1991.10466861.

[46] R.K. Sharma, B. Zhou, S. Tong, K.T. Chuane, A. Tg, Catalytic Destruction of Volatile Organic Compounds Using Supported Platinum and Palladium Hydrophobic Catalysts, (1995) 4310–4317.

[47] J.J. Spivey, Complete catalytic oxidation of volatile organics, Ind. Eng. Chem. Res. 26 (1987) 2165–2180. doi:10.1021/ie00071a001.

[48] A. Schwartz, L.L. Holbrook, H. Wise, Catalytic oxidation studies with platinum and palladium, J. Catal. 21 (1971) 199–207. doi:10.1016/0021-9517(71)90138-2.

[49] H. Huang, Y. Xu, Q. Feng, D.Y.C. Leung, Low temperature catalytic oxidation of

volatile organic compounds: A review, Catal. Sci. Technol. 5 (2015) 2649–2669. doi:10.1039/c4cy01733a.

[50] V.P. Santos, S.A.C. Carabineiro, P.B. Tavares, M.F.R. Pereira, J.J.M. Órfão, J.L. Figueiredo, Oxidation of CO, ethanol and toluene over TiO2 supported noble metal catalysts, Appl. Catal. B Environ. 99 (2010) 198–205. doi:10.1016/j.apcatb.2010.06.020.

[51] L.F. Liotta, Catalytic oxidation of volatile organic compounds on supported noble metals, Appl. Catal. B Environ. 100 (2010) 403–412. doi:10.1016/j.apcatb.2010.08.023.

[52] J.J. Spivey, J.B. Butt, Literature Review: Deactivation of catalysts in the oxidation of volatile organic compounds, Catal. Today. 11 (1992) 465–500.

[53] J.A. Moulijn, A.E. Van Diepen, F. Kapteijn, Catalyst deactivation: is it predictable? What to do?, Appl. Catal. A Gen. 212 (2001) 3–16. doi:10.1016/S0926-860X(00)00842-5.

[54] D. Roth, P. Gélin, M. Primet, E. Tena, Catalytic behaviour of Cl-free and Cl-containing Pd/Al2O3 catalysts in the total oxidation of methane at low temperature, Appl. Catal. A Gen. 203 (2000) 37–45. doi:10.1016/S0926-860X(00)00465-8.

[55] V. Meeyoo, D.L. Trimm, N.W. Cant, The effect of sulphur containing pollutants on the oxidation activity of precious metals used in vehicle exhaust catalysts, Appl. Catal. B Environ. 16 (1998) 101–104. doi:10.1016/S0926-3373(97)00094-5.

[56] T. Kolli, T. Kanerva, M. Huuhtanen, M. Vippola, K. Kallinen, T. Kinnunen, T. Lepistö, J. Lahtinen, R.L. Keiski, The activity of Pt/Al2O3 diesel oxidation catalyst after sulphur and calcium treatments, Catal. Today. 154 (2010) 303–307. doi:10.1016/j.cattod.2009.12.008.

[57] P. Euzen, J.H. Le Gal, B. Rebours, G. Martin, Deactivation of palladium catalyst in catalytic combustion of methane, Catal. Today. 47 (1999) 19–27. doi:10.1016/S0920-5861(98)00280-6.

[58] E.N. Ndifor, T. Garcia, S.H. Taylor, Naphthalene oxidation over vanadium-modified Pt catalysts supported on γ-Al2O3, Catal. Letters. 110 (2006) 125–128. doi:10.1007/s10562-006-0094-y.

[59] K.E. Voss, B.O. Yavus, R.J. Farrauto, M.P. Galligan, United States Patent 5,491,120, 1994. doi:US005485919A.

[60] B. Solsona, M. Pérez-Cabero, I. Vázquez, A. Dejoz, T. García, J. Álvarez-Rodríguez, J. El-Haskouri, D. Beltrán, P. Amorós, Total oxidation of VOCs on Au nanoparticles anchored on Co doped mesoporous UVM-7 silica, Chem. Eng. J. 187 (2012) 391–400. doi:10.1016/j.cej.2012.01.132.

[61] K. Rintramee, K. Föttinger, G. Rupprechter, J. Wittayakun, Ethanol adsorption and oxidation on bimetallic catalysts containing platinum and base metal oxide supported on MCM-41, Appl. Catal. B Environ. 115–116 (2012) 225–235. doi:10.1016/j.apcatb.2011.11.050.

[62] S. Liu, X. Wu, D. Weng, M. Li, H.R. Lee, Combined promoting effects of platinum and MnOx-CeO2 supported on alumina on NOx-assisted soot oxidation: Thermal stability and sulfur resistance, Chem. Eng. J. 203 (2012) 25–35. doi:10.1016/j.cej.2012.06.090.

[63] C. Lahousse, A. Bernier, P. Grange, B. Delmon, P. Papaefthimiou, T. Ioannides, X. Verykios, Evaluation of γ -MnO 2 as a VOC Removal Catalyst: Comparison with a Noble Metal Catalyst, J. Catal. 178 (1998) 214–225. doi:10.1006/jcat.1998.2148.

[64] A. Trovarelli, Catalysis by Ceria and Related Materials, Imperial College Press, 2002.

[65] A. Younis, D. Chu, S. Li, Functionalized Nanomaterials nanocrystals, Intech Open,

2012.

[66] T. Montini, M. Melchionna, M. Monai, P. Fornasiero, Fundamentals and Catalytic Applications of CeO2-Based Materials, Chem. Rev. 116 (2016) 5987–6041. doi:10.1021/acs.chemrev.5b00603.

[67] A. Trovarelli, C. De Leitenburg, M. Boaro, G. Dolcetti, The utilization of ceria in industrial catalysis, Catal. Today. 50 (1999) 353–367. doi:10.1016/S0920-5861(98)00515-X.

[68] R.J. Gorte, Ceria in Catalysis: From Automotive Applications to the Water–Gas Shift Reaction, React. Kinet. Catal. 60 (2009). doi:10.1002/aic.

[69] G. Kim, Ceria-Promoted Three-Way Catalysts for Auto Exhaust Emission Control, Ind. Eng. Chem. Prod. Res. Dev. 21 (1982) 267–274. doi:10.1021/i300006a014.

[70] M. Alifanti, M. Florea, V.I. Pârvulescu, Ceria-based oxides as supports for LaCoO3 perovskite; catalysts for total oxidation of VOC, Appl. Catal. B Environ. 70 (2007) 400–405. doi:10.1016/j.apcatb.2005.10.037.

[71] S. Scirè, S. Minicò, C. Crisafulli, C. Satriano, A. Pistone, Catalytic combustion of volatile organic compounds on gold/cerium oxide catalysts, Appl. Catal. B Environ. 40 (2003) 43–49. doi:10.1016/S0926-3373(02)00127-3.

[72] S.M. Saqer, D.I. Kondarides, X.E. Verykios, Catalytic activity of supported platinum and metal oxide catalysts for toluene oxidation, Top. Catal. 52 (2009) 517–527. doi:10.1007/s11244-009-9182-8.

[73] R. Bonelli, S. Albonetti, V. Morandi, L. Ortolani, P.M. Riccobene, S. Scirè, S. Zacchini, Design of nano-sized FeOx and Au/FeOx catalysts supported on CeO2 for total oxidation of VOC, Appl. Catal. A Gen. 395 (2011) 10–18. doi:10.1016/j.apcata.2011.01.017.

[74] J. Du, Z. Qu, C. Dong, L. Song, Y. Qin, N. Huang, Low-temperature abatement of toluene over Mn-Ce oxides catalysts synthesized by a modified hydrothermal approach, Appl. Surf. Sci. 433 (2018) 1025–1035. doi:10.1016/j.apsusc.2017.10.116.

[75] D. Yu, W. Xingyi, L. Dao, D. Qiguang, Catalytic combustion of chlorobenzene over Mn-Ce-La-O mixed oxide catalysts, J. Hazard. Mater. 188 (2011) 132–139. doi:10.1016/j.jhazmat.2011.01.084.

[76] T. García, B. Solsona, S.H. Taylor, Naphthalene total oxidation over metal oxide catalysts, Appl. Catal. B Environ. 66 (2006) 92–99. doi:10.1016/j.apcatb.2006.03.003.

[77] A. Aranda, B. Puértolas, B. Solsona, S. Agouram, R. Murillo, A.M. Mastral, S.H. Taylor, T. Garcia, Total oxidation of naphthalene using mesoporous CeO2 catalysts synthesized by nanocasting from two dimensional SBA-15 and three dimensional KIT-6 and MCM-48 silica templates, Catal. Letters. 134 (2010) 110–117. doi:10.1007/s10562-009-0203-9.

[78] A. Aranda, J.M. López, R. Murillo, A.M. Mastral, A. Dejoz, I. Vázquez, B. Solsona, S.H. Taylor, T. García, Total oxidation of naphthalene with high selectivity using a ceria catalyst prepared by a combustion method employing ethylene glycol., J. Hazard. Mater. 171 (2009) 393–9. doi:10.1016/j.jhazmat.2009.06.013.

[79] Q. Dai, X. Wang, G. Lu, Low-temperature catalytic combustion of trichloroethylene over cerium oxide and catalyst deactivation, Appl. Catal. B Environ. 81 (2008) 192–202. doi:10.1016/j.apcatb.2007.12.013.

[80] T.-Z. Ren, P.-B. Xu, Q.-F. Deng, Z.-Y. Yuan, Mesoporous Ce1− xMnxO2 mixed oxides with CuO loading for the catalytic total oxidation of propane, React. Kinet. Mech. Catal. 110 (2013) 405–420. doi:10.1007/s11144-013-0603-0.

[81] Z. Hu, S. Qiu, Y. You, Y. Guo, Y. Guo, L. Wang, W. Zhan, G. Lu, Hydrothermal synthesis of NiCeOx nanosheets and its application to the total oxidation of

propane, Appl. Catal. B Environ. 225 (2018) 110–120. doi:10.1016/j.apcatb.2017.08.068.

[82] H. Zhu, Y. Xu, X. Tang, Y. Li, W. Shen, J. Wang, X. Huang, MnOx–CeO2 mixed oxide catalysts for complete oxidation of formaldehyde: Effect of preparation method and calcination temperature, Appl. Catal. B Environ. 62 (2005) 265–273. doi:10.1016/j.apcatb.2005.08.004.

[83] X. Liu, J. Lu, K. Qian, W. Huang, M. Luo, A comparative study of formaldehyde and carbon monoxide complete oxidation on MnOx-CeO2 catalysts, J. Rare Earths. 27 (2009) 418–424. doi:10.1016/S1002-0721(08)60263-X.

[84] R. Dziembaj, M. Molenda, M.M. Zaitz, L. Chmielarz, K. Furczoń, Correlation of electrical properties of nanometric copper-doped ceria materials (Ce1 - XCuxO2 - δ) with their catalytic activity in incineration of VOCs, Solid State Ionics. 251 (2013) 18–22. doi:10.1016/j.ssi.2013.03.011.

[85] L. Liu, J. Shi, X. Zhang, J. Liu, Flower-Like Mn-Doped CeO2 Microstructures: Synthesis, Characterizations, and Catalytic Properties, J. Chem. 2015 (2015) 1–11.

[86] F. Zamar, A. Trovarelli, C. de Leitenburg, G. Dolcetti, CeO2-based solid solutions with the fluorite structure as novel and effective catalysts for methane combustion, J. Chem. Soc. Chem. Commun. 02 (1995) 965. doi:10.1039/c39950000965.

[87] M. Ozawa, H. Yuzuriha, M. Haneda, Total oxidation of toluene and oxygen storage capacity of zirconia-sol modified ceria zirconia, Catal. Commun. 30 (2013) 32–35. doi:10.1016/j.catcom.2012.10.008.

[88] B. de Rivas, J.I. Gutiérrez-Ortiz, R. López-Fonseca, J.R. González-Velasco, Analysis of the simultaneous catalytic combustion of chlorinated aliphatic pollutants and toluene over ceria-zirconia mixed oxides, Appl. Catal. A Gen. 314 (2006) 54–63. doi:10.1016/j.apcata.2006.08.005.

[89] T. Kondratowicz, M. Drozdek, A. Rokicińska, P. Natkański, M. Michalik, P. Kuśtrowski, Novel CuO-containing catalysts based on ZrO 2 hollow spheres for total oxidation of toluene, Microporous Mesoporous Mater. 279 (2019) 446–455. doi:10.1016/j.micromeso.2019.01.031.

[90] M. Labaki, J.F. Lamonier, S. Siffert, E.A. Zhilinskaya, A. Aboukaïs, Total oxidation of propene and toluene on copper/yttrium doped zirconia, Kinet. Catal. 45 (2004) 227–233. doi:10.1023/B:KICA.0000023796.52228.44.

[91] D. Döbber, D. Kießling, W. Schmitz, G. Wendt, MnOx/ZrO2 catalysts for the total oxidation of methane and chloromethane, Appl. Catal. B Environ. 52 (2004) 135–143. doi:10.1016/j.apcatb.2004.02.012.

[92] S. Pengpanich, V. Meeyoo, T. Rirksomboon, K. Bunyakiat, Catalytic oxidation of methane over CeO2-ZrO2mixed oxide solid solution catalysts prepared via urea hydrolysis, Appl. Catal. A Gen. 234 (2002) 221–233. doi:10.1016/S0926-860X(02)00230-2.

[93] Y. Zhang, Y. Shen, X. Yang, S. Sheng, T. Wang, M.F. Adebajo, H. Zhu, Gold catalysts supported on the mesoporous nanoparticles composited of zirconia and silicate for oxidation of formaldehyde, J. Mol. Catal. A Chem. 316 (2009) 100–105. doi:10.1016/j.molcata.2009.10.006.

[94] R. Nielsen, T.W. Chang, G. Wilfing, Zirconium and Zirconium Compounds, Wiley-VCH, 2012. doi:10.1002/14356007.a28.

[95] J.E. Bailey, The Monoclinic-Tetragonal Transformation and Associated Twinning in Thin Films of Zirconia, Proc. R. Soc. A Math. Phys. Eng. Sci. 279 (1964) 395–412. doi:10.1098/rspa.1964.0112.

[96] J.. Selby, The industrial uses of zircon and zirconia and the radiological consequences of these uses, Nat. Occur. Radioact. Mater. (2007). doi:10.1201/9780203746042.

[97] G.D. Yadav, J.J. Nair, Sulfated zirconia and its modified versions as promising

catalysts for industrial processes, Microporous Mesoporous Mater. 33 (1999) 1–48. doi:10.1016/S1387-1811(99)00147-X.

[98] K. Tanabe, W.F. Hölderich, Industrial application of solid acid-base catalysts, Appl. Catal. A Gen. 181 (1999) 399–434. doi:10.1016/S0926-860X(98)00397-4.

[99] X. Zhang, H. Shi, B.Q. Xu, Comparative study of Au/ZrO2 catalysts in CO oxidation and 1,3-butadiene hydrogenation, Catal. Today. 122 (2007) 330–337. doi:10.1016/j.cattod.2007.02.016.

[100] D.R. Sellick, A. Aranda, T. García, J.M. López, B. Solsona, A.M. Mastral, D.J. Morgan, A.F. Carley, S.H. Taylor, Influence of the preparation method on the activity of ceria zirconia mixed oxides for naphthalene total oxidation, Appl. Catal. B Environ. 132–133 (2013) 98–106. doi:10.1016/j.apcatb.2012.11.036.

[101] M. Piumetti, D. Fino, N. Russo, Mesoporous manganese oxides prepared by solution combustion synthesis as catalysts for the total oxidation of VOCs, Appl. Catal. B Environ. 163 (2015) 277–287. doi:10.1016/j.apcatb.2014.08.012.

[102] T. Garcia, D. Sellick, F. Varela, I. Vázquez, A. Dejoz, S. Agouram, S.H. Taylor, B. Solsona, Total oxidation of naphthalene using bulk manganese oxide catalysts, Appl. Catal. A Gen. 450 (2013) 169–177. doi:10.1016/j.apcata.2012.10.029.

[103] Y. Liao, M. Fu, L. Chen, J. Wu, B. Huang, D. Ye, Catalytic oxidation of toluene over nanorod-structured Mn-Ce mixed oxides, Catal. Today. 216 (2013) 220–228. doi:10.1016/j.cattod.2013.06.017.

[104] D. Delimaris, T. Ioannides, VOC oxidation over MnOx-CeO2 catalysts prepared by a combustion method, Appl. Catal. B Environ. 84 (2008) 303–312. doi:10.1016/j.apcatb.2008.04.006.

[105] J. Du, Z. Qu, C. Dong, L. Song, Y. Qin, N. Huang, Low-temperature abatement of toluene over Mn-Ce oxides catalysts synthesized by a modified hydrothermal approach, Appl. Surf. Sci. 433 (2018) 1025–1035. doi:10.1016/j.apsusc.2017.10.116.

[106] J. Chen, X. Chen, W. Xu, Z. Xu, J. Chen, H. Jia, J. Chen, Hydrolysis driving redox reaction to synthesize Mn-Fe binary oxides as highly active catalysts for the removal of toluene, Chem. Eng. J. 330 (2017) 281–293. doi:10.1016/j.cej.2017.07.147.

[107] F.G. Durán, B.P. Barbero, L.E. Cadús, C. Rojas, M.A. Centeno, J.A. Odriozola, Manganese and iron oxides as combustion catalysts of volatile organic compounds, Appl. Catal. B Environ. 92 (2009) 194–201. doi:10.1016/j.apcatb.2009.07.010.

[108] S.C. Kim, W.G. Shim, Catalytic combustion of VOCs over a series of manganese oxide catalysts, Appl. Catal. B Environ. 98 (2010) 180–185. doi:10.1016/j.apcatb.2010.05.027.

[109] B. Puértolas, A. Smith, I. Vázquez, A. Dejoz, A. Moragues, T. Garcia, B. Solsona, The different catalytic behaviour in the propane total oxidation of cobalt and manganese oxides prepared by a wet combustion procedure, Chem. Eng. J. 229 (2013) 547–558. doi:10.1016/j.cej.2013.06.041.

[110] V.P. Santos, M.F.R. Pereira, J.J.M. Órfão, J.L. Figueiredo, The role of lattice oxygen on the activity of manganese oxides towards the oxidation of volatile organic compounds, Appl. Catal. B Environ. 99 (2010) 353–363. doi:10.1016/j.apcatb.2010.07.007.

[111] J. Li, X. Liang, S. Xu, J. Hao, Catalytic performance of manganese cobalt oxides on methane combustion at low temperature, Appl. Catal. B Environ. 90 (2009) 307–312. doi:10.1016/j.apcatb.2009.03.027.

[112] W. Li, H. Liu, X. Ma, S. Mo, S. Li, Y. Chen, Fabrication of silica supported mn-ce benzene oxidation catalyst by a simple and environment-friendly oxalate approach, J. Porous Mater. 25 (2018) 107–117. doi:10.1007/s10934-017-0424-z.

[113] J.E. Post, Manganese oxide minerals : Crystal structures and economic and, Proc

Natl Acad Sci USA. 96 (1999) 3447–3454.

[114] K. Hagelstein, Globally sustainable manganese metal production and use, J. Environ. Manage. 90 (2009) 3736–3740. doi:10.1016/j.jenvman.2008.05.025.

[115] C. Clarke, S. Upson, A global portrait of the manganese industry—A socioeconomic perspective, Neurotoxicology. 58 (2017) 173–179. doi:10.1016/j.neuro.2016.03.013.

[116] M. Nitta, Characteristics of manganese nodules as adsorbents and catalysts, A review, Appl. Catal. (1984) 151–176.

[117] S. Noda, Y. Yamaguchi, Estimation of surface iron oxide abundance with suppression of grain size and topography effects, Ore Geol. Rev. 83 (2017) 312–320. doi:10.1016/j.oregeorev.2016.12.019.

[118] J.H. DeYoung, J.G. Price, Global Iron Ore Production, Min. Eng. (2017) 20–23. www.miningengineeringmagazine.com.

[119] R.M. Cornell, U. Schwertmann, The Iron Oxides: Structure, Properties, Reactions, Occurrences and Uses, John Wiley and Sons, 2003.

[120] M.C. Oliveira, Luiz C A; Fabris, José D.; Pereira, Óxidos De Ferro E Suas Aplicaões Em Processos Catalíticos: Uma Revisão, Quim. Nova. 36 (2013) 123–130. doi:10.1590/S0100-40422013000100022.

[121] H.J.H. Fenton, Oxidation of tartaric acid in the presence of iron, J. Chem. Soc. Trans. 65 (1894) 899–910.

[122] E. Neyens, J. Baeyens, A review of classic Fenton's peroxidation as an advanced oxidation technique, J. Hazard. Mater. 98 (2003) 33–50. doi:10.1016/S0304-3894(02)00282-0.

[123] M.R. Morales, B.P. Barbero, L.E. Cadús, Combustion of volatile organic compounds on manganese iron or nickel mixed oxide catalysts, Appl. Catal. B Environ. 74 (2007) 1–10. doi:10.1016/j.apcatb.2007.01.008.

[124] B. Solsona, T. García, R. Sanchis, M.D. Soriano, M. Moreno, E. Rodríguez-Castellón, S. Agouram, A. Dejoz, J.M. López Nieto, Total oxidation of VOCs on mesoporous iron oxide catalysts: Soft chemistry route versus hard template method, Chem. Eng. J. 290 (2016) 273–281. doi:10.1016/j.cej.2015.12.109.

[125] S. Minicò, S. Scirè, C. Crisafulli, S. Galvagno, Influence of catalyst pretreatments on volatile organic compounds oxidation over gold/iron oxide, Appl. Catal. B Environ. 34 (2001) 277–285. doi:10.1016/S0926-3373(01)00221-1.

[126] B. Solsona, T. Garcia, C. Jones, S. Taylor, A. Carley, G. Hutchings, Supported gold catalysts for the total oxidation of alkanes and carbon monoxide, Appl. Catal. A Gen. 312 (2006) 67–76. doi:10.1016/j.apcata.2006.06.016.

[127] S. Scirè, S. Minicò, C. Crisafulli, S. Galvagno, Catalytic combustion of volatile organic compounds over group IB metal catalysts on Fe2O3, Catal. Commun. 2 (2001) 229–232. doi:10.1016/S1566-7367(01)00035-8.

[128] X. Wang, Y. Xie, Total Oxidation of Ch 4 on Iron-Promoted Tin Oxide: Novel and Thermally Stable Catalysts, React. Kinetc Catlysis Lett. 72 (2001) 229–237.

[129] D. Devaiah, L.H. Reddy, S.-E. Park, B.M. Reddy, Ceria–zirconia mixed oxides: Synthetic methods and applications, Catal. Rev. 60 (2018) 177–277. doi:10.1080/01614940.2017.1415058.

[130] S. Damyanova, B. Pawelec, K. Arishtirova, M.V.M. Huerta, J.L.G. Fierro, Study of the surface and redox properties of ceria-zirconia oxides, Appl. Catal. A Gen. 337 (2008) 86–96. doi:10.1016/j.apcata.2007.12.005.

[131] S. Bedrane, C. Descorme, D. Duprez, Investigation of the oxygen storage process on ceria- and ceria-zirconia-supported catalysts, Catal. Today. 75 (2002) 401–405. doi:10.1016/S0920-5861(02)00089-5.

[132] M. Sugiura, Oxygen storage materials for automotive catalysts: Ceria-zirconia solid solutions, Catal. Surv. from Asia. 7 (2003) 77–87.

doi:10.1023/A:1023488709527.

[133] C. Bozo, F. Gaillard, N. Guilhaume, Characterisation of ceria-zirconia solid solutions after hydrothermal ageing, Appl. Catal. A Gen. 220 (2001) 69–77. doi:10.1016/S0926-860X(01)00710-4.

[134] A. Hirano, A. Suda, Oxygen Storage Capacity, Specific Surface Area, and Pore-Size Distribution of Ceria–Zirconia Solid Solutions Directly Formed by Thermal Hydrolysis, J. Am. Ceram. Soc. 11 (2003) 2209–2211.

[135] J. Soria, Surface properties of CeZrO 4 -based materials employed as catalysts supports * , 324 (2001) 605–609.

[136] B. Wang, X. Wu, R. Ran, Z. Si, D. Weng, IR characterization of propane oxidation on Pt/CeO 2-ZrO 2: The reaction mechanism and the role of Pt, J. Mol. Catal. A Chem. 356 (2012) 100–105. doi:10.1016/j.molcata.2011.12.030.

[137] A. Bampenrat, V. Meeyoo, B. Kitiyanan, P. Rangsunvigit, T. Rirksomboon, Catalytic oxidation of naphthalene over CeO2–ZrO2 mixed oxide catalysts, Catal. Commun. 9 (2008) 2349–2352. doi:10.1016/j.catcom.2008.05.029.

[138] C. Bozo, N. Guilhaume, E. Garbowski, M. Primet, Combustion of methane on CeO2–ZrO2 based catalysts, Catal. Today. 59 (2000) 33–45. doi:10.1016/S0920-5861(00)00270-4.

[139] L. Zhi Min, W. Jian Li, Z. Jun Bo, C. Yao Qiang, Y. Sheng Hui, G. Mao Chu, Catalytic combustion of toluene over platinum supported on Ce-Zr-O solid solution modified by Y and Mn., J. Hazard. Mater. 149 (2007) 742–6. doi:10.1016/j.jhazmat.2007.08.032.

[140] J.I. Gutiérrez-Ortiz, B. de Rivas, R. López-Fonseca, J.R. González-Velasco, Catalytic purification of waste gases containing VOC mixtures with Ce/Zr solid solutions, Appl. Catal. B Environ. 65 (2006) 191–200. doi:10.1016/j.apcatb.2006.02.001.

[141] R.N. Ivanova, M.D. Dimitrov, D.G. Kovacheva, Influence of the hydrothermal treatment temperature on the properties of mixed ceria-zirconia catalysts for ethyl acetate combustion, Bulg. Chem. Commun. 49 (2017) 84–90.

[142] A. Aranda, E. Aylón, B. Solsona, R. Murillo, A.M. Mastral, D.R. Sellick, S. Agouram, T. García, S.H. Taylor, High activity mesoporous copper doped cerium oxide catalysts for the total oxidation of polyaromatic hydrocarbon pollutants., Chem. Commun. (Camb). 48 (2012) 4704–6. doi:10.1039/c2cc31206a.

[143] Q. Shen, G. Lu, C. Du, Y. Guo, Y. Wang, Y. Guo, X. Gong, Role and reduction of NOx in the catalytic combustion of soot over iron-ceria mixed oxide catalyst, Chem. Eng. J. 218 (2013) 164–172. doi:10.1016/j.cej.2012.12.010.

[144] H. Li, G. Qi, Tana, X. Zhang, X. Huang, W. Li, W. Shen, Low-temperature oxidation of ethanol over a Mn0.6Ce0.4O2 mixed oxide, Appl. Catal. B Environ. 103 (2011) 54–61. doi:10.1016/j.apcatb.2011.01.008.

[145] D. Delimaris, T. Ioannides, Intrinsic Activity of MnOx-CeO2 Catalysts in Ethanol Oxidation, Catalysts. 7 (2017) 339. doi:10.3390/catal7110339.

[146] Y. Liang, Y. Huang, H. Zhang, L. Lan, M. Zhao, M. Gong, Y. Chen, J. Wang, Interactional effect of cerium and manganese on NO catalytic oxidation, Environ. Sci. Pollut. Res. 24 (2017) 9314–9324. doi:10.1007/s11356-017-8645-x.

[147] G. Qi, W. Li, NO oxidation to NO2over manganese-cerium mixed oxides, Catal. Today. 258 (2015) 205–213. doi:10.1016/j.cattod.2015.03.020.

[148] P. Venkataswamy, K.N. Rao, D. Jampaiah, B.M. Reddy, Nanostructured manganese doped ceria solid solutions for CO oxidation at lower temperatures, Appl. Catal. B Environ. 162 (2015) 122–132. doi:10.1016/j.apcatb.2014.06.038.

[149] H. Chen, A. Sayari, A. Adnot, F. Larachi, Composition-activity effects of Mn-Ce-O composites on phenol catalytic wet oxidation, Appl. Catal. B Environ. 32 (2001) 195–204. doi:10.1016/S0926-3373(01)00136-9.

[150] J. Chen, X. Chen, X. Chen, W. Xu, Z. Xu, H. Jia, J. Chen, Homogeneous introduction of CeOyinto MnOx-based catalyst for oxidation of aromatic VOCs, Appl. Catal. B Environ. 224 (2018) 825–835. doi:10.1016/j.apcatb.2017.11.036.

[151] W. Xingyi, K. Qian, L. Dao, Catalytic combustion of chlorobenzene over MnOx-CeO2 mixed oxide catalysts, Appl. Catal. B Environ. 86 (2009) 166–175. doi:10.1016/j.apcatb.2008.08.009.

[152] G. Picasso, M. Gutierrez, M.P. Pina, J. Herguido, Preparation and characterization of Ce-Zr and Ce-Mn based oxides for n-hexane combustion: Application to catalytic membrane reactors, Chem. Eng. J. 126 (2007) 119–130. doi:10.1016/j.cej.2006.09.005.

[153] H. Zhang, W. Yang, D. Li, X. Wang, Influence of preparation method on the performance of Mn-Ce-O catalysts, React. Kinet. Catal. Lett. 97 (2009) 263–268. doi:10.1007/s11144-009-0024-2.

[154] E.N. Ntainjua, T.E. Davies, T. Garcia, B. Solsona, S.H. Taylor, The influence of platinum addition on nano-crystalline ceria catalysts for the total oxidation of naphthalene a model polycyclic aromatic hydrocarbon, Catal. Letters. 141 (2011) 1732–1738. doi:10.1007/s10562-011-0710-3.

[155] T.J. Clarke, S.A. Kondrat, S.H. Taylor, Total oxidation of naphthalene using bulk manganese oxide catalysts, Appl. Catal. A Gen. 450 (2013) 169–177. doi:10.1016/j.apcata.2012.10.029.

[156] H.C. Genuino, S. Dharmarathna, E.C. Njagi, M.C. Mei, S.L. Suib, Gas-phase total oxidation of benzene, toluene, ethylbenzene, and xylenes using shape-selective manganese oxide and copper manganese oxide catalysts, J. Phys. Chem. C. 116 (2012) 12066–12078. doi:10.1021/jp301342f.

[157] W. Tang, X. Wu, S. Li, X. Shan, G. Liu, Y. Chen, Co-nanocasting synthesis of mesoporous Cu-Mn composite oxides and their promoted catalytic activities for gaseous benzene removal, Appl. Catal. B Environ. 162 (2015) 110–121. doi:10.1016/j.apcatb.2014.06.030.

[158] T.J. Clarke, T.E. Davies, S.A. Kondrat, S.H. Taylor, Mechanochemical synthesis of copper manganese oxide for the ambient temperature oxidation of carbon monoxide, Appl. Catal. B Environ. 165 (2015) 222–231. doi:10.1016/j.apcatb.2014.09.070.

[159] B. Solsona, T.E. Davies, T. Garcia, I. Vázquez, A. Dejoz, S.H. Taylor, Total oxidation of propane using nanocrystalline cobalt oxide and supported cobalt oxide catalysts, Appl. Catal. B Environ. 84 (2008) 176–184. doi:10.1016/j.apcatb.2008.03.021.

[160] M.H. Castaño, R. Molina, S. Moreno, Cooperative effect of the Co-mn Mixed oxides for the catalytic oxidation of VOCs: Influence of the synthesis method, Appl. Catal. A Gen. 492 (2015) 48–59. doi:10.1016/j.apcata.2014.12.009.

[161] T. Mishra, P. Mohapatra, K.M. Parida, Synthesis, characterisation and catalytic evaluation of iron-manganese mixed oxide pillared clay for VOC decomposition reaction, Appl. Catal. B Environ. 79 (2008) 279–285. doi:10.1016/j.apcatb.2007.10.030.

[162] E. Manova, T. Tsoncheva, C. Estournès, D. Paneva, K. Tenchev, I. Mitov, L. Petrov, Nanosized iron and iron – cobalt spinel oxides as catalysts for methanol decomposition, Appl. Catal. A Gen. 300 (2006) 170–180. doi:10.1016/j.apcata.2005.11.005.

[163] Y. Hammiche-Bellal, N. Zouaoui-Mahzoul, I. Lounas, A. Benadda, R. Benrabaa, A. Auroux, L. Meddour-Boukhobza, A. Djadoun, Cobalt and cobalt-iron spinel oxides as bulk and silica supported catalysts in the ethanol combustion reaction, J. Mol. Catal. A Chem. 426 (2017) 97–106. doi:10.1016/j.molcata.2016.11.005.

[164] A. Biabani-ravandi, M. Rezaei, Z. Fattah, Study of Fe – Co mixed metal oxide

nanoparticles in the catalytic low-temperature CO oxidation, Process Saf. Environ. Prot. 91 (2012) 489–494. doi:10.1016/j.psep.2012.10.015.

[165] J.B. Li, H.F. Ma, H.T. Zhang, Q.W. Sun, W.Y. Ying, D.Y. Fang, Comparison of FeMn, FeMnNa and FeMnK catalysts for the preparation of light olefins from syngas, Wuli Huaxue Xuebao/ Acta Phys. - Chim. Sin. 30 (2014) 1932–1940. doi:10.3866/PKU.WHXB201408051.

[166] A. Miyakoshi, A. Ueno, M. Ichikawa, XPS and TPD characterization of manganese-substituted iron-potassium oxide catalysts which are selective for dehydrogenation of ethylbenzene into styrene, Appl. Catal. A Gen. 219 (2001) 249–258. doi:10.1016/S0926-860X(01)00697-4.

[167] M. Baldi, V.S. Escribano, J.M.G. Amores, F. Milella, G. Busca, Characterization of manganese and iron oxides as combustion catalysts for propane and propene, Appl. Catal. B Environ. 17 (1998) 175–182. doi:10.1016/S0926-3373(98)00013-7.

[168] S.D. Neelapala, A. Shetty, G. Gaggar, R. Mall, H. Dasari, Development of Iron Doped Manganese oxide (Mn 2-x Fe x O 3) Catalysts for Soot Oxidation Applications, 13 (2018) 245–251.

[169] P. Mars, D.W. van Krevelen, Oxidations carried out by means of vanadium oxide catalysts, Chem. Eng. Sci. 3 (n.d.) 41–59. doi:10.1016/S0009-2509(54)80005-4.

[170] V. Balcaen, R. Roelant, H. Poelman, D. Poelman, G.B. Marin, TAP study on the active oxygen species in the total oxidation of propane over a CuO-CeO2/γ-Al2O3catalyst, Catal. Today. 157 (2010) 49–54. doi:10.1016/j.cattod.2010.02.048.

2 Experimental

This chapter explains the techniques used to synthesise, characterise and test the catalysts along with a brief introduction into the theory required to operate the techniques.

2.1 Catalyst Preparation

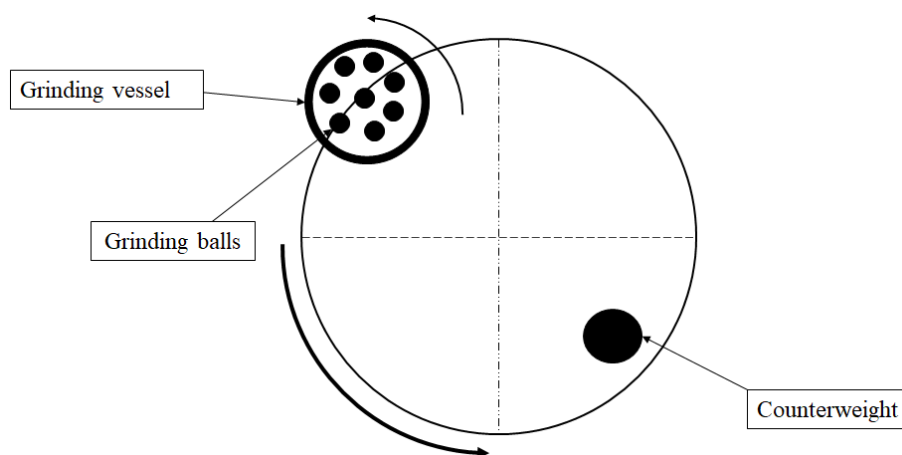### 2.1.1 Catalysts prepared via mechanochemical grinding

Figure 2-1: Schematic of a planetary ball mill

A Restch PM 100 planetary ball mill was used to prepare catalysts via mechanochemical grinding, Figure 2-1. This type of ball mill operates by rotation of a 10 cm zirconia grinding vessel containing seven, 15 mm zirconia balls around a central point. The vessel itself also rotates on its own axis, counter to the original rotation put into the system. This increases the kinetic energy of the system and energy transfer into the materials in the grinding vessel.

2.1.1.1 Preparation of ceria-zirconia mixed metal oxide catalysts using mechanochemical grinding

2.1.1.1.1 Preparation of Ce-Zr mixed metal oxide catalysts from nitrate precursors

$Ce(NO_3)_3 \cdot 6H_2O$ (Sigma-Aldrich, 99 %) and $ZrO(NO_3)_2 \cdot xH_2O$ (Sigma- Aldrich, 99 %) were weighed to appropriate Ce:Zr ratios and lightly ground with a pestle and mortar before being placed into the ball mill crucible. The Ce:Zr molar ratios investigated were 100:0, 95:5, 90:10, 75:25, 50:50, 0:100. The samples were ground for 4 hours at 300 rpm at room temperature. The resulting powders were collected and calcined under a flowing air atmosphere for 3 hours at 400 °C with a ramp rate of 1 °C min^{-1}.

2.1.1.1.2 Preparation of Ce-Zr mixed metal oxide catalysts from carbonate precursors

$Ce_2(CO_3)_3 \cdot 6H_2O$ (Sigma-Aldrich 99.9 %) and $Zr(OH)_2CO_3 \cdot ZrO_2$ (Sigma-Aldrich 95%) were weighed to appropriate Ce:Zr ratios. Once weighed out, the materials were lightly ground and placed into the ball mill crucible. The Ce: Zr ratios studied were 100:0, 95:5,

90:10, 75:25, 50:50 and 0:100. The samples were ground for 4 hours at 200 rpm at room temperature. The material was then collected and calcined at 400 °C for 3 hours under a flowing air atmosphere with a ramp rate of 1 °C min^{-1}.

2.1.1.2 Preparation of $Ce_{25}Mn_{75}O_x$ catalysts using mechanochemical grinding

2.1.1.2.1 Preparation of $Ce_{25}Mn_{75}O_x$ using nitrate precursors

A $Ce_{25}Mn_{75}O_x$ catalyst was prepared by the following method. Appropriate amounts of $Ce(NO_3)_3 \cdot 6H_2O$ (Sigma-Aldrich 99 %) and $Mn(NO_3)_2 \cdot 4H_2O$ (Sigma-Aldrich 99 %) were weighed out to a 1:3 metal atomic ratio. The materials were lightly ground then deposited into the ball mill crucible. The materials were ground for 4 hours at 100 rpm at room temperature. A slurry was recovered and placed into a glass calcination boat. The slurry was dried for 16 hours under flowing air at 120 °C. A solid sample was then collected and calcined at 500 °C under flowing air for 3 hours with a ramp rate of 1 °C min^{-1}.

2.1.1.2.2 Preparation of $Ce_{25}Mn_{75}O_x$ using carbonate precursors

$Ce_2(CO_3)_3$ (Sigma-Aldrich 99.9 %) and $MnCO_3$ (Sigma-Aldrich 99 %) were weighed out in a 1:3 metal ratio to produce the $Ce_{25}Mn_{75}O_x$ catalysts. The weighed samples were lightly milled before being placed in the ball mill crucible. The material was ground for 4 hours at 200 rpm. The resulting material was then calcined under flowing air for 3 hours at 500 °C with a ramp rate of 1 °C min^{-1}.

2.1.2 Catalyst preparation using co-precipitation methods

2.1.2.1 Co-precipitation with autotitrator

Another method used to prepare mixed metal oxides was co-precipitation using a Metrohm Titrando autotitrator, Figure 2-2. This system was used to control the co-addition of metal salts, normally in the form of nitrates, and a precipitating agent, usually a base. An electrochemical probe is used to monitor both pH and temperature of the solution. Both metal salts and precipitating agents were added into the precipitation vessel using two Dosino dosing units, which hold up to 50 ml of solution. The Dosino units are computer controlled and can dose solutions at flow rates between 50 µl min^{-1} and 50 ml min^{-1}.
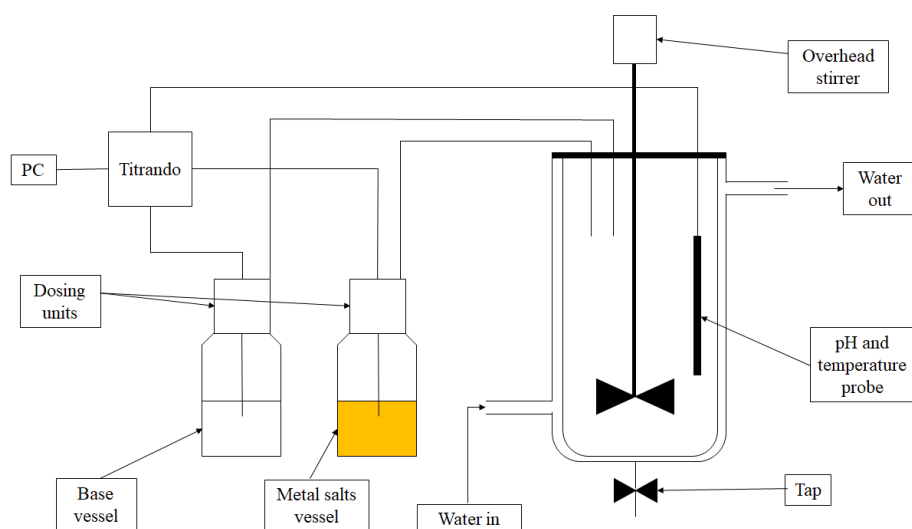
Figure 2-2: Schematic of the Titrando co-precipitation apparatus

The general preparation method is as follows. Initially the pH probe calibrated using pH 4, 7 and 10 buffer solutions (Acros Organics). The water bath that fills the single jacketed vessel is then set to temperature. Metal salt solutions were pre-mixed to the appropriate ratio and placed into a glass bottle. The base solution was also placed into a glass bottle and then both were attached to the Dosino units. Once the vessel is heated, 20 ml of metal salt solution is dosed to allow a part of the pH probe to become submerged in solution. Then the precipitating agent is dropped in to achieve the set pH. Following this both solutions are dosed at a constant rate to maintain the pH. Once 150 ml of the metal salt solutions were added, the resulting solution is then left to age for a set time and recovered by filtration. The precipitate is washed with 1 l of warm water and dried overnight at 110 °C. The materials are then calcined to form the catalyst samples.

2.1.2.1.1 Preparation of ceria-manganese mixed metal oxide catalysts using automated co-precipitation

A set of ceria-manganese mixed metal oxide catalysts were prepared using the auto-titrator system. Into the metal salt vessel, pre-measured volumes of $Ce(NO_3)_3$. $6H_2O$ (Sigma-Aldrich, 99 %, 0.25M) and $Mn(NO_3)_2$. $4H_2O$ (Sigma-Aldrich, 99 %, 0.25 M) and a Na_2CO_3 solution (anhydrous, Sigma-Aldrich, 1 M). The Ce:Mn ratios investigated were 100:0, 95:5, 90:10, 75:25, 50:50, 25:75 and 0:100. The salts were dosed at 3 ml min^{-1} at pH 9 with the resulting solution aged for 2 hours at 60 °C. The resulting precipitate was filtered and washed with warm water (1 l) and dried for 16 hours at 110 °C. The samples were then calcined at 500 °C for 3 hours with a ramp rate of 1 °C min^{-1} to produce the final catalyst sample.

2.1.2.1.2 The effect of washing on the preparation of ceria-manganese mixed metal oxide catalysts

The catalyst with the highest activity was prepared as mentioned in section 1.1.2.1 however the volume of water used to wash the catalyst was varied (0, 1 and 2 l were investigated).

2.1.2.2 Preparation of iron-manganese mixed metal oxide catalysts using automated co-precipitation

A series of iron-manganese mixed metal oxide catalysts were prepared using the co-precipitation method. The Fe:Mn ratios investigated were 100:0, 99:1, 90:10, 80:20, 50:50, 20:80, 10:90, 1:99, 0:100. $Fe(NO_3)_3 . 9H_2O$ (Sigma-Aldrich, 99%, 0.25 M) and $Mn(NO_3)_2 . 4H_2O$ (Sigma-Aldrich, 99 %, 0.25 M) were pre-mixed and precipitated against a Na_2CO_3 solution (anhydrous, Sigma-Aldrich, 1 M). The pH was set to 9 with metal salt solutions dosed at 3 ml min^{-1}. The solution was left to age for 2 hours and recovered via filtration. The recovered samples were dried and calcined at 500 °C for 3 hours with a ramp rate of 1 °C min^{-1}.

2.1.2.2.1 The effect precipitating agent on preparing iron-manganese mixed metal oxides

The catalysts were prepared as described in section 1.1.2.2 however the base used to precipitate the iron-manganese mixed metal oxide precursor was modified. The following carbonate species: Na_2CO_3, K_2CO_3 and $(NH_4)_2CO_3$ and hydroxide species: NaOH, KOH and NH_4OH solution were investigated.

2.1.2.2.2 The effect of calcination temperature on preparing iron-manganese mixed metal oxides

Catalysts were prepared using the process described in section 1.1.2.2 however using NH_4OH solution as the precipitating agent instead of Na_2CO_3. The calcination temperature was also varied with 400, 450 and 500 °C.

2.1.2.3 Preparation of ceria-manganese mixed metal oxide catalysts via urea co-precipitation

A $Ce_{25}Mn_{75}O_x$ catalyst was prepared using urea as the precipitating agent following a method from literature [1]. Appropriate amounts of $(NH_4)_2Ce(NO_3)_6$ (Sigma-Aldrich, 99.9 %)and $Mn(NO_3)_2 . 4H_2O$ (Sigma-Aldrich, 99 %) were weighed to produce a 1:3 metal ratio and placed into a 100 ml round bottom flask containing 50 ml of deionised H_2O. CH_4N_2O (3.235 g, Aldrich, 99-100.5 %) was then added. The solution was stirred and aged under reflux for 24 hours at 110 °C. The resulting slurry was filtered and washed

with 500 ml deionised water before being dried for 16 hours at 110 °C. The precursor was then calcined at 500 °C under flowing air for 3 hours at 1 °C min^{-1}.

2.1.2.4 Preparation of ceria-manganese mixed metal oxide catalysts via oxalic acid co-precipitation

A Ce$_{25}$Mn$_{75}$O$_x$ catalysts was prepared with a precipitating agent of oxalic acid, following a procedure from literature [2]. Ce(NO$_3$)$_3$. 6H$_2$O (0.005 moles, Sigma Aldrich, 99 %) and Mn(NO$_3$)$_2$. 4H$_2$O (0.015 moles, Sigma-Aldrich, 99 %) were weighed and placed into a beaker containing 200 ml ethanol (Sigma Aldrich, 99.8 %). The mixture was stirred allowing for the metal salts to dissolve before addition of oxalic acid (0.024 moles, Sigma Aldrich >99 %). The solution was left to age for 2 hours at room temperature. Once the aged, the solution was filtered and washed with 500 ml ethanol before dried in an oven at 110 °C for 16 hours. The resulting solid was calcined for 3 hours at 500 °C at 1 °C min^{-1} ramp rate under an atmosphere of flowing air.

2.1.2.5 Preparation of ceria-manganese mixed metal oxide catalyst via citric acid co-precipitation

A method from previous studies was used to prepare a Ce$_{25}$Mn$_{75}$O$_x$ catalyst using citric acid[3]. 50 ml deionised water was placed into a 250 ml round bottom flask which was heated to 50 °C. Ce(NO$_3$)$_3$. 6H$_2$O (0.006 moles, Sigma-Aldrich, 99 %) and Mn(NO$_3$)$_2$. 4H$_2$O (0.018 moles, Sigma-Aldrich 99 %) was added to the stirred water and allowed to dissolve. Citric acid (0.024 moles, Sigma-Aldrich, >99.5 %) was added to the solution and the temperature was raised to 90 °C for 30 minutes. The temperature was then increased to 110 °C and the solution was left to age for 16 hours. The material is then collected from the round bottom flask and dried in an oven at 110 °C for 16 hours. The dried material was then transferred into a ceramic crucible and heated in a muffle oven for 2 hours at 200 °C with a ramp rate of 1°C min^{-1}. To produce the catalyst, the sample is calcined at 500 °C for 3 hours with a ramp rate of 1 °C under a flowing air atmosphere.

2.2 Catalyst Characterisation

A range of analytical techniques were used to investigate the surface and bulk properties of the samples and these are described in this section.

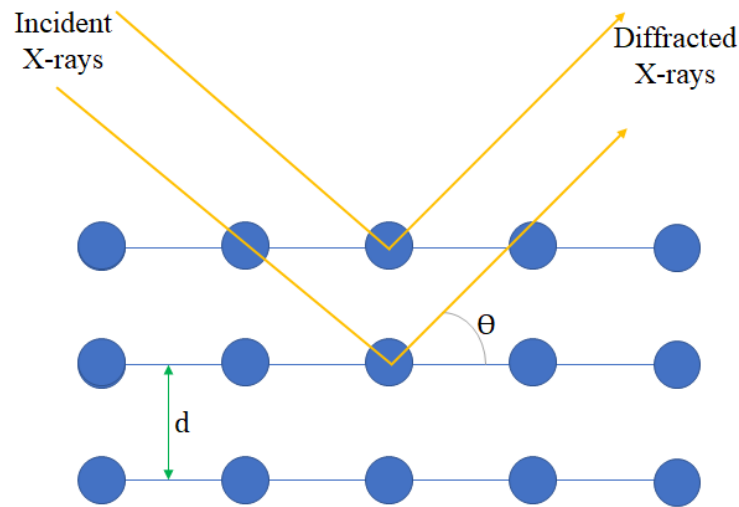### 2.2.1 X-ray diffraction (XRD)

2.2.1.1 Background

Figure 2-3: Diffraction of X-rays by a crystalline sample [4]

XRD is a non-destructive bulk technique which can be used to identify crystal phases of crystalline materials. Crystalline materials are considered to have long range 3-dimensional order and form planes is illustrated in Figure 2-3. When x-ray radiation interacts with a crystalline material, two possible interferences will occur: constructive or destructive. Destructive interference arises when the x-rays are out of phase causing the cancelling out of diffracted radiation. Constructive interference occurs when the interactions obey Bragg's law [5], below. This occurs when the incident x-rays are in phase and when the wavelengths of the reflected x-rays have the difference of an integer number.

$$2dsin\theta = n\lambda$$

Where:

d	inter planar spacing	n	integer multiple
Ө	angle of diffraction	λ	X-ray wavelength

Constructive interference results in a signal being produced. When an x-ray beam interacts with a powdered sample a cone of diffracted x-rays is produced for each angle of diffraction observed on the sample. Each cone of x-rays will vary in intensity depending on the occurrence of the phase or crystal in the sample. The x-rays are then detected and analysed by a detector moving in an arc over the sample to produce a series of closely packed dots which can be extracted and formed into a pattern. The pattern can then be compared to references from databases and the phases present can be identified.

2.2.1.2 Calculating crystallite size using the Scherrer equation

The crystallite size of a given crystal phase in a sample can be calculated using the Scherrer equation [6]. The equation relates the crystallite size to peak broadening as shown below:

$$L = \frac{K\lambda}{B\,cos\theta}$$

Where:

L	crystallite size	λ	wavelength of radiation
Θ	peak position	B	line broadening constant derived
K	shape factor		from FWHM

However, the equation has its limitations. Crystallites below 5 nm form broader and smaller peaks in diffractograms making the FWHM difficult to identify [7]. If the diffractogram has a low signal to noise ratio then smaller peaks may get hidden in the pattern. This leads to error when determining the crystallite size.

The strain and disorder in the sample and x-ray source need to be considered [8]. By using an internal Si standard, the contribution from the x-ray source is noted and adjusted in the line broadening constant. The samples' lattice strain in the sample is calculated using the following equation:

$$Lattice\ strain = \frac{B}{4\,tan\theta}$$

Where:

B	$\sqrt{(B_{obs}^2 - B_{std}^2)}$	B$_{std}$	instrument line broadening width
B$_{obs}$	peak width	Θ	peak position

2.2.1.3 Experimental procedure

2.2.1.3.1 Powder XRD

Samples were placed in metal sample holders and patterns were analysed using a Panalytical X'Pert diffractometer with a Cu X-ray source operating at 40 kV and 40 mA. Patterns were attained by 40 minute scans over a range of 5-80 ° 2Θ angles. Phase identification was performed by matching experimental patterns against entries from the International Centre for Diffraction Data (ICDD) database.

Calculating the crystallite size using the Scherrer equation is noted to have ~10 % error [9]. These errors arise from the Gaussian function used to define the peak shape, the line broadening occurring from the instrument and potential defects or changes in shape of the crystallites being investigated [10].
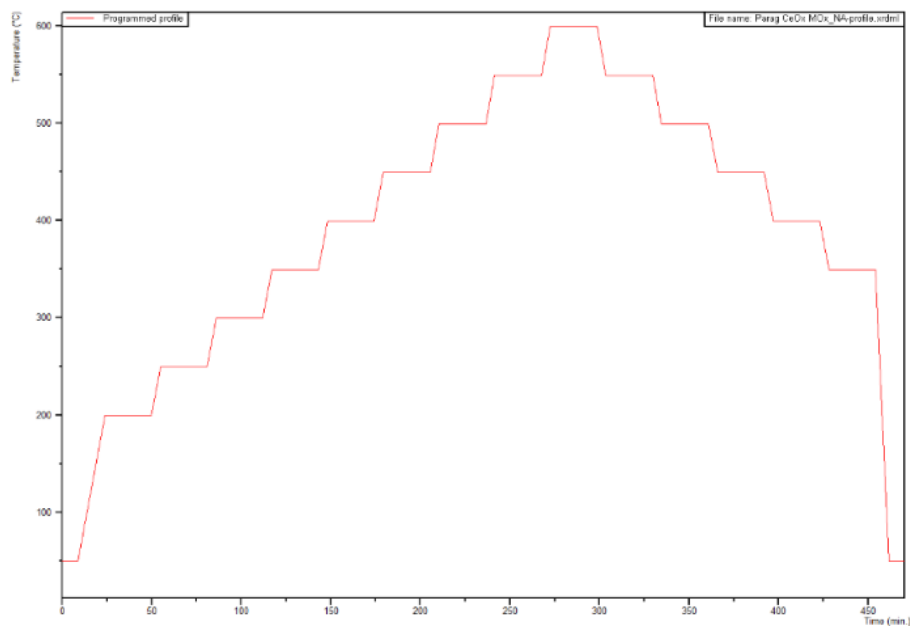
Figure 2-4: Temperature profile of the in-situ XRD experiments

In-situ XRD was used to investigate phase changes during decomposition and calcination of catalyst precursors. A Panalytical X'Pert diffractometer with an Anton Paar 900K *in-situ* cell was used to undertake these experiments. Data were collected by heating the sample from 200 to 600 °C under a flow of air (30 ml min^{-1}), holding the temperature isothermally at 50 °C intervals for 30 minutes to acquire data, Figure 2-4.

2.2.2 Raman spectroscopy

2.2.2.1 Background
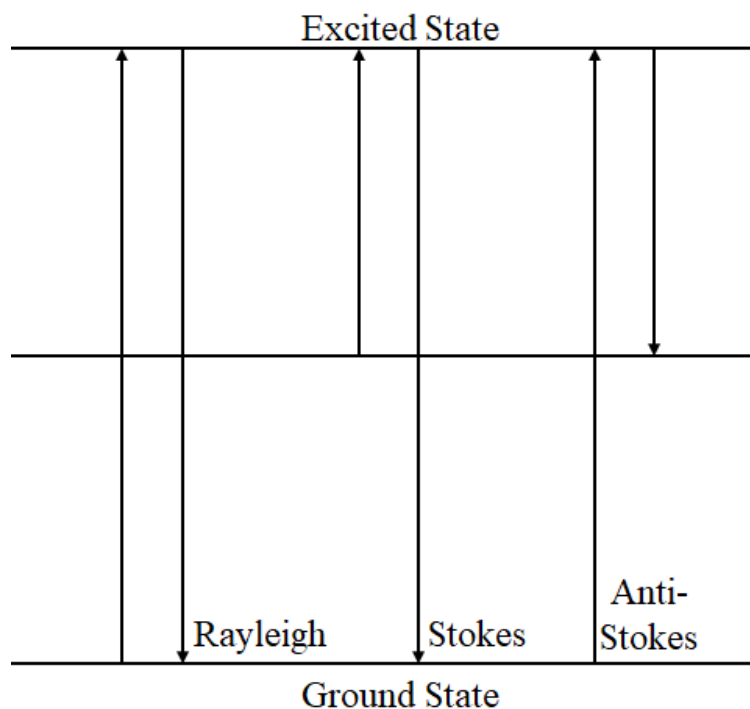
Figure 2-5: Excitation and relaxation of molecules when irradiated by electromagnetic radiation [11]

When a molecule is irradiated by electromagnetic radiation, the energy produced can behave in 3 ways: transmission, absorbance or scattering of the radiation. Raman spectroscopy is a technique that investigates scattering of electromagnetic radiation by a molecule [12]. The radiation can scatter either elastically or inelastically. Elastic scattering ($\Delta \upsilon = 0$) occurs when the energy of the photon returns to its original energy state which is referred to Rayleigh scattering, Figure 2-5. Raman scattering occurs when the reflection is inelastic ($\Delta \upsilon \neq 0$). If the photon gains energy, then the Stokes frequencies are observed and if it losses energy then Anti-stokes frequencies are observed.

$$\upsilon_i - \upsilon_s = \Delta \upsilon = \Delta E_m$$

Where:

υ_i	frequency of the incident light	$\Delta \upsilon$	frequency shift
		ΔE_m	energy change
υ_s	frequency of scattered light		

Not all molecules are Raman active. The molecule must have a change in polarizability, deformation in an electric field, for Raman scattering to occur. Raman spectroscopy measures the rotation or vibration transitions of the scattered molecule which are

observed in the visible region. Therefore, transitions of samples which can't be seen under visible light are also difficult to observe during Raman spectroscopy.

2.2.2.2 Experimental procedure

Raman spectra were obtained using a Renishaw inVia confocal Raman microscope equipped with an Ar+ visible green laser with an emission of 514 nm. The laser was focused using an Olympus BH2-UMA microscope. The catalyst samples were placed onto a steel plate and spectra were collected in a reflective mode by a highly sensitive charge couple device (CCD) detector.

2.2.3 Thermogravimetric analysis (TGA)

2.2.3.1 Background

Thermogravimetry is a technique which uses a highly sensitive balance in an oven to measure the mass loss of sample during its decomposition. Due to the methods used to synthesise the catalysts during the study, samples must be heat treated to produce the final metal oxide catalyst.

The samples have different decomposition patterns however follow the same decomposition path. Physiosorbed water is the initial species desorbed followed by the decomposition of the precursor species, nitrate or carbonate, to produce the final metal oxide. Using this information, it can be related to the conditions required to calcine the sample to produce the final catalyst sample.

2.2.3.2 Experimental procedure

Approximately 50 mg of sample was placed into ceramic crucibles and loaded into a Perkin Elmer TGA 4000 instrument using a robotic arm. The samples were then heated from 30 to 995 °C at a rate of 5 °C min^{-1} under a flowing nitrogen atmosphere. Profile attained as expressed as a percentage loss from the initial mass placed into the crucible.

2.2.4 Temperature programmed reduction (TPR)

2.2.4.1 Background

TPR is a method which investigates the reducibility of a sample under a flow a H_2 in an inert gas over a temperature range. During this study the reducibility of species on the surface and in the bulk of metal oxides will be studied. Oxygen species present in the samples are reduced into water. The water becomes trapped in a molecular sieve the TPR equipment. Any remaining hydrogen is then analysed using a TCD.

The reducibility of a sample can be correlated to its oxygen mobility. Peaks at low temperatures or which are very sharp in TPR patterns indicate high reducibility. The

reverse indicates that the sample has low oxygen lability. This is measured using the equation below, with the correlation factor calculated using a CuO reference.

$$\mu mol \ of \ H_2 \ consumed = Absolute \ area \ of \ reduction \ peak \ x \ 5.8682 \ x10^{-4}$$

This data can be correlated against catalytic activity data or used to find any alloying between the metals. Oxidation states can be calculated and identified using TPR studies [13].

2.2.4.2 Experimental procedure

Temperature Programmed Reduction (TPR) was performed using a Quantachrome ChemBET TPD/R/O apparatus. Samples were loaded into a quartz u-tube (~30 mg) and pre-treated under a flow of He at 120 °C for 1 hour prior to analysis. Reduction profiles were obtained by the sample under a flow of 10 % H_2 in Ar (30 ml min^{-1}) over a temperature range from ambient to 1100 °C with a ramp rate of 15 °C min^{-1}.

2.2.5 Brunauer-Emmet-Teller surface area analysis (BET)

2.2.5.1 Background
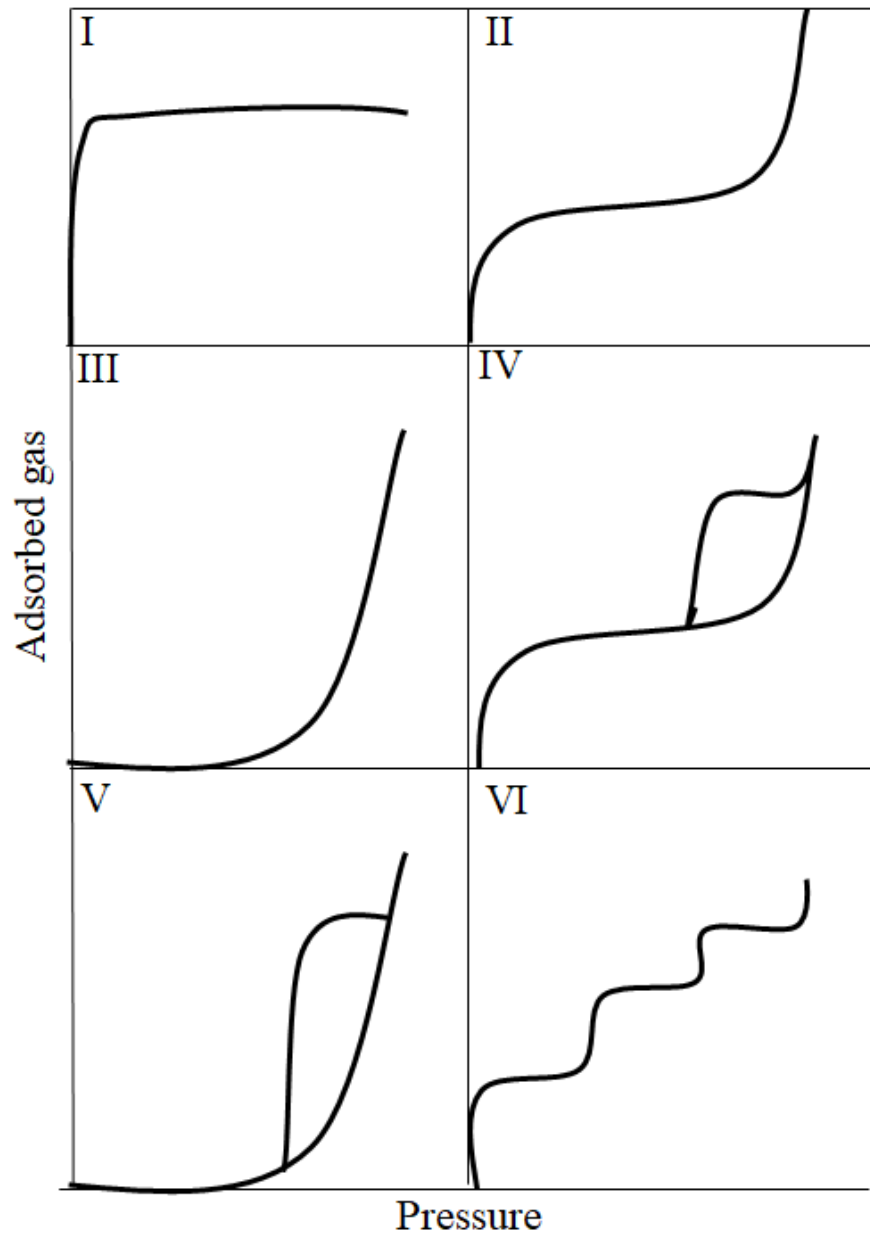
Figure 2-6: 6 Potential Isotherms. Type I is the Langmuir isotherm, type II the BET isotherm and IV the adsorption isotherm [7]

Gas adsorption techniques are used to characterise the surface area of materials. The BET isotherm takes its inspiration from previous work by Langmuir. Langmuir assumed that only one monolayer of non-interactive gas is adsorbed onto the surface [14], Figure 2-6, producing the type I isotherm. However, BET extended this assumption to include a simplified model of mono-layer and multi-layer adsorption, type II or IV. They theorised that the gases adsorb on the surface indefinitely, producing multilayers. Each individual layer can have the Langmuir theory applied to it to produce the equation below [15]:

$$\frac{1}{(V(\frac{P_{\circ}}{P} - 1))} = \frac{C - 1}{V_m\,C} \; x \; \frac{P}{P_{\circ}} + \frac{1}{V_m\,C}$$

Where:

P	Pressure	V_m	Volume of monolayer on the
P_o	Saturation Pressure		surface
V	Volume of gas adsorbed on the	C	BET constant
	surface		

The assumptions required for the multi-layer formation is expressed in the BET (C) constant, below. The first layer is adsorbed with a heat of adsorption with further layers adsorbed with equal heat of condensation. The C constant is also used to validate the application of the BET method. If the value is too low, then monolayer coverage is too high leading to poor interaction between the surface and adsorbate.

$$C = e(\frac{(E_1 - E_L)}{RT})$$

Where:

E_1	heat of adsorption	E_L	heat of condensation for the
			adsorbate

If the BET method is valid for the sample the surface area can be calculated using the n_m. N_2 is the standard adsorbent used to calculate the BET method.

$$S_{BET} = \frac{n_m}{M} N_A \sigma$$

Where:

n_m	molar volume of a monolayer of	N_A	Avagadro's number
gas		σ	molecular area of N_2 (16.2 Å^2)
M	mass of sample		

2.2.5.2 Experimental procedure

The catalyst surface areas were determined using a Quantachrome Quadrasorb Evo analyser. Samples (~100mg) were placed into 9 mm quartz tubes with bulbs. Samples were pre-treated under a vacuum to remove any surface species. Surface area was determined from collection of 5-point N_2 adsorption between $\frac{p}{p_o}$ values of 0.05 and 0.35. Each point was attained at -196 °C by submersing the tubes in liquid N_2. The data is then treated using the BET method.

Errors arise from the assumptions used to determine the values in the BET method and can account for a ~20 % error in specific surface areas [16]. Errors can be kept to a few

percent if the C constant is over 80 and this was the standard used to determine the surface areas in this investigation.

2.2.6 Microwave plasma- atomic emission spectroscopy (MP-AES)
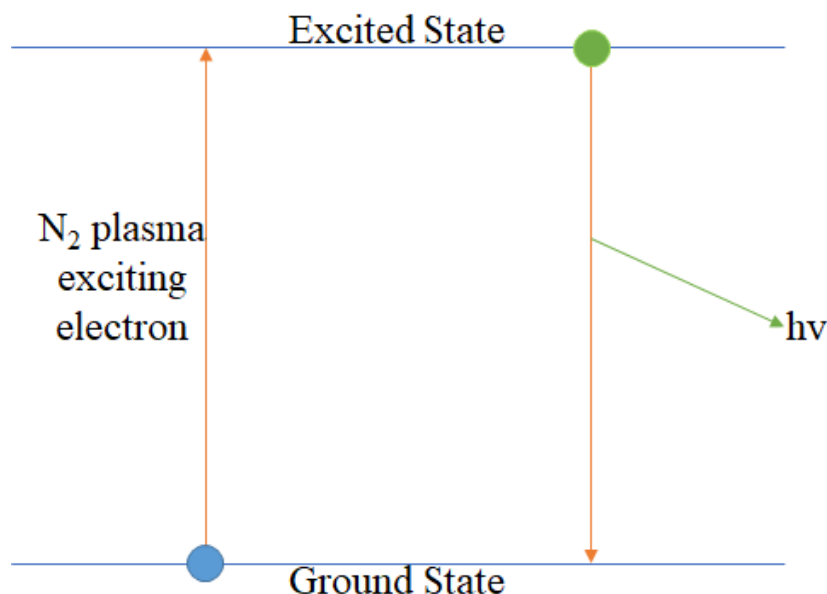
2.2.6.1 Background

Figure 2-7: Atomic emission from excited electrons returning to ground state [17]

Atomic emission spectroscopy is a technique which studies the wavelengths of photons emitted from electrons returning to a ground state after excitation, Figure 2-7. In MP-AES a nitrogen plasma is used to excite the sample to produce photons. Samples are present in liquid form and sprayed into the plasma which excites the electrons present. When the electrons relax, a characteristic wavelength is emitted. The wavelength is detected by a charge-coupled device (CCD) and correlated against standard solutions to quantify the concentration of elements present.

2.2.6.2 Experimental procedure

Initially standards solutions were prepared by diluting 1000ppm stock solutions of the metals. The catalyst samples are prepared via adding aqua regia ($\sim$4 cm^3) to a pre-weighed catalyst sample ($\sim$25 mg) in a 50 ml volumetric flask. The catalyst is left to digest overnight and topped up with deionised water. The solutions are then filtered to remove any undissolved material and analysed in an Agilent 4100 Microwave Plasma-Atomic Emission Spectrometer against the calibrated standard solutions. The solution is sprayed through a N$_2$ plasma producing a response factor to determine the concentration of the solution. The spray is pressurised to 120 kPA and injected with air. The solution is analysed 3 times at each wavelength.

Two or three different wavelengths for each element were used to determine the concentration of the element present in the sample. These values are then averaged to provide the final concentration of the element present. The error for each element ~1 % based on the standard deviation of the values obtained from MP-AES analysis. Each element has a range of unique wavelengths; therefore care must be taken when selecting wavelengths when analysing multiple elements. If the wavelengths are too close, overlapping of peaks can occur producing a false result. The wavelengths used during the study are mentioned in Table 2-1:

Table 2-1: Wavelengths used to analyse the element concentration of catalysts using MP-AES

Element	Wavelength used / nm
Fe	371.993, 373.713, 385.991
Mn	257.610, 403.076, 403.307
Na	588.995, 589.592
K	769.897, 766.491

2.2.7 X-ray photoelectron spectroscopy (XPS)

2.2.7.1 Background
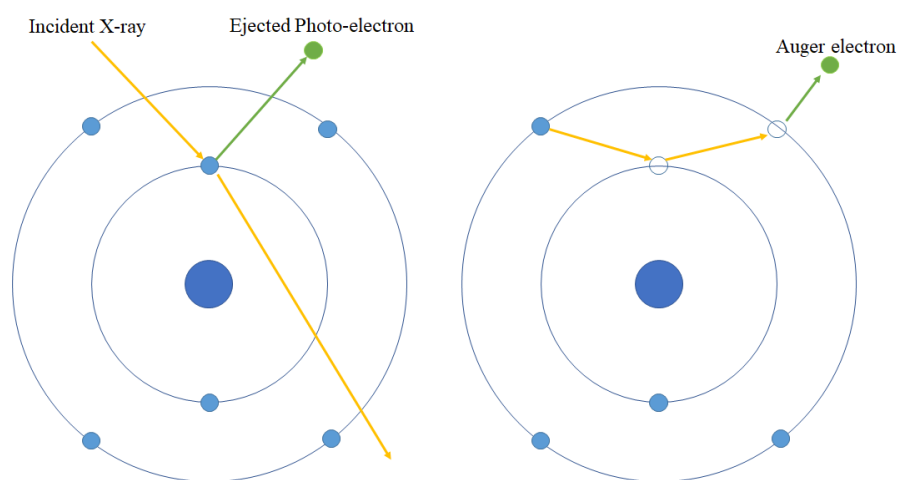
Figure 2-8: Schematic of an x-ray photo electron emission and proceeding Auger emission [18]

XPS is a near surface sensitive technique which uses x-rays in a vacuum to cause the emission of photo-electrons, Figure 2-8. These electrons are identified as photo-electrons due to the electromagnetic radiation causing their emission. The loss of the electron leaves an excited ionised atom. When the atom relaxes, an electron from a higher orbital fills the hole in the core orbital. This is a high energy process which may cause the emission of x-rays or another electron. The secondary electron is referred to as an Auger electron.

Due to conservation of energy, the relationship between the energy of the emitted electron can be calculated. This is calculated by measuring the kinetic energy of the electron and relating this to its binding energy:

$$E_{kinetic} = E_{photon} - (E_{binding} + \phi)$$

Where:

$E_{kinetic}$	kinetic energy of ejected electron	E_{photon}	energy of photon emitted
$E_{binding}$	binding energy of electron	ϕ	work function of spectrometer

The binding energy is affected by factors before (initial state effects) or after (in response to relaxation in the atom) photo-emission. This may cause peaks to shift to higher energies in the spectrum or formation of satellite peaks at lower energies. These effects are characteristic to certain elements or molecules. The kinetic and the binding energy is characteristic to its element allowing for identification and quatification of surface species. The oxidation states of metals can also be measured

2.2.7.2   Experimental procedure

X-ray photoelectron spectroscopy (XPS) was carried out using a Thermo Scientific K-Alpha+ Spectrometer, equipped with an Ar ion source and Al Kα micro-focused monochromator operating at 72 W (6 mA, 12 kV). Survey and high-resolution scans were carried out at pass energies of 150 and 40 eV respectively with a 1 or 0.1 eV step size. Charge neutralisation was achieved using a combination of flux of low-energy electrons and Ar ions. Spectra were calibrated against the C(1s) peak at 284.8 eV.

CasaXPS (v2.3.19rev1.1l) was used to analyse the data obtained from XPS, using a Scofield sensitivity factors and an energy dependence of -0.6, after removal of a Shirley background.

2.2.8 Scanning electron microscopy- energy dispersive x-ray spectroscopy (SEM-EDX)

2.2.8.1   Background

Optical microscopy uses visible light wavelengths to obtain images. However, images from optical microscopy are limited by its resolving power and magnification due to the energy of the electromagnetic radiation used to obtain images. Electron microscopy uses electron beams with higher energy, these limitations can be overcome. This produces a higher resolution topographical image of the sample [19].

Heated W hairpins or LaB_6 needles in a vacuum are common electron sources in SEM. The electron beams are focused onto the sample using a series of magnetic lenses. When the beam interacts with the sample elastically, high energy scattering occurs (>50 eV). Scattering occurs on the surface in a tear drop shape, the scattering volume. The higher the power, the larger scattering volume producing more backscattered electrons, Figure 2-9. These backscattered electrons can then be collected and passed through a detector to produce a signal which is converted into image. Heavier elements will appear brighter in images as they scatter the electron more efficiently producing a higher energy electron. Back scattered detectors are placed above the sample and provide a image of the composition and phases present in the sample.
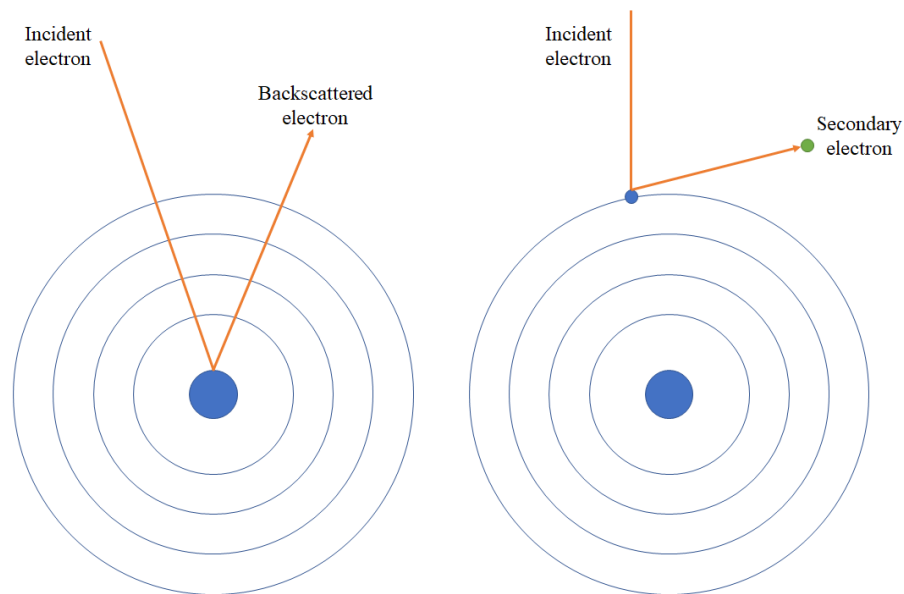
Figure 2-9: Schematic of interactions between used for imaging

If the electron path back to the detector becomes perturbed this causes inelastic scattering of electrons. This process produces secondary electrons which have an energy of 3-5 eV. Two types of secondary electron scattering can occur based on their energy and angular distribution. Secondary electrons can be detected from the surface or by backscattering electrons returning to the surface via several elastic interactions. The secondary electron is placed on the side of the sample stage and provides images of the topography of the sample.

EDX is a technique using the high energies involved in the electron beam. This causes the core electrons can be removed, akin to the process observed during XPS (section 2.2.7). When the atoms relax an electron from a higher orbital replaces the core electron. During this process a photon is emitted is remove the excess energy, in the form of x-ray radiation. Each element has a characteristic energy depending on the difference between in energy between the electrons. The technique is used to map multiple elements from an

image generated using SEM. Using this a samples bulk elemental distribution and quantification can be attained at a range of field views.

2.2.8.2   Experimental procedure

Microscopy was performed on a Tescan Maia3 field emission gun scanning electron microscope (FEG-SEM) fitted with an Oxford Instruments XMAX^N 80 energy dispersive X-ray detector (EDX). Samples were dispersed as a powder onto adhesive carbon Leit discs mounted onto aluminium stubs. Before analysing the stubs were then sprayed with a 15 nm Au:Pd (80:20 ratio) coating. Images were acquired using the secondary electron and backscattered electron detectors at varying magnification and field view.

EDX elemental analysis was undertaken by averaging elemental concentrations from three maps. The error in elemental analysis was ~5 %. However due to the small sample size of maps used to calculate the elemental concentrations the error may be significantly higher.

2.2.9   Transmission electron microscopy (TEM)

2.2.9.1   Background

TEM is another form of electron microscopy which relies on electrons passing through the material. The electrons are detected with a screen and placed below the sample holder with lenses focusing the beams onto them [20]. TEM microscopes use a high energy beam of electrons passing through an ultra-thin sample. If areas of the sample are too dense, then the electrons become adsorbed. Whereas other thinner areas will allow the electrons to pass through and are detected on the screen. Images are then obtained by the contrast in the different phases present in the sample.

The TEM equipment can also carry out electron diffraction experiments. This occurs due to wave-particle duality causing electrons to behave like a wave. Therefore the electrons can behave like the X-rays in XRD (section 2.2.1) and become diffracted by lattice planes in a sample [21]. The electrons are detected by a fluorescent screen producing either concentric rings or bright spots, depending on the crystallinity of the sample[22]. From these patterns, the crystal lattices present and the lattice spacing can be interpreted. This technique is limited by sample thickness, due to the high energies required to penetrate multiple layers of atoms.

2.2.9.2   Experimental procedure

A JEOL JEM-2100 operating at 200 kV was used to carry out TEM. Samples were prepared by suspension in ethanol by sonication and deposited on 300 mesh copper grids coated with holey carbon film.

2.3 Catalyst Testing

The catalytic activity of the catalysts was investigated by undertaking propane and naphthalene total oxidation. Both reactions were carried out in continuous flow reactors. This section discusses the equipment used.

2.3.1 Propane oxidation

2.3.1.1 Reactor set-up

Figure 2-10 shows the reactor set up of the testing of propane total oxidation which is attached to an Agilent 7090B GC. All the gas tubing was constructed out of 1/8-inch steel tubing. The lines leading out of the reactor and before the GC were heated using a heat tape and glass fibre insulation, to prevent any condensation of water or partial oxidation products. Propane in air cylinder (5000 vppm propane in air) was flowed at 50 ml min^{-1} into the system using Brooks MFCs. The propane gas mixture is then flowed through a reactor tube heated by a tubular Carbolite furnace. The temperature is controlled by a K-type thermocouple placed on top of the catalyst bed. An appropriate volume of catalysts was used to attain a desired GHSV with activity measured over a temperature range of 200-600 °C.
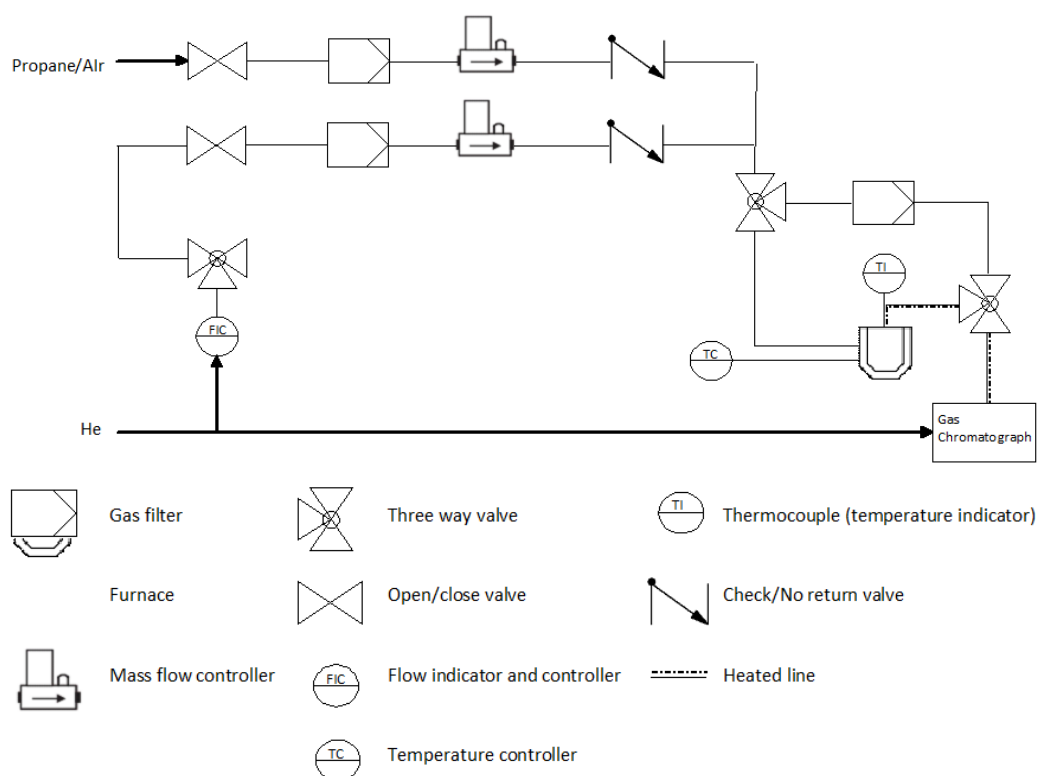
Figure 2-10: Piping & Instrumentation Diagram schematic of the propane total oxidation reactor

2.3.1.2 Gas chromatography

The products of the propane total oxidation reactions were analysed using an Agilent 7090B GC which separates gases based on their ability to adsorb and desorb on stationary phase on the column compared to a mobile phase flowing through it. The mobile phase for this GC system is He. The system uses one TCD and one FID to analyse the products once product separation has occurred.

2.3.1.2.1 Separation of products

Inside the Agilent 7090B GC has two separation columns located in series. The first column is a HayeSep Q column which separates carbon dioxide and light hydrocarbons and the second a Molecular Sieve column which separates oxygen, nitrogen and carbon monoxide. Table 2-2 shows the temperature program of the oven used to separate the products from the column during the analysis.

Table 2-2: Temperature program used to separate propane total oxidation products

Step	Temperature / °C	Ramp Rate / °C min^{-1}	Hold Time / min
Initial	80	-	3
1	200	20	5

The GC system has three six port valves (V1, V2 and V3) which control which gases pass through columns, detectors or are bypassed without interaction with both. Table 2-3 demonstrates the valve timings used to sample the reaction mixture for analysis.

Table 2-3: Propane total oxidation GC valve timings. Numbers in the position column refer to valves in figures Figure 2-11, Figure 2-12 and Figure 2-13

Step	Time / mins	Position
1	0.1	V1 OFF
		V2 and V3 ON
2	3	V1, V2 and V3 ON
3	9	V1 and V2 OFF
		V3 ON

Initially the sample loop fills up with reaction gas mixture. Once the GC system is ready to start analysing the effluent V3 and V2 switch, Figure 2-11, to allow the gases to be separated by the HayeSep Q column.
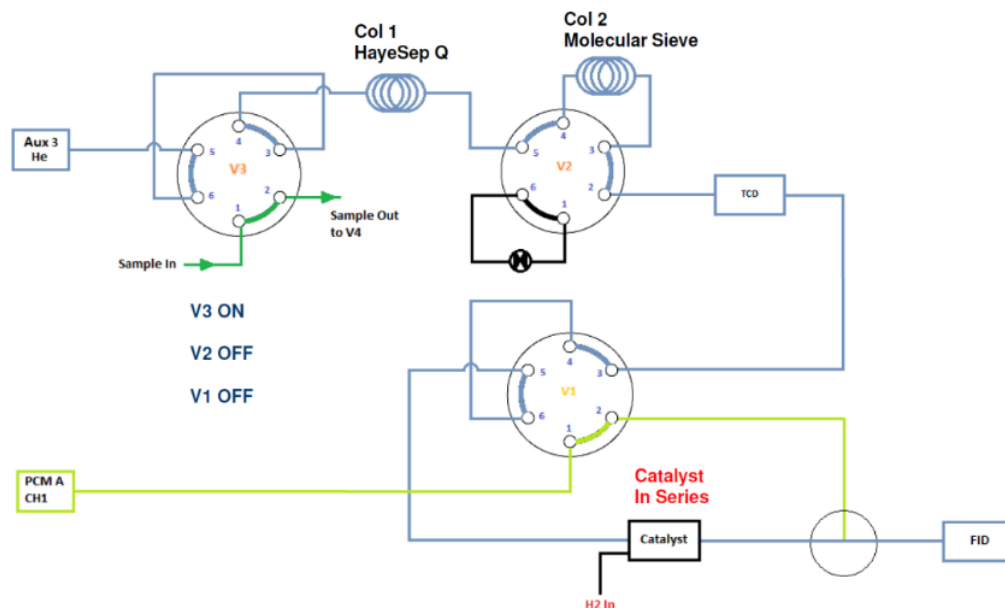
Figure 2-11: Injection of sample in GC during analysis of propane total oxidation products

The HaySep Q column traps the CO_2 and propane on it allowing the carbon monoxide, oxygen and nitrogen to flow into the molecular sieve for separation, figure 11. After 3 minutes the valves change, leaving the gases in the molecular sieve and allowing the CO_2 and propane to be detected and analysed by TCD and FID, Figure 2-12. It is important that the TCD is placed before the FID as the FID destroys the sample upon analysis.
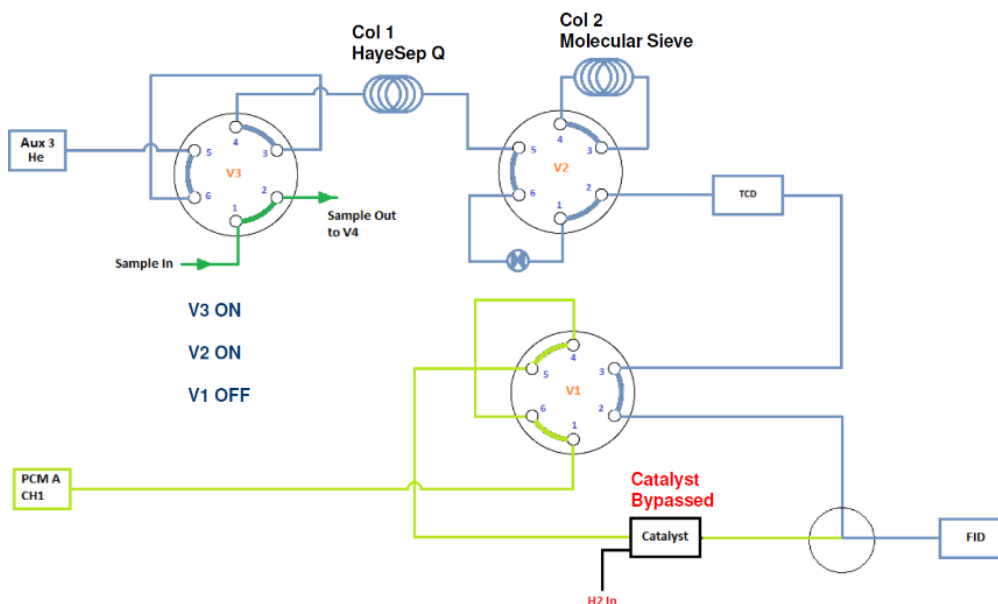
Figure 2-12: Analysis of products from propane total oxidation by the TCD

Once the sample from the Hayesep Q column have been analysed the nitrogen, oxygen, carbon dioxide and carbon monoxide from the molecular sieve column are analysed by passing them through the TCD, Figure 2-13. The carbon monoxide and carbon dioxide is

then further analysed by the FID equipped with a methaniser. This is the value used during the project.
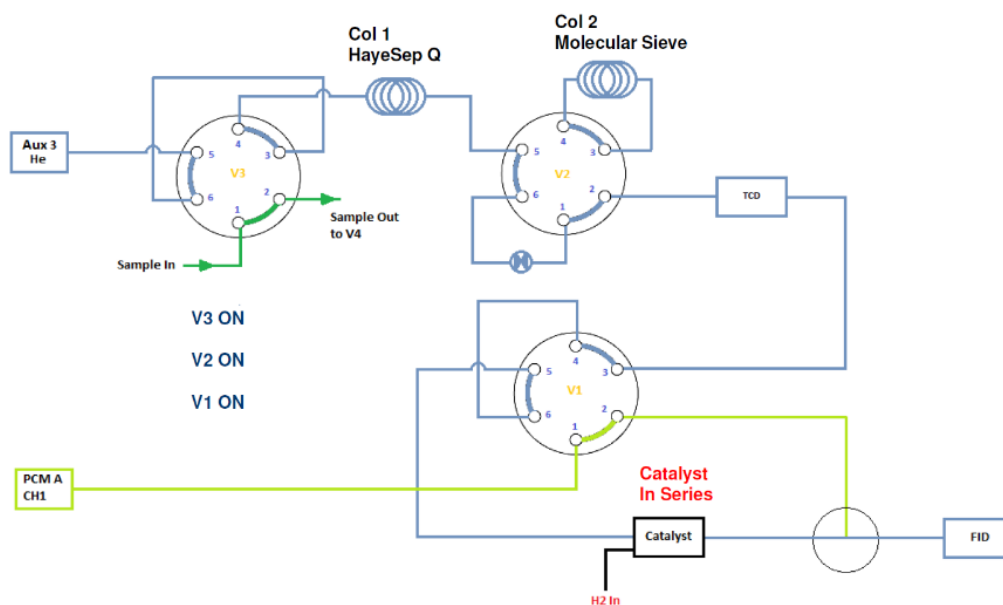
Figure 2-13: Analysis of propane total oxidation products by the FID

2.3.1.2.2 Analysis of products

The simple gases such as oxygen and nitrogen are analysed using a TCD. This detects compounds by analysing the change in thermal conductivity of the gas against a He reference. A metal filament resides in the TCD which undergoes changes in its resistance as the thermal conductivity changes compared to the reference. This resistance will produce a voltage which can be measured and detected to produce a signal.

The carbon dioxide, carbon monoxide and propane are analysed used a FID. Before analysis in the FID, the samples are treated using a methaniser which converts the gases into methane over a Ni catalyst under a H_2 stream. As CO and CO_2 can't be detected on the FID this is required and is used to improve the resolution of the propane in the FID. The FID detects signal by passing the sample through a H_2 flame and combusting it producing ions. The ions are then collected and analysed allowing for a signal to be generated. The elution times for the gases in the GC were, Figure 2-14:
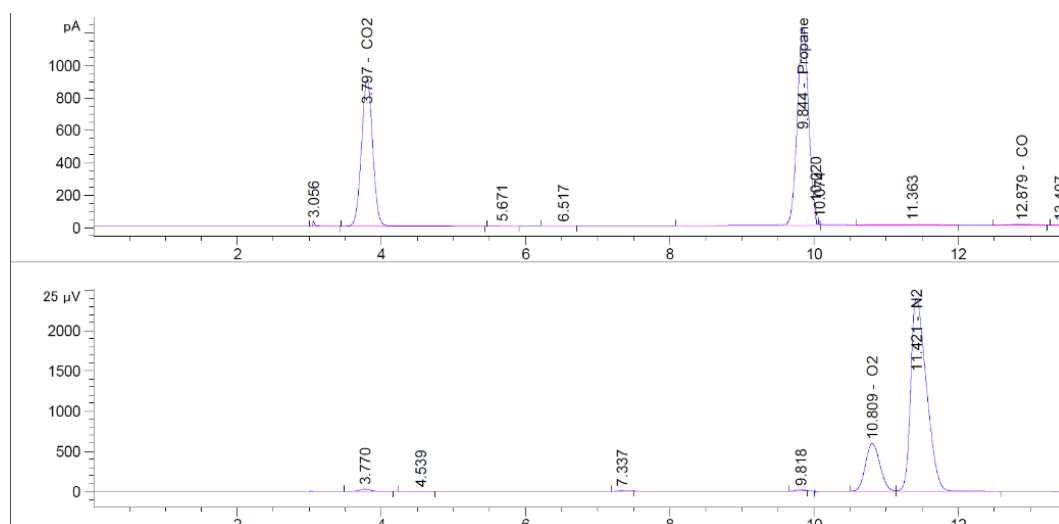
Figure 2-14: GC trace of propane total oxidation. Above is from the FID and below is from the TCD

- Carbon dioxide   3.7 minutes
- Propane   9.8 minutes
- Oxygen   10.8 minutes
- Nitrogen   11.4 minutes
- Carbon monoxide   12.8 minutes

Propane conversion is measured by comparing the % propane remaining against the counts a value when of 5000 ppm propane is present, which is taken by averaging four blank runs at the start of the experiment:

$$\% \, Propane \, Conversion = \left(100 \; x \; \left(\frac{Counts \; of \; propane \; remaining}{Counts \; of \; 5000 \; ppm \; propane}\right)\right)$$

Carbon balance was calculated by comparing the amount of carbon in the blank runs against the carbon present in the reaction runs:

$$\% \, Carbon \, balance$$

$$= 100 \; x \; \left(\frac{Counts \; of \; propane + Counts \; of \; carbon \; dioxide + Counts \; of \; carbon \; monoxide}{Counts \; of \; 5000 \; ppm \; propane}\right)$$

2.3.1.2.3 Propane total oxidation reference reaction

A commercial 5 % Pd/Al$_2$O$_3$ catalyst (Johnson Matthey) was used a reference catalyst, Figure 2-15, against which the mixed metal oxides will be compared to during the study. The catalyst showed appreciable propane total oxidation activity with 100 % propane conversion occurring at 550 °C along with a carbon balance (>99 %) throughout the reaction.

53
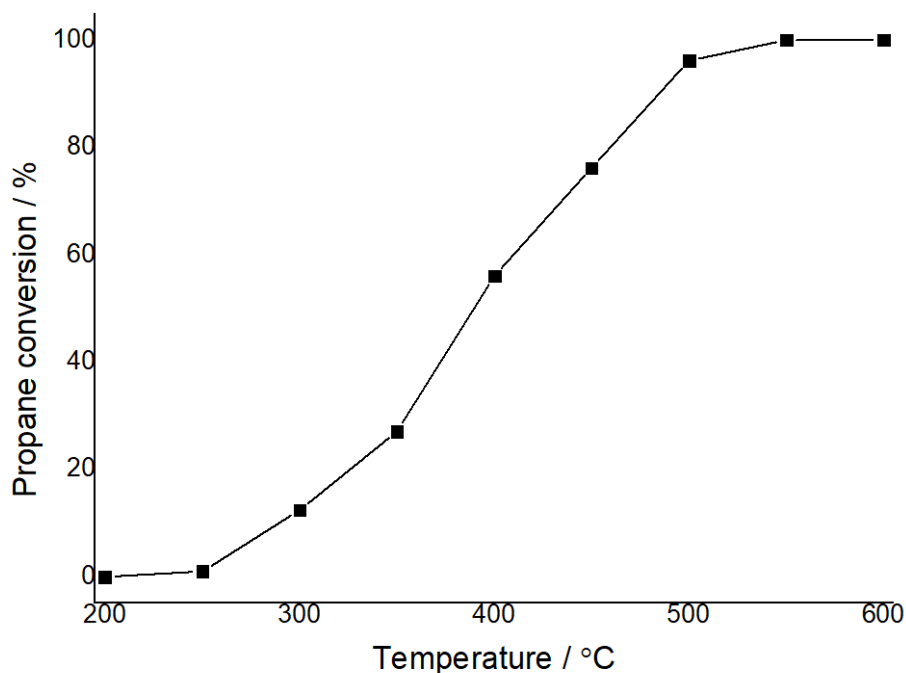
Figure 2-15: Catalytic activity for the total oxidation of propane over the 5 % Pd/Al$_2$O$_3$ reference catalyst. Reaction conditions: 45,000 h^{-1}, temperature range: 200-600 °C, 5000 ppm in air.

2.3.2 Naphthalene oxidation

2.3.2.1 Reactor set-up

The reactor set up for the naphthalene total oxidation is shown in Figure 2-16. All tubing was constructed out of 1/8-inch steel tubing, with all lines past the naphthalene generator heated to prevent condensation of hydrocarbons and water within the reactor set up. Both He and O$_2$ gas flow were controlled by Brooks MFCs. 100 vppm naphthalene was generated by subliming a small amount of naphthalene (Sigma-Aldrich, 99 %) under a He flow at 35 °C. Oxygen was then added into the system to provide a gas mixture of 80 % helium and 20 % oxygen. The gas flow is then passed through a reactor tube, containing an appropriate amount of catalyst, which is heated using clam-shell furnace. An appropriate volume of catalyst was used to establish a desired GHSV. The temperature is monitored using a k-type thermocouple placed underneath the catalyst bed with catalytic activity observed over a range of 100-350 °C. The gas flow then goes into an Agilient 7090B GC for analysis.
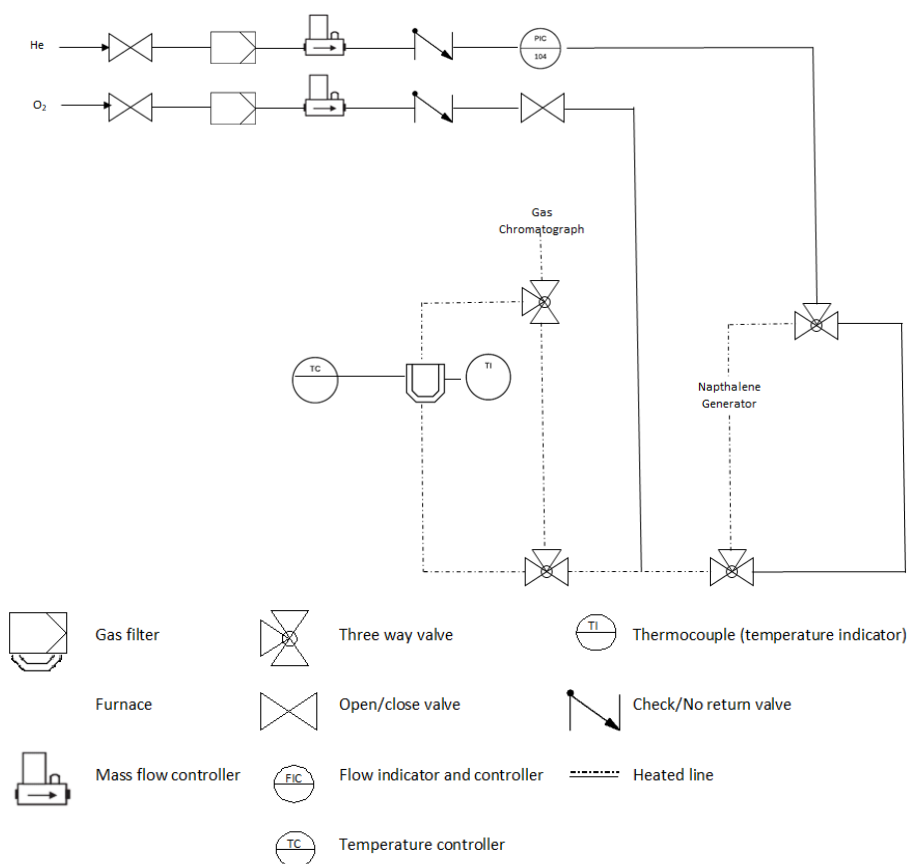
Figure 2-16: Piping & Instrumentation Diagram schematic of the naphthalene total oxidation reactor

2.3.2.2 Gas-chromatography

An Agilent 7090B GC was used to separate and analyse the products formed during the naphthalene total oxidation reactions. The set up for this GC is like the one used for propane total oxidation in section 1.2.1.2 with helium used as the carrier gas for this system. To analyse and quantify any reaction products formed two FID were used with one equipped with a methansier.

2.3.2.2.1 Separation of products

Separation of products occurs using an HP-5mn Ultra Inert column. Fast separation of CO and CO_2 occurs on the column at low temperatures. However due to the nature of naphthalene a temperature ramp must be incorporated into the method to allow for separation, Table 2-4.

Table 2-4: Temperature program used to separate naphthalene total oxidation products

Step	Temperature / °C	Ramp Rate / °C min^{-1}	Hold Time / min
Initial	65	-	3.1
1	160	20	5

In Table below, the order of valve switching is shown. 2 valves, 1 ten port valve (V1) and 1 six port valve (V2), are used to separate the carbon monoxide and carbon dioxide from naphthalene and other hydrocarbon products.

Table 2-5: Naphthalene total oxidation GC valve timings. Position refers to valves in Figure 2-17 and Figure 2-18

Step	Time / mins	Position
1	0.01	V1 ON
2	0.01	V2 ON
3	1	V1 and V2 OFF

Initially the reaction mixture fills the sample loop and once the valves turn on, step 1 and 2 in Table 2-5, analysis begins, Figure 2-17.
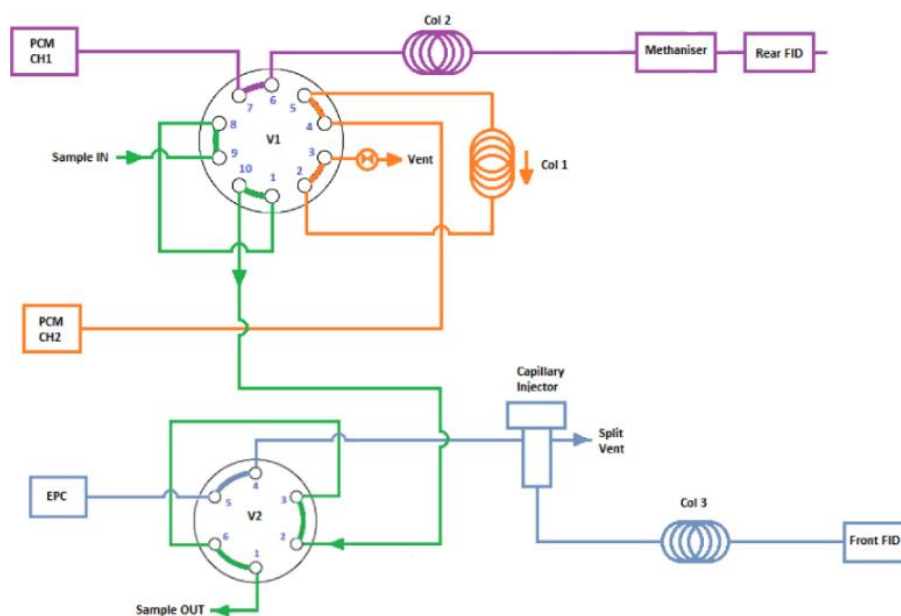
Figure 2-17: Filling of sample loop in GC during analysis of naphthalene total oxidation products

The sample loop takes 1 min to empty with portions of the mixture flowing into each FID, Figure 2-18. The front FID detects the hydrocarbons in the reaction effluent and the rear FID measures the amount of carbon monoxide and carbon dioxide. Once the

gases from the sample loop have been feed into the GC system, the GC valve returns to its original state, Figure 2-17, to allow for analysis of the subsequent reaction runs.
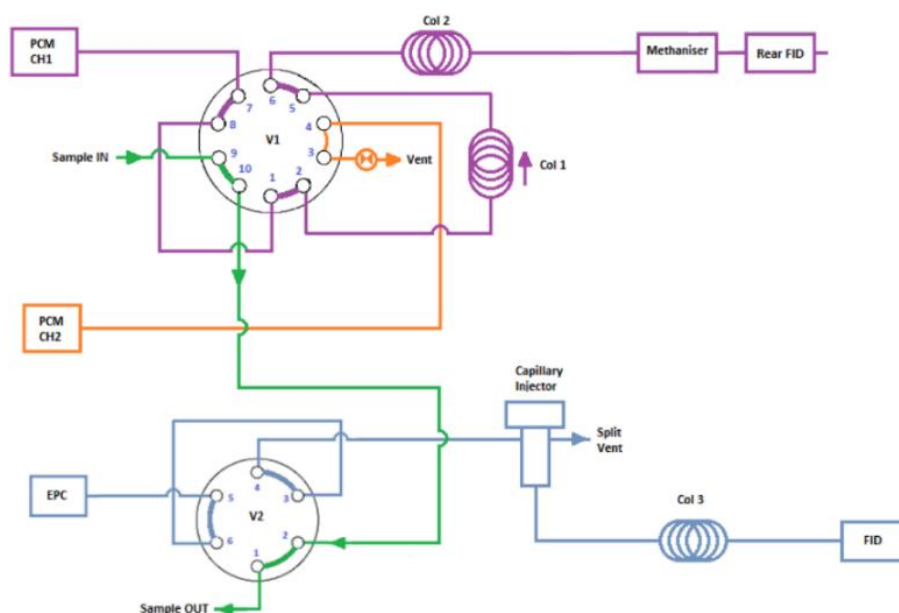
Figure 2-18: Analysis of naphthalene total oxidation products by FID

2.3.2.2.2 Analysis of products

Two FIDs are used to analyse the reaction products for the reaction. The front FID analyses the naphthalene and any partial oxidation products observed. The back FID analyses CO and CO_2, however these gases have to be converted into a hydrocarbon before analysis. This is because the FID requires a sample which is ionisable in a H_2 flame. The conversion occurs using a methaniser, which flows the reaction effluent over an Ni catalyst under a H_2 flow. All products are then analysed by passing the effluent into the FID.

The elution time for the products observed during naphthalene total oxidation are, Figure 2-19:
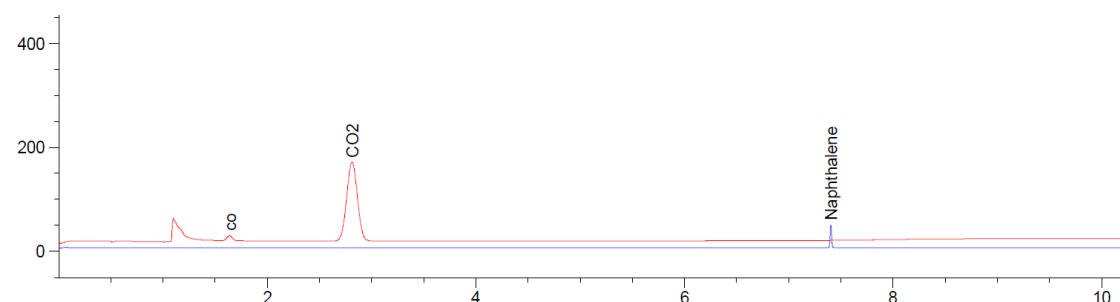
Figure 2-19: GC trace of naphthalene total oxidation. Red trace is from the back FID and blue trace from the back FID

57

- Carbon monoxide   1.65 minutes   • Naphthalene   7.5 minutes
- Carbon dioxide   2.75 minutes

Before each reaction run, four blank runs are undertaken to confirm the ppm of naphthalene during the reaction. Typically the value is 100 ppm, however can fluctuate between reactions. It is also used to determine the 100 % value of naphthalene present in during the reaction. This is used to calculate naphthalene conversion.

$$\% \ Naphthalene \ conversion = 100 \ x \ \left(\frac{Counts \ of \ Naphthalene \ remaining}{Counts \ of \ Naphthalene \ during \ blank}\right)$$

Naphthalene total oxidation reactions are measured using CO_2 yield rather than naphthalene conversion. If the naphthalene is totally converted into CO_2, a value of 1000 ppm CO_2 is expected to be produced. Naphthalene adsorption behaviour on catalysts surfaces at lower reaction temperatures leads to discrepancies between CO_2 yield and naphthalene conversion. However, at higher reaction temperatures if the CO_2 yield and the naphthalene conversion doesn't correlate, the naphthalene is adsorbing on the surface of the catalyst or oxidising via a partial oxidation pathway occurring during the reaction [23,24].

$$\% \ CO_2 \ yield$$
$$= 100 \ x \ \left(\frac{Counts \ of \ carbon \ dioxide}{Counts \ of \ 100\% \ conversion \ naphthalene \ to \ carbon \ dioxide}\right)$$
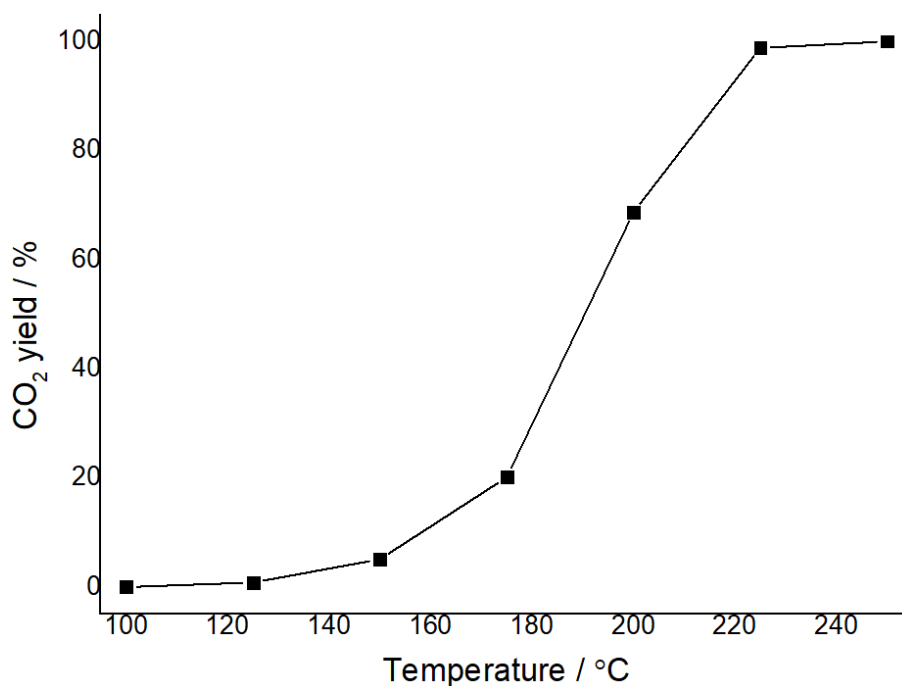
2.3.2.2.3 Naphthalene total oxidation reference reaction

Figure 2-20: Catalytic activity for the total oxidation of propane over the 5 % Pd/Al_2O_3 reference catalyst. Reaction conditions: 45,000 h^{-1}, temperature range 100-250 °C, 100 vppm naphthalene in 20 % O_2 balanced with He.

To compare the naphthalene total oxidation activity over the mixed metal oxides a commercial 5 % Pd/Al_2O_3 catalyst (Johnson Matthey) was used a reference catalyst, Figure 2-20. The catalyst showed appreciable propane total oxidation activity with 100 % naphthalene conversion achieved at 225 °C along with a steady carbon balance (>90 %) throughout the reaction.

2.4 References

[1]   D.R. Sellick, A. Aranda, T. García, J.M. López, B. Solsona, A.M. Mastral, D.J. Morgan, A.F. Carley, S.H. Taylor, Influence of the preparation method on the activity of ceria zirconia mixed oxides for naphthalene total oxidation, Appl. Catal. B Environ. 132–133 (2013) 98–106. doi:10.1016/j.apcatb.2012.11.036.

[2]   S. Ishikawa, D.R. Jones, S. Iqbal, C. Reece, D.J. Morgan, D.J. Willock, P.J. Miedziak, J.K. Bartley, J.K. Edwards, T. Murayama, W. Ueda, G.J. Hutchings, Identification of the catalytically active component of Cu-Zr-O catalyst for the hydrogenation of levulinic acid to γ-valerolactone, Green Chem. 19 (2017) 225–236. doi:10.1039/c6gc02598f.

[3]   P.N. Trikalitis, P.J. Pomonis, Catalytic activity and selectivity of perovskites LaSrV3+V4+O3 for the transformation of isopropanol, Appl. Catal. A Gen. 131 (1995) 309–322.

[4]   A.K. Chatterjee, Handbook of Analytical Techniques in Concrete Science and Technology, Elsevier, 2001.

[5]   W.H. Bragg, W.L. Bragg, The Reflection of X-rays By Crystals, Proc. R. Soc. A Math. Phys. Eng. Sci. 88 (1913) 428–438.

[6]   P. Scherrer, Kolloidchemie Ein Lehrbuch, Springer, 1912.

[7] C. Weidenthaler, Pitfalls in the characterization of nanoporous and nanosized materials, Nanoscale. 3 (2011) 792. doi:10.1039/c0nr00561d.

[8] J.S.J. Hargreaves, Some considerations related to the use of the Scherrer equation in powder X-ray diffraction as applied to heterogeneous catalysts, Catal. Struct. React. 2 (2016) 33–37. doi:10.1080/2055074X.2016.1252548.

[9] A.S. Vorokh, Scherrer formula : estimation of error in determining small nanoparticle size, Nanosyst. Physics, Chem. Math. 9 (2018) 364–369. doi:10.17586/2220-8054-2018-9-3-364-369.

[10] A. Monshi, M.R. Foroughi, Modified Scherrer Equation to Estimate More Accurately Nano-Crystallite Size Using XRD, (2014). doi:10.4236/wjnse.2012.23020.

[11] A. Zumbusch, G.R. Holtom, X.S. Xie, Three-Dimensional Vibrational Imaging by Coherent Anti-Stokes Raman Scattering, (1999) 1–4.

[12] C. V. Raman, K.S. Krishnan, A New Type of Secondary Radiation, Nature. 121 (1928) 501–502. doi:10.1038/121501c0.

[13] H. Knozinger, Handbook of Heterogeneous Catalysis, John Wiley and Sons, 2008.

[14] I. Langmuir, The adsorption of gases on plane surfaces of glass, mica and platinum, J. Am. Chem. Soc. 40 (1918) 1361–1403. doi:10.1021/ja02242a004.

[15] S. Brunauer, P.H. Emmett, E. Teller, Adsorption of Gases in Multimolecular Layers, J. Am. Chem. Soc. 60 (1938) 309–319. doi:10.1021/ja01269a023.

[16] K.S.W. Sing, Adsorption by Powders and Porous Solids Principles, Methodology and Applications, 2nd ed., Elsevier Ltd., 2014. doi:10.1016/B978-0-08-097035-6.00007-3.

[17] B. Vysetti, D. Vummiti, P. Roy, C. Taylor, C.T. Kamala, M. Satyanarayanan, Analysis of Geochemical Samples by Microwave Plasma-AES, At. Spectrosc. 35 (2014) 65–78.

[18] Z. Embong, U. Tun, H. Onn, XPS , AES and laser raman spectroscopy : A fingerprint for a materials surface characterisation, (2015).

[19] J.I. Goldstein, D.E. Newbury, J.R. Michael, N.W.M. Ritchie, J.H.J. Scott, D.C. Joy, Scanning Electron Microscopy and X-Ray Microanalysis, 4th ed., Springer US, 2018. doi:10.1007/978-1-4939-6676-9.

[20] D. Chescoe, P.J. Goodhew, The operation of the transmission electron microscope, Oxford University Press: New York, 1984.

[21] T.B. Rymer, Electron Diffraction, Butler and Tanner Ltd, 1970.

[22] R. Glauber, V. Schomaker, The Theory of Electron Diffraction, Phys. Rev. 89 (1953) 667–671. doi:10.1103/PhysRev.89.667.

[23] X.-W. Zhang, S.-C. Shen, L.E. Yu, S. Kawi, K. Hidajat, K.Y. Simon Ng, Oxidative Decomposition of Naphthalene by Supported Metal Catalysts, Appl. Catal. A Gen. 250 (2003) 341–352. doi:10.1016/S0926-860X(03)00412-5.

[24] M.M. Marisic, Heteropoly-acids as Catalysts for the Vapor Phase Partial Oxidation of Naphthalene, J. Am. Chem. Soc. 62 (1940) 2312–2317. doi:10.1021/ja01866a016.

3 Mechano-chemically prepared ceria-zirconia mixed metal oxide catalysts for the total oxidation of VOCs.

3.1 Introduction

Currently, there is a move away from traditional supported noble metal catalysts for VOC total oxidation. Ceria has been proposed as a suitable material [1] and has been widely studied due to its favourable redox properties and ability to form non-stoichiometric CeO_{2-x} [2–4]. The formation of non-stoichiometric CeO_{2-x} produces active oxygen species from increased presence of oxygen vacancies and surface defect sites, which produces catalysts with high activity for VOC total oxidation. This effect is also observed in zirconia [5]. These effects are enhanced when ceria and zirconia are mixed together to form mixed metal oxide catalysts [6]. Synergy, when the combination of the two components are more active than the sum of the individual components, between the two metal oxides has been observed for a large range of total oxidation reactions: including naphthalene [7,8], methane [9] and soot particles [10]. In most studies, ceria-zirconia metal oxides containing low concentrations of zirconia produced the most active catalysts.

Previous studies have reported many methods to prepare ceria-zirconia mixed metal oxide catalysts. Many of these preparation methods involve co-precipitation of metal salts which produces large quantities of aqueous waste, which must be purified before disposal. The catalyst is also affected due to the formation of potential poisons, such as alkali metals or nitrate, chloride or sulfur groups, on the surface from the precipitating agents or metal salt precursors [11]. Mechanochemical grinding provides an alternative catalyst preparation method, which doesn't require multiple steps, generates less unwanted waste or surface poisons on the catalyst surface. A large range of catalytic materials have been prepared mechanochemically [12] including ceria-zirconia mixed metal oxides [13–15]. However these mechanochemically prepared ceria-zirconia mixed metal oxide materials were not widely investigated for VOC total oxidation.

The focus of this chapter is the investigation of mechanochemically preparing ceria-zirconia mixed metal oxide catalysts for the total oxidation of propane and naphthalene. Two factors will be examined: the ratio Ce:Zr within the mixed metal oxide and the precursor used to prepared the ceria-zirconia mixed metal oxides. The first section of this chapter will focus on nitrate precursors and the second section will focus on carbonate precursors on the performance and nature of the ceria-zirconia mixed metal oxide

catalysts. The ceria-zirconia mixed metal oxides surface and structure will be characterised via a range of methods. The stability of the most active ceria-zirconia mixed metal oxide catalysts for naphthalene and propane total oxidation reactions, prepared from both precursors will also be investigated.

3.2 Results of the ceria-zirconia mixed metal oxide catalysts prepared from nitrate precursors

The mechanochemical synthesis of the ceria-zirconia mixed metal oxide catalyst using nitrate precursors is shown in section 2.1.1. $Ce(NO_3)_3. 6H_2O$ and $ZrO(NO_3)_2 .xH_2O$ were weighed in appropriate amounts before light grinding and placement into the ball mill crucible. The nitrate salts were ground at 300 rpm for 4 h before calcination at 400 °C for 3 h.

3.2.1 Precursor characterisation

3.2.1.1 Thermal gravimetric analysis
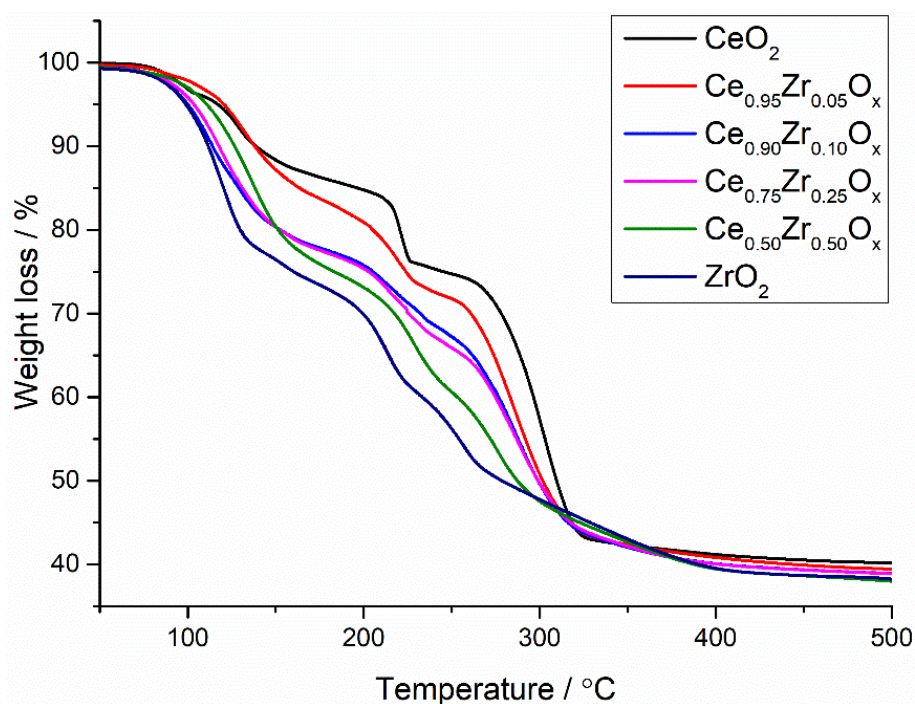
Figure 3-1: Thermogravimetric analysis of all the post-milled ceria-zirconia mixed metal oxide catalysts prepared from nitrate precursors. Samples heated in a flowing N_2 atmosphere from 30 to 500 °C at a ramp rate of 5 °C min⁻¹

The thermal gravimetric analysis profiles for the decomposition of the milled ceria-zirconia mixed metal oxide prior to calcination are shown in Figure 3-1. All the catalyst precursors show a gradual weight loss from 100-150 °C related to physisorbed water. The desorption of water accounts for a total loss of 15 % and 30 % for the milled cerium and zirconium nitrate precursors respectively. The addition of zirconium into the mixed ceria-

zirconia nitrate precursor increased the weight loss attributed to water, however this value wasn't as high as the zirconium nitrate precursor.

All the precursors also have a multi-stage weight loss starting at 210 °C relating the decomposition of nitrate groups and formation of a metal oxide. The decomposition of nitrate in the cerium nitrate precursor occurs at 260 °C, whereas the zirconium nitrate groups start decomposing at 220 °C. This accounts for a 30 % and 45 % weight loss respectively. This weight loss is very similar to the theoretical weight loss for the formation of the ceria and zirconia. This indicates only small amounts of water and nitrates were lost during the milling of the nitrate precursors.

All the mixed ceria-zirconia precursors, regardless of the ratio, showed a decrease in the temperature at which nitrate decomposition occurred compared to the cerium nitrate decomposition. All samples showed nitrate decomposition temperature in the region between the limits of the single cerium and zirconium nitrate precursors rather than showing additive traces of the single nitrates. This may indicate the ceria-zirconia are very well mixed after milling.

3.2.1.2 *In situ* XRD
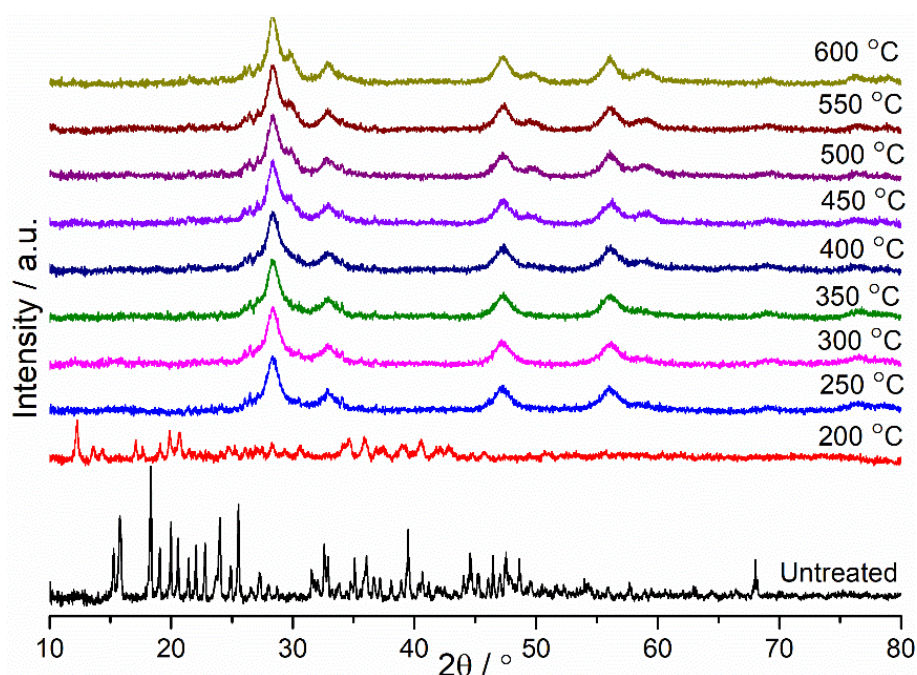
Figure 3-2: In situ powder X-ray diffraction patterns of the post milled $Ce_{0.50}Zr_{0.50}O_x$ nitrate precursor with increasing temperature. Reaction conditions: temperature range 200- 600 °C under a flow of 30 ml min^{-1} air. 10 minute scan duration

To gain further understanding on the effects of calcination on the formation of the final ceria-zirconia mixed metal oxide catalysts *in situ* XRD under flowing air was conducted. The post milled $Ce_{0.50}Zr_{0.50}O_x$ nitrate precursor was selected as the representative material for this investigation.

The *in situ* XRD patterns are shown in Figure 3-2. The pattern of the untreated $Ce_{0.50}Zr_{0.50}O_x$ sample indicates the presence of numerous cerium and zirconium nitrate and hydroxy species. The hydroxy species are not present upon heating the sample to 200 °C. This is consistent with the observations from TGA, with water and hydroxide desorption occurring from 100 to 150 °C. The presence of cerium and zirconium nitrate species diminishes as the temperature is increased to 250 °C.

At 250 °C, four predominant peaks emerge at 29 °, 33 °, 48 ° and 56 °. These peaks are characteristic of ceria in its cubic structure and are assigned to the (111), (200), (220) and (311) planes respectively [7,16]. These four peaks are consistently observed as the temperature is increased until 400 °C. This correlates with the TGA profiles as nitrate decomposition starts around this temperature leading to the formation of the metal oxide. No peaks indicating the formation of bulk zirconia indicating intimate mixing of the ceria-zirconia at these temperatures. As the temperature is increased above 400 °C a peak is observed on the shoulder of the ceria peak at 29 °. This peak can be prescribed to the formation of bulk tetragonal zirconia. This is observed in previous studies using ceria-zirconia mixed metal oxide materials. The higher temperatures cause the zirconia to segregate from the ceria-zirconia mixed phase and form bulk zirconia in the tetragonal phase [17–19].

Following the TGA and *in situ* XRD analysis a calcination temperature of 400 °C was used to prepare the ceria-zirconia mixed metal oxide catalysts. This is due to full decomposition of the nitrate precursors and minimise the occurrence of ceria and zirconia phase segregation.

3.2.2 Catalyst performance for VOC total oxidation

3.2.2.1 Propane total oxidation

Figure 3-3 shows the catalytic activity for the total oxidation of propane over the range of ceria-zirconia mixed metal oxides. All the ceria-zirconia mixed metal oxide catalysts showed activity for propane total oxidation and had high carbon dioxide selectivity (>99 %) throughout the reaction. Error for propane total oxidation prepared using catalysts prepared using mechanochemical grinding was ~2.5 %. The ceria and zirconia showed similar propane total oxidation reactivity profiles with both metal oxides achieving ~90 % propane conversion at 600 °C. The 5 % Pd/Al_2O_3 had significantly higher performance for propane total oxidation than ceria and zirconia prepared *via* mechanochemical grinding. Upon addition of zirconia into the ceria there was a noticeable increase in the activity compared to the mono-metallic oxides. The ceria-zirconia mixed metal oxide

catalysts containing low concentrations of zirconia performed better than the reference catalyst. The order of catalyst activity over the range of ceria-zirconia mixed metal oxide catalysts followed the general trend:
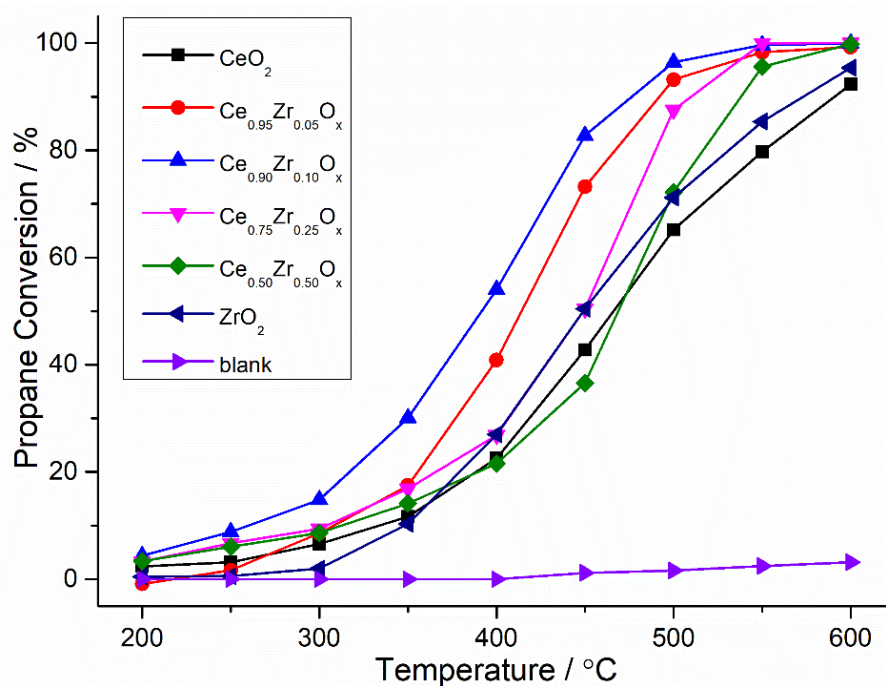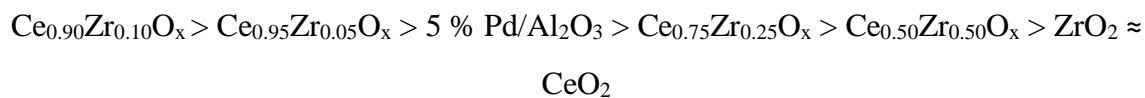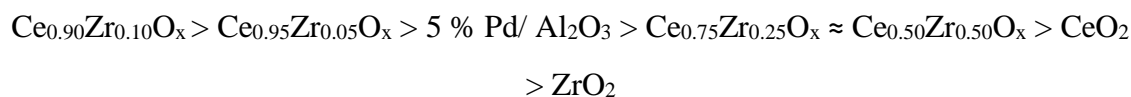
$$Ce_{0.90}Zr_{0.10}O_x > Ce_{0.95}Zr_{0.05}O_x > 5\ \%\ Pd/Al_2O_3 > Ce_{0.75}Zr_{0.25}O_x > Ce_{0.50}Zr_{0.50}O_x > ZrO_2 \approx CeO_2$$

Figure 3-3: Catalytic activities for the total oxidation of propane of the ceria-zirconia mixed metal oxide catalysts prepared from nitrate precursors. Reaction conditions: 45,000 h^{-1}, temperature range 200-600 °C, 5000 ppm propane in air. Legend refers to the different Ce:Zr ratios

3.2.2.2 Naphthalene total oxidation

The catalytic activity for the ceria-zirconia mixed metal oxide catalysts for the total oxidation of naphthalene is shown in Figure 3-4. During all reactions, there was a variation in the carbon balance at lower temperatures (100-175 °C). However only carbon dioxide and naphthalene were observed during GC analysis during all reactions. The errors associated for naphthalene total oxidation over the mechanochemically prepared catalysts are ~5 %. A factor is the error can be ascribed to the variation in carbon balance occurring due to naphthalene adsorption on the surface of the catalysts [20]. The ceria and zirconia showed similar activity profiles with 21% and 17% CO_2 yield at 250 °C respectively. Both catalysts showed poor performance compared to the reference catalyst. The trend for naphthalene total oxidation follows the one observed for propane total oxidation over the ceria-zirconia mixed metal oxide catalysts:

$$Ce_{0.90}Zr_{0.10}O_x > Ce_{0.95}Zr_{0.05}O_x > 5\ \%\ Pd/\ Al_2O_3 > Ce_{0.75}Zr_{0.25}O_x \approx Ce_{0.50}Zr_{0.50}O_x > CeO_2$$
$$> ZrO_2$$

In both experiments, the ceria-zirconia mixed metal oxides with lower amounts of zirconium were the most active catalysts, compared to the reference catalyst. This is consistent with previous studies in which ceria-zirconia mixed metal oxides were prepared using urea and sodium carbonate [7,8].
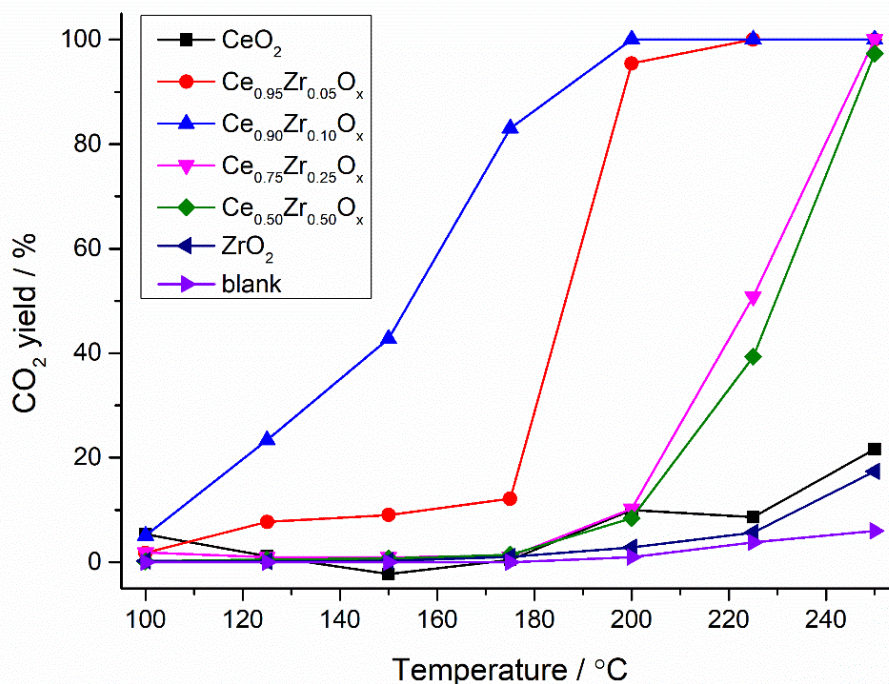

Figure 3-4: Catalytic activities for the total oxidation of naphthalene of the ceria-zirconia mixed metal oxide catalysts prepared from nitrate precursors. Reaction conditions: GHSV: 45,000 h^{-1}, Temperature range 100-250 °C, 100 vppm naphthalene in 20 % O_2 balanced with He. Legend refers to the different Ce:Zr ratios

3.2.3 Catalyst characterisation

3.2.3.1 X-ray diffraction

The ceria-zirconia mixed metal oxide powder XRD patterns are shown in Figure 3-5 and further derived data are presented in Table 3-1. There are four reflections in the ceria XRD pattern: present at 28 °, 33 °, 49 ° and 57 °. These reflections indicate the presence of cubic fluorite ceria with the reflections corresponding to the (111), (200), (220) and (311) planes respectively [21]. The zirconia is present in the tetragonal phase as indicated by reflections at 30 °, 34 °, 50 ° and 59 °. These reflections correspond to the (111), (200), (202) and (311) phases respectively [22]. There is a noticeable peak on the shoulder of the 30 ° peak suggesting the presence of monoclinic phase zirconia in this sample
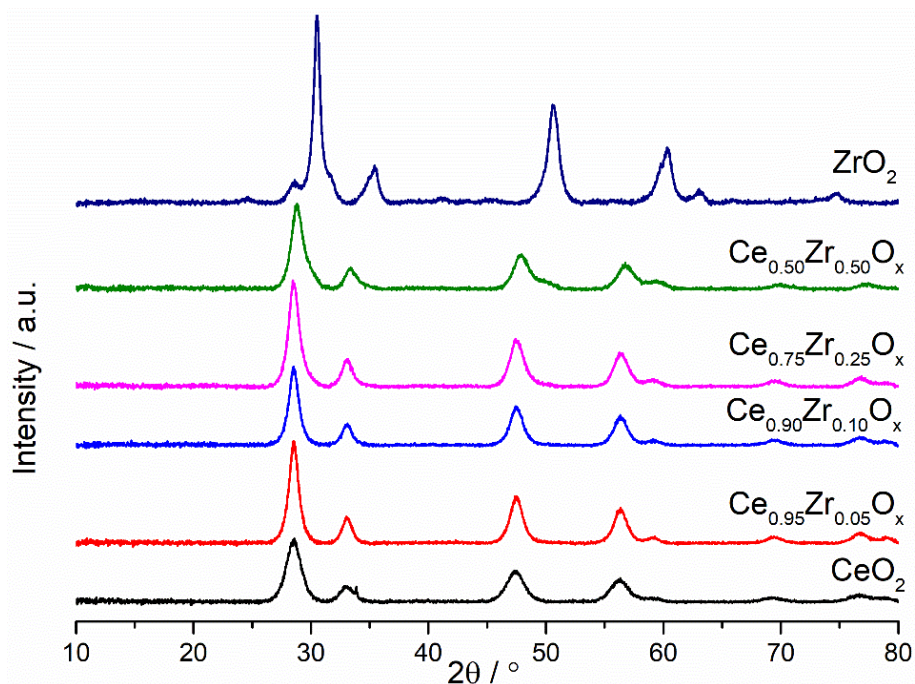
Figure 3-5: Powder XRD patterns of the calcined ceria-zirconia mixed metal oxide catalysts prepared from nitrate precursors

The mixed ceria-zirconia metal oxide samples all had four distinct reflections attributed to the ceria cubic phase. However the four reflections broadened as the zirconium content of the ceria-zirconia mixed metal oxides increased. With no reflections from zirconia present and the shift in reflections, this suggests the size of the ceria lattice has been modified by zirconium incorporation. The reflection of the (111) plane shifts to slightly higher values as the zirconia content of the ceria-zirconia mixed metal oxides increases, Table 3-1. This is observed in previous studies, in which ceria-zirconia mixed metal oxides were synthesised using urea and carbonate precipitation agents [7], impregnation of zirconia into a cerium precursor [23] and mechanochemical grinding of ceria with zirconia balls [13]. This suggests the formation of ceria-zirconia solid solution has occurred in all ceria-zirconia mixed metal oxides.

The average crystallite size was calculated from the powder XRD patterns using the Scherrer equation, Table 3-1. The widths of the four dominant reflections in each pattern were used to calculate the average crystallite size. The ceria had the largest crystallite size and the addition of any amount of zirconium led to a decrease in crystallite size. There was no systematic trend of decreasing crystallite with zirconium content of the ceria-zirconia mixed metal oxide. However the $Ce_{0.90}Zr_{0.10}O_x$, which had the smallest average crystallite size has the highest propane and naphthalene total oxidation activity.

Table 3-1: Physical properties of the ceria-zirconia mixed metal oxide catalysts prepared using nitrate precursors from XRD

Sample	Phases present	Position of ceria (111) reflection / °	Average crystallite size / Å	d-spacing from (200) lattice plane / Å	Unit cell volume / Å³	Incorporation of zirconium into Ce / %
CeO_2	CeO_2	28.4	118	2.694	156.436	-
$Ce_{0.95}Zr_{0.05}O_x$	CeO_2	28.5	105	2.692	156.067	1.5
$Ce_{0.90}Zr_{0.10}O_x$	CeO_2	28.6	95	2.691	155.921	2.1
$Ce_{0.75}Zr_{0.25}O_x$	CeO_2	28.6	103	2.684	154.749	7.1
$Ce_{0.50}Zr_{0.50}O_x$	CeO_2	28.8	97	2.667	151.766	19.6
ZrO_2	ZrO_2	-	99	2.550[24]	132.651	-

The d-spacing and unit cell volume of the ceria-zirconia mixed metal oxides was calculated using the ceria (200) lattice plane, Table 3-1. The ceria had the largest d-spacing and as zirconium was introduced into the ceria lattice this led to a decrease in the d-spacing. The decrease in d-spacing indicates the formation of ceria-zirconia mixed metal oxide solution. This is expected due to the smaller ionic radius of the zirconium compared to the cerium, 0.72 Å compared to 1.14 Å respectively [25]. As the smaller zirconium atom becomes incorporated into the ceria lattice, this will cause the substitution of cerium with zirconium atom causing the d-spacing to decrease [26,27]. In turn, as observed, this causes the unit cell volume to decrease.

The unit cell volume follows the same trend as d-spacing. Figure 3-6 shows the comparison of zirconium incorporation into the ceria between experimental and expected in the ceria-zirconia mixed metal oxides, using Vegard's law [28]. There is a noticeable decrease in the unit cell volume as the cerium content of the ceria-zirconia mixed metal oxide decreases, however the trend doesn't correlate with the expected values if all the zirconium is incorporated into the ceria. This indicates that not all the zirconium is being incorporated into the ceria lattice, as shown in Table 3-1. These values were acquired by comparing the value of the experimental value to its related expected cerium percentage. This would mean large amounts of zirconium would either be on the surface or not within the samples. This will be discussed in later sections of this chapter.
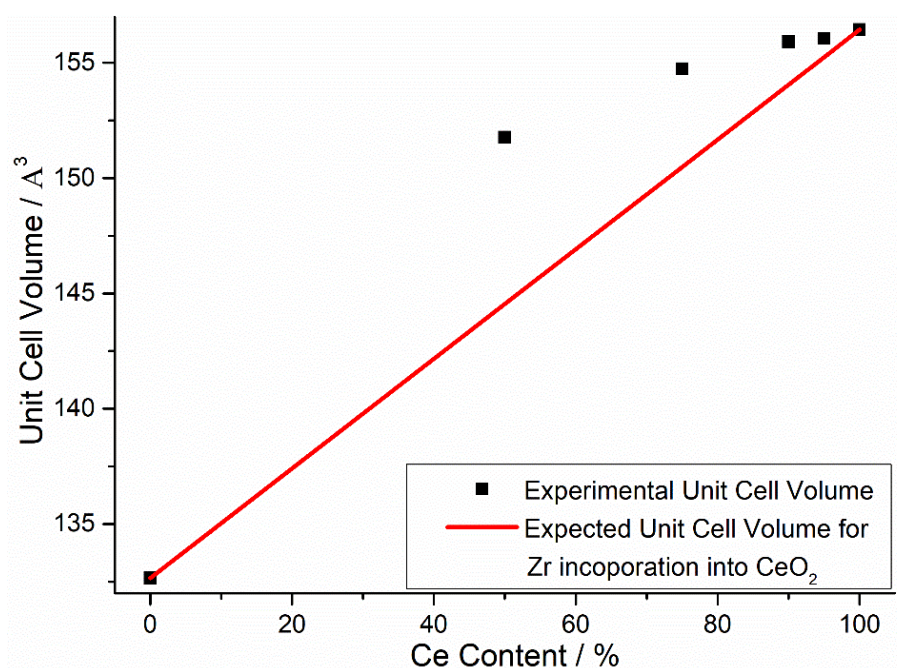
Figure 3-6: Comparison of experimental and expected unit cell volume of the ceria-zirconia mixed metal oxide catalysts prepared from nitrate precursors. Calculated using the (200) lattice parameter from XRD

3.2.3.2 Surface area

Table 3-2: Surface area of the ceria-zirconia mixed metal oxide catalysts prepared from nitrate precursors. Calculated using the 5-point N_2 adsorption BET analysis

Sample	BET Surface area / $m^2 g^{-1}$	Surface area normalised rate of propane total oxidation at 450 °C (10^{-8}) / mol s^{-1} m^{-2}	Surface area normalised rate of naphthalene total oxidation at 150 °C (10^{-11}) / mol s^{-1} m^{-2}
CeO_2	88	1.68	0.19
$Ce_{0.95}Zr_{0.05}O_x$	127	2.00	1.25
$Ce_{0.90}Zr_{0.10}O_x$	130	2.21	1.28
$Ce_{0.75}Zr_{0.25}O_x$	109	1.60	0.13
$Ce_{0.50}Zr_{0.50}O_x$	124	1.02	0.14
ZrO_2	93	1.90	0.05

Table 3-2 shows the surface areas of the ceria-zirconia mixed metal oxide catalysts. The ceria and zirconia had the lowest surface area of the series of catalysts. The addition of any amount of zirconium into the ceria led to an increase in the surface area compared to the monometallic oxides. This is reported to occur in ceria-zirconia mixed metal oxides prepared via hydrothermal aging [29] and thermal hydrolysis [30]. There is no significant trend in the increase of surface area to zirconium content of the ceria-zirconia mixed metal

oxide. The increase in surface area of the ceria-zirconia mixed metal oxide samples can be related to their decreased crystallite size compared to the ceria [31].

Previous studies have investigated the effects of surface area on naphtalene total oxidation using ceria catalysts [32]. It was found that high surface area ceria produced naphthalene total oxidation catalysts with higher activity. Surface area normalised rates of propane and naphthalene total oxidation at 450 °C and 150 °C respectively, are shown in Table 3-2. In both reactions the $Ce_{0.90}Zr_{0.10}O_x$ is still the most active catalyst. Even though the $Ce_{0.50}Zr_{0.50}O_x$ and the $Ce_{0.95}Zr_{0.05}O_x$ have similar surface areas to the $Ce_{0.90}Zr_{0.10}O_x$, the activities of these samples are much lower. This would indicate other factors beyond surface area will need to be considered for the increased activity of the $Ce_{0.90}Zr_{0.10}O_x$ and ceria-zirconia mixed metal oxide samples.

3.2.3.3 Raman spectroscopy

The bulk characteristics of the ceria-zirconia mixed metal oxide catalysts were analysed using Raman spectroscopy, Figure 3-7. The ceria and ceria-zirconia mixed metal oxides only had one peak present at 464 cm^{-1}, which is the Raman mode for the ceria cubic fluorite phase (F_{2g}) [16]. This confirms the XRD analysis of the ceria-zirconia mixed metal oxides in which only the cubic fluorite phase was observed for these samples. There is a peak with low intensity on these samples at 600 cm^{-1} indicating the presence of Frenkel-type oxygen vacancies [33]. The zirconia showed four weak peaks centred at 260, 315, 464 and 640 cm^{-1}. These peaks are characteristic of the zirconia in the tetragonal phase, which confirms XRD analysis. Due to the intensity of the ceria peak at 464 cm^{-1} it is hard to observe the zirconia peak at this value on the ceria-zirconia mixed metal oxide samples. However as the other peaks characteristic to zirconia were not observed we can confirm the zirconia is not present in its bulk phase of the ceria-zirconia mixed metal oxide samples.

As the concentration of zirconium into the ceria increases, the intensity of the peak at 464 cm^{-1} decreases. This is seen in Table 3-3, in which the FWHM of the peak at 464 cm^{-1} is shown. As expected, the ceria has the smallest FWHM and the ceria-zirconia mixed metal oxide sample containing the most zirconia, the $Ce_{0.50}Zr_{0.50}O_x$ has the largest FWHM. This observation can be assigned to the decreasing content of ceria in the materials. However, it is also influenced by the reduction of crystallinity and crystallite size can also lead to the band broadening [34]. The FWHM value is also inversely related to concentration of oxygen vacancies in the metal oxide lattice [35]. As the crystallite size remains consistent between the ceria-zirconia mixed metal oxides, ranging between 95-105 Å. The

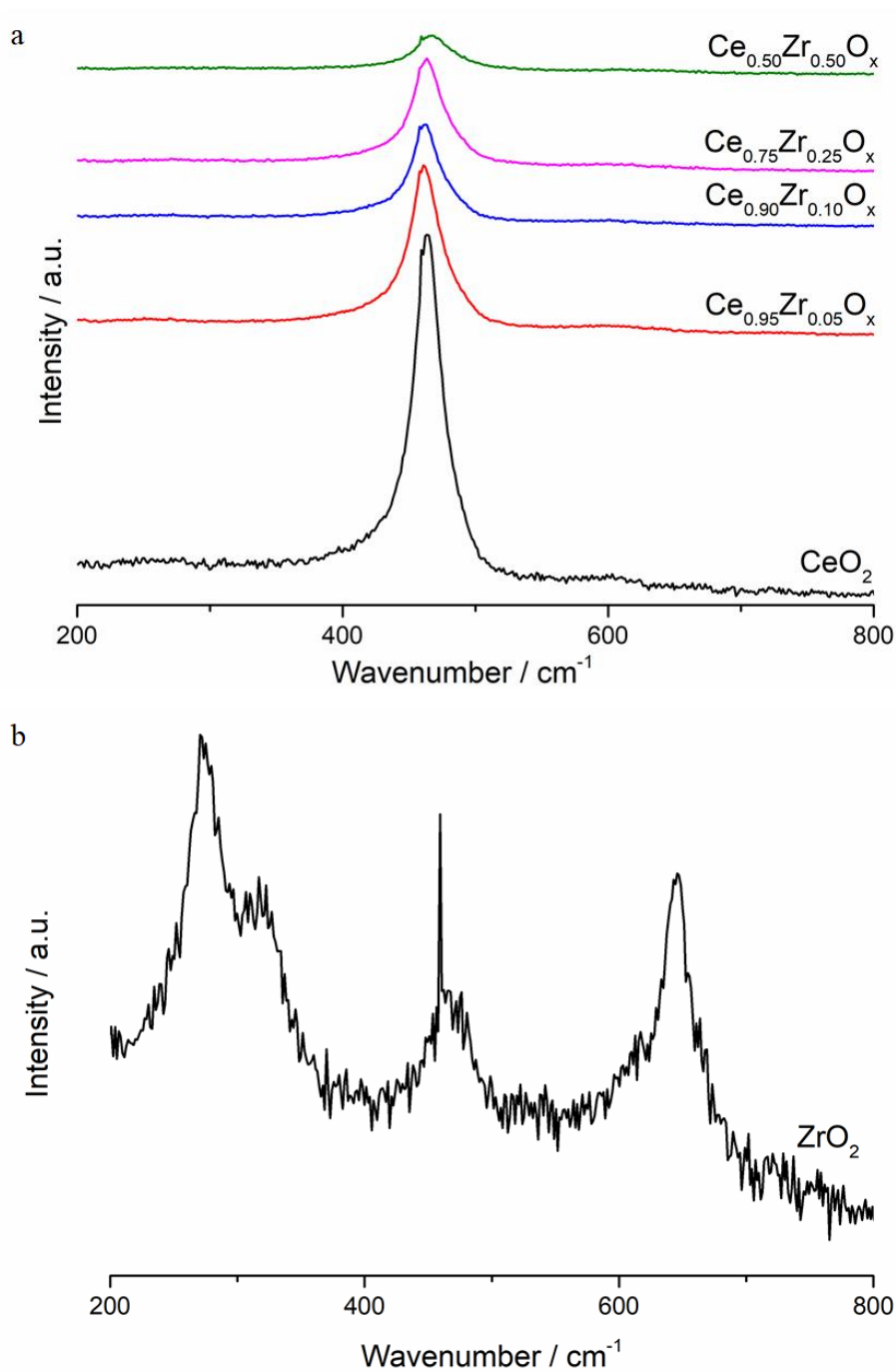increasing FWHM values can be atrributed to the presence of oxygen vacancies in the metal oxides.

Figure 3-7: Laser Raman spectra of ceria-zirconia mixed metal oxide catalysts prepared using nitrate precursors (a) CeO_2, $Ce_{0.95}Zr_{0.05}O_x$, $Ce_{0.90}Zr_{0.10}O_x$, $Ce_{0.75}Zr_{0.25}O_x$, $Ce_{0.50}Zr_{0.50}O_x$ and (b) ZrO_2 (enhanced 7.5 x). Laser $\lambda = 514$ nm

The oxygen vacancies can be determined by examining the Raman peak at 600 cm^{-1}, which is assigned to the extrinsic oxygen vacancies created by substitution of Zr^{4+} into the Ce^{4+} lattice [36]. The ceria has the lowest ratio and all ceria-zirconia mixed metal oxides show increased area ratio compared to it. The trend is linear as the $Ce_{0.50}Zr_{0.50}O_x$

sample has the largest area ratio compared to the other ceria-zirconia mixed metal oxide samples. However the relationship between Raman peak area ratios and activity doesn't correlate indicating other factors have to be considered.

Table 3-3: Chemical properties of ceria-zirconia mixed metal oxide catalysts prepared using nitrate precursors from laser Raman analysis

Sample	Raman FWHM of 464 cm^{-1} peak / cm^{-1}	Peak area ratio of 600 cm^{-1} / 464 cm^{-1}
CeO$_2$	28.6	0.0217
Ce$_{0.95}$Zr$_{0.05}$O$_x$	32.5	0.0352
Ce$_{0.90}$Zr$_{0.10}$O$_x$	33.3	0.0442
Ce$_{0.75}$Zr$_{0.25}$O$_x$	34.5	0.0423
Ce$_{0.50}$Zr$_{0.50}$O$_x$	44.9	0.0930

3.2.3.4 Temperature programmed reduction

Temperature programmed reduction profiles of the ceria-zirconia mixed metal oxides are shown in Figure 3-8. Characteristically ceria has two reduction peaks around 500 and 800 °C. The reduction peak represents formation of surface and bulk ceria species respectively [37,38]. Typically, zirconia is difficult to reduce under these conditions. However, two reduction peaks are observed on the zirconia sample at 450 °C and 550 °C. These peaks represent the reduction of surface zirconia and formation of hydroxy species [39].
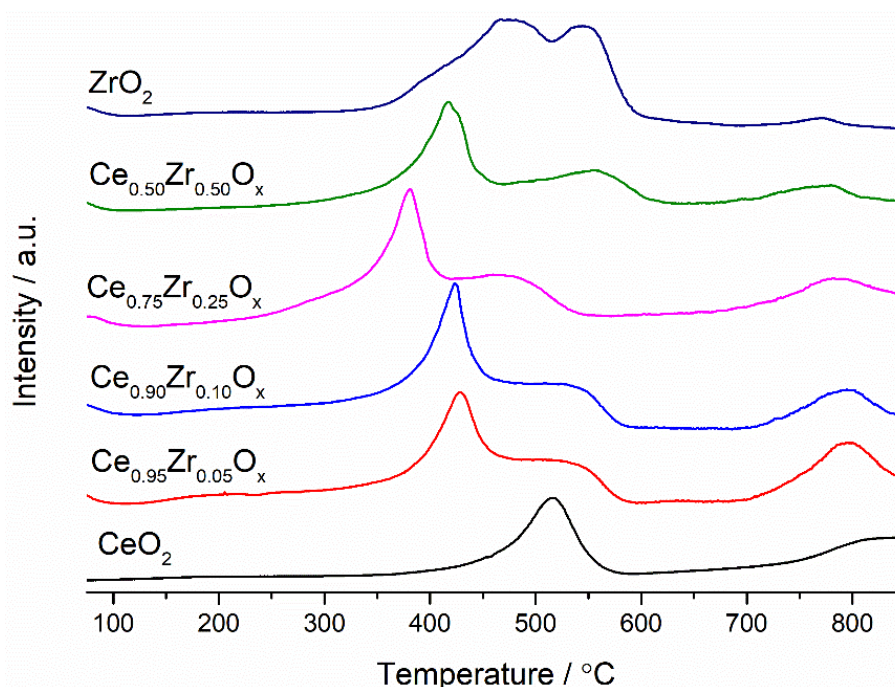
Figure 3-8: Hydrogen temperature-programmed reduction profiles of the ceria-zirconia mixed metal oxide catalysts prepared using nitrate precursors. Reaction conditions: 30mg sample, 30 ml min^{-1} 10 % H$_2$/Ar, temperature range: 50-850 °C

When zirconium was added into the ceria, the profiles changed in shape. The temperature of the reduction peak of surface ceria was significantly decreased and two peaks were observed during surface reduction for all the ceria-zirconia mixed metal oxides, Table 3-4. The presence of two surface reduction peaks relates to the Ce^{4+} and Ce^{3+} oxidation states. The Ce^{4+} is reported to be easier to reduce than the Ce^{3+} oxidation state [32] suggesting the first surface reduction peak is the Ce^{4+} and the second peak is assigned to reduction of Ce^{3+} species. The bulk reduction peak has also been shifted to lower temperatures upon addition of zirconium into the ceria, with the value decreasing upon increased zirconium concentrations. This is in line with previous studies, as increasing zirconium content of ceria-zirconia mixed metal oxides lead to an increase in reducibility of ceria [27,40–42] leading to the lowering of ceria reduction temperatures.

This follows the observations seen in section 3.2.3.3, with the ceria-zirconia mixed metal oxide samples noted to have more oxygen vacancies compared to the ceria. This will make the ceria easier to reduce and leads to increased presence of Ce^{3+} species on the surface of these samples. With a notable Ce^{3+} peak observed in all ceria-zirconia mixed metal oxides, this confirms the trends seen during Raman analysis. The decrease in surface reduction temperature will also lead to increased activity, for naphthalene [20,43] and propane total oxidation [44] which follow a Mars van-Krevelen mechanism. The surface will have more active oxygen and Ce^{3+} for the total oxidation reactions leading to increased activity observed during naphthalene and propane total oxidation for the ceria-zirconia mixed metal oxide catalysts compared to the ceria.

Table 3-4: Properties derived from TPR analysis of the ceria-zirconia mixed metal oxide catalysts prepared using nitrate precursors

Sample	CeO_2 Reduction temperature / °C		Surface hydrogen consumption / $\mu mol\ H_2$	Surface area normalised hydrogen consumption / $\mu mol\ H_2\ m^{-2}$
	Surface	Bulk		
CeO_2	515	822	2.61	1.02
$Ce_{0.95}Zr_{0.05}O_x$	427, 520	798	5.04	1.28
$Ce_{0.90}Zr_{0.10}O_x$	422, 525	795	5.55	1.47
$Ce_{0.75}Zr_{0.25}O_x$	380, 470	780	5.40	1.55
$Ce_{0.50}Zr_{0.50}O_x$	418, 556	766	4.58	1.29
ZrO_2	-	-	7.81	-

The hydrogen consumption during reduction of surface ceria is shown in Table 3-4. The ceria had the lowest hydrogen consumption. When any amount of zirconium was incorporated into the ceria, this led to a significant increase in surface hydrogen

consumption. The $Ce_{0.90}Zr_{0.10}O_x$ sample had the highest hydrogen consumption and the least active ceria-zirconia mixed metal oxide, $Ce_{0.50}Zr_{0.50}O_x$, had the lowest hydrogen consumption. The increase in surface hydrogen consumption also follows the surface area with the sample with the lowest surface area, ceria, also has the lowest hydrogen consumption. Surface area normalised hydrogen consumption is also shown in Table 3-4, will all ceria-zirconia mixed metal oxides showing increased hydrogen consumption compared to the ceria. This shows that the addition of zirconium does lead to an increase in reducibility of the sample and it's not just a surface area effect. This increase in reducibility is in line with the increase in VOC total oxidation activity noted for these samples.

3.2.3.5 Electron microscopy

3.2.3.5.1 Scanning electron microscopy
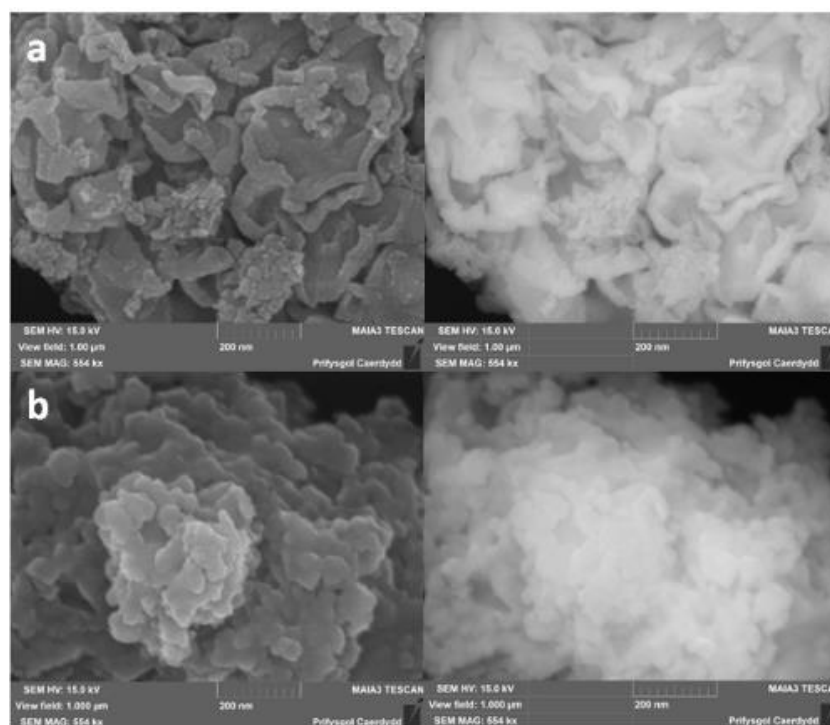
Figure 3-9: Secondary electron (left) and back-scattered electron (right) micrographs of (a) ceria and (b) zirconia prepared using nitrate precursors. Image magnification: 554 kx

Figure 3-9 shows the secondary electron and backscattered electron images of the ceria and zirconia. The pure ceria has a distinct *folded plate-like* morphology, whereas the morphology of the zirconia is more *coral-like*.

The secondary and backscattered electron images of the ceria-zirconia mixed metal oxide catalysts are shown in Figure 3-10. The morphology of the ceria-zirconia mixed metal oxides remains constant with increasing zirconium content. Furthermore, no phase segregation is observed on the ceria-zirconia mixed metal oxide catalysts. The

74

backscattered electron images show a uniform contrast and no bright spots indicating this observation. This agrees with the analysis of XRD patterns and Raman spectra in which only reflections from a cubic fluorite ceria-like phase were observed for the ceria-zirconia mixed metal oxides.
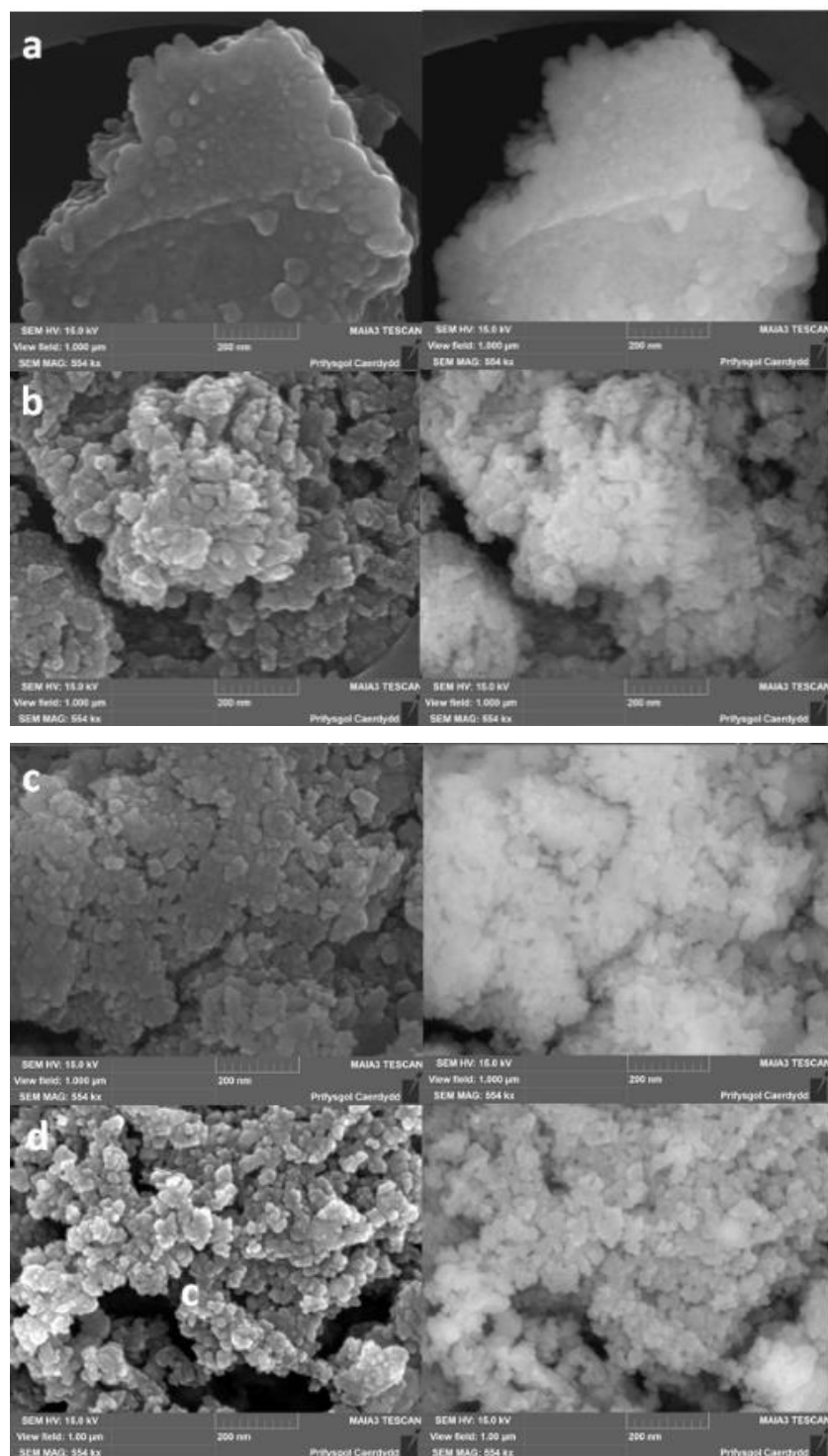

Figure 3-10: Secondary electron (left) and back-scattered electron (right) micrographs of (a) $Ce_{0.95}Zr_{0.05}O_x$ (b) $Ce_{0.90}Zr_{0.10}O_x$, (c) $Ce_{0.75}Zr_{0.25}O_x$ and (d) $Ce_{0.50}Zr_{0.50}O_x$ prepared using nitrate precursors. Image magnification: 554 kx

3.2.3.5.2 Energy-dispersive x-ray spectroscopy

Table 3-5: SEM-EDX derived bulk element analysis of the ceria-zirconia mixed metal oxide catalysts prepared using nitrate precursors

Sample	Concentration / %			Ce:Zr ratio
	Ce	Zr	O	
CeO_2	59.3	-	40.7	100:0
$Ce_{0.95}Zr_{0.05}O_x$	47.8	3.3	48.9	93.1:6.9
$Ce_{0.90}Zr_{0.10}O_x$	48.8	6.4	48.8	88.6:11.4
$Ce_{0.75}Zr_{0.25}O_x$	38.8	10.7	50.5	78.3:21.7
$Ce_{0.50}Zr_{0.50}O_x$	29.3	28.4	42.3	50.8:49.2
ZrO_2	-	57.6	42.3	0:100

EDX analysis was performed alongside the SEM imaging. Bulk elemental analysis of the ceria-zirconia mixed metal oxides are shown in Table 3-5. The ceria sample has no zirconium present indicating there was no contamination of the bulk by the zirconia milling material. The bulk content of all the ceria-zirconia mixed metal oxide catalysts were close to those expected from the starting ratios. The $Ce_{0.75}Zr_{0.25}O_x$ had the largest variation compared to the original ratios, with only 21.7 % zirconium present in the bulk. Slight variations in the final Ce:Zr ratios could have occurred during weighing of the precursors or during the removal of the material from the ball mill.

The resulting bulk Ce:Zr ratios are similar to the original values. There is a clear deviation between zirconium incorporated into the lattice, by unit cell volume analysis, and the amount present from the EDX analysis. As there weren't any discrete zirconium or zirconia phases observed in the other analytical techniques, XRD and Raman spectroscopy. This may indicate that zirconium may have formed amorphous zirconia particles along with ceria-zirconia mixed metal oxide species. This has been reported in previous studies, in which ceria-zirconia mixed metal oxides were synthesised using cerium/ zirconium precursor salts in an organic surfactant [17] and *via* mechanochemical grinding [14].
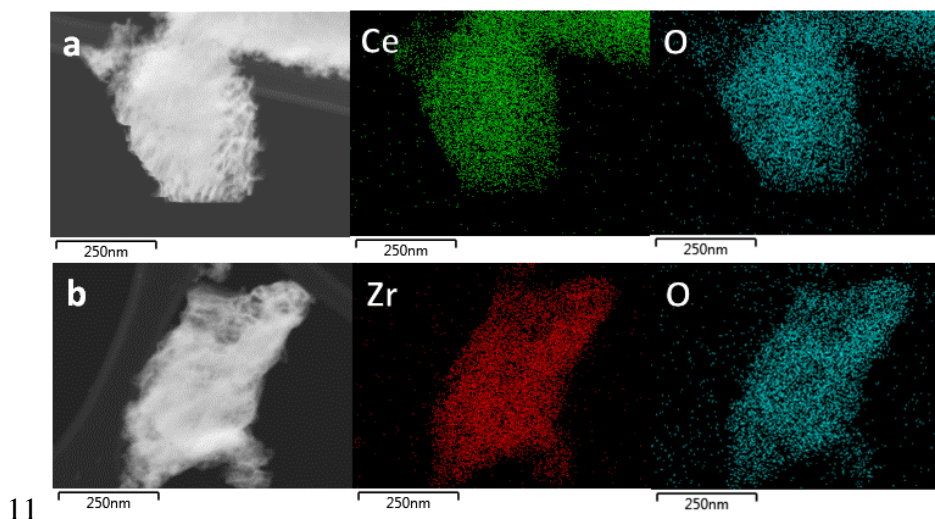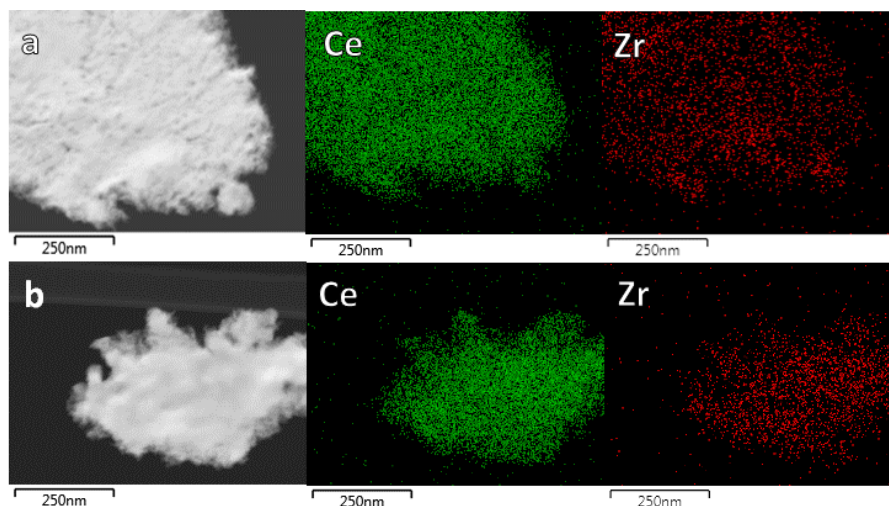
Figure 3-11: SEM-EDX mapping of (a) ceria and (b) zirconia prepared using nitrate precursors. Cerium (green), zirconium (red) and oxygen (blue)

Elemental maps of the ceria and zirconia samples prepared from nitrate precursors are shown in Figure 3-11. The ceria-zirconia mixed metal oxide samples are presented in Figure 3-12. As seen in the EDX elemental analysis, no zirconium was seen in the mapping of the ceria sample. There is a homogenous distribution of cerium and zirconium in the ceria-zirconia mixed metal oxide catalysts except the $Ce_{0.50}Zr_{0.50}O_x$, in which large areas of zirconium are observed along with islands of cerium within the sample. As mentioned above, the phase separated zirconium is not observed in XRD patterns or Raman spectra indicating the potential formation of amorphous zirconia.
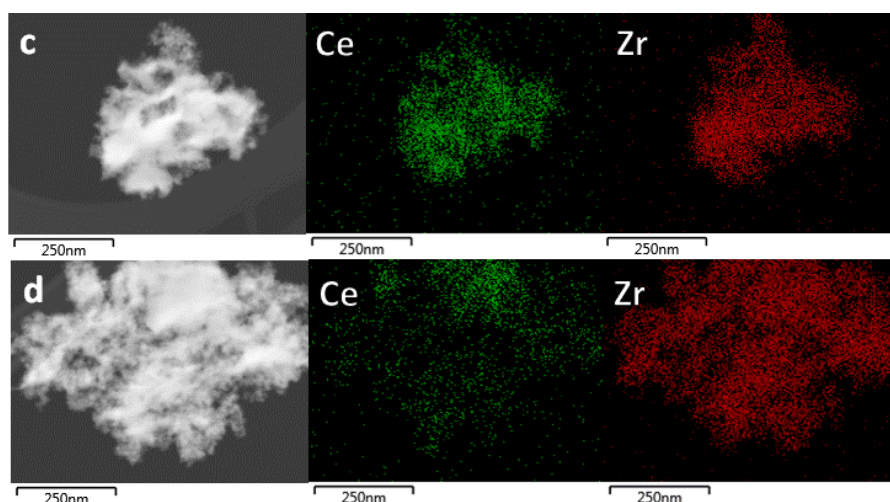
Figure 3-12: SEM-EDX mapping of (a) $Ce_{0.95}Zr_{0.05}O_x$, (b) $Ce_{0.90}Zr_{0.10}O_x$, (c) $Ce_{0.75}Zr_{0.25}O_x$ and (d) $Ce_{0.50}Zr_{0.50}O_x$ prepared using nitrate precursors. Cerium (green) and zirconium (red)

3.2.3.5.3 Transmission electron microscopy

Figure 3-13 shows high magnification TEM images and selected area electron diffraction patterns of the ceria-zirconia mixed metal oxides. The TEM image of ceria shows an assortment of random layered crystallites with clear lattice planes. This structure remains present for all the ceria-zirconia mixed metal oxides regardless of the concentration of zirconium present. The zirconia shows a similar structure to the other samples as there is also a large array of randomly arranged crystallites.
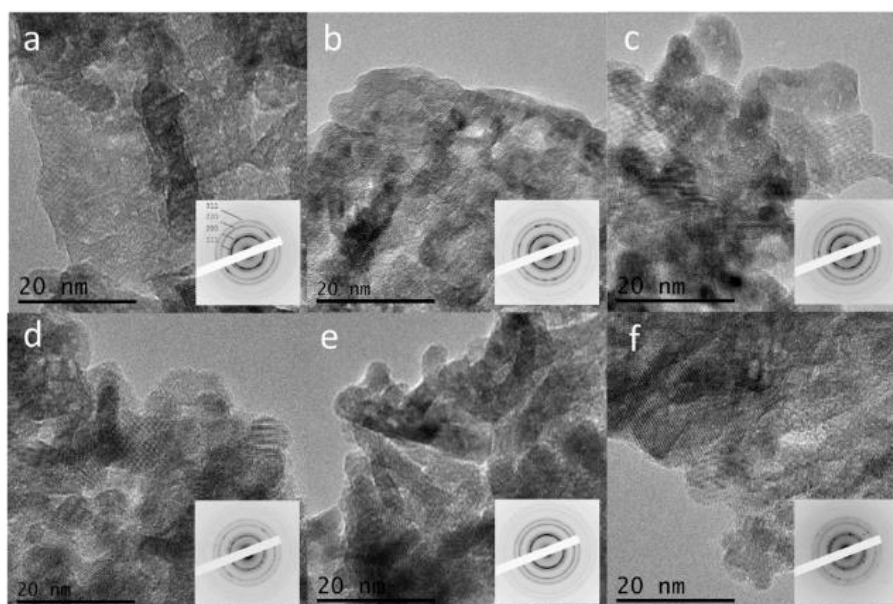
Figure 3-13: High magnification TEM images of the ceria-zirconia mixed metal oxide catalysts prepared using nitrate precursors. Inset: selected area electron diffraction patterns of larger 250 nm areas. (a) CeO_2, (b) $Ce_{0.95}Zr_{0.05}O_x$, (c) $Ce_{0.90}Zr_{0.10}O_x$, (d) $Ce_{0.75}Zr_{0.25}O_x$, (e) $Ce_{0.50}Zr_{0.50}O_x$ and (f) ZrO_2

Selected area electron diffraction of the ceria-zirconia mixed metal oxides were undertaken and are shown in the inset of Figure 3-13. All the samples were observed to contain four distinct diffraction rings. As no distinct single bright spots are observed, no single crystals have been observed. This shows the patterns are consistent with a polycrystalline material comprising of small, randomly orientated crystallite domains. The ceria diffraction rings are indexed to the (111), (200), (220) and (311) cubic fluorite structure, therefore confirming the observations from XRD and Raman analysis. The zirconia shows diffraction rings consistent with a mixture of monoclinic and tetragonal phases. This is in line with the XRD analysis in which a shoulder peak allocated to the presence of monoclinic zirconia was observed [45].

Four diffraction rings are also seen in the ceria-zirconia mixed metal oxides. The diffraction rings are characteristic of the ceria cubic fluorite structure therefore confirming the analysis of XRD and Raman spectroscopy. However, the effects from the presence of zirconia is difficult to determine due to the similarity of the diffraction rings of zirconia and ceria.

The d-spacings derived from selected area electron diffraction are shown in Table 3-6. The d-spacings of ceria from literature is 5.4 Å and the value derived from selected area diffraction is similar to this. The d-spacing for tetragonal zirconia is 5.08 Å and monoclinic zirconia is 7.38 Å [45]. The value obtained from the ball milled sample of zirconia is in between the 2 values. As it is closer to the value for tetragonal ZrO_2, the increase in the value can be due to the presence of monoclinic ZrO_2, as seen in XRD

Table 3-6: The d-spacings of the ceria-zirconia mixed metal oxide catalysts prepared using nitrate precursors determined from selected area electron diffraction

Sample	d-spacing calculated from selected area electron diffraction / Å
CeO_2	5.22
$Ce_{0.95}Zr_{0.05}O_x$	5.28
$Ce_{0.90}Zr_{0.10}O_x$	5.26
$Ce_{0.75}Zr_{0.25}O_x$	5.20
$Ce_{0.50}Zr_{0.50}O_x$	5.12
ZrO_2	5.25

The d-spacings of the ceria-zirconia mixed metal oxide catalysts decrease as zirconium content increases. This decrease is in line to the trend observed in d-spacing calculated from XRD. The decreasing d-spacing is as expected due to the smaller d-spacing of the ZrO_2. The d-spacings calculated for the $Ce_{0.95}Zr_{0.05}O_x$ and $Ce_{0.90}Zr_{0.10}O_x$ from selected area electron diffraction are slightly higher than the value observed for ceria. These values

are still within the d-spacing of ceria from literature indicating the cubic structure remains upon addition of zirconium into the ceria. The d-spacing for $Ce_{0.50}Zr_{0.50}O_x$ is very close to the value for tetragonal zirconia. However this could be attributed to the values of the ceria and tetragonal zirconia d-spacings being very close to each other. This makes it difficult to distinguish which is this dominant phase of this sample. This may also help explain the phase separated areas observed in EDX analysis.

3.2.3.6 X-ray photoelectron spectroscopy

Table 3-7: XPS derived surface elemental concentrations for the ceria-zirconia mixed metal oxide catalysts prepared using nitrate precursors

Sample	Concentration / at%			Relative Ce / %	Relative Zr / %
	Ce	O	Zr		
CeO_2	28.2	71.8	-	100	-
$Ce_{0.95}Zr_{0.05}O_x$	24.6	61.9	6.3	80.0	20.0
$Ce_{0.90}Zr_{0.10}O_x$	20.7	72.8	6.5	75.9	24.1
$Ce_{0.75}Zr_{0.25}O_x$	15.5	69.6	14.9	51.1	48.9
$Ce_{0.50}Zr_{0.50}O_x$	9.7	69.1	21.2	32.3	67.7
ZrO_2	-	67.4	32.6	-	100

XPS was used to analyse the surface of the ceria-zirconia mixed metal oxide catalysts. The surface composition of all the ceria-zirconia mixed metal oxide catalysts are presented in Table 3-7. The ceria showed no contamination of zirconium milling surface during EDX analysis. The surface of the ceria also contained no zirconium indicating no contamination has occurred during the mechanochemical grinding process. EDX of the ceria-zirconia mixed metal oxide samples indicates that the Ce:Zr ratios close to that of the theoretical values expected. However the analysis of the surface using XPS indicates the Ce:Zr ratios are much different to the bulk. Every ceria-zirconia mixed metal oxide has relative zirconium content higher than the expected value. The $Ce_{0.95}Zr_{0.05}O_x$, $Ce_{0.90}Zr_{0.10}O_x$ and $Ce_{0.50}Zr_{0.50}O_x$ all have a ~15 % excess of relative zirconium surface concentrations and the $Ce_{0.75}Zr_{0.25}O_x$ sample has ~25 % extra zirconium present on its surface.

There could be zirconium contamination on the surface of the ceria-zirconia mixed metal oxides which may lead to the higher zirconium concentrations observed on the surface. However as the ceria showed no signs of contamination from the zirconia ball mill surface we can assume this has not occurred. According to XRD analysis, a large portion of the zirconium didn't enter the ceria lattice. EDX showed the Ce:Zr ratios are consistent with those expected: therefore the excess zirconium could have been deposited on the surface

of the ceria-zirconia mixed metal oxide samples. As these zirconium containing species would be on the surface, they would be undetectable by XRD and Raman techniques. The potential amorphous nature of the zirconium species will also make it impossible to detect using XRD [14]. Therefore the decline in activity of the ceria-zirconia mixed metal oxides with high zirconium content could be due to blockage of active surface oxygen species and lattice defects by the excess zirconia. Zirconia was to be less active for propane and naphthalene total oxidation reactions compared to ceria. As more of the active mixed phase ceria-zirconia oxide surface will be exposed in the lower zirconium content ceria-zirconia mixed metal oxides, this will lead to the increased activity of these samples.

Figure 3-14 shows the Ce 3d XPS spectra for the ceria-zirconia mixed metal oxides. As expected, the ceria sample had the most intense peaks in this region. The intensity of the cerium 3d spectra decrease upon increasing zirconium concentrations in the ceria-zirconia mixed metal oxides. Cerium can be present in 2 oxidation states: Ce^{4+} and Ce^{3+}. The Ce^{4+} oxidation state is characterised by a large independent peak at 913 eV and an unsymmetrical doublet peaks at 879 and 897 eV. The Ce^{3+} oxidation state had characteristic symmetric doublet peaks at 881 and 900 eV [46]. A large portion of the surface cerium in the ceria and the ceria-zirconia mixed metal oxides is present as Ce^{4+}. This seen by the large peak present at 913 eV in all samples as well as the set of doublet peaks. The doublet peak between 895-900 eV is more symmetrical than characteristic Ce^{4+} 3d peaks indicating some Ce^{3+} is also present within the samples.
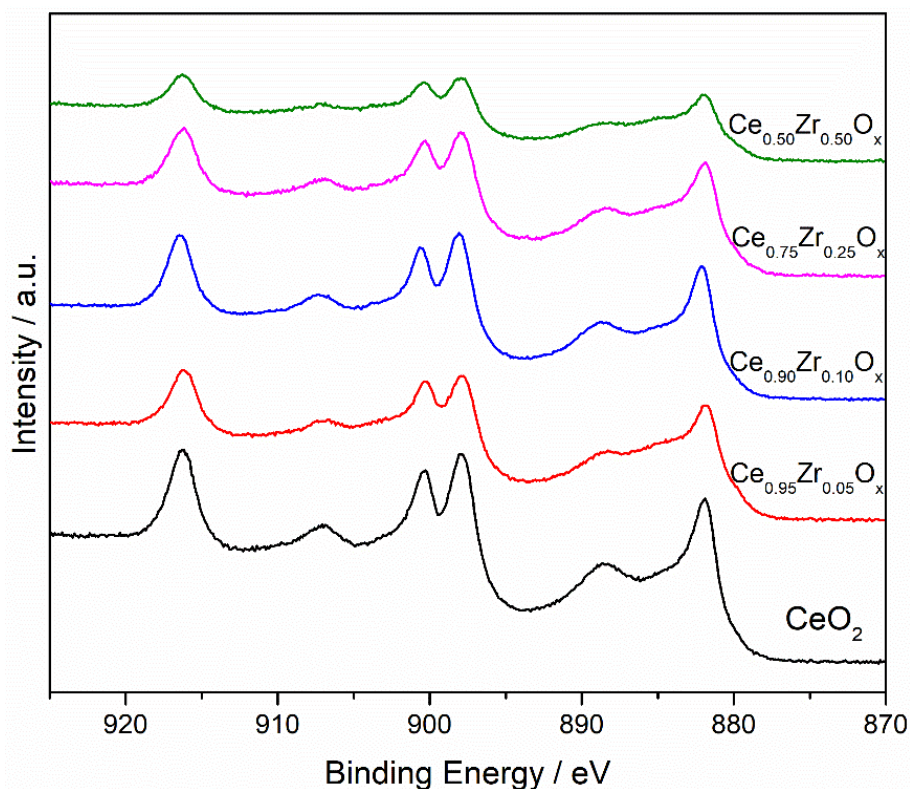
Figure 3-14: XPS spectra of the Ce 3d peaks for the ceria-zirconia mixed metal oxide catalysts prepared using nitrate precursors

The ceria-zirconia mixed metal oxides peaks shifted to slightly higher eV compared to the pure ceria indicating the increased presence of Ce^{3+} in these samples. This is in line with TPR profiles for the ceria-zirconia mixed metal oxides which all had an observable second surface reduction peak indicating the presence of two cerium oxidation states on the surface. The increased amount of Ce^{3+} will also lead to more defect sites and oxygen vacancies, as seen in analysis of the Raman spectra, on the surface of the ceria-zirconia mixed metal oxide catalysts, leading to the increased total oxidation activity noted for these samples.

The fitted oxygen 1s spectra of the ceria-zirconia mixed metal oxides are shown in Figure 3-15, with two surface oxygen species are present. Lattice oxygen is seen in a region between 529-30 eV and is denotated as O_α and surface/defect oxygen, represented as O_β is present in the region between 531-33 eV [47]. Previous studies using ceria based catalysts reported the concentration of surface oxygen defect sites have an significant effect on naphthalene total oxidation activity [48]. All the samples had both oxygen species present on the surface of the catalysts and the relative concentrations are shown in Table 3-8.
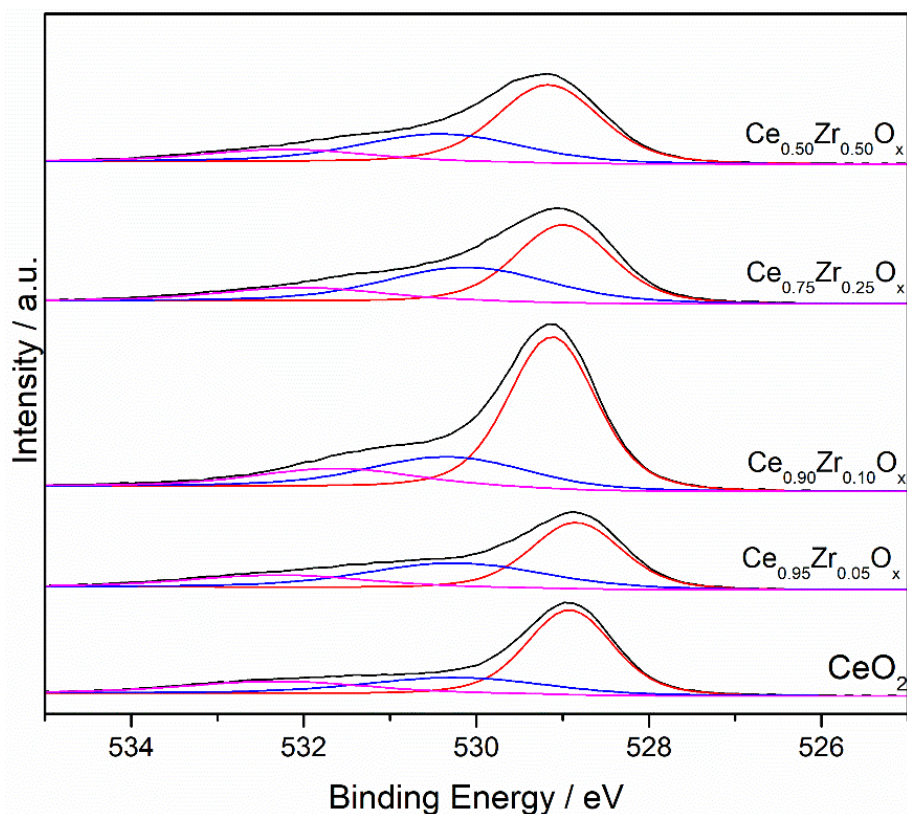
Figure 3-15: XPS spectra of the oxygen 1s peaks of the ceria-zirconia mixed metal oxide catalysts prepared using nitrate precursors

The ceria had the lowest relative concentration of surface oxygen compared to any of the ceria-zirconia mixed metal oxide samples. The $Ce_{0.95}Zr_{0.05}O_x$ and $Ce_{0.90}Zr_{0.10}O_x$ samples had ~25 % increase in the relative surface oxygen concentrations and the $Ce_{0.75}Zr_{0.25}O_x$ had ~10 % increase in surface oxygen concentrations compared to the ceria sample. The $Ce_{0.50}Zr_{0.50}O_x$ had similar surface oxygen concentration compared to the CeO_2. This increase in surface O_β species indicates the zirconium is increasing the oxygen defect site concentration on the surface. The increased presence of Ce^{3+} species on the surface of the ceria-zirconia mixed metal oxides will lead to more defect sites and oxygen vacancies, producing more surface oxygen species observed above. The hydrogen consumption for the surface of the ceria-zirconia mixed metal oxides, Table 3-4, was significantly higher than ceria. As the ceria-zirconia mixed metal oxides have more surface oxygen compared to the ceria, this will mean more hydrogen is required to reduce these surface oxygen species. As the trend of higher surface areas produced higher surface hydrogen consumption wasn't linear. This deviation could be due to the increased surface oxygen present on the ceria-zirconia mixed metal oxides compared to the ceria.

Table 3-8: XPS derived concentrations of lattice and surface oxygen species for the ceria-zirconia mixed metal oxide catalysts prepared using nitrate precursors

Sample	Relative concentration of O_α / %	Relative concentration of O_β / %
CeO_2	60.1	39.9
$Ce_{0.95}Zr_{0.05}O_x$	48.4	51.6
$Ce_{0.90}Zr_{0.10}O_x$	48.2	51.8
$Ce_{0.75}Zr_{0.25}O_x$	55.5	44.5
$Ce_{0.50}Zr_{0.50}O_x$	58.4	41.6

The relationship between surface oxygen concentration on propane and naphthalene total oxidation activity is shown in Figure 3-16. A clear trend is observed, as the concentration of surface O_β increases, this leads to a significant increase in rate of propane and naphthalene total oxidation. This trend is observed in studies using copper doped ceria in which higher relative concentrations of O_β lead to an increase in naphthalene total oxidation[49]. The $Ce_{0.95}Zr_{0.05}O_x$ and $Ce_{0.90}Zr_{0.10}O_x$ showed a doubling of the rate of propane total oxidation and nearly 14 x the rate of naphthalene total oxidation compared to the CeO_2. The $Ce_{0.75}Zr_{0.25}O_x$ only showed a small increase in both rates of propane and naphthalene total oxidation. The $Ce_{0.50}Zr_{0.50}O_x$ is the outlier as its rate of propane and naphthalene total oxidation is lower in than ceria even though it has a slightly higher O_β concentration. As mentioned previously in this section the $Ce_{0.50}Zr_{0.50}O_x$ had the highest surface zirconium content. Therefore the surface zirconia species could interfere with the active surface species causing blocking of the active sites. This may also block the potential oxygen defect and vacancies leading to a reduction in the activity observed for $Ce_{0.50}Zr_{0.50}O_x$ compared to the other ceria-zirconia mixed metal oxide catalysts.
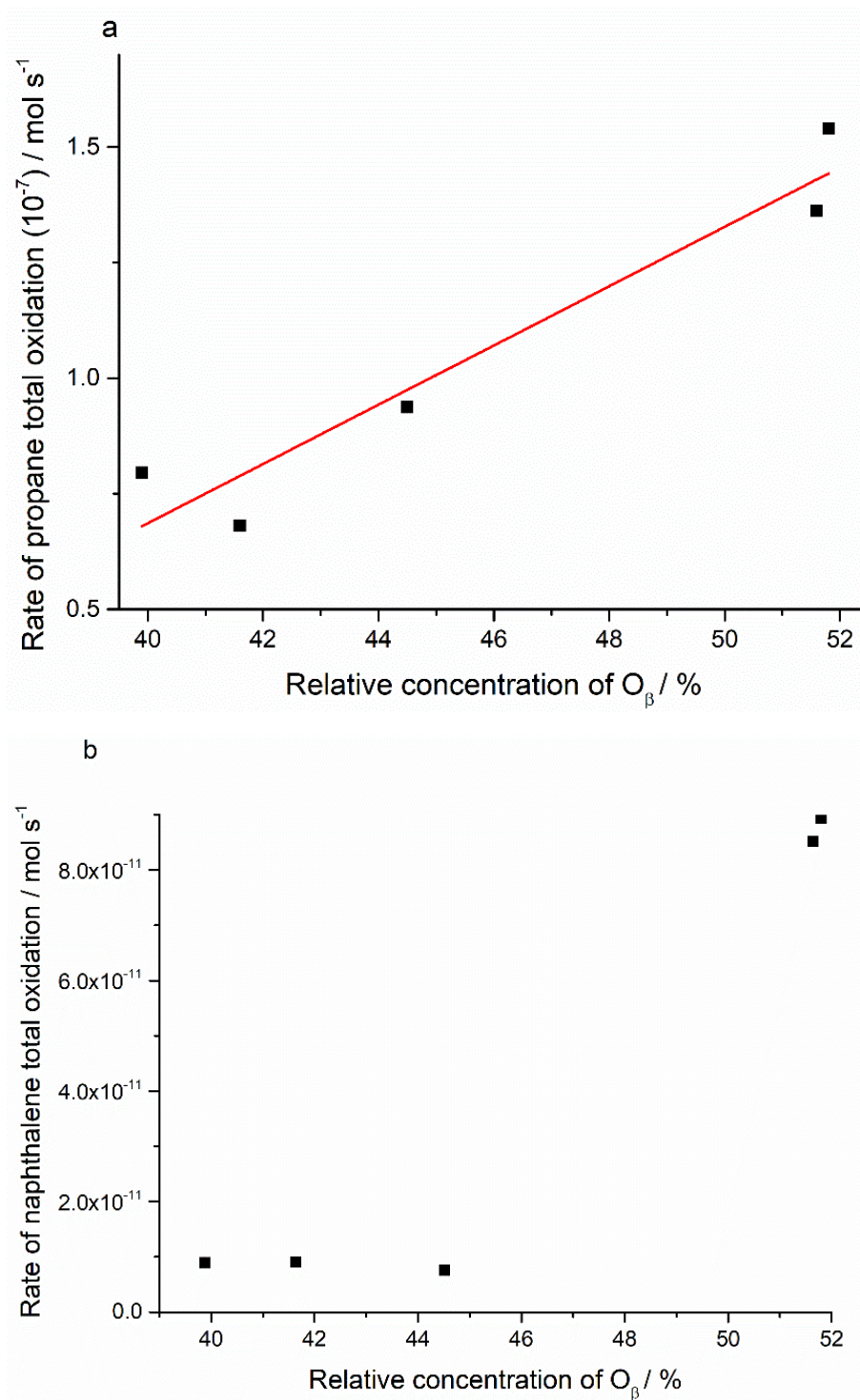
Figure 3-16: The relationship between relative concentration of O_β calculated from XPS on (a) propane total oxidation activity at 450 °C and (b) on naphthalene total oxidation activity at 150 °C for the ceria-zirconia mixed metal oxide catalysts prepared using nitrate precursors

3.2.4 Stability testing of $Ce_{0.90}Zr_{0.10}O_x$ sample
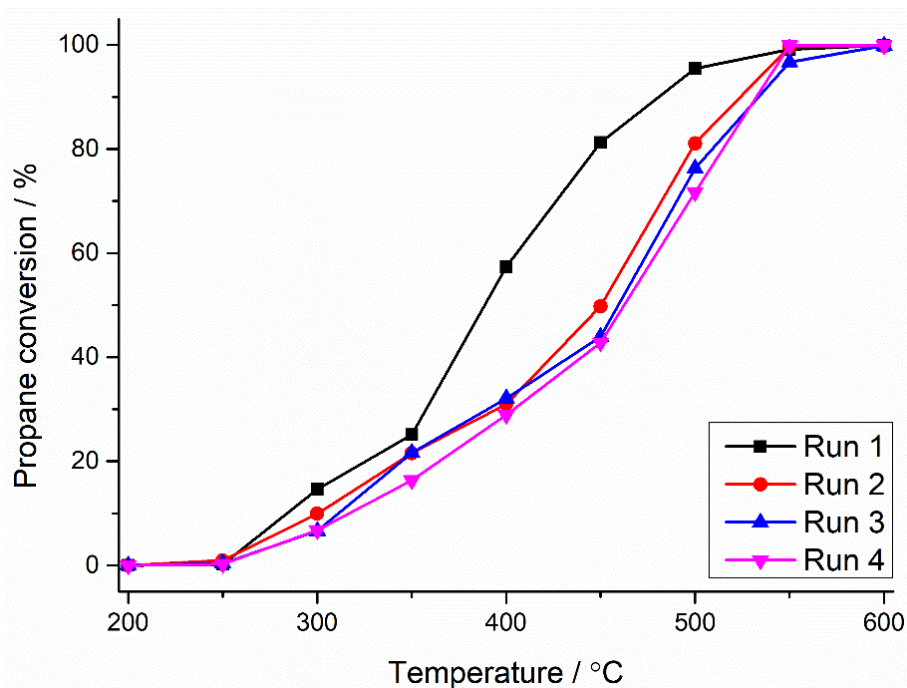
3.2.4.1 Propane total oxidation

Figure 3-17:Multiple run propane total oxidation stability study of the $Ce_{0.90}Zr_{0.10}O_x$. Temperature range: 200-600 °C, GHSV: 45,000 h^{-1}, 5000 ppm propane in air

The stability of the most active propane total oxidation ceria-zirconia mixed metal oxide catalyst, $Ce_{0.90}Zr_{0.10}O_x$, was evaluated by recycling the catalyst by undertaking 4 runs of the light off reaction curve, Figure 3-17. All runs showed high selectivity to CO_2 (> 99 %) and no change was observed with each successive cycle. However, the activity changed upon each successive reaction cycle. The first run showed the same light off profile as the original sample but when the sample was used for the second time a significant decrease is noted at lower temperatures. All successive reaction profiles showed an increase in the T_{100} temperature of 50 °C from 500 °C to 550 °C compared to the original reaction run. The propane total oxidation activity at 500 °C decreases from 100 % propane conversion which drops to 81 %, 76 % and 71 % upon successive reaction runs.

Due to the small amounts of catalyst sample used during the propane total oxidation reactions and the mixing of the solid sample within quartz wool, post reaction analysis was difficult to carry out. The reaction temperatures at the end of the propane oxidation light off curve are above the calcination temperature. This may cause sintering to occur and formation of bulk zirconia as observed in the *in situ* XRD of these samples. With phase separation occurring, this may lead to decrease in the active phase of the catalyst. Other possible explanations for the decrease in activity between each catalyst can be

attributed to loss of surface area or surface oxygen species however further studies will need to be carried out to confirm this.
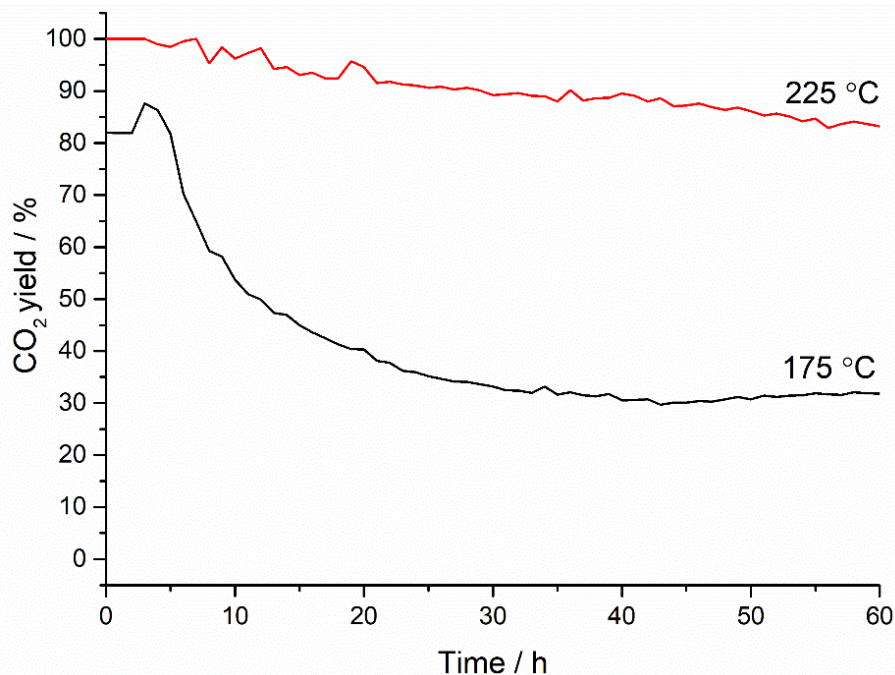
3.2.4.2   Naphthalene total oxidation

Figure 3-18: Time on line naphthalene total oxidation stability study of the $Ce_{0.90}Zr_{0.10}O_x$ catalyst prepared using nitrate precursors. Reaction conditions: GHSV= 45,000 h^{-1} 100 vppm naphthalene in 20 % O_2 balanced with He

As well as being the most active propane total oxidation catalyst, the $Ce_{0.90}Zr_{0.10}O_x$ was also the most active sample for naphthalene total oxidation. The stability of naphthalene total oxidation was investigated during a time on line study over 60 hour period at 2 temperatures, 175 °C and 225 °C.

Both reaction temperatures showed very different profiles. When the stability of $Ce_{0.90}Zr_{0.10}O_x$ was tested at 175 °C, there was a slight increase in the CO_2 yield, from 82 % to 87%, during the initial 5 hours of the reaction. However after the rise in activity came a prolonged decay in activity, as CO_2 yield decreased to ~35 % after 35 hours after which the CO_2 yield remained stable. The carbon balance varied over time suggesting some of the naphthalene may remain adsorbed or form partial oxidation products on the surface of the catalysts. The time on line naphthalene total oxidation reaction undertaken at 225 °C also showed a decrease in activity during the 60 hour period however this decrease wasn't as drastic as observed during the 175 °C reaction. The CO_2 yield decreased from 100% to 90% over the 60 hour period.

Once again, there was difficulty in analysis of the post reaction catalysts. However the large decrease in activity during the time on line study at 175 °C could be due to

adsorption and formation of the partial oxidation products on the catalyst over time. As conversion is only at ~85 %, small amounts of naphthalene may remain adsorbed on the surface. A build-up of these species will lead to a decrease in binding sites leading to the decrease in activity observed over the period. This will also decrease the surface area and potentially decrease the oxygen defects causing the reduction in activity. As the sample tested at 225 °C starts off at 100 % CO_2 yield, there will less adsorption of naphthalene on the surface of these catalysts. However over time, the surface may change leading to decrease in surface area leading to a modification of surface species. Over an increased reaction period, this may lead to coking or blocking of active sites causing the decrease in activity observed.

3.3 Results of the ceria-zirconia mixed metal oxide catalysts prepared from carbonate precursors

The mechanochemical synthesis of the ceria-zirconia mixed metal oxide catalyst using carbonate precursors is shown in section 2.1.2. $Ce_2(CO_3)_3$. $6H_2O$ and $Zr(OH)_2CO_3.ZrO_2$ were weighed in appropriate amounts before light grinding and placed into the ball mill crucible. The carbonate salts were ground at 200 rpm for 4 h before calcination at 400 °C for 3 h. The samples prepared from carbonates were milled at lower speeds compared to the nitrates due to difficulty in removing the samples from the crucible at higher ball milling speeds.

3.3.1 Precursor characterisation

3.3.1.1 Thermal gravimetric analysis

Figure 3-19 shows the decomposition profiles of the ceria-zirconia mixed metal oxide precursors prepared from carbonates. Desorption of water between 100-200 °C accounts for 15 % and ~23 % weight loss for the cerium and zirconium carbonate precursors, respectively. There is a further weight loss event on the cerium carbonate precursor sample at 250 °C from the decomposition of carbonates, which accounts for a further 20 % weight loss, which matches with previous cerium carbonate decomposition studies [50]. The zirconium carbonate sample doesn't have a distinct weight loss region accounting for loss of carbonates, however a further 10 % weight loss is noted within the experimental temperature range.

Unlike the decomposition of ceria-zirconia nitrate precursors in section 3.2.1.1, the decomposition profiles of the ceria-zirconia mixed metal precursor samples don't fit in between the limits of the cerium and zirconium carbonate decomposition profiles. Only $Ce_{0.95}Zr_{0.05}O_x$ follows a similar pattern to the ceria and shows an increase in weight loss

by ~3 % at each decomposition region. The decomposition profiles of the $Ce_{0.90}Zr_{0.10}O_x$ and $Ce_{0.75}Zr_{0.25}O_x$ show decreased weight loss compared to the ceria over the temperature range. The $Ce_{0.50}Zr_{0.50}O_x$ decomposition profile follows the decomposition of zirconium carbonate, however a noticeable region of cerium carbonate decomposition is noted at 300 °C. This may indicate poor mixing between the cerium and zirconium carbonate precursors. The endothermic nature of carbonate decomposition may also explain the difference in decomposition profiles between carbonate and nitrate decomposition [50,51].
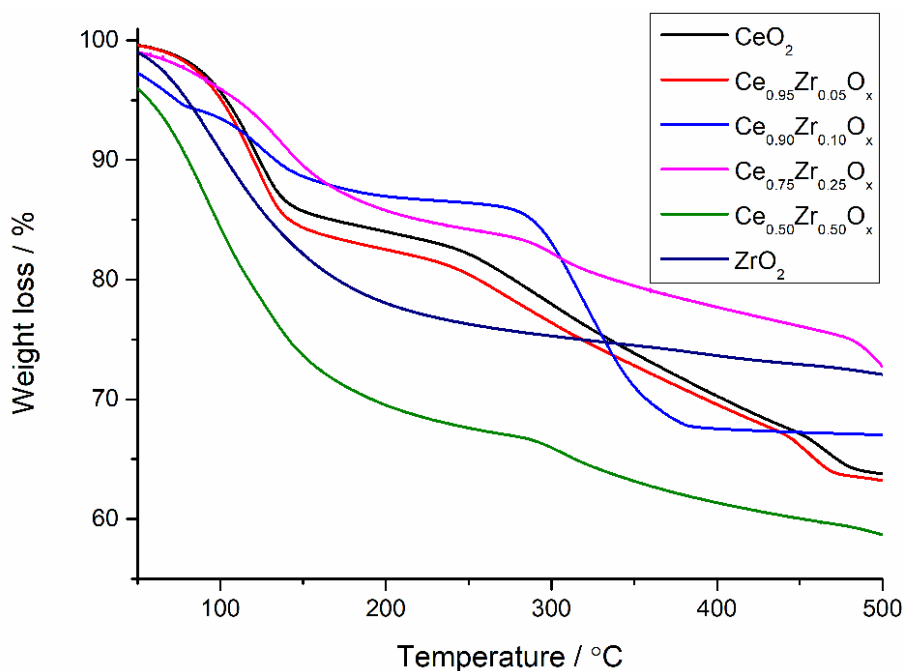
Figure 3-19: Thermogravimetric analysis of all the pre-calcined mechanochemically prepared ceria-zirconia mixed metal oxides prepared using carbonate precursors. Samples heated in flowing N_2 atmosphere from 30-600 °C at 5 °C min^{-1} ramp rate

3.3.1.2 *In situ* XRD

In situ XRD analysis was used to gain understanding of the effects of calcination on the formation of the final ceria-zirconia mixed metal oxide, Figure 3-20. The pattern of the untreated sample had many reflections originating from cerium and zirconium carbonate and hydroxide groups. The reflections associated with water and hydroxide groups are not present at 200 °C, as expected from TGA, due to these species decomposing at this temperature. Some reflections from carbonates species are still seen however these are not present as the sample is heated above 250 °C, indicating these species have started to decompose. As seen in the *in situ* XRD of the ceria-zirconia mixed metal oxide sample prepared using nitrate precursors, only four reflections are observed related to the ceria cubic structure. The patterns of the $Ce_{0.50}Zr_{0.50}O_x$ heated above 450 °C all show an extra

four reflections from bulk zirconia. This indicates significant phase separation has occurred at higher calcination temperatures. Reflections from zirconia also are higher in intensity compared to the ones observed during *in situ* XRD of the ceria-zirconia mixed metal oxide prepared using nitrate precursors.
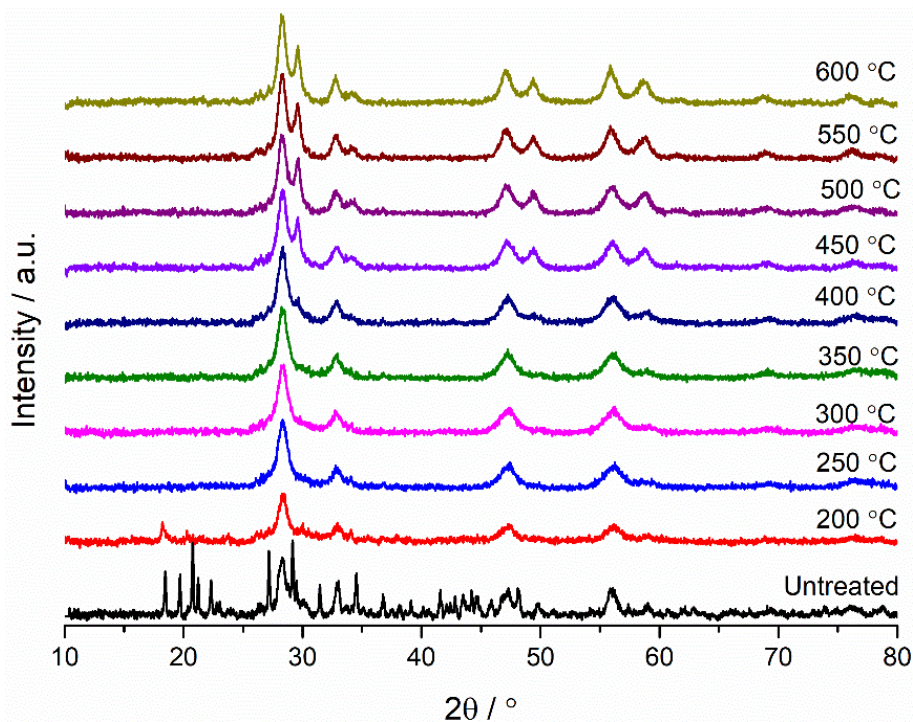

Figure 3-20: In situ XRD patterns of $Ce_{0.50}Zr_{0.50}O_x$ catalyst carbonate precursor with increasing temperature. Reaction conditions: 200-600 °C under a flow of 30 ml min^{-1} air, 10 minute scan duration.

Therefore, using the analysis from *in situ* XRD and TGA, a calcination temperature of 400 ℃ was used to treat the ceria-zirconia mixed metal oxide samples prepared using carbonate precursors. This is to keep the phase separation in the bulk to a minimum and ensure the complete decomposition of the carbonate species.

3.3.2 Catalyst performance for VOC total oxidation

3.3.2.1 Propane total oxidation

Propane total oxidation was carried out over the ceria-zirconia mixed metal oxides, Figure 3-21. All catalysts showed some activity towards propane total oxidation with high selectivity (> 99 %) to carbon dioxide. The errors associated for propane total oxidation over ceria-zirconia prepared by mechanochemically grinding carbonates was 3 %. Unlike the ceria and zirconia prepared from nitrate precursors, there was a difference in propane total oxidation activity with ceria achieving 100 % propane conversion at 550 ℃ whereas the zirconia couldn't fully convert all the propane to carbon dioxide within the temperature range.

In similar fashion to the ceria-zirconia mixed metal oxides prepared using nitrate precursors, there was an increase in propane total oxidation activity compared the reference catalyst and the mono-metallic oxides upon addition of small amounts of zirconia. The general trend of catalyst activity is shown below:

$$Ce_{0.95}Zr_{0.05}O_x > Ce_{0.90}Zr_{0.10}O_x > 5 \% \ Pd/Al_2O_3 > Ce_{0.75}Zr_{0.25}O_x \sim CeO_2 > Ce_{0.50}Zr_{0.50}O_x > ZrO_2$$
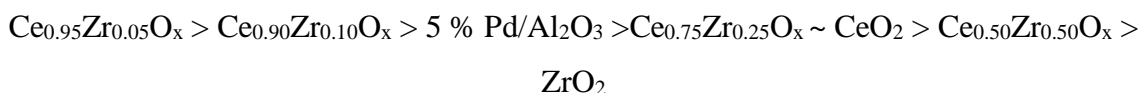
However, unlike the observations from ceria-zirconia mixed metal oxides made from nitrate precursors, not all ceria-zirconia mixed metal oxide catalysts showed increased propane total oxidation activity. Only ceria-zirconia mixed metal oxides with low zirconium content showed propane total oxidation activity higher than the ceria. However the $Ce_{0.95}Zr_{0.05}O_x$ prepared from carbonate precursors had a T_{100} temperature 50 °C lower than the $Ce_{0.90}Zr_{0.10}O_x$ prepared using nitrate precursors.
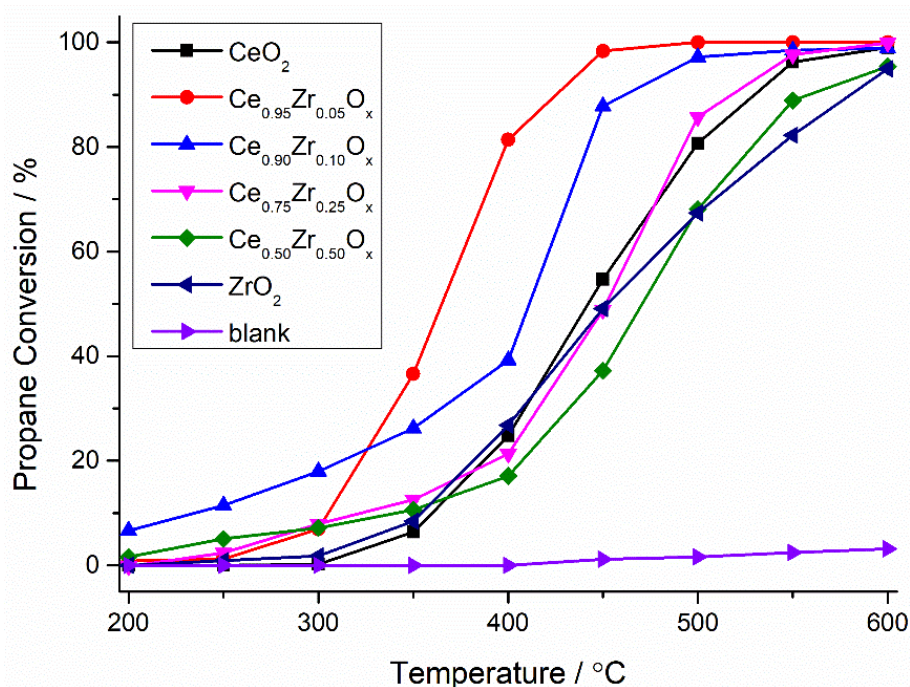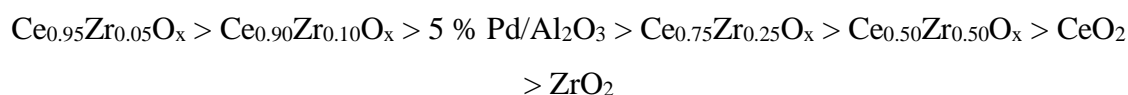

Figure 3-21: Catalytic activities for the total oxidation of propane over the ceria-zirconia mixed metal oxide catalysts prepared using carbonate precursors. Reaction conditions: temperature range: 200-600 °C, GHSV= 45,000 h^{-1}, 5000 ppm propane in air. Legend refer to Ce:Zr ratios

3.3.2.2 Naphthalene total oxidation

The naphthalene total oxidation activity for the ceria-zirconia mixed metal oxide catalysts is shown in Figure 3-22. The ceria had 40 % carbon dioxide yield at 250 °C whereas no naphthalene total oxidation activity was observed on the zirconia sample. There was a 4 % error in the naphthalene total oxidation activity over these catalyst systems. This has been observed in zirconia synthesised using by precipitation with sodium carbonate [7].

However this is contrary to the activity shown of the zirconia produced from a nitrate precursor. The ceria prepared using carbonates also had nearly double the naphthalene total oxidation activity of the sample prepared using nitrate precursors.

Unlike during propane total oxidation, all the ceria-zirconia mixed metal oxides showed increased activity compared to the ceria. However only ceria-zirconia mixed metal oxides containing low concentrations of zirconium performed better than the reference catalyst. The trend in naphthalene total oxidation activity is:

$$Ce_{0.95}Zr_{0.05}O_x > Ce_{0.90}Zr_{0.10}O_x > 5\ \%\ Pd/Al_2O_3 > Ce_{0.75}Zr_{0.25}O_x > Ce_{0.50}Zr_{0.50}O_x > CeO_2$$
$$> ZrO_2$$

The $Ce_{0.95}Zr_{0.05}O_x$ prepared from carbonates was the most active catalyst for naphthalene total oxidation. However, unlike the results from propane total oxidation, the catalysts prepared using carbonate precursors had less activity for naphthalene total oxidation compared to the $Ce_{0.90}Zr_{0.10}O_x$ prepared from nitrate precursors, with T_{100} temperature 25 °C higher. However, in both cases, the samples with the lower zirconium content were the most active for naphthalene total oxidation
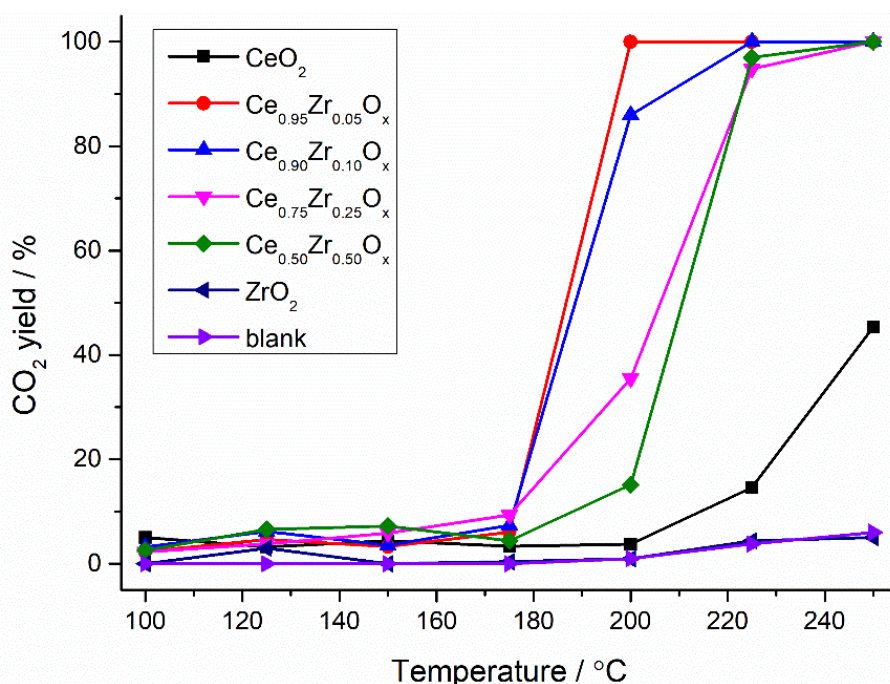

Figure 3-22: Catalytic activities for the total oxidation of naphthalene for the ceria-zirconia mixed metal oxide catalysts prepared using carbonate precursors. Reaction conditions: temperature range: 100-250 °C, GHSV= 45,000 h^{-1}, 100 vppm naphthalene in 20 % O_2 balanced with He. Legend refer to different Ce:Zr ratios

3.3.3 Catalyst characterisation

3.3.3.1 X-ray diffraction

Figure 3-23 shows the XRD patterns of the ceria, zirconia and ceria-zirconia mixed metal oxides prepared using carbonate precursors. The ceria sample has four reflections which are characteristic of the cubic fluorite phase, which concurs with the ceria sample prepared from nitrate precursors. However, there is a noticeable variation in the zirconia prepared from carbonate and nitrate precursors. The zirconia prepared from a carbonate precursor has four reflections characteristic of the tetragonal phase. However, due to the weak intensity of the reflections, it was difficult to analyse if there was any monoclinic phase present, as was observed in the zirconia prepared using nitrate precursors. Another noticeable difference is the crystallinity of the sample prepared from the two precursors. Reflections from the carbonate precursor are significantly less defined and broader compared to the reflections from zirconia prepared using nitrate precursors, indicating the sample prepared using nitrates is significantly more crystalline than the sample prepared using carbonates
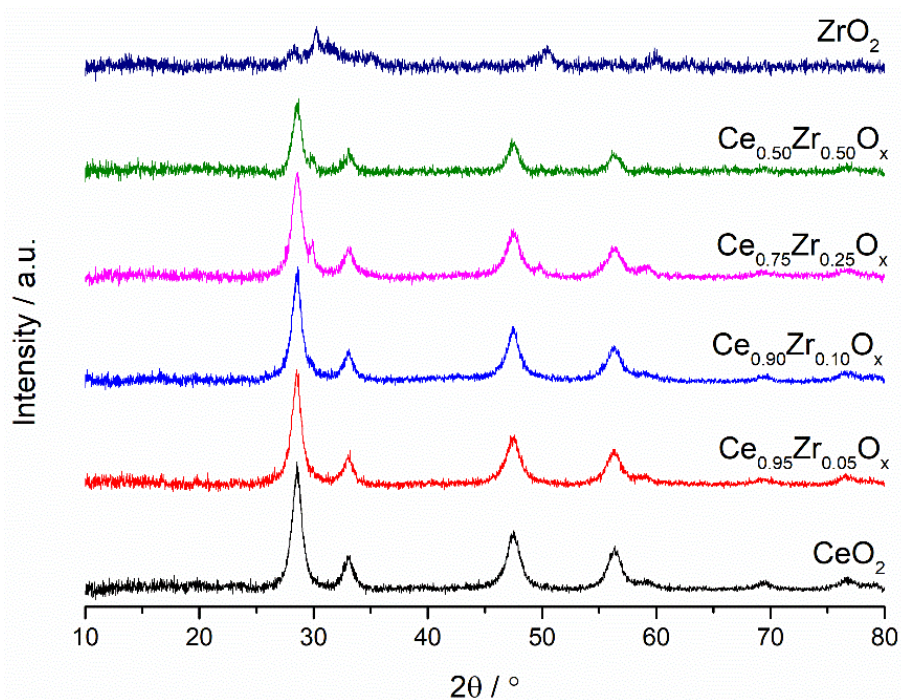

Figure 3-23: Powder XRD patterns of the ceria-zirconia mixed metal oxide catalysts prepared from carbonate precursors

All the patterns of the ceria-zirconia mixed metal oxides had four dominant reflections assigned to the ceria cubic fluorite phase. As seen in the ceria-zirconia mixed metal oxides prepared using nitrate precursors, the intensity of the reflections decreased as the zirconium content of the ceria-zirconia mixed metal oxide increases. There is a shift in

the position of the ceria (111) reflection, Table 3-9, as zirconium content of the ceria-zirconia mixed metal oxide increases. These observations indicate the incorporation of zirconium into the ceria and the formation of a solid solution. However, an evident shoulder reflection at 30 ° is present on the $Ce_{0.75}Zr_{0.25}O_x$ and $Ce_{0.50}Zr_{0.50}O_x$. This reflection denotes the presence of tetragonal phase zirconia, suggesting potentially that ceria-zirconia phase separation has occurred.

The crystallite size was calculated using the Scherrer equation from the four major reflections in the XRD patterns. As seen in the ceria-zirconia mixed metal oxides synthesised from nitrate precursors, the ceria had the largest crystallite size and the zirconia the smallest. The crystallite size of the ceria-zirconia mixed metal oxides decreases upon addition of higher concentrations of zirconium into the lattice. No systematic trend was observed, however the decrease in crystallite size was accompanied by a decrease in the d-spacing. It is noted that the crystallite size of the ceria-zirconia mixed metal oxides produced from carbonates had a ~40 % decrease in crystallite size compared to ceria-zirconia mixed metal oxides produced from nitrates.

Table 3-9: Physical properties of the ceria-zirconia mixed metal oxides prepared using carbonates derived from XRD

Sample	Phases present	Position of ceria (111) reflection / °	Average crystallite size / Å	d-spacing from (200) lattice plane / Å	Unit Cell Volume / Å³	Incorporation of zirconium into Ce / %
CeO_2	CeO_2	28.5	78	2.725	161.879	-
$Ce_{0.95}Zr_{0.05}O_x$	CeO_2	28.6	73	2.711	159.396	5
$Ce_{0.90}Zr_{0.10}O_x$	CeO_2	28.7	58	2.683	154.508	10
$Ce_{0.75}Zr_{0.25}O_x$	CeO_2	28.9	56	2.633	146.030	25
$Ce_{0.50}Zr_{0.50}O_x$	CeO_2	28.9	65	2.618	143.549	50
ZrO_2	ZrO_2	-	43	2.550[24]	132.651	-

As mentioned above, the d-spacings of the ceria-zirconia mixed metal oxides decreased upon increasing zirconium content. This follows the trends observed from the mixed metal oxides prepared using nitrate precursors. However, the d-spacings of the ceria-zirconia mixed metal oxides prepared from nitrate precursors are slightly smaller than the ones prepared from carbonates. The crystallite size effects d-spacing which may cause the differences observed between the precursors [52].

The extent of zirconium incorporation into the ceria lattice in the ceria-zirconia mixed metal oxides is shown in Figure 3-24. There is a noticeable decrease in unit cell volume as the zirconium content increases. However unlike the observations from ceria-zirconia

mixed metal oxides prepared from nitrate precursors, the experimental values are lower than the expected values. This suggests all the zirconium has been incorporated into the ceria lattice for all the ceria-zirconia mixed metal oxide samples. However the contraction of the unit cell is not always linear in ceria-zirconia mixed metal oxide solutions [53,54]. Effects such as crystallite size [55] and defect concentration, leading to oxygen and cerium/ zirconium displacement [56], cause variation in unit cell volume. As zirconium content of a ceria-zirconia mixed metal oxide increases the oxygen becomes increasingly displaced from the lattice forming $CeZrO_{2-x}$ structures. To consolidate the loss of oxygen ions, the lattice structure will compress causing increased contraction of the ceria lattice. This in turn will cause the lattice to contract more than expected leading to decrease in unit cell volume not behaving linearly.
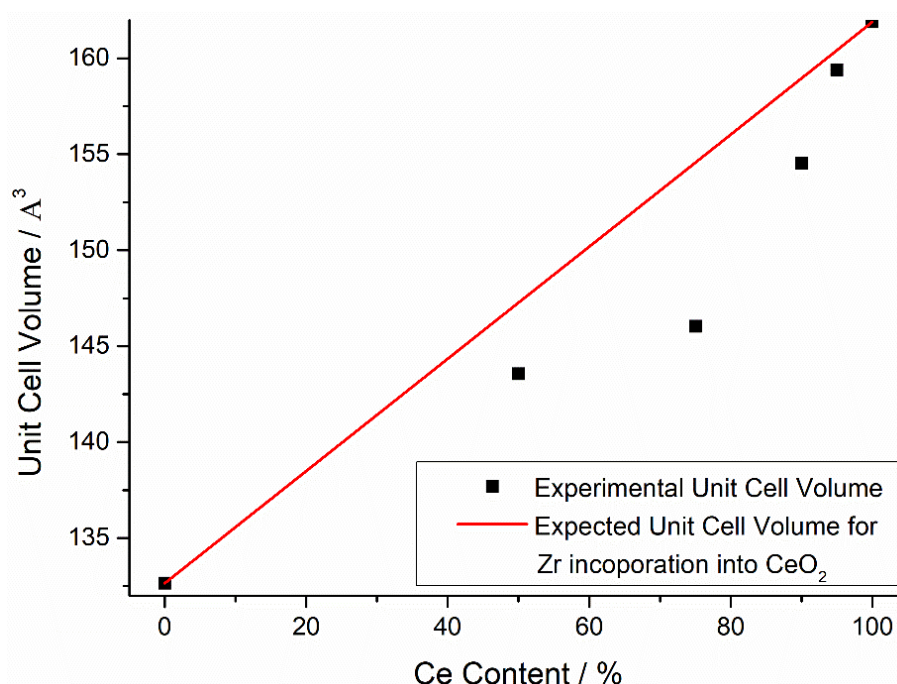
Figure 3-24: Comparison of experimental and expected unit cell volume of the ceria-zirconia mixed metal oxide catalysts prepared from carbonate precursors. Calculated using the (200) lattice parameter from XRD

3.3.3.2 Surface area

The surface areas of the ceria-zirconia mixed metal oxides are shown in Table 3-10. The ceria and the zirconia had similar surface areas. Any amount of zirconium added to the ceria lattice led to an increase in the surface area of ~20 % compared to the pure metal oxide samples. This trend coincides with the surface areas of the ceria-zirconia mixed metal oxides prepared using nitrate precursors. However the surface areas of the samples prepared using nitrates are ~40 % higher than the samples prepared using carbonates.

Table 3-10: Surface area of the ceria-zirconia mixed metal oxide catalysts prepared from carbonate precursors. Calculated using the 5-point N_2 adsorption BET analysis

Sample	BET Surface area / $m^2\,g^{-1}$	Surface area normalised rate of propane total oxidation at 400 °C (10^{-8}) / mol $s^{-1}\,m^{-2}$	Surface area normalised rate of naphthalene total oxidation at 200 °C (10^{-11}) / mol $s^{-1}\,m^{-2}$
CeO_2	62	0.36	0.10
$Ce_{0.95}Zr_{0.05}O_x$	77	1.65	2.16
$Ce_{0.90}Zr_{0.10}O_x$	79	1.15	1.81
$Ce_{0.75}Zr_{0.25}O_x$	75	0.58	0.79
$Ce_{0.50}Zr_{0.50}O_x$	71	0.52	0.35
ZrO_2	58	0.00	0.02

The effect of surface area on the rate of propane and naphthalene total oxidation on the ceria-zirconia mixed metal oxides are shown in Table 3-10. As mentioned previously, the surface area has a significant effect on the rates of VOC total oxidation. The $Ce_{0.95}Zr_{0.05}O_x$ sample has the highest propane and naphthalene total oxidation activity. However even when the rates are normalised to surface area, the $Ce_{0.95}Zr_{0.05}O_x$ still has the highest activity indicating other factors such as surface oxygen and oxygen vacancies influence the activity of the samples more than the surface area.

3.3.3.3 Raman spectroscopy

Raman spectroscopy was carried out on the ceria-zirconia mixed metal oxides prepared from carbonate precursors, Figure 3-25. There was only one peak present on the cerium containing ceria-zirconia mixed metal oxides centring at 464 cm^{-1}, which is characteristic of the ceria fluorite phase. Even though small shoulder peaks indicating the presence of zirconia were observed in XRD analysis of the $Ce_{0.75}Zr_{0.25}O_x$ and $Ce_{0.50}Zr_{0.50}O_x$, no peaks from zirconia were observed. The ceria sample also had a low intensity peak at 600 cm^{-1} indicating the presence of oxygen vacancies. The zirconia sample has four very weak peaks, which are characteristic of tetragonal phase zirconia therefore confirming the phase identification from XRD.
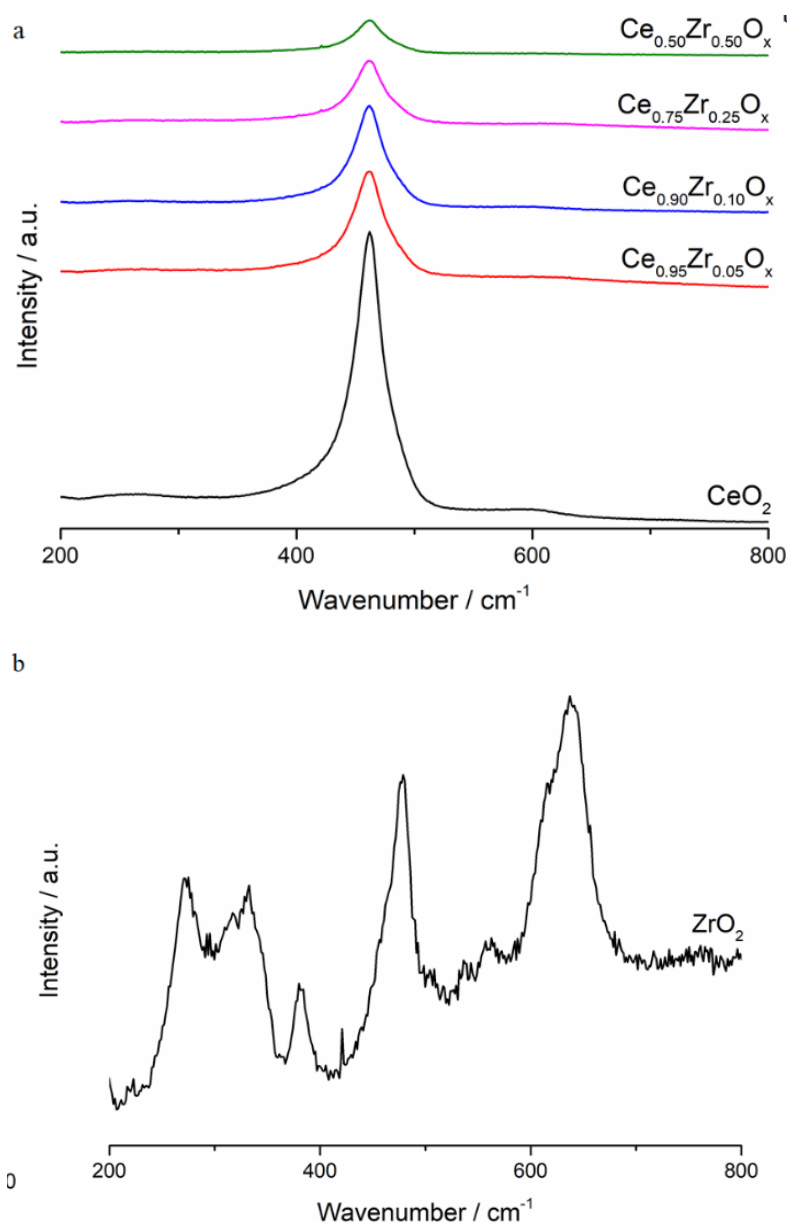
Figure 3-25: Laser Raman spectra for the (a) CeO_2, $Ce_{0.95}Zr_{0.05}O_x$, $Ce_{0.90}Zr_{0.10}O_x$, $Ce_{0.75}Zr_{0.25}O_x$ and $Ce_{0.50}Zr_{0.50}O_x$ and (b) ZrO_2 (spectra enhanced 10x) prepared from carbonate precursors. Laser $\lambda = 514$ nm

As seen from the Raman spectroscopy from the ceria-zirconia mixed metal oxides produced from nitrate precursors, as the concentration of zirconium in the ceria-zirconia mixed metal oxide increases, the height of the peak at 464 cm^{-1} decreases, Table 3-11. With crystallite size decreasing upon increasing zirconium content of the ceria-zirconia mixed metal oxide, this will lead to the increase in FWHM. The value of the FWHM are ~15 % larger in the ceria-zirconia mixed metal oxides prepared from nitrates compared to carbonates for all ratios except the $Ce_{0.50}Zr_{0.50}O_x$ which is ~10 % lower. The difference in FWHM between the precursors is due to the crystallite size. As large ceria crystallites are noted to have smaller FWHM values at 464 cm^{-1}[34,35].

Table 3-11: Chemical properties of ceria-zirconia mixed metal oxide catalysts prepared using carbonate precursors from laser Raman analysis

Sample	Raman FWHM of 464 cm^{-1} peak / cm^{-1}	Peak area ratio of 600 cm^{-1} / 464 cm^{-1}
CeO_2	30.9	0.0215
$Ce_{0.95}Zr_{0.05}O_x$	33.9	0.0265
$Ce_{0.90}Zr_{0.10}O_x$	38.8	0.0273
$Ce_{0.75}Zr_{0.25}O_x$	39.4	0.0492
$Ce_{0.50}Zr_{0.50}O_x$	40.1	0.0907

Extrinsic oxygen vacancies created from substitution of Zr^{4+} into the ceria lattice can be analysed by comparing the peak areas of the 600 cm^{-1} and 464 cm^{-1}, as seen in Table 3-11. The ceria had the lowest ratio with the value increasing as zirconium content increased. This indicates there is some increase in oxygen vacancies between the ceria and the ceria-zirconia mixed metal oxides. However as mentioned previously, this relationship between Raman peak area and oxygen vacancies isn't linear indicating other factors will affect this trend. The ratios for the ceria-zirconia mixed metal oxides from carbonates are lower than those observed for samples prepared from nitrates, suggesting less oxygen vacancies are present on these samples.
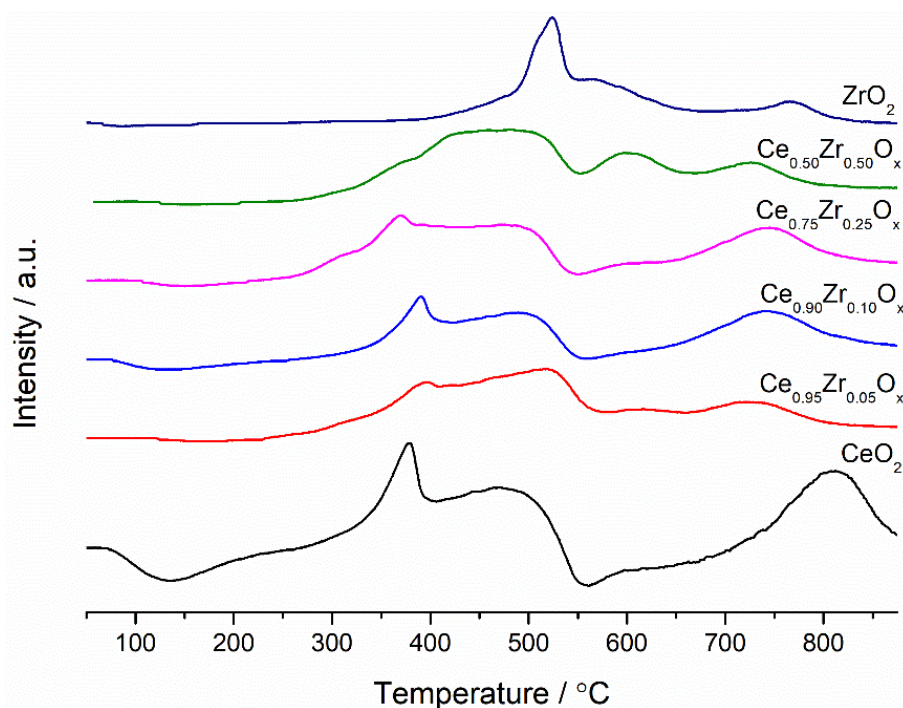
3.3.3.4 Temperature programmed reduction

Figure 3-26: Hydrogen temperature programmed reduction profiles of the ceria-zirconia mixed metal oxide catalysts prepared from carbonate precursors. Reaction conditions: 30 mg sample, 30 ml min^{-1} of 10 % H_2/Ar, temperature range 50-900 °C

Reduction profiles of the ceria-zirconia mixed metal oxides are shown in Figure 3-26. Like the ceria sample prepared from nitrate salts, there were two noticeable reduction regions. One region was centred around 400 °C and the other around 800 °C, attributed to the reduction of surface and bulk ceria respectively. Rather than having a single reduction peak, Two peaks were noted on the ceria prepared from carbonates suggesting the presence of both Ce^{3+} and Ce^{4+} on the surface. There were two peaks observed during the reduction of zirconia centred at 535 °C and a shallow peak at 750 °C. The peak at a lower temperature is due to reduction of zirconia species, as mentioned previously, and the peak at the higher temperature representing bulk zirconia reduction[57]. The bulk reduction peak is very small confirming the difficulty of bulk zirconia reduction within the temperature range

The ceria-zirconia mixed metal oxides profiles are less defined than the ceria and zirconia however two distinct regions are observed. A broad region between 350 and 550 °C, indicating the reduction of surface species and a region centred around 730 °C, showing the reduction of bulk. The large temperature range required to reduce the surface suggests there is a mixture of Ce^{4+} and Ce^{3+} species present and a significant number of defect sites present on the surface. The smaller crystallite size will form more oxygen vacancies and defect sites as seen in XRD and Raman spectroscopy. There could also be a contribution from zirconia species on the $Ce_{0.75}Zr_{0.25}O_x$ and $Ce_{0.50}Zr_{0.50}O_x$, as seen in XRD, causing the reduction peaks to be less defined. However, due to the difficulty of identifying these species will be hard to quantify.

Table 3-12: Chemical properties derived from TPR analysis of the ceria-zirconia mixed metal oxide catalysts prepared using carbonate precursors

Sample	CeO_2 Reduction temperature / °C		Surface hydrogen consumption / $\mu mol\ H_2$	Surface area normalised hydrogen consumption / $\mu mol\ H_2\ m^{-2}$
	Surface	**Bulk**		
CeO_2	378, 466	813	2.28	1.23
$Ce_{0.95}Zr_{0.05}O_x$	396, 516	722	2.35	1.02
$Ce_{0.90}Zr_{0.10}O_x$	390, 483	743	2.71	1.14
$Ce_{0.75}Zr_{0.25}O_x$	369, 473	744	2.73	1.21
$Ce_{0.50}Zr_{0.50}O_x$	450	722	2.74	1.29
ZrO_2	-	-	1.25	-

The surface and bulk reduction temperatures of ceria species in the ceria-zirconia mixed metal oxides are shown in Table 3-12. The incorporation of zirconium into ceria caused an increase in surface reduction temperature suggesting the addition of zirconium makes

reduction more difficult. However all temperatures were lower than the surface reduction peaks recorded for the ceria-zirconia prepared from nitrate precursors. This could be due to the increased defect sites and disorder seen in XRD analysis which may promote the reduction compared to the ceria-zirconia mixed metal oxides prepared from nitrates. The lower reduction temperature helps explain increased propane total oxidation activity of the ceria-zirconia mixed metal oxides prepared from carbonate precursors compared to the nitrates. With surface reduction temperatures ~30 °C lower for the samples prepared from carbonates compared to the nitrates. This will mean the oxygen required for propane total oxidation via a Mars van-Krevelen mechanism will be easier to extract from the surface and form active oxygen species.

The hydrogen consumption for surface ceria reduction is shown in Table 3-12. The ceria had the lowest hydrogen consumption of cerium containing samples and this value increased upon addition of zirconia. However, when these values are normalised to surface area, the difference between the hydrogen consumption of the ceria and ceria-zirconia mixed metal oxides isn't as distinct, as only the $Ce_{0.50}Zr_{0.50}O_x$ sample has an hydrogen consumption larger than the CeO_2. This suggests that unlike in the ceria-zirconia mixed metal oxides prepared from nitrates, the zirconium doesn't have a significant effect on the ease of reduction as the samples prepared from carbonates. However, there is a decrease in the ceria reduction temperature between the ceria-zirconia mixed metal oxides prepared carbonates and nitrates. This suggests the zirconium is changing the reduction pattern of the carbonates sample but not to the same extent as the nitrate samples.

3.3.3.5 Electron microscopy

3.3.3.5.1 Scanning electron microscopy

The secondary and back scattered electron microscopy images of ceria and zirconia produced from carbonates are shown in Figure 3-27. As seen for the samples prepared from nitrates, the ceria has its typical plate-like morphology whereas the zirconia has a coral-like morphology. Some bright areas are seen on the zirconia secondary electron image, which has occurred due to charging of the surface under the electron beam.
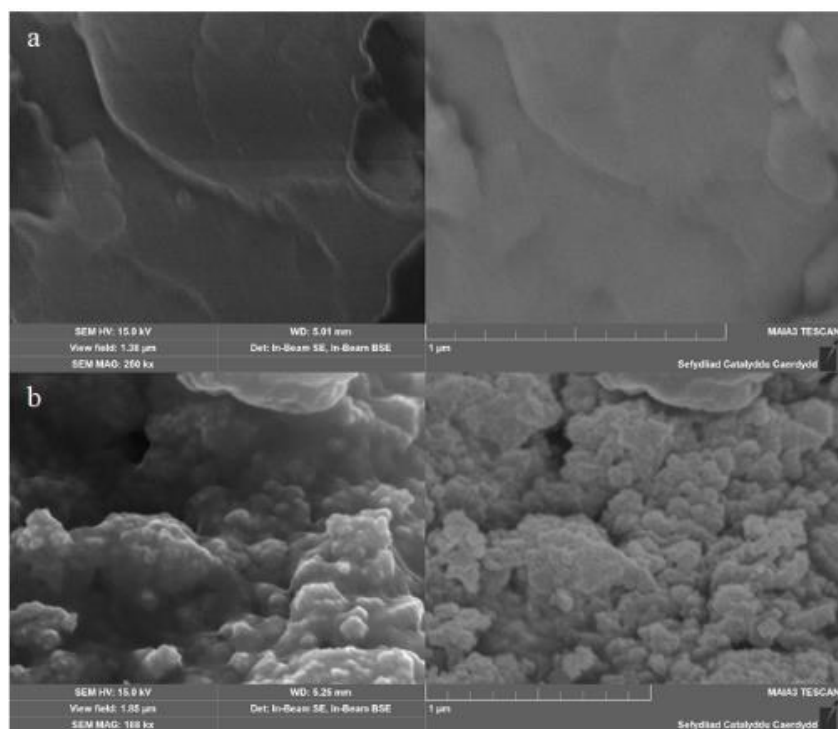
Figure 3-27: Secondary electron (left) and back scattered electron (right) micrographs of (a) ceria and (b) ZrO$_2$. Image magnification: 250 kx

The secondary and back scattered electron micrographs of the ceria-zirconia mixed metal oxides are shown in Figure 3-28. The plate-like morphology is observed in all ratios, however, as the amount of zirconium increases in the ceria-zirconia mixed metal oxide some islands start to appear on the images over the plate-like structures. The number of these increase as the zirconium content of the ceria-zirconia mixed metal oxide increases the number of these islands increase. These islands maybe the zirconium species observed in XRD.
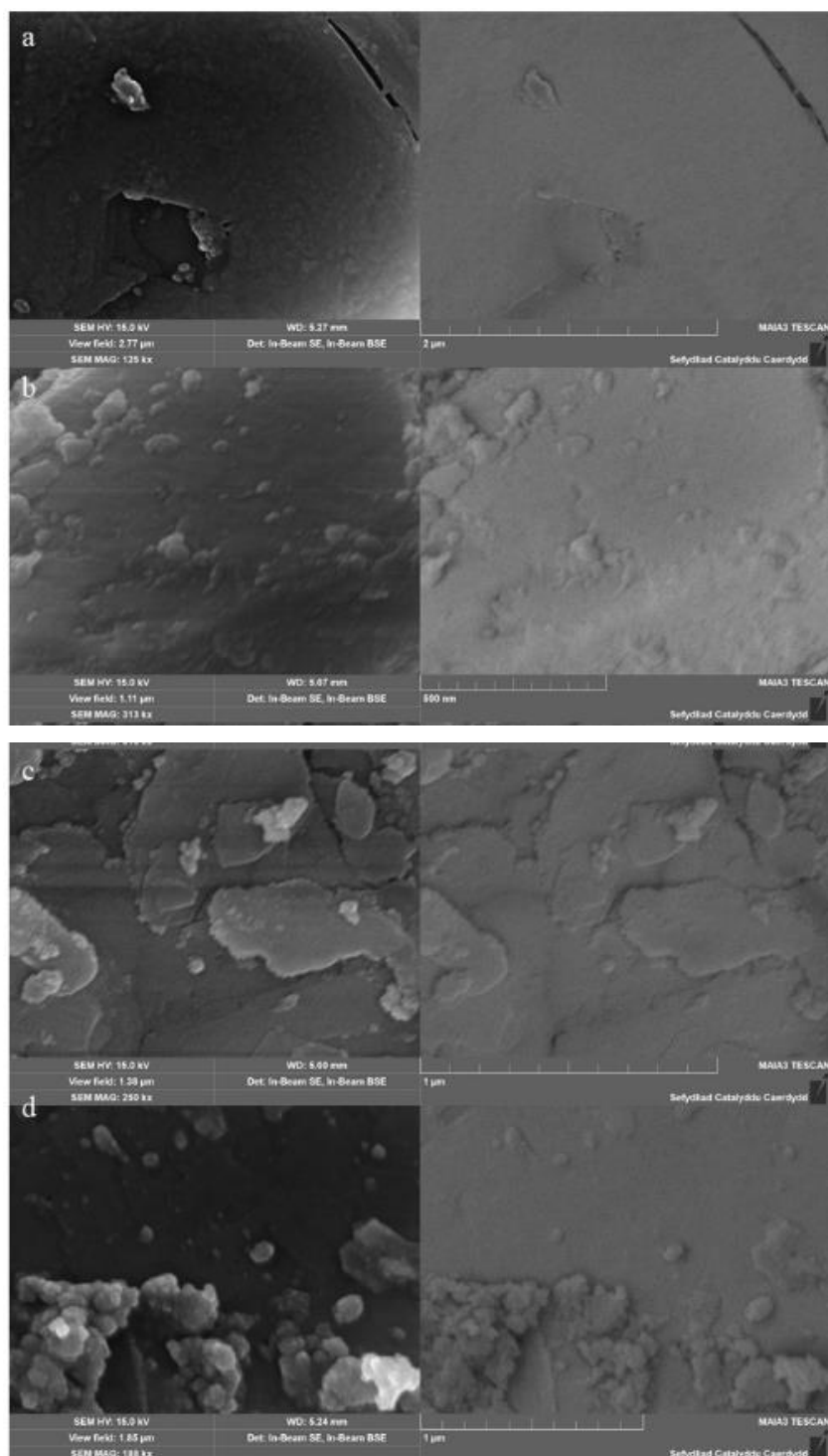
Figure 3-28: Secondary electron (left) and back scattered electron (right) micrographs of (a) $Ce_{0.95}Zr_{0.05}O_x$, (b) $Ce_{0.90}Zr_{0.10}O_x$, (c) $Ce_{0.75}Zr_{0.25}O_x$ and (d) $Ce_{0.50}Zr_{0.50}O_x$. Image magnification: 250 kx

3.3.3.5.2 Energy dispersive x-ray spectroscopy

EDX analysis was undertaken to examine the bulk composition of the ceria-zirconia mixed metal oxides prepared from carbonates, with the bulk concentration shown in Table 3-13. As seen in the EDX analysis of the ceria sample prepared from nitrates, there was

no zirconium observed in the ceria prepared from carbonates indicating no contamination from the zirconia bulk material has occurred during the milling procedure.

Table 3-13: SEM-EDX derived bulk element analysis of the ceria-zirconia mixed metal oxide catalysts prepared using carbonate precursors

| Sample | Concentration / % | | | |
	Ce	Zr	O	Ce:Zr ratio
CeO_2	54.7	-	45.3	100:0
$Ce_{0.95}Zr_{0.05}O_x$	42.1	2.3	55.6	94.8:5.2
$Ce_{0.90}Zr_{0.10}O_x$	21.6	2.5	75.9	89.6:10.4
$Ce_{0.75}Zr_{0.25}O_x$	23.5	7.2	69.2	76.5:23.5
$Ce_{0.50}Zr_{0.50}O_x$	14.7	11.8	73.5	55.5:44.5
ZrO_2	-	19.2	80.8	0:100

Similar to the ceria-zirconia mixed metal oxides prepared from nitrates, the Ce:Zr ratios of the bulk were all similar to Ce:Zr ratios expected from the starting ratios. The $Ce_{0.95}Zr_{0.05}O_x$, $Ce_{0.90}Zr_{0.10}O_x$ and $Ce_{0.75}Zr_{0.25}O_x$ prepared from carbonates all had Ce:Zr ratios closer to the original compared to the nitrates. However the Ce:Zr ratio of the $Ce_{0.50}Zr_{0.50}O_x$ prepared from carbonates was different compared to the ratio of the sample prepared from nitrates. The excess cerium noted in this sample could be due to the phase separation occurring in the sample.
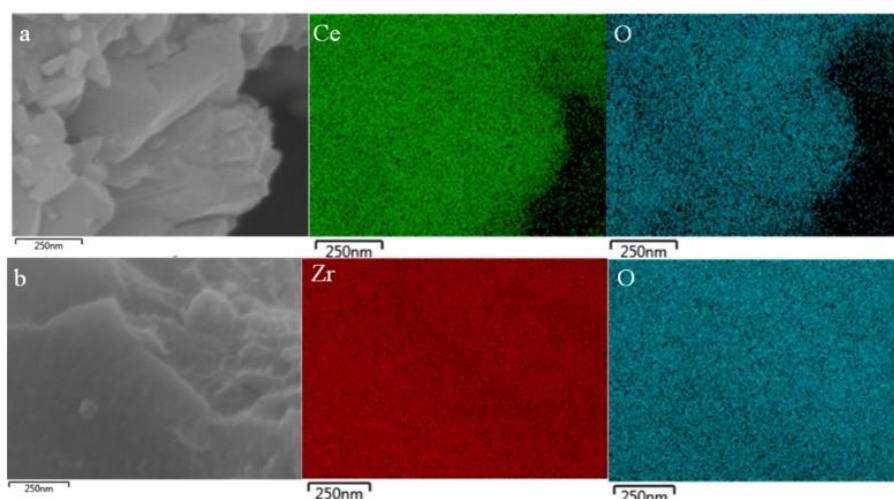

Figure 3-29: SEM-EDX mapping of (a) ceria and (b) zirconia prepared using carbonate precursors. Cerium (green), zirconium (red) and oxygen (blue)

EDX maps of the ceria, zirconia and the ceria-zirconia mixed metal oxides prepared from carbonates are shown in Figure 3-29 and Figure 3-30. The $Ce_{0.95}Zr_{0.05}O_x$ and $Ce_{0.90}Zr_{0.10}O_x$ had a homogeneous distribution of cerium and zirconium over the map area indicating good mixing between the two metal oxides. This confirms observations from XRD, in which only cubic fluorite ceria was observed suggesting good mixing between

the Ce and zirconium in the bulk phase. However, the two samples with high zirconium content, $Ce_{0.75}Zr_{0.25}O_x$ and $Ce_{0.50}Zr_{0.50}O_x$ showed separated cerium and zirconium regions indicating phase separation had occurred in the catalysts. Phase separation is noted in XRD analysis of these samples, with EDX mapping also confirming these observations.
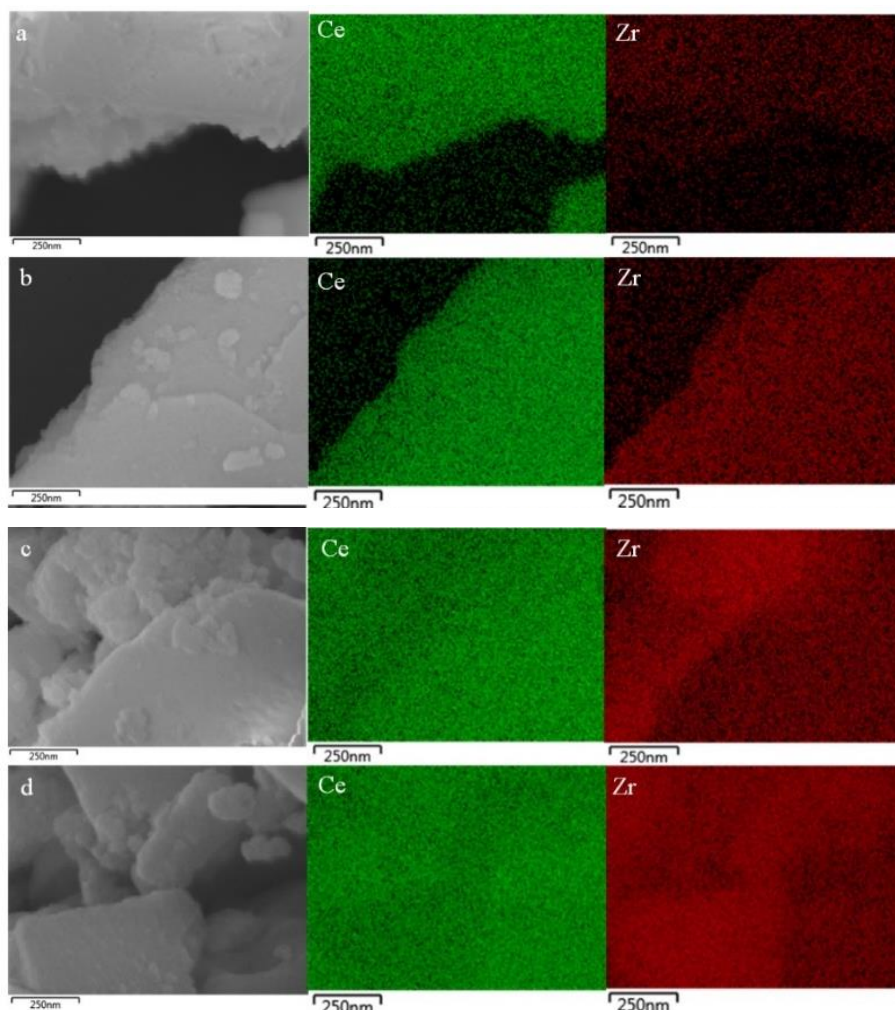

Figure 3-30: : SEM-EDX mapping of (a) $Ce_{0.95}Zr_{0.05}O_x$, (b) $Ce_{0.90}Zr_{0.10}O_x$, (c) $Ce_{0.75}Zr_{0.25}O_x$ and (d) $Ce_{0.50}Zr_{0.50}O_x$ prepared using carbonate precursors. Cerium (green) and zirconium (red)

3.3.3.5.3 Transmission electron microscopy

TEM images and selected area electron diffraction of the ceria-zirconia mixed metal oxides prepared from carbonates are shown in Figure 3-31. The images show an array of random layered crystallites for all ceria containing samples. The image of the zirconia shows large layers of round crystallites. Previous studies show these are representative of tetragonal zirconia, therefore confirming the XRD analysis of the sample[58].

The inset of the TEM images in Figure 3-31 show the selected area electron diffraction of the ceria-zirconia mixed metal oxides prepared from carbonates. Four distinct rings are observed for the ceria representing the ceria cubic fluorite structure, as seen from XRD

and Raman analysis of the sample. There was an array of spots from diffraction of the zirconia sample suggesting the zirconia shows a crystalline structure. Although the intensity of the spots are low, which indicates the zirconia crystallites have a low order. This is in accordance with the intensity of the reflections of the zirconia in XRD.
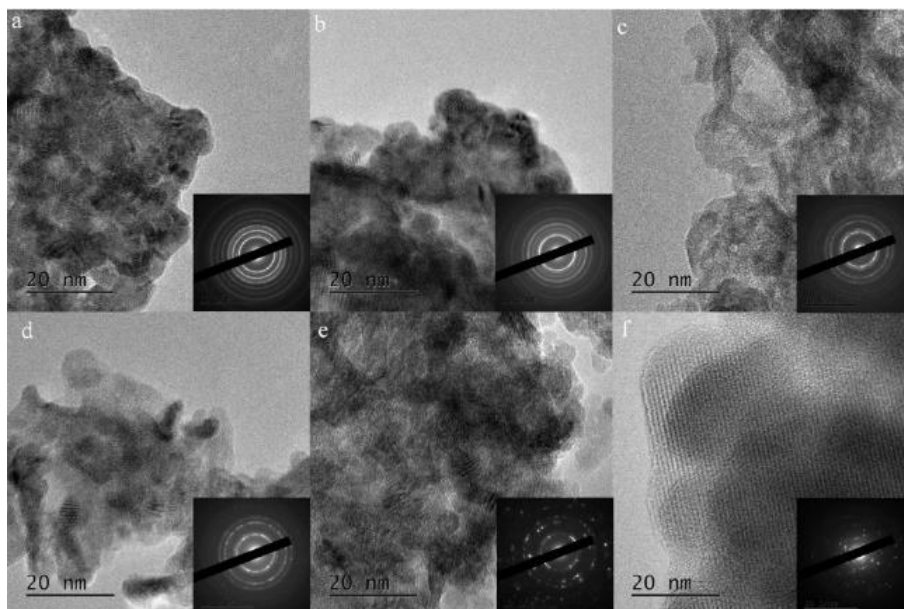

Figure 3-31: High magnification TEM images of the ceria-zirconia mixed metal oxide catalysts prepared using carbonate precursors. Inset: selected area electron diffraction pattern of larger 250 nm areas. (a) CeO_2, (b) $Ce_{0.95}Zr_{0.05}O_x$, (c) $Ce_{0.90}Zr_{0.10}O_x$, (d) $Ce_{0.75}Zr_{0.25}O_x$ (e) $Ce_{0.50}Zr_{0.50}O_x$ and (f) ZrO_2

The ceria-zirconia mixed metal oxides all have two diffraction rings which are assigned to the ceria fluorite structure. The structure of the diffraction rings become less defined as the zirconium content of the ceria-zirconia mixed metal oxides increases. This is seen by the formation of spots rather than diffuse rings as seen in the diffraction patterns of the $Ce_{0.75}Zr_{0.25}O_x$ and especially in the $Ce_{0.50}Zr_{0.50}O_x$. This suggests the ceria and zirconia are becoming phase separated leading to formation of single metal oxide crystallites. This confirms the data observed from XRD of the ceria-zirconia mixed metal oxides in which these two samples showed phase separation of ceria and zirconia. However it is difficult to distinguish between the two metal oxides due to the complementary patterns from each metal oxide leading to diffusion of the diffraction rings.

Table 3-14: The d-spacings of the ceria-zirconia mixed metal oxide catalysts prepared using carbonate precursors determined from selected area electron diffraction

Sample	d-spacing calculated from selected area electron diffraction / Å
CeO_2	5.24
$Ce_{0.95}Zr_{0.05}O_x$	5.22
$Ce_{0.90}Zr_{0.10}O_x$	5.20
$Ce_{0.75}Zr_{0.25}O_x$	5.14
$Ce_{0.50}Zr_{0.50}O_x$	4.98
ZrO_2	5.02

The d-spacings calculated from selected area electron diffraction of the ceria-zirconia mixed metal oxides prepared from carbonates as shown in Table 3-14. The d-spacing of the ceria is typical for cubic fluorite structure and the zirconia d-spacing is very close to the value for the tetragonal phase. This confirms the phase identification from XRD and Raman analysis. The d-spacings of the ceria-zirconia mixed metal oxides all decrease as the zirconium content of the mixed metal oxide increases. All the values are close to the d-spacing of the ceria fluorite phase except for the $Ce_{0.50}Zr_{0.50}O_x$, which had a lower d-spacing than zirconia. This follows the observations from XRD, in which d-spacings decreased as zirconium content of the ceria-zirconia mixed metal oxide increased due to contraction of the ceria lattice. This also confirms the XRD and Raman analysis of the samples in which fluorite ceria is the dominant phase. However, as mentioned earlier, the d-spacing of the ceria and zirconia are comparable making it difficult to distinguish the contribution of d-spacing from each metal oxide phase.

3.3.3.6 X-ray photoelectron spectroscopy

Table 3-15: XPS derived surface elemental concentrations for the ceria-zirconia mixed metal oxide catalysts prepared using carbonate precursors

Sample	Concentration / at%			Relative Ce / %	Relative Zr / %
	Ce	O	Zr		
CeO_2	32.8	67.2	0	100	-
$Ce_{0.95}Zr_{0.05}O_x$	22.9	70.6	6.5	77.8	22.2
$Ce_{0.90}Zr_{0.10}O_x$	21.9	69.4	8.7	71.5	28.5
$Ce_{0.75}Zr_{0.25}O_x$	16.4	69.4	14.2	53.7	46.3
$Ce_{0.50}Zr_{0.50}O_x$	12.0	70.8	17.2	41.1	58.9
ZrO_2	0	78.3	21.7	-	100

The surface composition of the ceria-zirconia mixed metal oxides prepared from carbonates are shown in Table 3-15. As seen in surface analysis of ceria prepared from

nitrates, no zirconium is present indicating no contamination from the milling material has occurred on the surface of these materials. The EDX analysis of the ceria-zirconia mixed metal oxides showed bulk Ce:Zr ratios similar to the original synthesis Ce:Zr ratios. Although analysis of the surface of the ceria-zirconia mixed metal oxides all contained increased concentrations of zirconium compared to the original Ce:Zr ratio of the mixed metal oxide.

The same observation was noted for the ceria-zirconia mixed metal oxides prepared from nitrates. This suggests that, as seen in the ceria-zirconia mixed metal oxides prepared from nitrates, only small amounts of the zirconium incorporates into the ceria lattice and the extra zirconium deposits on the surface. This differs due the to the XRD analysis which suggested all the zirconium had incorporated into the ceria lattice due to the contraction of lattice volume. The surface zirconia could be present in the amorphous phase making it undetectable during XRD analysis. A trend between VOC total oxidation activity and surface zirconium is observed, in which high surface zirconium lead to poorer total oxidation activity. This observation is seen in ceria-zirconia mixed metal oxides prepared from nitrates confirming that low loading of zirconium produce catalysts with increased activity for VOC total oxidation, no matter what the preparation method[7].
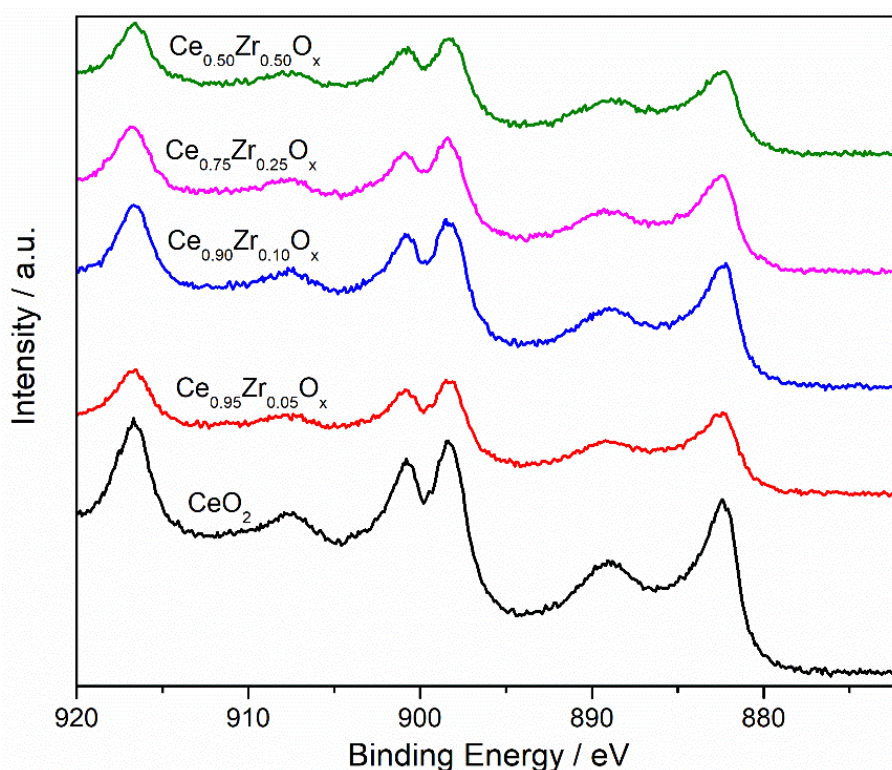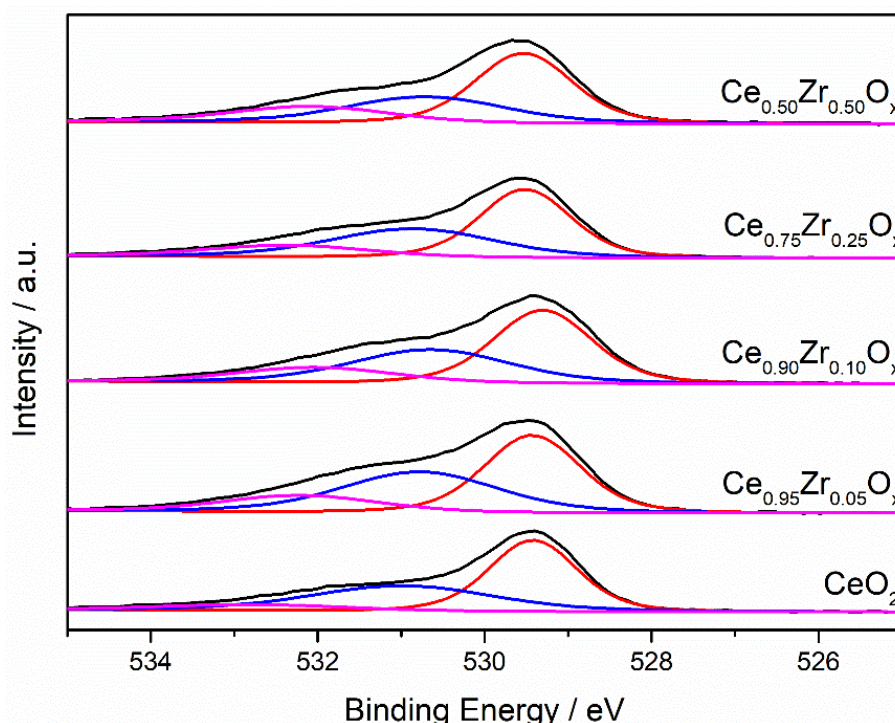

Figure 3-32: XPS spectra of the Ce 3d peaks for the ceria-zirconia mixed metal oxide catalysts prepared from carbonate precursors

The Ce 3d XPS spectra of the ceria-zirconia mixed metal oxides prepared from carbonates are shown in Figure 3-32. As seen in previous section the ceria had the most intense XPS peaks with the intensity decreasing upon increasing zirconium content. All samples showed Ce^{4+} to be the dominant oxidation state of cerium due to the presence of a large peak at 913 eV on all samples. However the increased symmetry of the doublet peak at 895-900 eV suggests Ce^{3+} is also present. Compared to the spectra of the ceria-zirconia mixed metal oxides prepared from nitrates, there was not a significant shift in the ceria compared to the ceria-zirconia mixed metal oxides. This suggests the relative amounts of Ce^{4+} and Ce^{3+} remains constant independent of the zirconium content. This also follows the TPR patterns in which two surface oxidation peaks were observed in all cerium containing samples suggesting both cerium oxidation states are present.

Figure 3-33: XPS spectra of the oxygen 1s peaks of the ceria-zirconia mixed metal oxides prepared from carbonate precursors

The fitted oxygen 1s spectra of the ceria-zirconia mixed metal oxides prepared from carbonates are shown in Figure 3-33. All samples had two oxygen regions, lattice (O_α) and surface defects (O_β), with the relative concentrations shown in Table 3-16.

Table 3-16: XPS derived concentrations of lattice and surface oxygen species for the ceria-zirconia mixed metal oxide catalysts prepared using carbonate precursors

Sample	Relative concentration of O_α / %	Relative concentration of O_β / %
CeO_2	54.1	45.9
$Ce_{0.95}Zr_{0.05}O_x$	44.4	55.6
$Ce_{0.90}Zr_{0.10}O_x$	48.1	51.9
$Ce_{0.75}Zr_{0.25}O_x$	48.8	51.2
$Ce_{0.50}Zr_{0.50}O_x$	53.3	46.7

The effect of surface oxygen on VOC total oxidation activity on the ceria-zirconia mixed metal oxides are shown in Figure 3-34. A clear trend is seen in which increasing O_β concentration leads to increased propane and naphthalene total oxidation activity. This coincides with the observations from the ceria-zirconia mixed metal oxides produced from nitrates suggesting O_β has a significant effect on ceria-zirconia mixed metal oxide total oxidation activity.
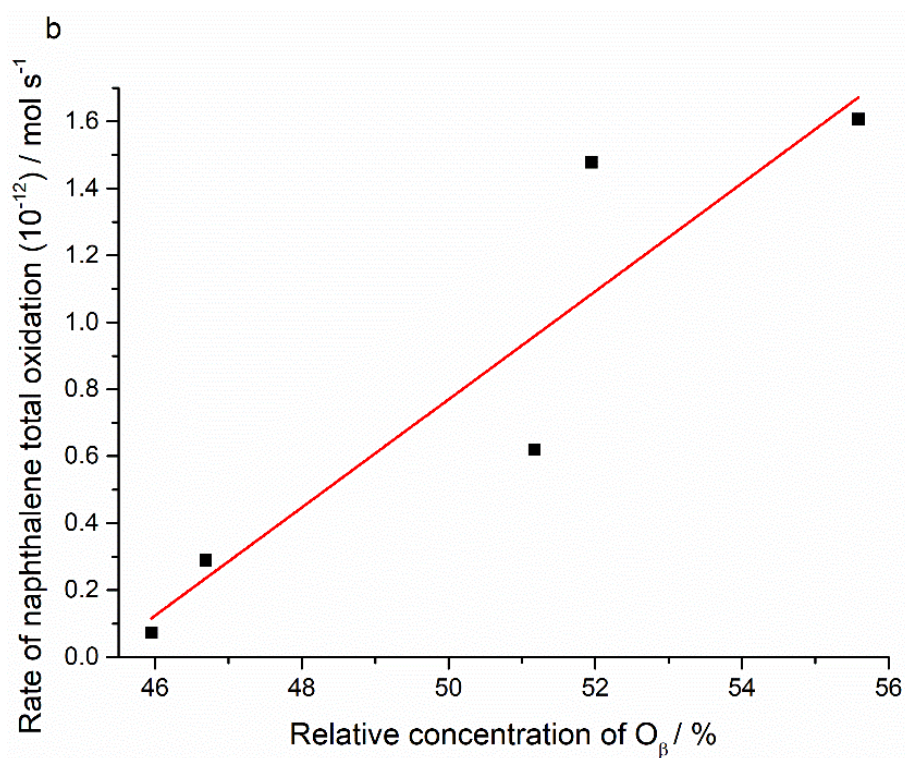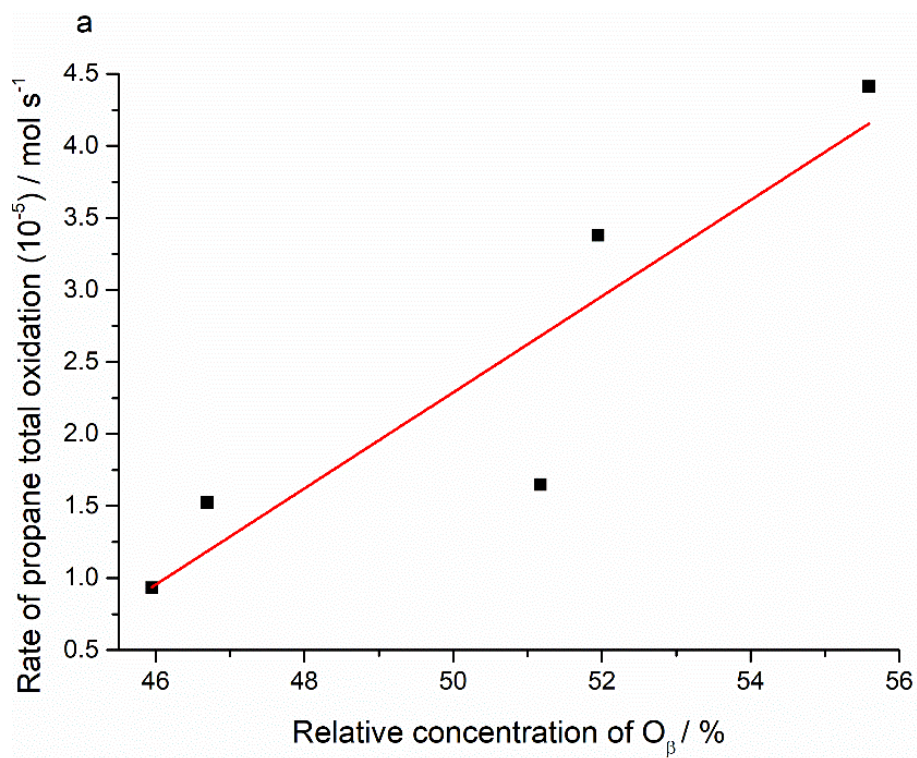
Figure 3-34: The effect of relative concentration of O_β calculated from XPS on (a) propane total oxidation activity at 350 °C and (b) on naphthalene total oxidation activity at 200 °C for the ceria-zirconia mixed metal oxide catalysts prepared using carbonate precursors

3.3.4 Stability testing of $Ce_{0.95}Zr_{0.05}O_x$ sample

3.3.4.1 Propane total oxidation

The stability of the most active ceria-zirconia mixed metal oxide catalyst prepared from carbonates, $Ce_{0.95}Zr_{0.05}O_x$, was assessed by undertaking four light off curves, Figure 3-35. All runs had high selectivity to CO_2 (> 99 %) at all reaction temperatures. However the activity significantly declined after the first reaction run. The T_{100} decreased from 450 °C to 600 °C after the second reaction run. The third and fourth run did not fully convert all the propane to carbon dioxide within the temperature range
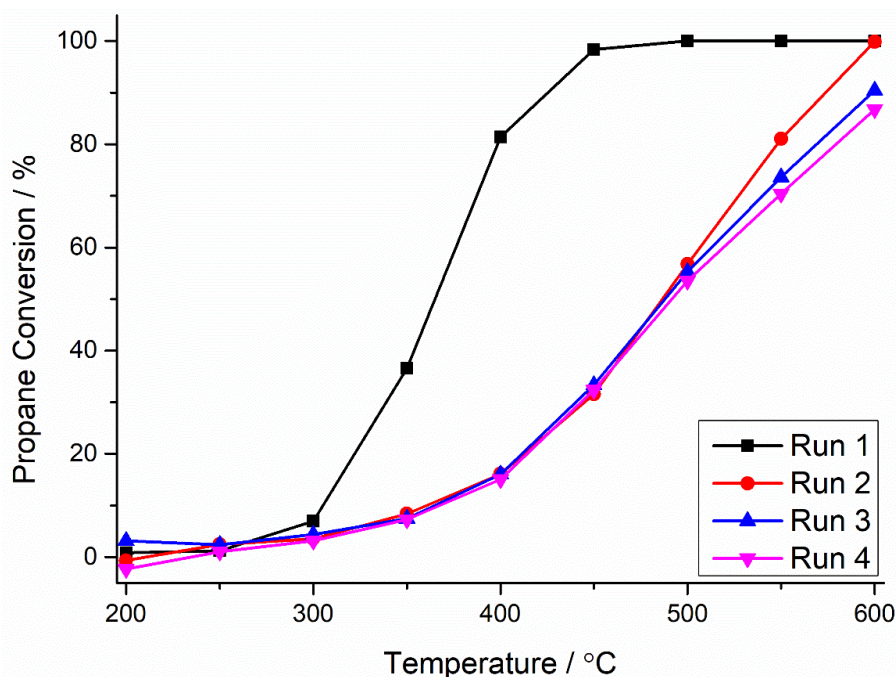
Figure 3-35: Multiple run propane total oxidation stability study of the $Ce_{0.95}Zr_{0.05}O_x$.
Temperature range: 200-600 °C, GHSV: 45,000 h^{-1}, 5000 ppm propane in air

Once again post reaction analysis of the sample was difficult to carry out. However it is noted significant phase segregation is observed at high temperatures on the ceria-zirconia mixed metal oxides during *in situ* XRD analysis. Even though only small amounts of zirconium are present in this sample, a significant amount of the zirconium is on the surface of the catalyst. This could lead to increased surface segregation of zirconium on the surface. The higher temperatures will also cause significant amounts of sintering to occur which could lead to a reduction in the surface area and increase in crystallite size. Both effects will decrease the available active sites on the surface of the catalysts and potentially decrease or block the number of oxygen defect species leading to the significant reduction in activity observed during the stability assessment of the catalyst.

3.3.4.2 Naphthalene total oxidation

The $Ce_{0.95}Zr_{0.05}O_x$ was also the most active catalyst for naphthalene total oxidation. The stability of this sample was analysed by a time on line study over a 45 hour period at 200 °C in Figure 3-36. The catalyst originally showed 100 % CO_2 yield however by 17 hours the activity had decreased to ~70 % CO_2 yield. After the initial 17 hours there was a substantial decline in the CO_2 yield as after 25 hours the CO_2 yield had decreased to ~15 %. The activity stabilised to ~8 % at the end of the 45 hour reaction run. This profile is considerably different to the one observed on the $Ce_{0.90}Zr_{0.10}O_x$ sample prepared from nitrate precursors, with this sample showing ~90 % CO_2 yield after testing at 225 °C for 60 hours

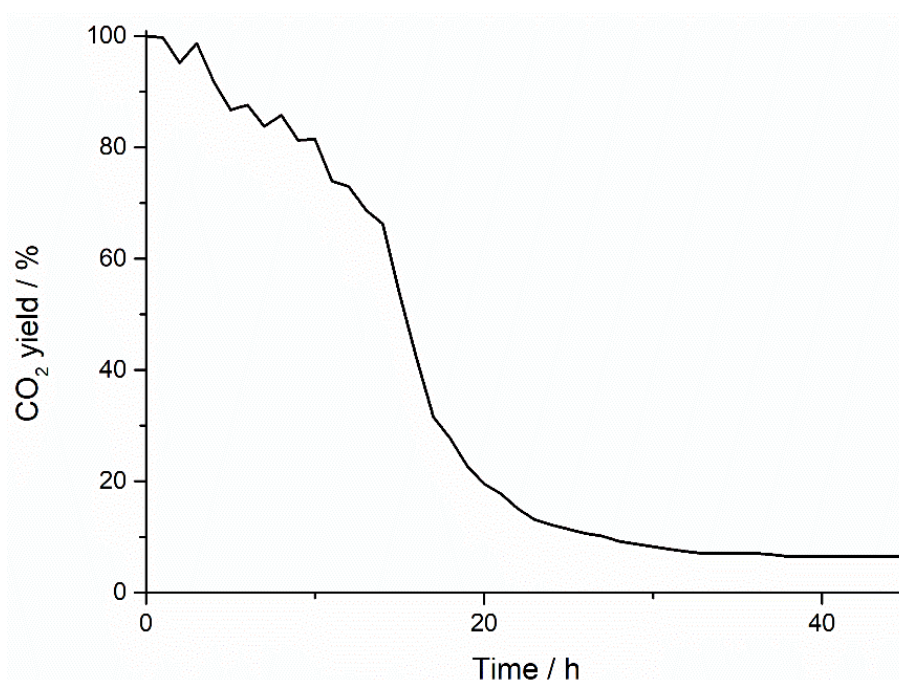Figure 3-36: Time on line naphthalene total oxidation stability study of the $Ce_{0.95}Zr_{0.05}O_x$ catalyst prepared using carbonate precursors. Reaction conditions: GHSV= 45,000 h^{-1}, 100 vppm naphthalene in 20 % O_2 balanced with He, Reaction temperature 200 °C

The catalyst surface will change over time, which may cause the adsorption of naphthalene on the surface. The structure of the surface may also change during the reaction period. This will lead to a decrease in the surface area and blockage of binding and active sites leading to a reduction in naphthalene total oxidation.

3.4 Conclusions

It has been shown that mechanochemical preparation is a viable method to synthesis ceria-zirconia mixed metal oxides from both nitrate and carbonate precursors. Synergy between

both ceria and zirconia was observed for both total oxidation reactions. However, in both cases, it was shown that small amounts of zirconium content lead to significant improvement in catalytic activity for propane and naphthalene total oxidation. The catalysts prepared from nitrates showed higher activity for naphthalene total oxidation whereas catalysts prepared from carbonates showed higher activity for propane total oxidation, when compared to the other precursor.

XRD analysis showed solid solutions were formed in all ceria-zirconia mixed metal oxide catalysts formed from nitrates. This observation was confirmed from Raman spectroscopy in which only cubic phase ceria was observed in all ceria-zirconia mixed metal oxides. However only in the $Ce_{0.95}Zr_{0.05}O_x$ and $Ce_{0.90}Zr_{0.10}O_x$ made from carbonates showed this. A shoulder peak assigned to tetragonal zirconia was observed in samples with higher zirconium content, suggesting phase separation had occurred. In all samples, the unit cell volume decreased as the zirconium content of the ceria-zirconia mixed metal oxide. However according to Vegard's law, only small portions of the zirconium had been incorporated in the samples prepared from nitrates. Samples prepared from carbonates showed significant decrease in unit cell volume implying all the zirconium had been incorporated into the ceria lattice. However, with phase separation observed at higher loading of zirconium, the unit cell contraction was assigned to the decrease of cerium present in the mixed metal oxide rather than incorporation of zirconium into the lattice.

In both sets of catalysts, the crystallite size decreased upon addition of zirconium into the ceria lattice, which led to an increase in surface area compared to the pure metal oxides. This in turn lead to an increase in the total oxidation activity however surface area normalised rates of oxidation still showed the lower zirconium content catalysts were the most active. The reducibility of ceria species were also affected by zirconium incorporation. The samples produced from nitrates all showed increased hydrogen consumption and a lowering in surface reduction temperature of ceria. Whereas the samples prepared from carbonates all showed changes in the bulk properties of the ceria with significant decrease in bulk reduction temperatures observed.

SEM studies of both ceria-zirconia mixed metal oxides catalyst systems containing low concentrations zirconia showed no phase separation between cerium and zirconium in the mixed metal oxide catalysts. Although a change in morphology was noted once zirconium had been incorporated into the ceria lattice in both sets of catalysts. SEM-EDX analysis of samples produced from carbonates displayed good agreement with XRD data in which the lower loadings of zirconium showed good mixing of both cerium and zirconia. However, in the samples with higher zirconium content, significant phase separation was

observed. This trend was also seen in the samples produced from nitrates however only the $Ce_{0.50}Zr_{0.50}O_x$ showed phase separation. Due to the potential amorphous nature of the zirconium species on the surface of the ceria-zirconia mixed metal oxides, this made it difficult to detect this from XRD and Raman analysis. TEM analysis confirms the XRD analysis, in which an array of layered crystallites are observed in all cerium containing samples. Selected area electron diffraction shows four dominant diffraction rings which are comparable to peaks in XRD. These rings are maintained in all the ceria-zirconia mixed metal oxides produced from nitrates, however, as the zirconium ratio increases in the carbonates the rings become less define and intense. This indicates phase separation had occurred. However with the diffraction patterns of ceria and zirconia being close to each other, it was difficult to distinguish which diffraction pattern was assigned to each phase.

Bulk elemental analysis of the ceria-zirconia mixed metal oxides showed ratios close to the original synthesis values indicating there was no loss of material during the ball mill process. Also in both ceria samples, no zirconium was detected suggesting no potential contamination had occurred during the catalyst preparation process. Also, no contamination from the zirconia milling material was observed during XPS analysis of the surface of both ceria materials. However the elemental composition of the surface showed substantially higher zirconium content compared to original ratios, indicating surface enrichment of zirconia. With the ratios close to the original values, the zirconium which was not incorporated in the ceria lattice may be present on the surface leading to the higher ratio observed in XPS. The amount of surface zirconium increases as the zirconium content of the ceria-zirconia mixed metal oxide increases. This will lead to more blockage of surface binding and active sites leading the decrease total oxidation activity observed as the zirconium content of the ceria-zirconia mixed metal oxides increases in both systems. Incorporation of low amounts of zirconium into the ceria lead to an increase in relative surface oxygen compared to pure ceria in both nitrate and carbonate catalyst systems. This increase corresponded with a large increase in activity of the samples indicating this was a significant factor for the increased activity.

The stability of both $Ce_{0.90}Zr_{0.10}O_x$ prepared from nitrates and $Ce_{0.95}Zr_{0.05}O_x$ prepared from carbonates was analysed for both total oxidation reactions. Both showed decreased activity after consecutive propane total oxidation reactions due to potential loss of surface area, surface oxygen species and phase separation of zirconia. Naphthalene total oxidation over both samples showed differing results with the sample prepared from nitrates showing increased stability over a 60 hour period compared to the sample

prepared from carbonates. Both showed decrease in activity over an extended period of time. However the sample prepared from nitrate only showed a decrease in 10 % CO_2 yield whereas the carbonate sample had a decrease of 90 % over the time period. Coking due to adsorption of naphthalene and loss of surface oxygen species could lead to the decrease in activity observed on these catalysts, however further investigation will need to be carried out.

3.5 References

[1] A. Trovarelli, Catalytic Properties of Ceria Materials, Catal. Rev. 38 (1996) 439–518. doi:10.1080/01614949608006464.

[2] F. Menegazzo, P. Burti, M. Signoretto, M. Manzoli, S. Vankova, F. Boccuzzi, F. Pinna, G. Strukul, Effect of the addition of Au in zirconia and ceria supported Pd catalysts for the direct synthesis of hydrogen peroxide, J. Catal. 257 (2008) 369–381. doi:10.1016/j.jcat.2008.05.019.

[3] V. Shapovalov, H. Metiu, Catalysis by doped oxides: CO oxidation by AuxCe1-xO2, J. Catal. 245 (2007) 205–214. doi:10.1016/j.jcat.2006.10.009.

[4] X.S. Huang, H. Sun, L.C. Wang, Y.M. Liu, K.N. Fan, Y. Cao, Morphology effects of nanoscale ceria on the activity of Au/CeO2 catalysts for low-temperature CO oxidation, Appl. Catal. B Environ. 90 (2009) 224–232. doi:10.1016/j.apcatb.2009.03.015.

[5] X. Zhang, H. Shi, B.Q. Xu, Comparative study of Au/ZrO2 catalysts in CO oxidation and 1,3-butadiene hydrogenation, Catal. Today. 122 (2007) 330–337. doi:10.1016/j.cattod.2007.02.016.

[6] A.T. Bell, The impact of nanoscience on heterogeneous catalysis., Science (80-.). 299 (2003) 1688–91. doi:10.1126/science.1083671.

[7] D.R. Sellick, A. Aranda, T. García, J.M. López, B. Solsona, A.M. Mastral, D.J. Morgan, A.F. Carley, S.H. Taylor, Influence of the preparation method on the activity of ceria zirconia mixed oxides for naphthalene total oxidation, Appl. Catal. B Environ. 132–133 (2013) 98–106. doi:10.1016/j.apcatb.2012.11.036.

[8] A. Bampenrat, V. Meeyoo, B. Kitiyanan, P. Rangsunvigit, T. Rirksomboon, Catalytic oxidation of naphthalene over CeO2–ZrO2 mixed oxide catalysts, Catal. Commun. 9 (2008) 2349–2352. doi:10.1016/j.catcom.2008.05.029.

[9] F. Zamar, A. Trovarelli, C. de Leitenburg, G. Dolcetti, CeO2-based solid solutions with the fluorite structure as novel and effective catalysts for methane combustion, J. Chem. Soc. Chem. Commun. 02 (1995) 965. doi:10.1039/c39950000965.

[10] H. Omidvarborna, A. Kumar, D.S. Kim, Recent studies on soot modeling for diesel combustion, Renew. Sustain. Energy Rev. 48 (2015) 635–647. doi:10.1016/j.rser.2015.04.019.

[11] A.A. Mirzaei, H.R. Shaterian, R.W. Joyner, M. Stockenhuber, S.H. Taylor, G.J. Hutchings, Ambient temperature carbon monoxide oxidation using copper manganese oxide catalysts: Effect of residual Na+ acting as catalyst poison, Catal. Commun. 4 (2003) 17–20. doi:10.1016/S1566-7367(02)00231-5.

[12] K. Ralphs, C. Hardacre, S.L. James, Application of heterogeneous catalysts prepared by mechanochemical synthesis., Chem. Soc. Rev. 42 (2013) 7701–18. doi:10.1039/c3cs60066a.

[13] A. Suda, T. Kandori, Y. Ukyo, H. Sobukawa, M. Sugiura, Room Temperature Synthesis Solid Phase of Ceria-Zirconia Reaction Solid Solution by, J. Ceram. Soc. Japan. 108 (2000) 473–477.

[14] I.A. Carbajal-Ramos, J. Andrade-Gamboa, F.C. Gennari, Nanostructured Ce1-

xZrxO2 solid solutions produced by mechanochemical processing, Mater. Chem. Phys. 137 (2013) 1073–1080. doi:10.1016/j.matchemphys.2012.11.039.

[15] D. Devaiah, L.H. Reddy, S.-E. Park, B.M. Reddy, Ceria–zirconia mixed oxides: Synthetic methods and applications, Catal. Rev. 60 (2018) 177–277. doi:10.1080/01614940.2017.1415058.

[16] M. Teng, L. Luo, X. Yang, Synthesis of mesoporous Ce1-xZrxO2 (x = 0.2-0.5) and catalytic properties of CuO based catalysts, Microporous Mesoporous Mater. 119 (2009) 158–164. doi:10.1016/j.micromeso.2008.10.019.

[17] F. Zhang, C.-H. Chen, J.C. Hanson, R.D. Robinson, I.P. Herman, S.-W. Chan, Phases in Ceria-Zirconia Binary Oxide (1-x)CeO2-xZrO2 Nanoparticles: The Effect of Particle Size, J. Am. Ceram. Soc. 89 (2006) 1028–1036. doi:10.1111/j.1551-2916.2005.00788.x.

[18] R. Grau-Crespo, N.H. de Leeuw, S. Hamad, U. V. Waghmare, Phase separation and surface segregation in ceria-zirconia solid solutions, Proc. R. Soc. A Math. Phys. Eng. Sci. 467 (2011) 1925–1938. doi:10.1098/rspa.2010.0512.

[19] R. Di Monte, J. Kašpar, Nanostructured CeO $_2$ –ZrO $_2$ mixed oxides, J. Mater. Chem. 15 (2005) 633–648. doi:10.1039/B414244F.

[20] X.-W. Zhang, S.-C. Shen, L.E. Yu, S. Kawi, K. Hidajat, K.Y. Simon Ng, Oxidative Decomposition of Naphthalene by Supported Metal Catalysts, Appl. Catal. A Gen. 250 (2003) 341–352. doi:10.1016/S0926-860X(03)00412-5.

[21] R. Yang, L. Guo, Synthesis of the Nanotublar Cubic Fluorite CeO2, J. Mater. Sci. 40 (2005) 1305–1307. doi:10.1007/s10853-005-6958-5.

[22] L. Chen, T. Mashimo, E. Omurzak, H. Okudera, C. Iwamoto, A. Yoshiasa, Pure tetragonal ZrO2 nanoparticles synthesized by pulsed plasma in liquid, J. Phys. Chem. C. 115 (2011) 9370–9375. doi:10.1021/jp111367k.

[23] S. Damyanova, B. Pawelec, K. Arishtirova, M.V.M. Huerta, J.L.G. Fierro, Study of the surface and redox properties of ceria-zirconia oxides, Appl. Catal. A Gen. 337 (2008) 86–96. doi:10.1016/j.apcata.2007.12.005.

[24] G. Katz, X-Ray Diffraction Powder Pattern of Metastable Cubic ZrO2, J. Am. Ceram. Soc. 54 (1971) 531–531. doi:10.1111/j.1151-2916.1971.tb12197.x.

[25] L. Ahrens, The use of ionization potentials Part 1. Ionic radii of the elements, Geochim. Cosmochim. Acta. 2 (1952) 155–169. doi:10.1016/0016-7037(52)90004-5.

[26] A. Chen, Y. Zhou, N. Ta, Y. Li, W. Shen, Redox properties and catalytic performance of ceria–zirconia nanorods, Catal. Sci. Technol. 5 (2015) 4184–4192. doi:10.1039/C5CY00564G.

[27] G. Vlaic, R. Di Monte, P. Fornasiero, E. Fonda, J. Kašpar, M. Graziani, Redox Property–Local Structure Relationships in the Rh-Loaded CeO2–ZrO2Mixed Oxides, J. Catal. 182 (1999) 378–389. doi:10.1006/jcat.1998.2335.

[28] L. Vegard, The constitution of the mixed crystals and the filling of the atoms, J. Phys. 5 (1921) 17–26.

[29] C. Bozo, F. Gaillard, N. Guilhaume, Characterisation of ceria-zirconia solid solutions after hydrothermal ageing, Appl. Catal. A Gen. 220 (2001) 69–77. doi:10.1016/S0926-860X(01)00710-4.

[30] A. Hirano, A. Suda, Oxygen Storage Capacity, Specific Surface Area, and Pore-Size Distribution of Ceria–Zirconia Solid Solutions Directly Formed by Thermal Hydrolysis, J. Am. Ceram. Soc. 11 (2003) 2209–2211.

[31] S.T. Aruna, K.C. Patil, Combustion Synthesis and Properties of Nanostructured Ceria-Zirconia Solid Solutions, 10 (1998) 955–964.

[32] T. Garcia, B. Solsona, S.H. Taylor, Nano-crystalline Ceria Catalysts for the Abatement of Polycyclic Aromatic Hydrocarbons, Catal. Letters. 105 (2005) 183–189. doi:10.1007/s10562-005-8689-2.

[33] Z. Wu, M. Li, J. Howe, H.M.M. Iii, S.H. Overbury, Probing Defect Sites on CeO 2 Nanocrystals with Well-Defined Surface Planes by Raman Spectroscopy and O 2 Adsorption †, Langmuir. 104 (2010) 16595–16606. doi:10.1021/la101723w.

[34] J.E. Spanier, R.D. Robinson, F. Zhang, S.-W. Chan, I.P. Herman, Size-dependent properties of CeO2-y nanoparticles as studied by Raman scattering, Phys. Rev. B. 64 (2001) 245407. doi:10.1103/PhysRevB.64.245407.

[35] I. Kosacki, T. Suzuki, H.U. Anderson, P. Colomban, Raman scattering and lattice defects in nanocrystalline CeO 2 thin films, Solid State Ionics. 149 (2002) 99–105.

[36] H. Du, T. Wan, B. Qu, J. Scott, X. Lin, A. Younis, D. Chu, Tailoring the multi-functionalities of one-dimensional ceria nanostructures via oxygen vacancy modulation, J. Colloid Interface Sci. 504 (2017) 305–314. doi:10.1016/j.jcis.2017.05.057.

[37] B.B. Harrison, A.F. Diwell, C. Hallett, Promoting Platinum Metals by Ceria - metal-support interactions in autocatalysts, Platin. Met. Rev. (1988) 73–83.

[38] H.C. Yao, Y.F.Y. Yao, Ceria in automotive exhaust catalysts. I. Oxygen storage, J. Catal. 86 (1984) 254–265. doi:10.1016/0021-9517(84)90371-3.

[39] J.M. Pigos, C.J. Brooks, G. Jacobs, B.H. Davis, Low temperature water-gas shift: Characterization of Pt-based ZrO2 catalyst promoted with Na discovered by combinatorial methods, Appl. Catal. A Gen. 319 (2007) 47–57. doi:10.1016/j.apcata.2006.11.014.

[40] M. Thammachart, V. Meeyoo, T. Risksomboon, S. Osuwan, Catalytic activity of CeO 2 – ZrO 2 mixed oxide catalysts prepared via sol – gel technique : CO oxidation, Catal. Today. 68 (2001) 53–61. doi:10.1016/S0920-5861(01)00322-4.

[41] S. Bedrane, C. Descorme, D. Duprez, Investigation of the oxygen storage process on ceria- and ceria-zirconia-supported catalysts, Catal. Today. 75 (2002) 401–405. doi:10.1016/S0920-5861(02)00089-5.

[42] M. Boaro, The Dynamics of Oxygen Storage in Ceria–Zirconia Model Catalysts Measured by CO Oxidation under Stationary and Cycling Feedstream Compositions, J. Catal. 193 (2000) 338–347. doi:10.1006/jcat.2000.2887.

[43] E. Ntainjua N., S.H. Taylor, The Catalytic Total Oxidation of Polycyclic Aromatic Hydrocarbons, Top. Catal. 52 (2009) 528–541. doi:10.1007/s11244-009-9180-x.

[44] K. Alexopoulos, M. Anilkumar, H. Poelman, S. Cristol, V. Balcaen, P.M. Heynderickx, D. Poelman, G.B. Marin, Time-resolved operando X-ray absorption study of CuO – CeO 2 / Al 2 O 3 catalyst during total oxidation of propane, 97 (2010) 381–388. doi:10.1016/j.apcatb.2010.04.022.

[45] J.E. Bailey, The Monoclinic-Tetragonal Transformation and Associated Twinning in Thin Films of Zirconia, Proc. R. Soc. A Math. Phys. Eng. Sci. 279 (1964) 395–412. doi:10.1098/rspa.1964.0112.

[46] E. Beche, P. Charvin, D. Perarnau, S. Abanades, G. Flamant, Ce 3d XPS investigation of cerium oxides and mixed cerium oxide (Ce x Ti y O z) ∗, Surf. Interface Anal. 40 (2008) 264–267. doi:10.1002/sia.2686.

[47] A. Galtayries, R. Sporken, J. Riga, G. Blanchard, R. Caudano, XPS comparative study of ceria/zirconia mixed oxides: powders and thin film characterisation, J. Electron Spectros. Relat. Phenomena. 88–91 (1998) 951–956. doi:10.1016/S0368-2048(97)00134-5.

[48] E.N. Ntainjua, T.E. Davies, T. Garcia, B. Solsona, S.H. Taylor, Influence of preparation conditions of nano-crystalline ceria catalysts on the total oxidation of naphthalene, a model polycyclic aromatic hydrocarbon, Catal. Letters. 141 (2011) 1732–1738. doi:10.1007/s10562-011-0710-3.

[49] A. Aranda, E. Aylón, B. Solsona, R. Murillo, A.M. Mastral, D.R. Sellick, S. Agouram, T. García, S.H. Taylor, High activity mesoporous copper doped cerium oxide catalysts for the total oxidation of polyaromatic hydrocarbon pollutants,

Chem. Commun. 48 (2012) 4704. doi:10.1039/c2cc31206a.

[50] C. Padeste, N.W. Cant, D.L. Trimm, Thermal decomposition of pure and rhodium impregnated cerium(III) carbonate hydrate in different atmospheres, Catal. Letters. 24 (1994) 95–105. doi:10.1007/BF00807379.

[51] Y.X. Li, X.Z. Zhou, Y. Wang, X.Z. You, Preparation of nano-sized CeO2 by mechanochemical reaction of cerium carbonate with sodium hydroxide, Mater. Lett. 58 (2004) 245–249. doi:10.1016/S0167-577X(03)00454-3.

[52] M. Kurian, C. Kunjachan, Investigation of size dependency on lattice strain of nanoceria particles synthesised by wet chemical methods, Int. Nano Lett. 4 (2014) 73–80. doi:10.1007/s40089-014-0122-7.

[53] C.E. Hori, H. Permana, K.Y.S. Ng, A. Brenner, K. More, K.M. Rahmoeller, D. Belton, Thermal stability of oxygen storage properties in a mixed CeO2-ZrO2 system, Appl. Catal. B-Environmental. 16 (1998) 105–117. doi:10.1016/s0926-3373(97)00060-x.

[54] M. Yashima, K. Morimoto, N. Ishizawa, M. Yoshimura, Zirconia–Ceria Solid Solution Synthesis and the Temperature–Time–Transformation Diagram for the 1:1 Composition, J. Am. Ceram. Soc. 76 (1993) 1745–1750. doi:10.1111/j.1151-2916.1993.tb06643.x.

[55] S. Deshpande, S. Patil, S.V. Kuchibhatla, S. Seal, Size dependency variation in lattice parameter and valency states in nanocrystalline cerium oxide, Appl. Phys. Lett. 87 (2005) 1–3. doi:10.1063/1.2061873.

[56] A. Trovarelli, P. Fornasiero, Catalysis by Ceria and Related Materials, 2nd ed., Imperial College Press, 2013.

[57] S.. Maity, M.. Rana, B.. Srinivas, S.. Bej, G. Murali Dhar, T.S.. Prasada Rao, Characterization and evaluation of ZrO2 supported hydrotreating catalysts, J. Mol. Catal. A Chem. 153 (2000) 121–127. doi:10.1016/S1381-1169(99)00311-8.

[58] D.S.S. Padovini, D.S.L. Pontes, C.J. Dalmaschio, F.M. Pontes, E. Longo, Facile synthesis and characterization of ZrO2 nanoparticles prepared by the AOP/hydrothermal route, RSC Adv. 4 (2014) 38484–38490. doi:10.1039/c4ra04861j.

4 The effect of Ce:Mn ratio and preparation method of ceria-manganese mixed metal oxides for the total oxidation of VOCs

4.1 Introduction

The high cost and increasing rarity of components for supported noble metal catalysts has led to a shift away from these materials for VOC total oxidation. As seen from the previous results chapter, ceria is noted to have favourable properties to produce active catalysts for VOC total oxidation. Along with zirconia, other metal oxides have also been investigated for naphthalene total oxidation. Manganese oxides were also noted to have high naphthalene total oxidation activity [1]. Like ceria, manganese oxides can change between oxidation states leading to high oxygen mobility and surface defect sites [2]. Further studies showed manganese oxides present as Mn_2O_3 rather than MnO_2 produce catalysts with high naphthalene total oxidation activity [3].

Several studies have shown synergy between cerium and manganese metal oxides for pollutant control by total oxidation. The higher activity of the mixed metal oxides are ascribed to an electron rich surface, which can activate adsorbed oxygen species. Cerium and manganese mixed metal oxides with equal Ce:Mn ratios have been reported to be active for oxidation of small molecules such as NO [4,5] and CO [6,7] as well as larger molecules such as ethanol [8,9], while cerium manganese mixed metal oxides with low Ce:Mn ratios have shown high activity for the oxidation of aromatic VOCs, such as phenol [10,11] and toluene [12,13]. Notable activity is reported for naphthalene total oxidation on both ceria [14] and manganese oxides [3] and with synergy observed for total oxidation for other aromatic VOCs, it will be interesting to see if there is any synergy for the naphthalene and propane total oxidation reactions.

Co-precipitation is the most prevalent method used to produce cerium-manganese mixed metal oxides. Using this method, a range of precipitating agents can be used to synthesise the catalyst. Previous studies which prepared manganese containing mixed metal oxides, have used sodium carbonate [15], so this will be the precipitating agent of choice during this investigation. However, as mentioned in previous studies, sodium containing precipitating agents lead to surface poisons causing decreased activity due to blocking of active sites. To investigate the effect of sodium on the final catalyst, the effect of washing will also be studied. Following this a range of traditional sodium free methods will be

used to prepare catalysts. All cerium-manganese mixed metal oxides will be characterised by a range of bulk and surface methods. Finally, the stability of the most active sample for both propane and naphthalene total oxidation will be studied.

4.2 The effects of Ce:Mn ratios on cerium-manganese mixed metal oxide catalysts

For the catalysts in the study of Ce:Mn ratios, the catalysts were precipitated from a 0.25 M premixed solution of cerium and manganese nitrates. A 1 M sodium carbonate solution was used as the precipitating agent. The solution was aged at 60 °C at pH 9 for 2 hours. The precipitate was filtered and washed with 1 l of warm water and dried for 16 hours at 110 °C. The solid was then calcined at 500 °C for 3 hours under flowing air.

4.2.1 Precursor Characterisation

4.2.1.1 Thermal gravimetric analysis
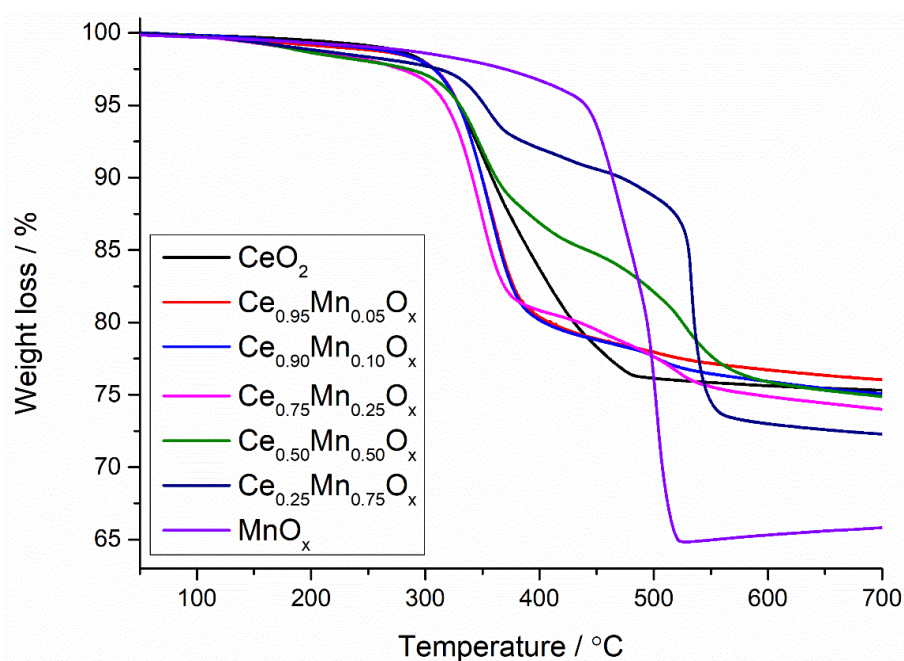
Figure 4-1: Thermogravimetric analysis of all the dried cerium-manganese mixed metal oxide catalysts prepared by coprecipitation with sodium carbonate. Samples heated in a flowing N_2 atmosphere from 30 to 700 ºC at a ramp rate of 5 ºC min^{-1}

The decomposition profiles of the pre-calcined cerium-manganese mixed metal oxides are shown in Figure 4-1. No weight loss events are noted below 300 °C in any of the decomposition profiles. This suggests the 16 hour drying period has successfully removed any water or hydroxide groups from the samples. The decomposition profile of the ceria has one significant weight loss event starting at 350 °C, accounting for a 25 % loss in weight. This suggests the cerium nitrate is converted into cerium carbonate, as only one

120

weight loss event was observed, unlike the TGA profiles seen for the ceria-zirconia ball mill results (Chapter 3), in which multiple weight loss events were noted. The manganese oxide sample also only has one weight loss event during its decomposition. This weight loss occurs over a very short temperature range, 470-500 °C and accounts for a 35 % weight loss. This profile is very similar to decomposition of manganese carbonate [16] suggesting the manganese nitrate has been converted into manganese carbonates during the precipitation process.

The decomposition profiles of the $Ce_{0.95}Mn_{0.05}O_x$, $Ce_{0.90}Mn_{0.10}O_x$ and $Ce_{0.75}Mn_{0.25}O_x$ precursors are similar to the profile of ceria and have a weight loss of ~20 %. The end of the weight loss event was shifted by ~60 °C compared to the ceria, suggesting the small amounts of manganese has affected the decomposition of the precursors. The profiles of the $Ce_{0.50}Mn_{0.50}O_x$ and $Ce_{0.25}Mn_{0.75}O_x$ have two weight loss regions, starting at 350 °C and 500 °C. The decomposition profiles of these samples seem to be additive of both cerium and manganese carbonate decomposition. This suggests the cerium and manganese are not as well mixed as the samples with higher cerium content.
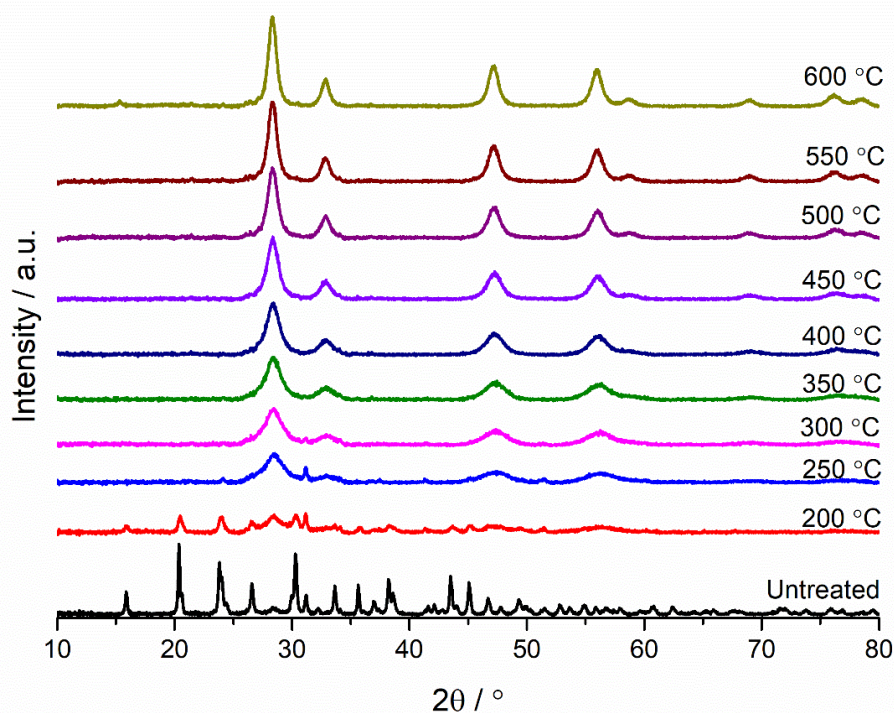
4.2.1.2 *In situ* XRD

Figure 4-2: In situ powder X-ray diffraction patterns of the dried $Ce_{0.50}Mn_{0.50}O_x$ precursor with increasing temperature. Reaction conditions: temperature range 200- 600 °C under a flow of 30 ml min^{-1} air. 10 minute scan duration

In situ XRD analysis was undertaken to understand the effects of calcination in flowing air on the decomposition of the cerium-manganese carbonate precursors, Figure 4-2. The

dried $Ce_{0.50}Mn_{0.50}O_x$ precursor was used as a representative material for this. There were many reflections identifying the presence of cerium carbonate and manganese carbonate in the pattern of the untreated $Ce_{0.50}Mn_{0.50}O_x$ sample, with no reflections attributed to the cerium or manganese hydroxide species, confirming the findings from TGA. The intensity of the reflections decrease as the sample is heated to 200 °C. This suggests the decomposition of the precursors has commenced, as seen by the small weight loss observed at the start of the TGA profile of this sample.

As the temperature was increased to 250 °C, four observable reflections appear indicating the formation of the cubic fluorite ceria phase. A small number of low intensity reflections are observable, suggesting the manganese carbonates are starting to decompose to form manganese oxides. These reflections disappeared once the temperature was above 300 °C and were not observed within the temperature range. The reflections assigned to cubic ceria become more intense as the temperature is increased. This indicates the ceria is sintering at higher temperatures causing the crystallite size to increase. However, with no reflections observed from manganese oxides, this suggests phase separation has not occurred within the temperature range.

Following analysis of TGA and *in situ* XRD, a calcination temperature of 500 °C was used to prepare the final cerium-manganese mixed metal oxide catalyst. This was to allow the carbonates to become fully decomposed and to minimise phase separation between ceria and manganese oxides.

4.2.2 Catalyst performance for VOC total oxidation

4.2.2.1 Propane total oxidation

The activity of propane total oxidation over the cerium-manganese mixed metal oxides is shown in Figure 4-3. All samples showed appreciable activity for propane total oxidation and high carbon dioxide selectivity (>99 %). The error of catalysts prepared using auto-titration for propane total oxidation was 3 %. The ceria was only able to convert ~80 % of the propane within the temperature range. This was significantly lower than the activity of the ceria prepared from *via* mechanochemical grinding of cerium nitrates and carbonates. The preparation method used to synthesise ceria [17,18] has a significant effect on the activity of ceria for VOC total oxidation and this effect may cause the difference in activity observed between the ceria samples. The propane total oxidation activity of the manganese oxide sample was considerably higher than the ceria sample with 100 % propane conversion observed at 500 °C. Manganese oxides are noted to have

higher total oxidation activity than ceria for a range of VOCs including ethanol, ethyl acetate, toluene [19] and propane [20].
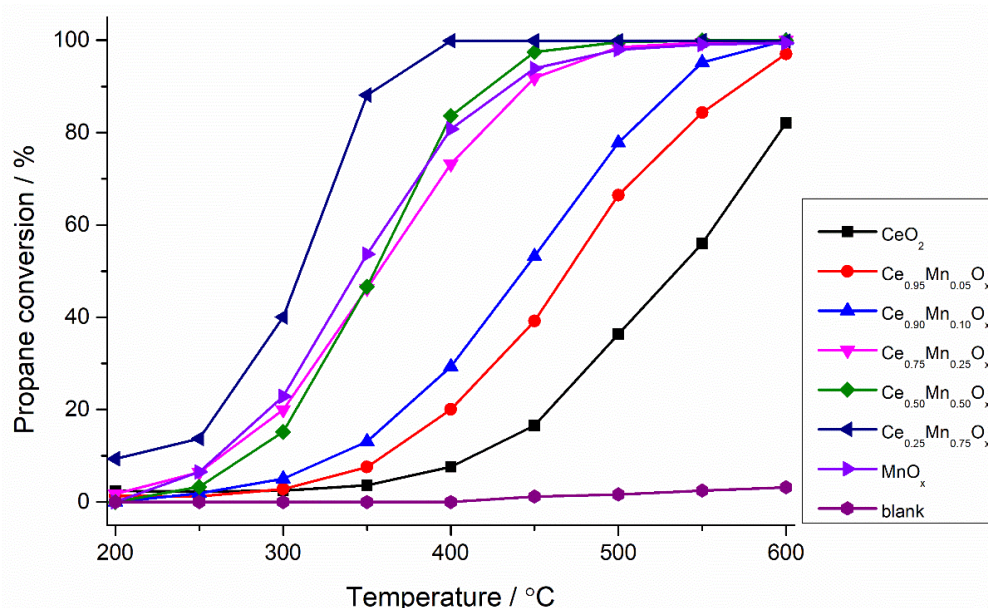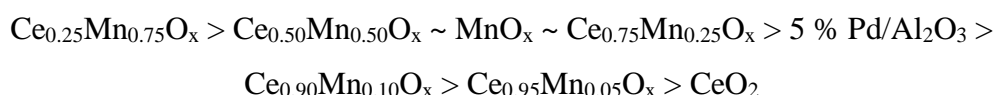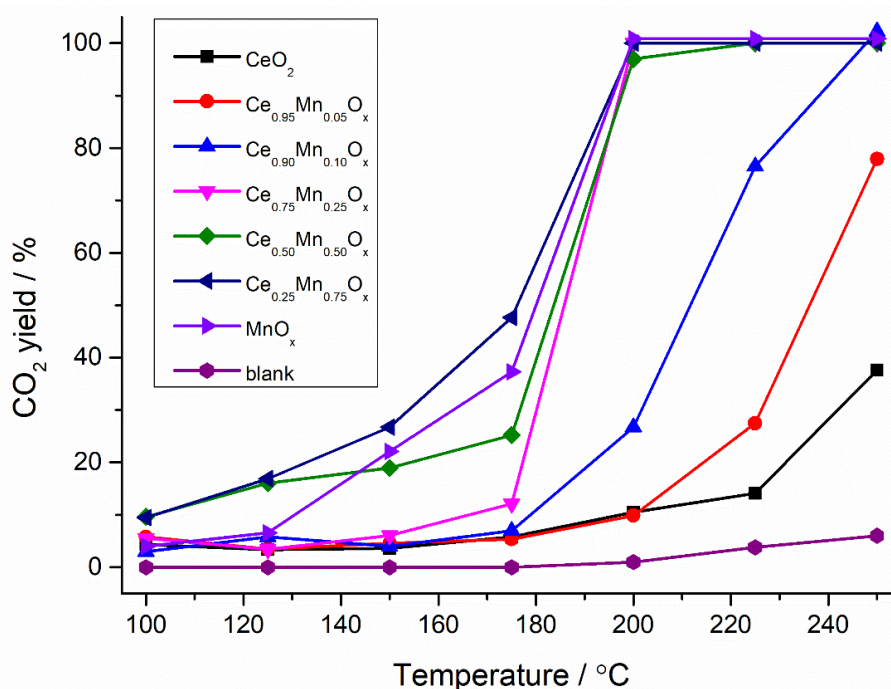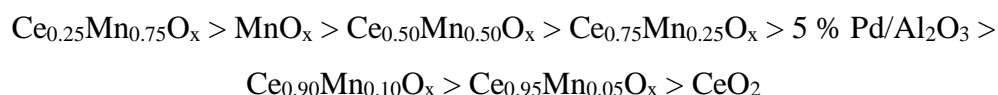

Figure 4-3: Catalytic activities for the total oxidation of propane for the cerium-manganese mixed metal oxide catalysts prepared *via* co-precipitation with sodium carbonate . Reaction conditions: GHSV = 45,000 h^{-1}, temperature range 200-600 °C, 5000 ppm propane in air. Legend refers to the different Ce-Mn ratios

Upon addition of manganese into the ceria, there was a visible increase in propane total oxidation activity. All the catalysts containing high concentrations of manganese performed significantly better than the reference catalyst for propane total oxidation. As the manganese content of the mixed metal oxide increased there was a significant increase in activity which followed the general trend:

$$Ce_{0.25}Mn_{0.75}O_x > Ce_{0.50}Mn_{0.50}O_x \sim MnO_x \sim Ce_{0.75}Mn_{0.25}O_x > 5\ \%\ Pd/Al_2O_3 >$$

$$Ce_{0.90}Mn_{0.10}O_x > Ce_{0.95}Mn_{0.05}O_x > CeO_2$$

4.2.2.2 Naphthalene total oxidation

The naphthalene total oxidation activity of the cerium-manganese mixed metal oxides is shown in Figure 4-4. All reactions showed appreciable activity during the experiments, however, the carbon balance varied during the initial temperatures. This could be due to the ceria's ability to adsorb naphthalene below 200 °C [18] leading to deviations in the carbon balance. The error for naphthalene total oxidation over catalysts prepared using auto-titrator was ~4 %. However, no partial oxidation products were observed, indicating only the total oxidation pathway occurred during catalyst testing. The ceria had the lowest naphthalene total oxidation activity of the samples tested, with only 35 % carbon dioxide yield at 250 °C. Variation in total oxidation activity between the ceria prepared *via*

mechanochemical grinding and autotitration were also observed during this reaction. The ceria sampled tested above had higher activity than the ceria mechanochemically prepared from nitrates but lower than the sample mechanochemically prepared from carbonates. As mentioned above, the preparation method has a significant effect naphthalene total oxidation. The calcination temperature used to form ceria also has an effect on total oxidation activity [14]. It was noted that when ceria was prepared using urea as a precipitating agent, that higher calcination temperatures produced catalysts more active for naphthalene total oxidation. As the ceria prepared *via* autotitration calcined at 500 °C, which may lead to the difference in activity observed between the different preparation methods.

Figure 4-4: Catalytic activities for the total oxidation of naphthalene for the cerium-manganese mixed metal oxide catalysts prepared *via* co-precipitation with sodium carbonate . Reaction conditions: GHSV: 45,000 h^{-1}, Temperature range 100-250 °C, 100 vppm naphthalene in 20 % O_2 balanced with He. Legend refers to the different Ce-Mn ratios

The manganese oxide had substantially higher naphthalene total oxidation activity compared to the ceria, with 100 % CO_2 yield observed at 200 °C. When cerium and manganese oxides were mixed together, a noticeable increase in naphthalene total oxidation was observed, with activity increasing as the manganese content increased. As seen in the propane total oxidation over these catalysts, the ceria-manganese mixed metal oxides containing high concentrations of manganese performed better than the reference

catalyst. This lead to a similar trend from propane total oxidation over the cerium-manganese mixed metal oxides were observed for naphthalene total oxidation:

$$Ce_{0.25}Mn_{0.75}O_x > MnO_x > Ce_{0.50}Mn_{0.50}O_x > Ce_{0.75}Mn_{0.25}O_x > 5\ \%\ Pd/Al_2O_3 >$$

$$Ce_{0.90}Mn_{0.10}O_x > Ce_{0.95}Mn_{0.05}O_x > CeO_2$$

4.2.3 Catalyst characterisation

4.2.3.1 X-ray diffraction

The XRD patterns of the ceria-manganese mixed metal oxides and parent oxides are presented in Figure 4-5, with corresponding derived data in Table 4-1. No characteristic reflections from sodium carbonate [21] were observed in any of the patterns. This suggests the washing and calcination has removed any bulk sodium carbonates. However the sodium may be present in the amorphous phase or incorporated into the lattice of the mixed metal oxide. Ceria prepared *via* autotitration had four main reflections in its XRD pattern which are characteristic of cubic fluorite phase ceria. The manganese oxide can be present in a variety of phases. Characteristic reflections of MnO_2 can be observed at 29 °, 39 °, 57 °, and 74 ° [22]. Reflections at 32 °, 37 ° 44 ° and 52 ° indicate the presence of Mn_2O_3 and reflections at 33 °, 38 ° and 56 ° indicate the presence of Mn_3O_4 [23]. Most of the reflections of the manganese oxide are attributed to the Mn_2O_3, with the other reflections ascribed to MnO_2.
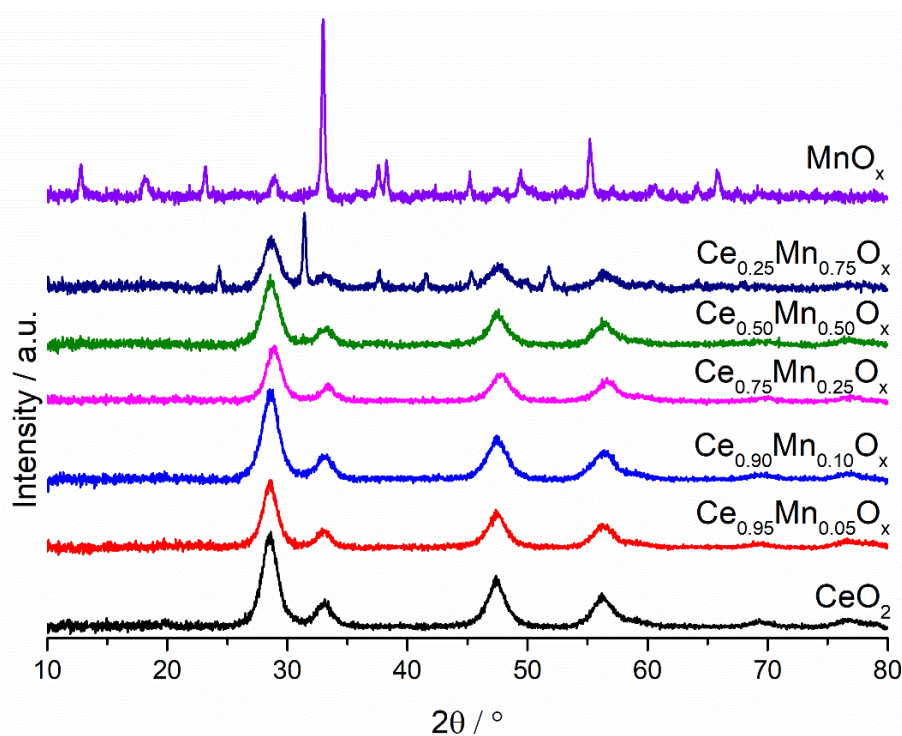

Figure 4-5: Powder XRD patterns of the calcined cerium-manganese mixed metal oxide catalysts prepared co-precipitation with sodium carbonate

Examination of the ceria-manganese mixed metal oxide patterns, apart from the $Ce_{0.25}Mn_{0.75}O_x$, only had reflections from cubic ceria. The $Ce_{0.25}Mn_{0.75}O_x$ has the lowest intensity ceria reflections of the series of catalysts, as well as additional reflections centred at 32 °, 37 ° and 52 °. These indicate the presence of bulk Mn_2O_3. The formation of phase separated mixed metal oxides has been reported in previous studies, in which cerium-manganese mixed metal oxides were produced from coprecipitation ammonium hydroxide [24]. Bulk Mn_2O_3 is reported to be more active for naphthalene total oxidation. The increased presence of this phase in the $Ce_{0.25}Mn_{0.75}O_x$ sample may lead to the higher activity for the total oxidation of propane and naphthalene compared to the manganese oxides.

The intensity of the ceria-like reflections decreases as the manganese content of the ceria-manganese mixed metal oxide increases. Table 4-1. Along with this, the position of the cubic ceria (111) peak shifts to higher angles as the manganese content of the cerium-manganese mixed metal oxide increases. With these observations, as well as no discrete reflections from manganese oxides, this suggests a cerium-manganese solid solution has been formed in the bulk of these samples. However when the manganese content is more than the cerium content in cerium-manganese mixed metal oxides, phase separation between the two metal oxides occurs. This has also been observed in cerium-manganese mixed metal oxides produced *via* co-precipitation using ammonium hydroxide solution as a precipitating agent [10,25].

Table 4-1: Physical properties of the cerium-manganes mixed metal oxide catalysts prepared co-precipitation with sodium carbonate from XRD

Sample	Phases present	Position of CeO_2 (111) reflection / °	Average crystallite size / Å		d-spacing from (200) lattice plane / Å	Unit Cell Volume / Å³
			CeO_2	MnO_x		
CeO_2	CeO_2	28.6	106	-	2.74	164.567
$Ce_{0.95}Mn_{0.05}O_x$	CeO_2	28.7	47	-	2.72	160.989
$Ce_{0.90}Mn_{0.10}O_x$	CeO_2	28.7	43	-	2.71	159.220
$Ce_{0.75}Mn_{0.25}O_x$	CeO_2	29.0	63	-	2.70	157.464
$Ce_{0.50}Mn_{0.50}O_x$	CeO_2	28.8	60	-	2.68	153.991
$Ce_{0.25}Mn_{0.75}O_x$	CeO_2 Mn_2O_3	28.8	41	152	2.69	155.721
MnO_x	MnO_2 Mn_2O_3	-	-	361	-	-

Using the (200) reflection from the ceria phase, the d-spacings and unit cell volume has been calculated, Table 4-1. The ceria had the highest d-spacing from all ceria containing mixed metal oxide samples and this value decreased as the manganese content increased. As the ionic radius of the manganese is smaller than the cerium, 0.53Å and 1.14 Å respectively [26]. With increasing substitution of manganese into the ceria lattice, this will cause contraction of the lattice leading to smaller d-spacing. The smaller d-spacing will lead to a contraction of the unit cell leading to the decrease in unit cell volume observed.

The average crystallite size of ceria, calculated from the four dominant reflections of each phase, significantly decreased upon addition of manganese into the ceria lattice. Addition of any amount of manganese into the ceria lattice led to a ~50 % decrease in crystallite size compared to the ceria sample. This large decrease in crystallite size has been observed in ceria-manganese mixed metal oxides prepared *via* citric acid [27]. It is reported that manganese inhibits ceria crystallite growth [4]. With all ceria crystallite sizes of the manganese containing mixed metal oxides being of similar size, this suggests that any amount of manganese can lead to inhibition of crystal growth. Only $Ce_{0.25}Mn_{0.75}O_x$ had observable peaks from manganese oxide phases. The presence of manganese oxide phases with higher activity explains the increased activity of the $Ce_{0.25}Mn_{0.75}O_x$ sample compared to the MnO_x.

4.2.3.2 Surface Area

Table 4-2: Surface area of the ceria-manganese mixed metal oxide catalysts prepared co-precipitation with sodium carbonate. Calculated using the 5-point N_2 adsorption BET analysis

Sample	BET Surface area / $m^2\,g^{-1}$	Surface area normalised rate of propane total oxidation at 350 °C (10^{-7}) / $mol\,s^{-1}\,m^{-2}$	Surface area normalised rate of naphthalene total oxidation at 175 °C (10^{-11}) / $mol\,s^{-1}\,m^{-2}$
CeO_2	21	0.06	0.45
$Ce_{0.95}Mn_{0.05}O_x$	29	0.09	0.31
$Ce_{0.90}Mn_{0.10}O_x$	29	0.16	0.40
$Ce_{0.75}Mn_{0.25}O_x$	34	0.47	0.59
$Ce_{0.50}Mn_{0.50}O_x$	39	0.41	1.07
$Ce_{0.25}Mn_{0.75}O_x$	41	0.74	1.93
MnO_x	18	1.03	3.44

Surface areas calculated using the BET method, of the ceria-manganese mixed metal oxides are shown in Table 4-2. The ceria and manganese oxide had the lowest surface area and the combination of both components lead to a significant increase compared to

the parent oxides. The surface area increased as the manganese content of the ceria-manganese mixed metal oxide increased. Lower loadings of manganese had a ~50 % increase and higher loadings of manganese had a ~ 100% increase in surface area. There is non-linear trend between surface area increase and decrease in the crystallite size of the ceria.

The surface area normalised propane and naphthalene total oxidation rates are shown in Table 4-2. The ceria produced *via* autotitration had significanlty higher surface area normalised naphthalene total oxidation compared to both of the mechanochemically prepared ceria samples. However the surface area normalised rates for propane total oxidation are higher on the mechanochemically prepared ceria compared to the auto-titrated ceria. The normalised rates showed a variety of values between the catalysts, indicating that there is no direct relationship between surface area and activity. Therefore other factors have to be considered for the increased catalyst performance of the mixed metal oxides.

4.2.3.3 Raman spectroscopy

The Raman spectra of the ceria-manganese mixed metal oxides and further derived data are shown in Figure 4-6 and Table 4-3. Two peaks were observed in spectra of ceria, a peak with high intensity at 464 cm^{-1} and a peak with low intensity at 600 cm^{-1}. These are the Raman modes for cubic fluorite ceria and Frenkel-type oxygen vacancies respectively. Due to the nature of the manganese oxide, it was difficult to detect any peaks during Raman analysis of the sample. The ceria-manganese mixed metal oxide samples only had two peaks at 464 cm^{-1} and 600 cm^{-1} confirming the cubic fluorite ceria observed during XRD analysis. However, as the as the manganese content of the mixed metal oxides increased above 50 % it was difficult to detect these peaks. As the manganese content of the ceria-manganese mixed metal oxide increased, the intensity decreases. This is seen in the increase in FWHM of the peak at 464 cm^{-1} as the manganese content of the ceria-manganese mixed metal oxide increases in Table 4-3. Along with decreasing ceria content: the increase in FWHM can be due to a number of factors including, increasing disorder, increasing oxygen vacancies and decrease in crystallite size [28]. It is difficult to determine the relative influence of each factor. However, as the crystallite sizes are relatively similar for each ceria-manganese mixed metal oxide, compared to the ceria, it can be assumed the effect of crystallite size is not as significant, and the increasing FWHM can be attributed to increasing defect sites and oxygen vacancies. The increase in defect sites can lead to increased total oxidation activity on ceria based catalysts, as seen in earlier studies for toluene total oxidation [29].
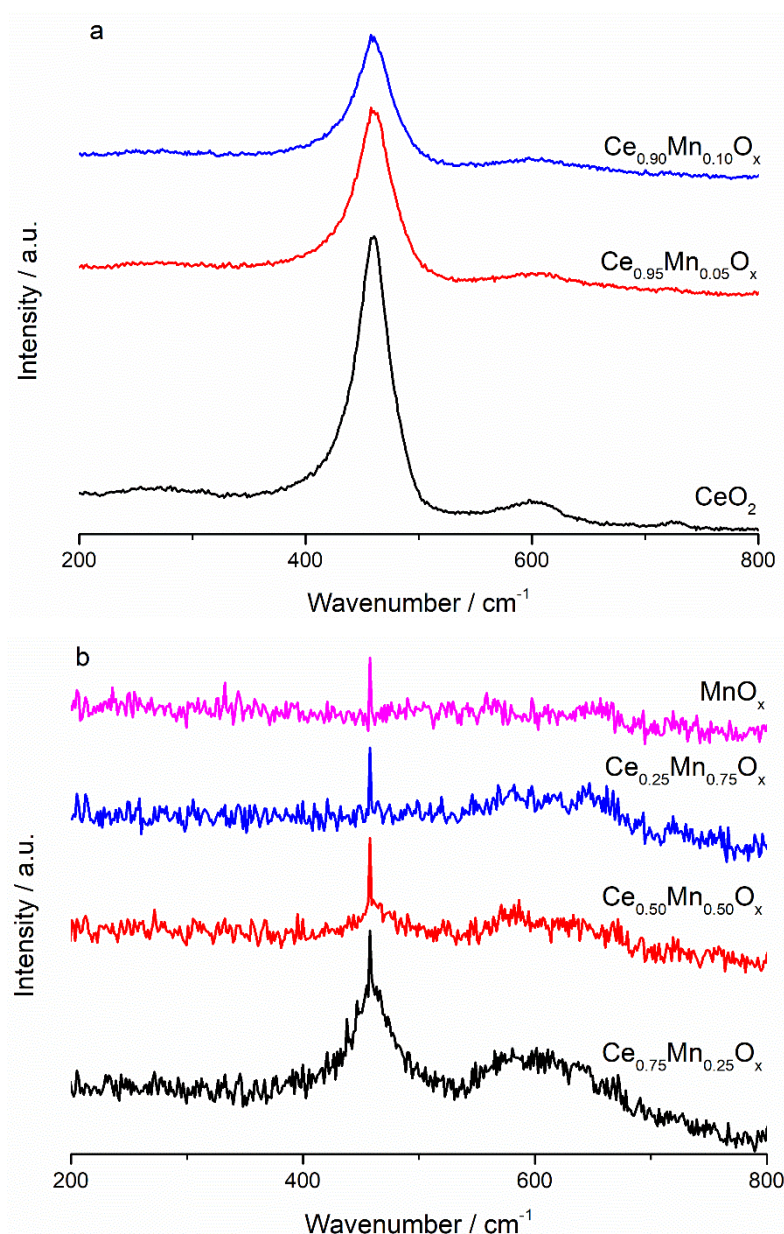
Figure 4-6: Laser Raman spectra of the ceria-manganese mixed metal oxides prepared *via* co-precipitation with sodium carbonate . (a) CeO_2, $Ce_{0.95}Mn_{0.05}O_x$ and $Ce_{0.90}Mn_{0.10}O_x$ (b) $Ce_{0.75}Mn_{0.25}O_x$, $Ce_{0.50}Mn_{0.50}O_x$, $Ce_{0.25}Mn_{0.75}O_x$ and MnO_x (all enhanced 5x). Laser $\lambda= 514$ nm

The oxygen vacancies created by substitution of manganese into the ceria lattice and are seen by the broad peak at 600 cm^{-1}. By comparing the peak areas of the 464 cm^{-1} and 600 cm^{-1}, the relative amounts of oxygen vacancies can be calculated. As increasing amounts of manganese are incorporated into the ceria lattice, the ratio increases. This suggests the lattice structure is becoming more disordered leading to more lattice defects and formation of oxygen vacancies. The more defects will lead to more activity and this trend is followed between these samples and total oxidation activity. Unfortunately, as the peak

area ratio of high manganese concentrations couldn't be calculated it is difficult to see the full extent of this trend.

Table 4-3: Chemical properties of the ceria-manganese mixed metal oxides prepared *via* co-precipitation with sodium carbonate from laser Raman analysis

Sample	Raman FWHM of 464 cm^{-1} peak / cm^{-1}	Peak area ratio of 600 cm^{-1} / 464 cm^{-1}
CeO$_2$	38.4	0.0627
Ce$_{0.95}$Mn$_{0.05}$O$_x$	48.3	0.0671
Ce$_{0.90}$Mn$_{0.10}$O$_x$	50.3	0.0996
Ce$_{0.75}$Mn$_{0.25}$O$_x$	81.2	0.5408
Ce$_{0.50}$Mn$_{0.50}$O$_x$	-	-
Ce$_{0.25}$Mn$_{0.75}$O$_x$	-	-

4.2.3.4 Temperature programmed reduction
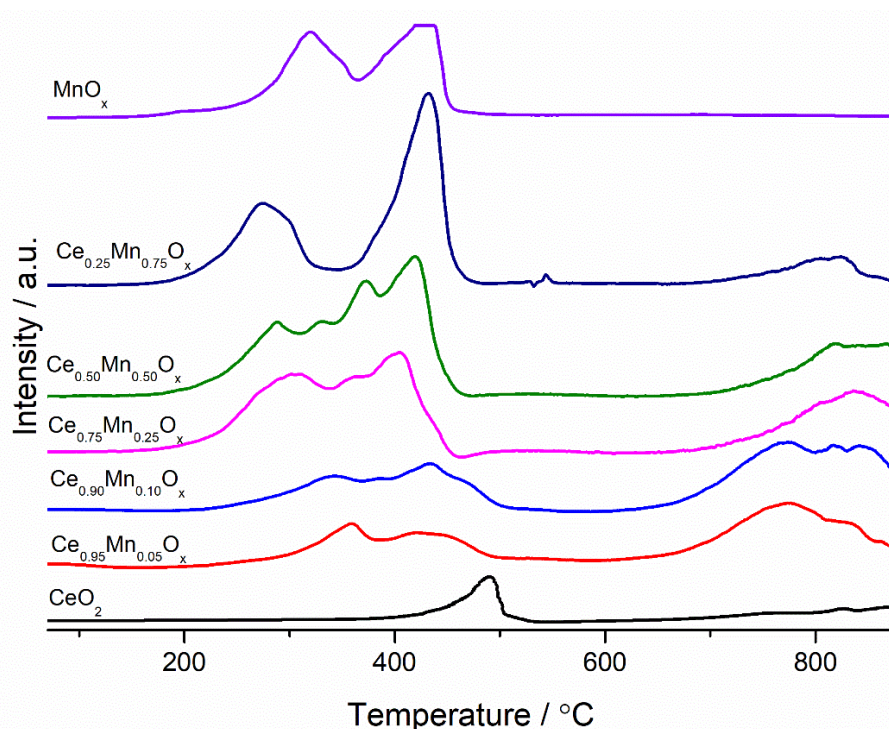
Figure 4-7: Hydrogen temperature-programmed reduction profiles of the ceria-manganese mixed metal oxide catalysts prepared *via* co-precipitation with sodium carbonate. Reaction conditions: 30 mg sample, 30 ml min^{-1} 10 % H$_2$/Ar, temperature range: 50- 850 °C

Temperature programmed reduction profiles of the ceria-manganese mixed metal oxide catalysts are shown in Figure 4-7. As seen in reduction of ceria in the previous chapter, there are two reduction regions at 500 °C and 800 °C representing surface and bulk ceria reduction respectively. The reduction peaks of ceria prepared *via* co-precipitation with sodium carbonate are significantly less defined compared to ceria prepared *via*

130

mechanochemical grinding. Manganese oxides can be present in many phases, which all have distinct reduction profiles. MnO_2 has two reduction features, a minor peak at 330 °C and a major peak at 500 °C, Mn_2O_3 has two peaks at 280 °C and 380 °C and Mn_3O_4 has one reduction peak at 480 °C [30]. The reduction profile of manganese oxide has two peaks centred at 320 °C and 420 °C, which indicates the MnO_x is in the MnO_2 phase. The variation between the reduction temperature from literature and experimental value could arise from the presence of additional cations, such as sodium from the precipitating agent. Previous studies reported changes in reduction temperatures and profiles when potassium, calcium and magnesium were added to manganese oxides [31].

The reduction profiles of the ceria-manganese mixed metal oxide samples contain many convoluted features at lower temperatures when compared to ceria. The surface reduction temperature of ceria also decreases as the manganese content of the mixed metal oxide increases. This suggests the samples have become easier to reduce as manganese is incorporated into the ceria. This indicates mixing of the two metal oxides, however, it is difficult to confirm the extent of this observation [19,32]. The peak areas of the surface reduction are significantly increased as the manganese content of the mixed metal oxide increases, compared to the ceria. This is due to the increasing surface areas noted for the ceria-manganese mixed metal oxides when compared to ceria. This will lead to more surface exposed for reduction and therefore increased intensity of peaks. This indicates the extent of reduction increases as the manganese content of the mixed metal oxide increases.

The $Ce_{0.95}Mn_{0.05}O_x$ and $Ce_{0.90}Mn_{0.10}O_x$ surface reduction profiles seem to be a combination of two peaks. This could mean small amounts of manganese causes the formation of Ce^{3+} on the surface along with Ce^{4+}. This was seen in the previous chapter as zirconia was added into the lattice. The $Ce_{0.75}Mn_{0.25}O_x$ and $Ce_{0.50}Mn_{0.50}O_x$ have three and four reduction peaks present, respectively, in the surface reduction region. With multiple peaks present on the surface of these catalysts, this suggests the surface may not be as well mixed as the bulk in these materials. There were no discrete manganese oxide phases observed in XRD for these samples. However, other species may reside on the surface or are amorphous which can't be detected by XRD. The reduction profile of the $Ce_{0.25}Mn_{0.75}O_x$ follows a similar shape to the reduction of the manganese oxide with two peaks observed. The first peak represents the reduction of Mn_2O_3 to Mn_3O_4 and the second peak the combination of reduction of manganese oxide species and ceria.

There is also a noticeable effect on bulk ceria reduction upon addition of manganese into the lattice. Each reduction profile of the ceria-manganese mixed metal oxides contains a

broad peak at 800 °C. This reduction region is significantly larger than the reduction region for bulk ceria, indicating the manganese has a noticeable impact on the bulk of the catalysts. This effect has been observed in previous studies using ceria-manganese mixed metal oxides [5,7,33], and suggests the manganese increases the lattice defects leading to increased migration of oxygen [33]. This in turn could lead to increased activity for total oxidation reactions.

4.2.3.5 Electron microscopy

4.2.3.5.1 Scanning electron microscopy
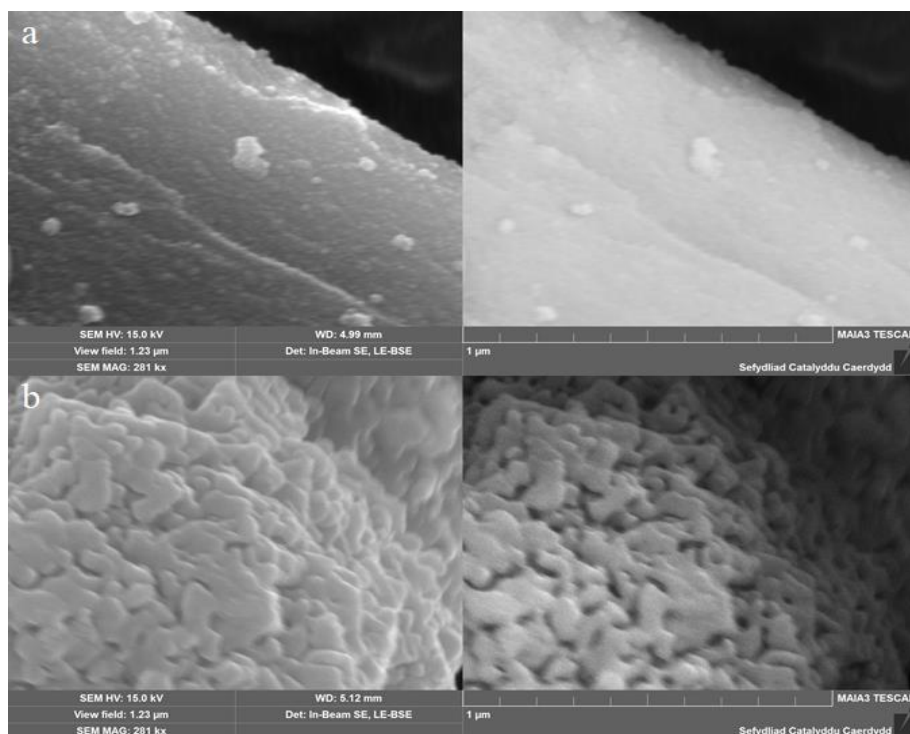
Figure 4-8: The secondary electron (left) and backscattered electron (right) micrographs of (a) CeO$_2$ and (b) MnO$_x$ prepared using autotitration. Image magnification: 281 kx

Figure 4-8 shows the scanning electron micrographs of the ceria and manganese oxide. The plate-like morphology observed in ceria prepared *via* mechanochemical grinding is retained in ceria prepared *via* precipitation. The manganese oxide sample is an array of small crystallites layered on top of each other.
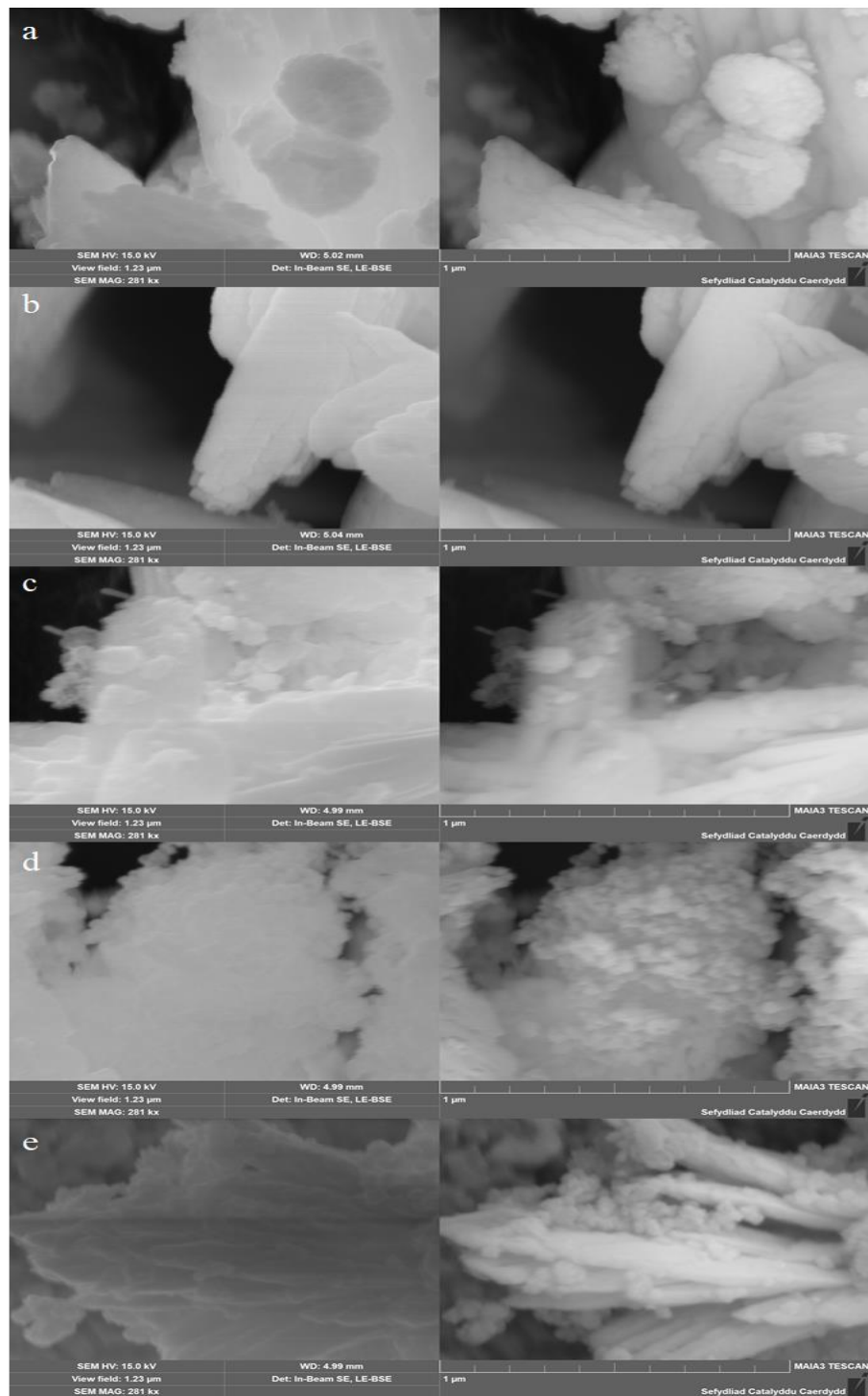
Figure 4-9: Secondary (left) and backscattered (right) electron micrographs of the ceria-manganese mixed metal oxides. (a) $Ce_{0.95}Mn_{0.05}O_x$, (b) $Ce_{0.90}Mn_{0.10}O_x$, (c) $Ce_{0.75}Mn_{0.25}O_x$, (d) $Ce_{0.50}Mn_{0.50}O_x$ and (e) $Ce_{0.25}Mn_{0.75}O_x$

The scanning electron micrographs of the ceria-manganese mixed metal oxides are shown in Figure 4-9. The ceria plate-like morphology is maintained throughout the ceria-manganese mixed metal oxides. However, as the manganese content of the mixed metal oxide increases, bulbous deposits start to appear on these "ceria" plates. No layering of crystallites was observed, indicating the ceria has the dominant morphology in the mixed

metal oxides. There was no difference in contrast observed in the ceria-manganese mixed metal oxides containing lower than 25 % manganese. This suggests the ceria and manganese are well mixed as seen in XRD and Raman analysis of the samples. However, noticeable differences in contrast are observed in the ceria-manganese mixed metal oxides containing more than 50 % manganese. This is in line with the XRD analysis of the $Ce_{0.25}Mn_{0.75}O_x$, in which phase separation between bulk ceria and manganese oxide phases were observed. This observation differs to the XRD analysis of the $Ce_{0.50}Mn_{0.50}O_x$ sample. No manganese oxide phases were observed in the XRD pattern of this sample. This suggests the manganese oxide phases are either very small or amorphous and therefore can't be detected using XRD

4.2.3.5.2 Electron dispersive x-ray spectroscopy

EDX analysis and elemental mapping were carried out alongside the scanning electron microscopy imaging of the ceria-manganese mixed metal oxides. The bulk elemental analysis is shown in Table 4-4. All the Ce:Mn ratios were close to the nominal values expected from the synthesis ratio for all the ceria-manganese mixed metal oxide catalysts. The largest variation was observed for the $Ce_{0.25}Mn_{0.75}O_x$, however, the value was not too different to the nominal value. The variation could be due to phase separation occurring in the bulk phase leading to ceria or manganese oxide enriched areas.

Table 4-4: SEM-EDX derived bulk elemental analysis of the ceria-manganese mixed metal oxides *via* prepared co-precipitation with sodium carbonate

Sample	Concentration / At.%				Relative Ce:Mn concentrations / %	
	Ce	Mn	O	Na	Ce	Mn
CeO₂	17.6	0	69.0	13.4	100.0	0.0
Ce₉₅Mn₅Oₓ	30.6	2.0	62.2	5.2	93.7	6.3
Ce₉₀Mn₁₀Oₓ	21.8	2.7	67.2	6.4	89.1	10.9
Ce₇₅Mn₂₅Oₓ	23.4	7.0	63.6	6.0	77.0	23.0
Ce₅₀Mn₅₀Oₓ	11.8	13.0	67.8	7.4	47.6	52.4
Ce₂₅Mn₇₅Oₓ	5.1	22.8	66.8	5.3	18.2	81.8
MnOₓ	0	36.1	59.9	4.1	0	100.0

Sodium is present in all the ceria-manganese mixed metal oxides. The ceria sample has the highest concentration, and the value decreases upon manganese incorporation into the ceria. The high concentrations of sodium in the ceria may explain the low activity of this ceria prepared *via* autotitration compared to mechanochemically prepared ceria. Sodium present in ceria is reported to have a detrimental effect on the activity for the oxidation of nitrous oxide [34]. Both mechanochemically prepared ceria catalysts are more active for

propane total oxidation. However, the ceria prepared by autotitration was more active for naphthalene total oxidation compared to the ceria prepared *via* mechanochemical grinding of carbonates. This suggests multiple factors including sodium may influence the activity of the ceria catalysts, for VOC total oxidation. This may lead to the poor propane total oxidation activity observed over ceria producing using auto-titration compared to mechanochemical grinding.

The effect of sodium has also been investigated on mixed metal oxides containing manganese. The presence of sodium on copper-manganese mixed metal oxides showed a detrimental effect for catalytic CO oxidation [35]. With all the ceria-manganese mixed metal oxides containing a similar amount of sodium, however, significantly lower than the ceria, this may affect the activity of the catalysts. The effect of sodium poisoning on the catalytic performance of the ceria-manganese mixed metal oxide will be investigated in the next section of this chapter.
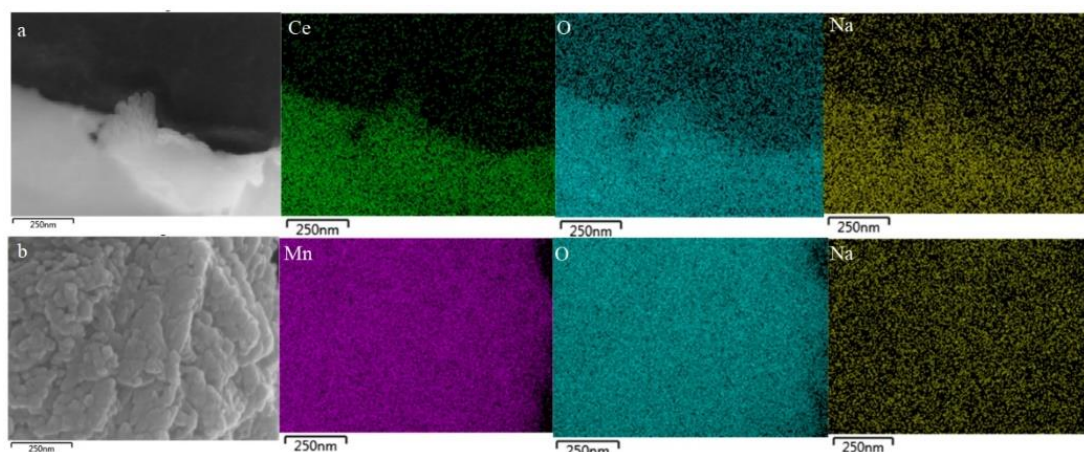
Figure 4-10: SEM-EDX mapping of (a) CeO_2 and (b) MnO_x. Cerium (green), manganese (pink), oxygen (blue) and sodium (yellow)

The SEM-EDX maps of the single metal oxides are shown in Figure 4-10 and the ceria-manganese mixed metal oxides are shown in Figure 4-11. Sodium is an ever-present species in the bulk and is homogenously distributed across all ceria-manganese mixed metal oxides. The cerium and manganese are evenly distributed across the $Ce_{0.95}Mn_{0.05}O_x$, $Ce_{0.90}Mn_{0.10}O_x$ and $Ce_{0.75}Mn_{0.25}O_x$ samples. This is in-line with XRD data, indicating the ceria and manganese are well mixed in the lattice of the mixed metal oxides.

However, in the $Ce_{0.50}Mn_{0.50}O_x$ phase separation has occurred, with large regions of ceria and manganese seen in the maps. This coincides with the difference in contrast observed in the SEM imaging and the multiple reduction regions seen in the TPR profile of the sample. However, with no distinct manganese oxides reflections seen in the XRD pattern, the manganese oxide may be in an amorphous phase. The same observation was noted

135

for higher zirconium content of ceria-zirconia mixed metal oxides prepared *via* mechanochemical grinding. This suggests that higher loadings of a secondary metal oxide into the ceria lattice may lead to poor incorporation of the metal into the ceria lattice. The metal which isn't incorporated into the lattice may form amorphous layers on the surface or in the bulk making it difficult to detect using the techniques used in this investigation. Phase segregation between ceria and manganese oxides observed in the XRD analysis of the $Ce_{0.25}Mn_{0.75}O_x$ is confirmed in the SEM-EDX mapping of the sample.
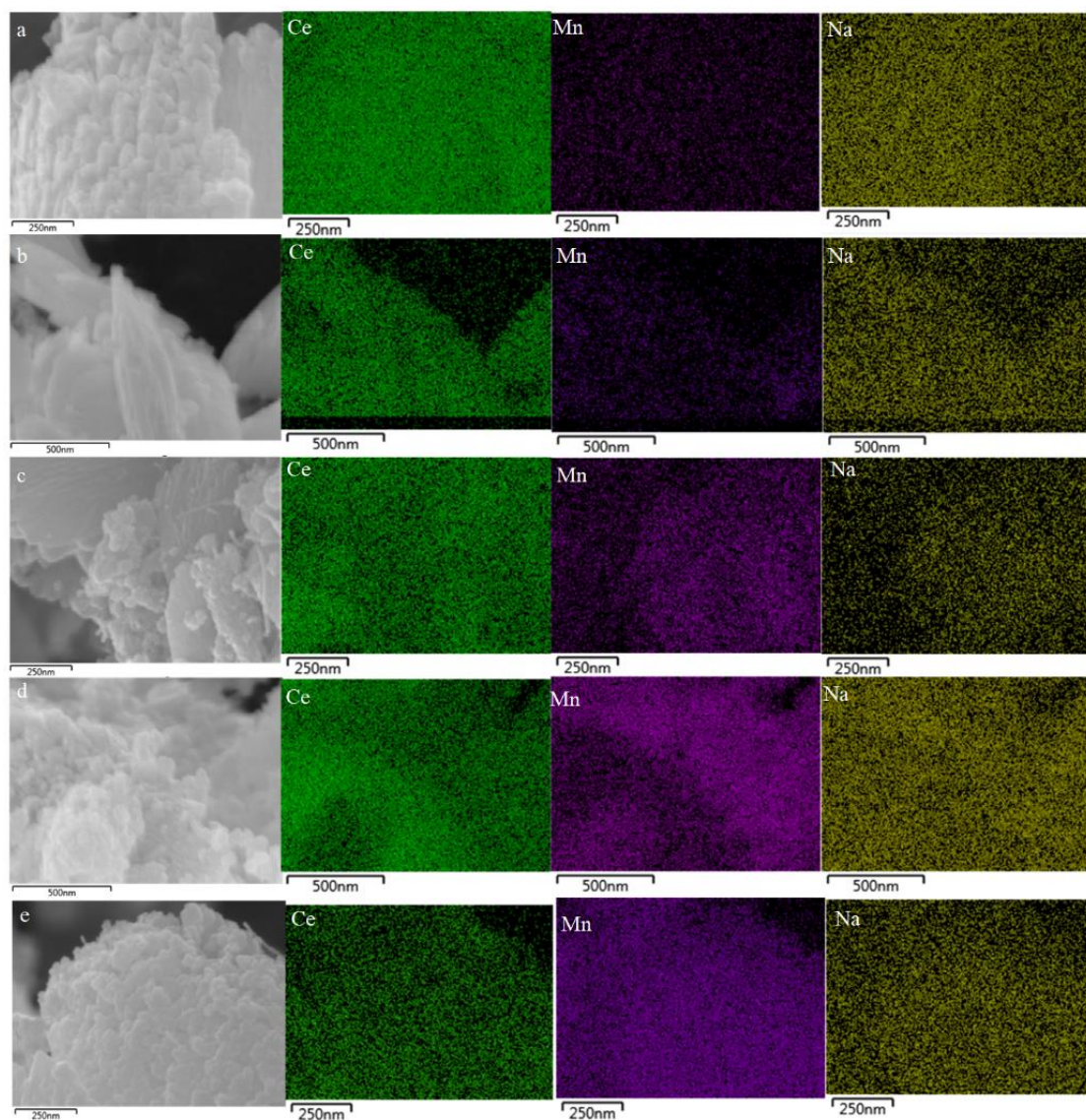
Figure 4-11: SEM-EDX elemental mapping of (a) $Ce_{0.95}Mn_{0.05}O_x$, (b) $Ce_{0.90}Mn_{0.10}O_x$, (c) $Ce_{0.75}Mn_{0.25}O_x$, (d) $Ce_{0.50}Mn_{0.50}O_x$ and (e) $Ce_{0.25}Mn_{0.75}O_x$. Cerium (green), manganese (pink) and sodium (yellow)

4.2.3.5.3 Transmission electron microscopy
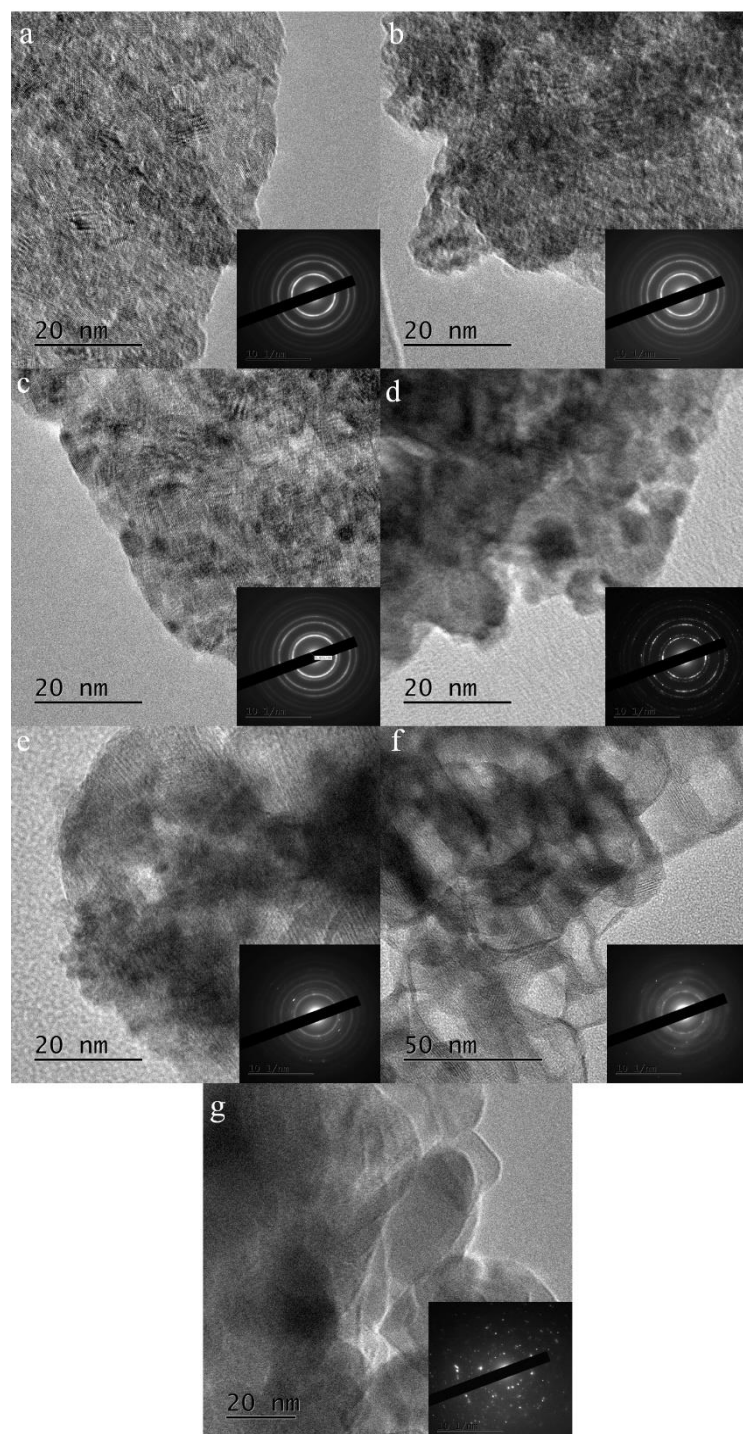
Figure 4-12: High magnification TEM images of the ceria-manganese mixed metal oxide catalysts prepared *via* prepared co-precipitation with sodium carbonate. Inset: selected area electron diffraction patterns of larger 250 nm areas. (a) CeO_2, (b) $Ce_{0.95}Mn_{0.05}O_x$, (c) $Ce_{0.90}Mn_{0.10}O_x$, (d) $Ce_{0.75}Mn_{0.25}O_x$, (e) $Ce_{0.50}Mn_{0.50}O_x$, (f) $Ce_{0.25}Mn_{0.75}O_x$ and (g) MnO_x

TEM images and selected area electron diffraction, along with derived d-spacings, of the ceria-manganese mixed metal oxides are shown in Figure 4-12 and Table 4-5. The TEM

images of the ceria display a mixture of randomly layered crystallites with pronounced lattice planes. This is very similar to the ceria synthesised from mechanochemical grinding. This indicates the presence of sodium hasn't affected the ceria lattice formation. An array of plate-like structures is observed in the TEM image of the manganese oxide. This plate-like structure has been observed in previous TEM imaging of manganese oxides [36]. The plate like structure was more readily seen once sodium or lithium were added into the manganese lattice [37].

The morphology of the ceria-manganese mixed metal oxides changes upon increasing manganese content of the sample. Low loadings of manganese ($< 10\,\%$) seem to have the same morphology as the ceria only sample. This is complementary to the XRD and Raman spectroscopy in which only cubic ceria structures were observed. However in the images of $Ce_{0.75}Mn_{0.25}O_x$ and $Ce_{0.50}Mn_{0.50}O_x$ the crystallites become less defined and the plate like shapes start to form. The $Ce_{0.25}Mn_{0.75}O_x$ has a similar plate like structure as the manganese oxide. However, some small ceria crystallites were also observed. This coincides with the XRD data, as both ceria and manganese oxide species were observed. Four diffraction rings are observed in the selected area electron diffraction pattern of the ceria sample, which are indexed to the (111), (200), (220) and (311) cubic ceria lattice planes. The diffraction pattern of the manganese oxide had an array of spots, suggesting the sample is more like a single crystal rather than randomly orientated crystallites. Due to the irregularity of the spots, identifying the phases and lattice planes of the manganese oxide is difficult. The $Ce_{0.95}Mn_{0.05}O_x$ and $Ce_{0.90}Mn_{0.10}O_x$ diffraction patterns consist of four rings, indicating the cubic ceria structure seen in XRD and from the TEM images is retained. The four rings break up in the $Ce_{0.75}Mn_{0.25}O_x$ and once the manganese content is above 50 %, only diffuse rings along with bright spots are observed in the diffraction patterns. This confirms the cubic ceria lattice structure becomes less dominant as the manganese content increases.

The lattice parameter was calculated either by using the indexed lattice plane or from the most intense spot. The ceria prepared using auto-titration had a smaller lattice parameter compared to the ceria prepared *via* mechanochemical grinding. This could be due to the presence of the sodium atoms, which have a significantly smaller atomic radius [38], in the ceria lattice causing the compression of the ceria lattice. This in turn will cause the lattice parameter to decrease compared to any undoped ceria. The lattice parameter of the manganese oxide was between the values for MnO_2 and Mn_2O_3, 4.398 Å and 9.413 Å respectively [39,40]. This suggests the manganese oxide is a combination of the two

metals, as seen in XRD. However, majority of the manganese oxide is present in the MnO_2 phase, with the presence of Mn_2O_3 causing the increase in lattice parameter.

Table 4-5: The lattice parameter of the ceria-manganese mixed metal oxides prepared *via* co-precipitation with sodium carbonate, determined from selected area electron diffraction

Sample	Lattice parameter calculated from selected area electron diffraction / Å
CeO_2	5.18
$Ce_{0.95}Mn_{0.05}O_x$	5.12
$Ce_{0.90}Mn_{0.10}O_x$	5.04
$Ce_{0.75}Mn_{0.25}O_x$	4.80
$Ce_{0.50}Mn_{0.50}O_x$	5.12
$C_{0.25}Mn_{0.75}O_x$	8.36
MnO_x	5.46

Once manganese was incorporated into the ceria lattice, the lattice parameter decreases, and it decreases as the manganese content of the mixed metal oxide increases. However once the manganese content is above 50 %, the value starts to increase. This follows the trend observed from XRD, although the decrease in lattice parameter upon increasing manganese content is more pronounced when lattice parameters are calculated from selected area electron diffraction. This confirms that only mixing between ceria and manganese occurs at manganese content below 50 %. With phase separation observed in EDX of the ceria-manganese mixed metal oxides with high content of manganese, this will form segregated areas of ceria and manganese oxides. With less manganese present in the ceria lattice, this will mean the lattice won't contract as much as mixed metal oxides with good mixing between the two metal oxides.

4.2.3.6 X-ray photoelectron spectroscopy

Table 4-6: XPS derived surface elemental concentrations for the ceria-manganese mixed metal oxide catalysts prepared *via* co-precipitation with sodium carbonate

	Concentration / At.%				Relative Ce:Mn concentrations / %	
Sample	Ce	Mn	O	Na	Ce	Mn
CeO_2	18.7	0.0	67.1	14.2	100.0	0.0
$Ce_{95}Mn_5O_x$	20.5	0.5	65.3	13.7	97.4	2.6
$Ce_{90}Mn_{10}O_x$	19.7	1.5	65.3	13.5	92.8	7.2
$Ce_{75}Mn_{25}O_x$	16.5	8.3	63.9	11.3	66.5	33.5
$Ce_{50}Mn_{50}O_x$	11.9	16.9	65.6	5.7	41.3	58.7
$Ce_{25}Mn_{75}O_x$	9.2	15.9	63.0	11.9	36.7	63.3
MnO_x	0.0	31.5	61.8	6.7	0.0	100.0

The surface of the ceria-manganese mixed metal oxides was analysed using XPS, with the surface composition shown in Table 4-6. High amounts of sodium were observed in the EDX analysis of the samples and the same observation was seen in XPS. However, the XPS values are around 50 % higher than the EDX values. As mentioned in the section discussing EDX, the presence of this sodium has affected the ceria prepared *via* autotitration compared to the mechanochemically prepared ceria. With high amounts of sodium on the surface and within the catalysts, this may block the active sites leading to less adsorption of VOC on the surface and subsequent oxidation. All the mixed metal oxides have a lower surface sodium content compared to the ceria.

Another difference between the EDX and XPS elemental analysis, is the relative concentrations of cerium and manganese. The EDX showed the bulk values of cerium and manganese were close to the nominal values. However the relative concentrations calculated using XPS vary from the original values. The samples with less than 10 % manganese had higher cerium content compared to the nominal values, the $Ce_{0.75}Mn_{0.25}O_x$ and $Ce_{0.50}Mn_{0.50}O_x$ had cerium content lower than the nominal value and the $Ce_{0.25}Mn_{0.75}O_x$ had cerium content higher than the nominal value. Variation in surface ceria and manganese ratios has also been observed in mixed metal oxides prepared *via* citric acid [41] and urea combustion methods.[19].
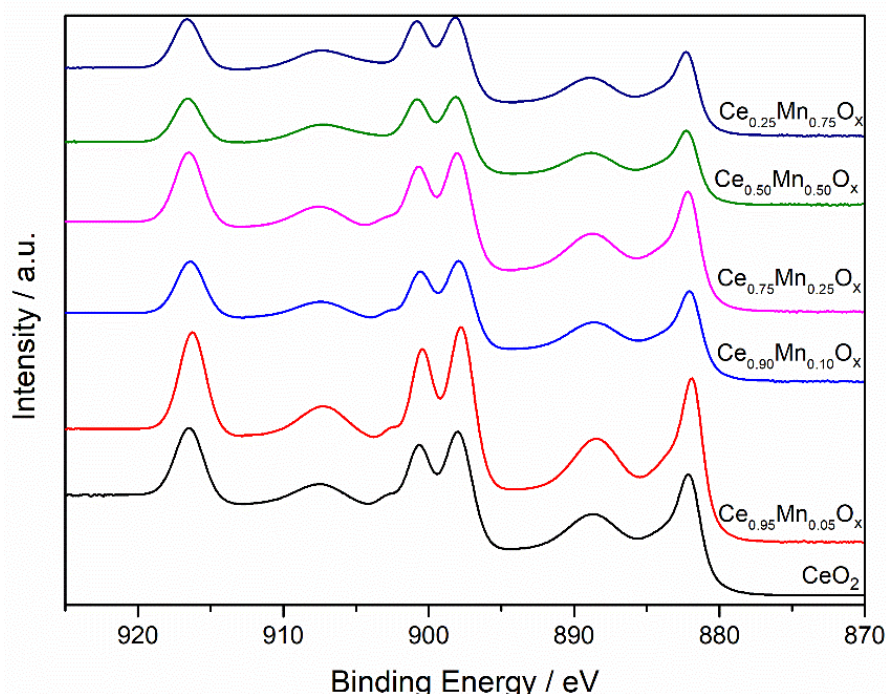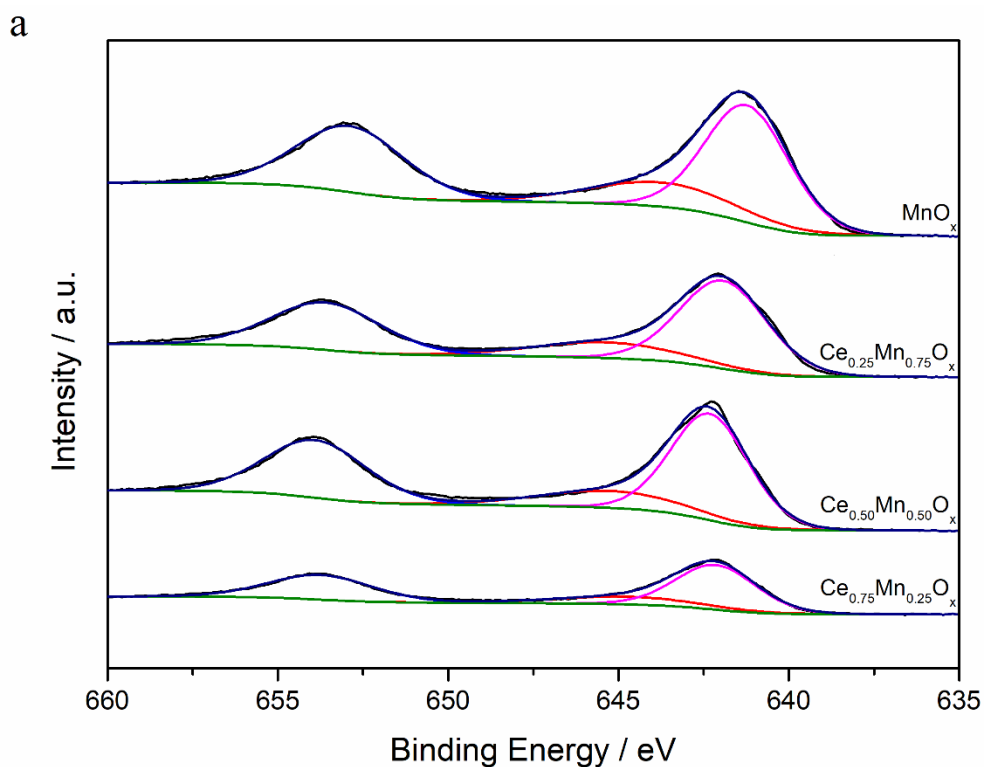

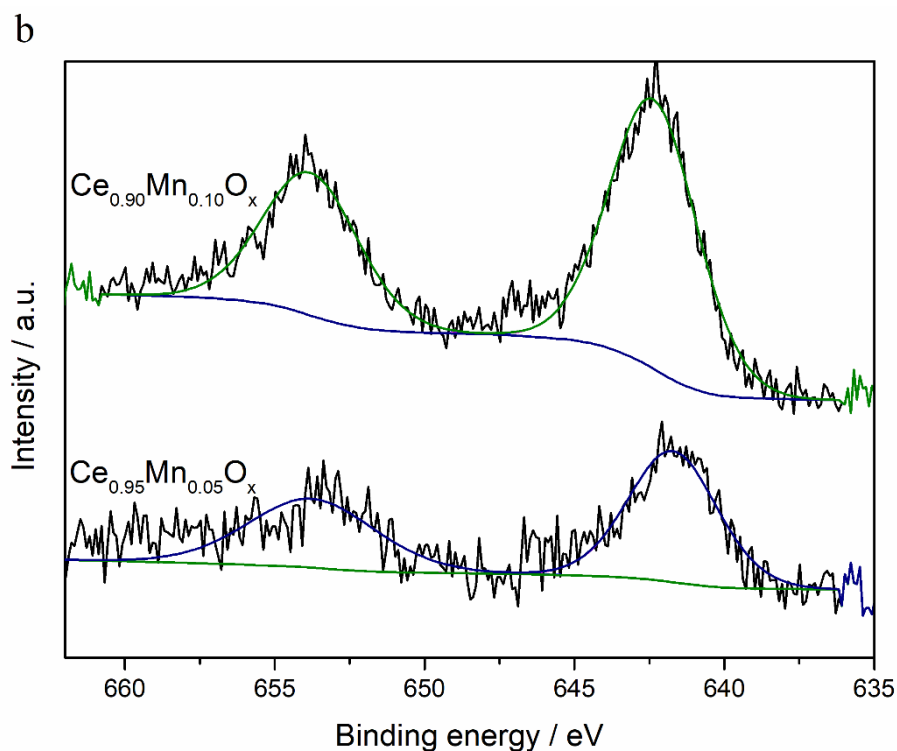Figure 4-13: XPS spectra of the Ce 3d peaks for the ceria-manganese catalysts prepared *via* co-precipitation with sodium carbonate

The Ce 3d XPS spectra of the ceria-manganese mixed metal oxides is shown in Figure 4-13. As the concentration of cerium in the ceria-manganese mixed metal oxide decreases the intensity of the peaks also decrease. Characteristic Ce^{4+} peaks are at 917 eV and an unsymmetrical, doublet at 879 and 897 eV, and symmetric doublet peaks 881 and 900 eV are characteristic Ce^{3+} peaks. All the ceria containing samples have a large peak at 917 eV, confirming the presence of Ce^{4+} in all the samples. The doublet peak between 903-895 eV becomes more symmetrical as the manganese content of the ceria-manganese mixed metal oxide increases. The presence of the Ce^{3+} can be seen in the TPR profiles of the samples with additional peaks noted in the surface reduction of ceria species, in the mixed metal oxide samples. This suggests the proportion of Ce^{3+} present on the surface increases as the manganese content increases. The surface manganese will distort the surface causing formation of defect sites and oxygen vacancies on the surface leading to increased total oxidation activity.

a

MnO_x

$Ce_{0.25}Mn_{0.75}O_x$

$Ce_{0.50}Mn_{0.50}O_x$

$Ce_{0.75}Mn_{0.25}O_x$

Intensity / a.u.

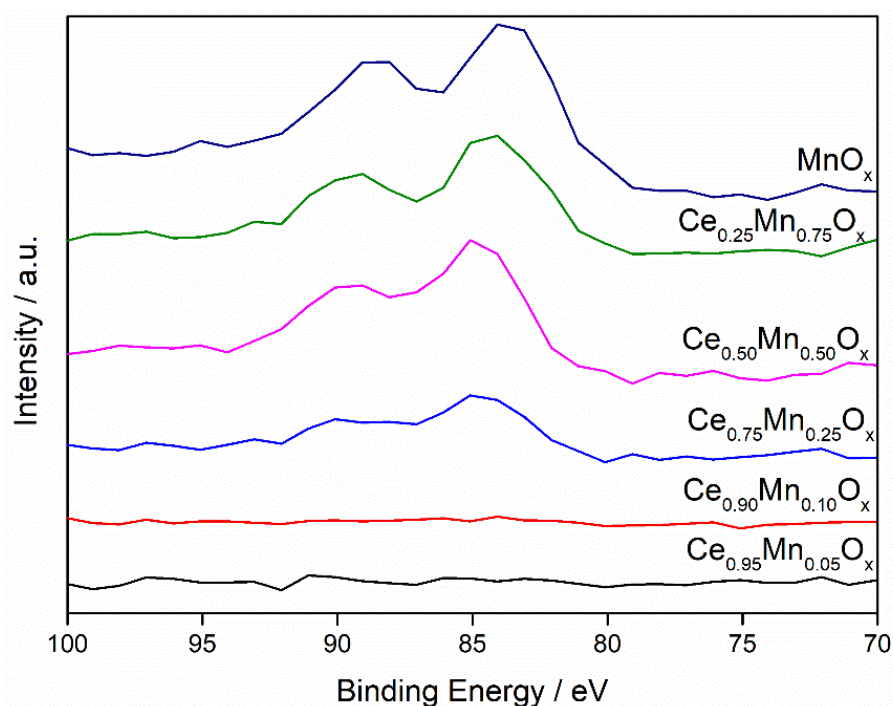Binding Energy / eV

660   655   650   645   640   635

b

Figure 4-14: XPS spectra of the Mn 2p peaks for the ceria-manganese mixed metal oxides prepared *via* co-precipitation with sodium carbonate. (a) $Ce_{0.75}Mn_{0.25}O_x$, $Ce_{0.50}Mn_{0.50}O_x$, $Ce_{0.25}Mn_{0.75}O_x$ and MnO_x (b) $Ce_{0.95}Mn_{0.05}O_x$ and $Ce_{0.90}Mn_{0.10}O_x$ (enhanced 5x)

The Mn 3p XPS spectra of the ceria-manganese mixed metal oxides is shown in Figure 4-14. As the manganese content of the ceria-manganese mixed metal oxide decreases the intensity of the peaks decrease. The oxidation state of manganese is difficult to identify from the 3p spectra. However the MnO phase can be identified by a satellite peak at 647 eV. None of the spectra contain this feature, therefore confirming the oxidation state of the manganese is either 3+ or 4+.

Figure 4-15: XPS spectra of the Mn 3s peaks for the ceria-manganese mixed metal oxide catalysts *via* co-precipitation with sodium carbonate

The oxidation state of manganese can be determined from the peak splitting in the 3s spectra, Figure 4-15. The peak splitting was determined by comparing the energy difference between peaks situated between 89 and 85 eV and this is shown in Table 4-7. Manganese is present in the 2+ oxidation if the difference is 6.0 eV, in the 3+ oxidation state between 6.0-5.3 eV and in the 4+ oxidation state if it is below 5.3 eV [42].

As seen in Table 4-7, only the splitting of the $Ce_{0.25}Mn_{0.75}O_x$ was between 6.0-5.3 eV, which indicates the manganese is in the 3+ oxidation state and present in the Mn_2O_3 phase. All other manganese containing samples with observable peak splitting were present in the 4+ oxidation state of the MnO_2 phase. This is in line with the analysis by XRD, in which Mn_2O_3 was observed on the $Ce_{0.25}Mn_{0.75}O_x$ and MnO_2 was the dominant phase of the manganese oxide. With Mn_2O_3 more active for VOC total oxidation compared to MnO_2 [3], this explains the increased activity observed on the $Ce_{0.25}Mn_{0.75}O_x$ compared to the manganese oxide.

Table 4-7: Magnitude of peak splitting in the Mn 3s spectra for the ceria-manganese mixed metal oxides prepared *via* autotitration

Sample	Magnitude of Mn 3s peak splitting / eV	Surface oxidation state of Mn (all +)
$Ce_{0.95}Mn_{0.05}O_x$	0	-
$Ce_{0.90}Mn_{0.10}O_x$	0	-
$Ce_{0.75}Mn_{0.25}O_x$	4.7	4
$Ce_{0.50}Mn_{0.50}O_x$	4.9	4
$Ce_{0.25}Mn_{0.75}O_x$	5.5	3
MnO_x	4.8	4

The fitted O 1s spectra of the ceria-manganese mixed metal oxide are shown in Figure 4-16. Lattice oxygen species (O_α) are present on both ceria and manganese oxides between 529-31 eV and surface defect oxygen species (O_β) are present between 531-3 eV [14,43]. Both species are present on all catalysts, with the relative concentrations shown in Table 4-8. Both ceria and manganese oxide have the O 1s peaks at a similar position. However, a shift towards a higher binding energy in the peak position is noted as the manganese content of the ceria-manganese mixed metal oxide increases. The shift towards higher binding energies is noted in previously studied ceria-manganese mixed metal oxides [28,44], and is assigned to synergistic interactions between ceria and manganese oxide species.

The ceria has the highest relative concentration of O_β of all the ceria-manganese mixed metal oxides, whereas the manganese oxide had one of the lowest relative concentration of O_β. The addition of any amount of manganese significantly reduced the O_β. The mixed metal oxides with manganese content below 10 % had the highest O_β concentration out of the range of mixed metal oxides. However, no clear trend was observed between concentration of manganese and relative concentration of O_β. Weak peaks from sodium hydroxide phases are present at 531.3 eV and these may lead to differences in O_β concentrations observed on the surface of these samples [45]. High concentrations of sodium are present on the surface of all ceria-manganese mixed metal oxides, this may affect the relative concentrations of oxygen on each catalyst. The ceria, $Ce_{0.95}Mn_{0.05}O_x$ and $Ce_{0.90}Mn_{0.10}O_x$ all had the highest concentration of surface sodium of all the samples. Therefore the higher percentage of relative O_β could be assigned increased oxygen species arising from sodium.
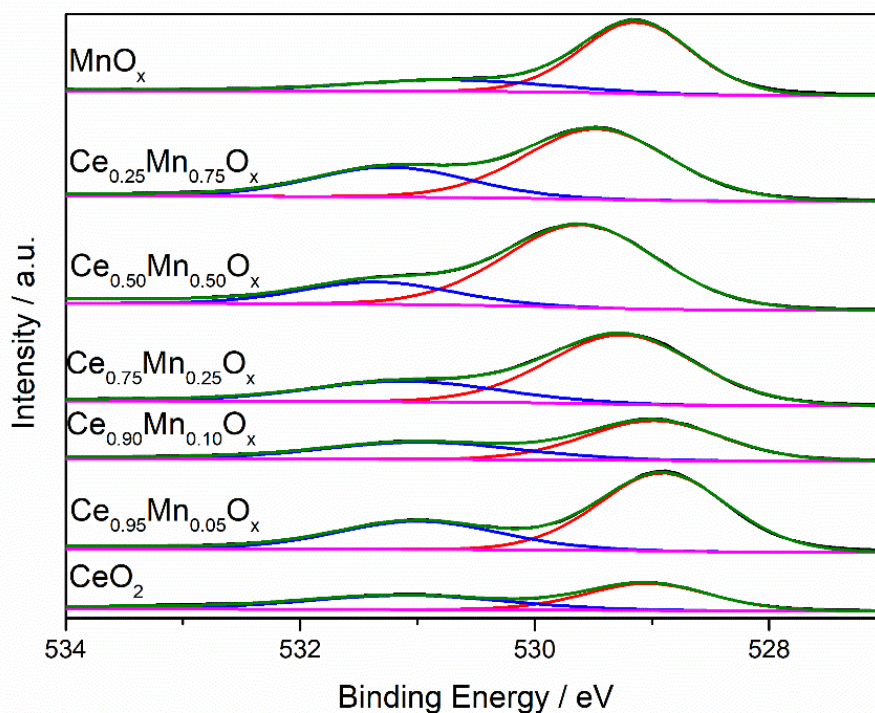
Figure 4-16: XPS spectra of the O 1s peaks of the ceria-manganese mixed metal oxide catalysts prepared *via* co-precipitation with sodium carbonate

As seen in the previous chapter, the concentration of O_β has a significant effect on total oxidation performance. However with no observable trends noted between total oxidation activity and O_β other factors have to be considered for the higher activity of the $Ce_{0.25}Mn_{0.75}O_x$.

Table 4-8: XPS derived concentration of latticed and surface O species for the ceria-manganese mixed metal oxide catalysts prepared *via* co-precipitation with sodium carbonate

Sample	Relative concentration of O_α / %	Relative concentration of O_β / %
CeO_2	54.4	45.6
$Ce_{0.95}Mn_{0.05}O_x$	68.9	31.1
$Ce_{0.90}Mn_{0.10}O_x$	62.0	38.0
$Ce_{0.75}Mn_{0.25}O_x$	72.7	27.3
$Ce_{0.50}Mn_{0.50}O_x$	79.1	20.9
$Ce_{0.25}Mn_{0.75}O_x$	68.7	31.3
$MnOx$	78.1	21.9

4.3 The effect of washing of the $Ce_{0.25}Mn_{75}O_x$ catalyst on the activity for VOC total oxidation

The best ratio of ceria-manganese mixed metal oxide prepared using auto-titration for propane and naphthalene total oxidation was the $Ce_{0.25}Mn_{0.75}O_x$. It was noticed that each of the ceria-manganese mixed metal oxides contained significantly high concentrations of surface and bulk sodium, which is reported to poison oxidation reactions. Therefore in this section the effect of removal of sodium by washing is investigated. The same preparation used as used above to prepare the ceria-manganese catalysts, except the volume of warm water used to wash the sample was altered. Along with 1 l washing, 0 l and 2 l washing were investigated with the catalyst performance and characterisation shown below.

4.3.1 Catalyst performance

4.3.1.1 Propane total oxidation
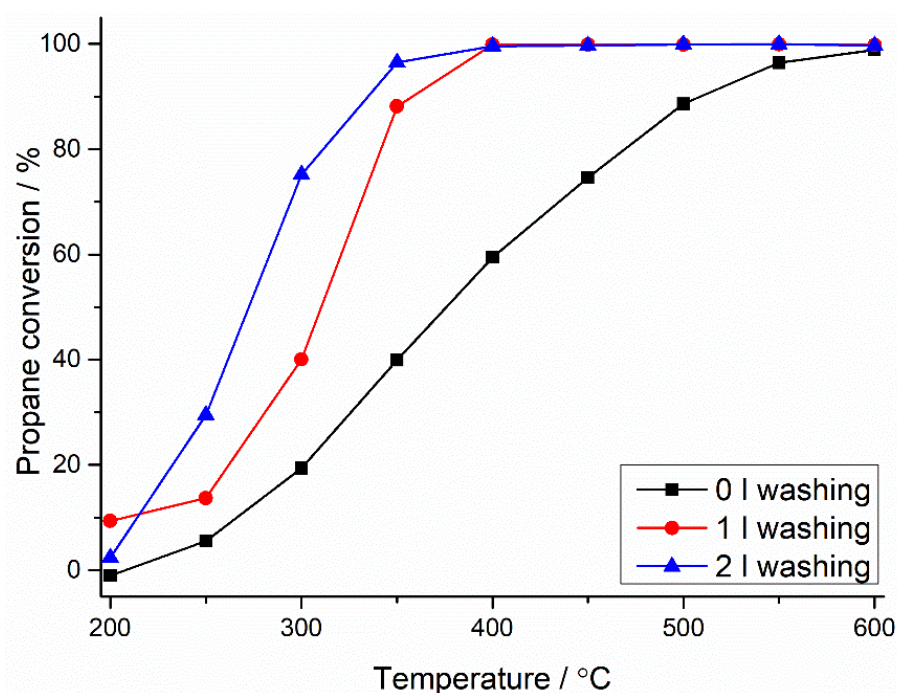
Figure 4-17: Catalytic activities for the total oxidation of propane of the $Ce_{0.25}Mn_{0.75}O_x$ prepared *via* co-precipitation with sodium carbonate using different washing protocols. Reaction conditions: GHSV = 45,000 h^{-1}, temperature 200-600 °C, 5000 ppm propane in air. Legend refers to different litres of water used to wash the catalyst.

The effect of extent of washing of the $Ce_{0.25}Mn_{0.75}O_x$ on the performance of propane total oxidation is shown in Figure 4-17. All the catalytic runs showed high selectivity for CO_2

(>99 %). A correlation between the volume of water used to wash the $Ce_{0.25}Mn_{0.75}O_x$ and propane total oxidation activity was observed. The unwashed $Ce_{0.25}Mn_{0.75}O_x$ performed on par with the palladium reference catalyst. However when compared to the original catalyst preparation conditions, the T_{100} temperature increased by 200 °C when the catalyst wasn't washed, and it lowered by 50 °C upon increased washing.
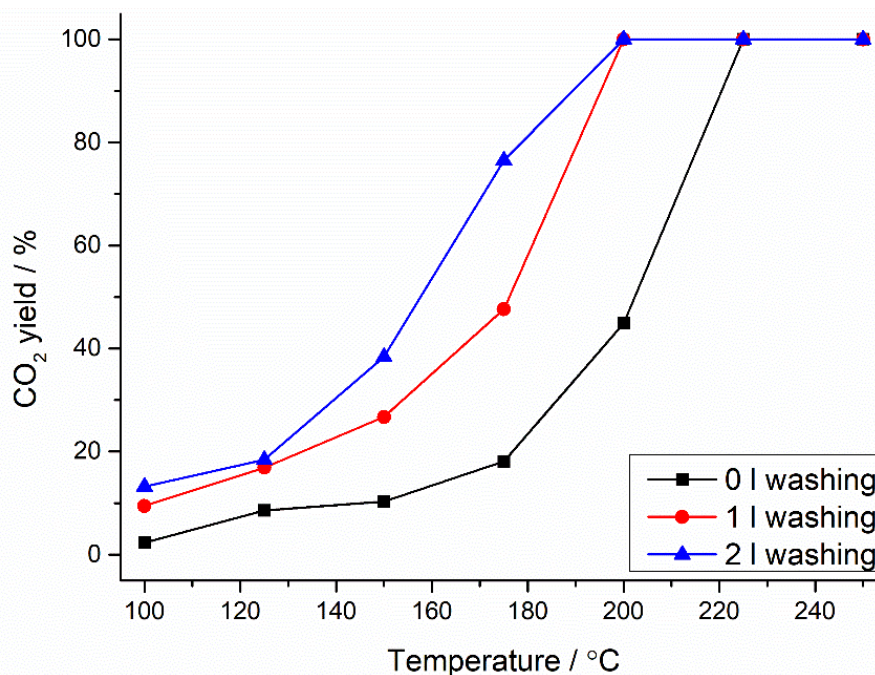
4.3.1.2 Naphthalene total oxidation

Figure 4-18: Catalytic activities for the total oxidation of naphthalene of the $Ce_{0.25}Mn_{0.75}O_x$ prepared *via* co-precipitation with sodium carbonate using different washing protocols. Reaction conditions: GHSV = 45,000 h^{-1}, temperature 200-600 °C, 100 vppm naphthalene in 20 % O_2 balanced with He. Legend refers to different litres of water used to wash the catalyst

The effect of washing the $Ce_{0.25}Mn_{0.75}O_x$ on catalytic activity for naphthalene total oxidation is shown in Figure 4-18. The carbon balance varied at lower temperatures (below 150 °C) indicating adsorption of naphthalene was occurring at these temperatures. Only CO_2 and naphthalene were observed in the GC traces, indicating no gaseous partial oxidation products were formed. The trends observed from propane total oxidation are mirrored for naphthalene total oxidation, with the catalyst with the most washing showing the highest activity. Decreasing the amount of water used to wash the $Ce_{0.25}Mn_{0.75}O_x$ lead to a decrease in 25 °C in the T_{100} temperature. As seen in the propane total oxidation, the unwashed $Ce_{0.25}Mn_{0.75}O_x$ had a similar naphthalene total oxidation activity compared to the reference catalyst. Whereas the increased amount of washing didn't affect the T_{100}

temperature for naphthalene total oxidation. Activity at lower temperatures were significantly enhanced by the increased washing of the $Ce_{0.25}Mn_{0.75}O_x$ catalyst.

4.3.2 Catalyst characterisation

4.3.2.1 X-ray diffraction

The XRD patterns of the $Ce_{0.25}Mn_{0.75}O_x$ with different washing protocols is shown in Figure 4-19. The pattern of the sample washed with 0 l of water showed dominant reflections with high intensity at 28 °, 32 °, 48 ° and 57 °. This indicates the presence of cubic ceria. Along with these large reflections, minor reflections at 38 ° were observed. These indicate the presence of manganese oxides with the MnO_2 phase. Characteristic reflections from ceria along with reflections at 37 °, 44 ° and 57 ° were observed on the catalyst washed with 2 l of water. This indicates manganese oxide is present in the Mn_2O_3 phase. The sample washed with 2 l of water similar pattern to the one observed for the sample washed with 1 l of water. However the reflections were more defined indicating the samples become more crystalline as the volume of water used for washing increased. The presence of bulk phase MnO_2 in the 0 l washed sample is a factor for the poor total oxidation activity observed for the sample. MnO_2 reported to have lower VOC total oxidation activity compared to Mn_2O_3. Therefore, with the $Ce_{0.25}Mn_{0.75}O_x$ washed with more water showing the Mn_2O_3 phase, this could lead to the higher activity observed in these samples.

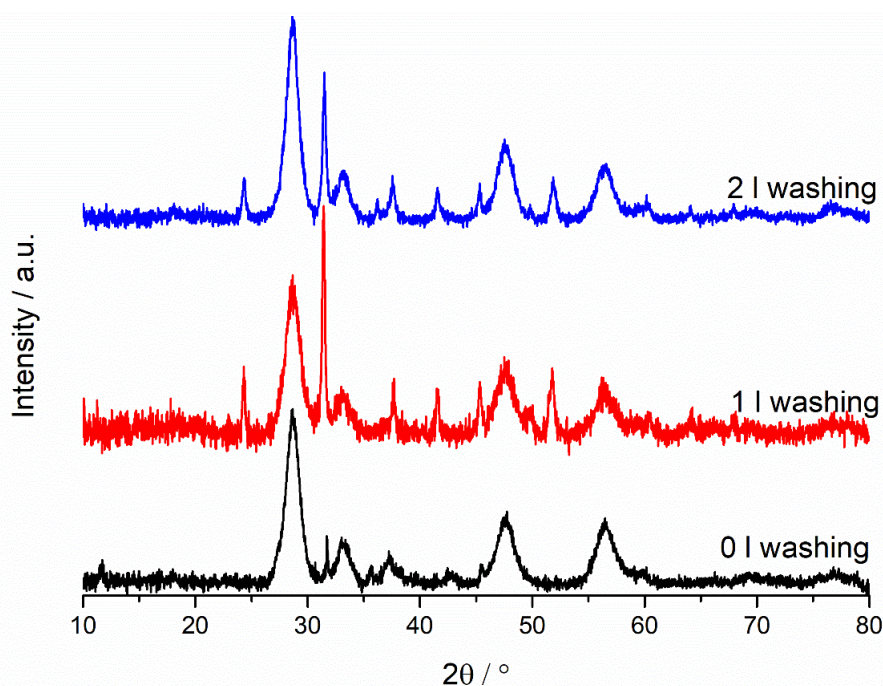Figure 4-19: Powder XRD patterns of the $Ce_{0.25}Mn_{0.75}O_x$ prepared using *via* co-precipitation with sodium carbonate using different washing protocols

Along with increasing crystallinity of the manganese oxide sample, the average crystallite size increased, Table 4-9, as the amount of water used for washing increased. As the amount of water used to wash the catalysts increases, there was a decrease in crystallite size of ceria. Along with this there was an increase in the manganese oxide crystallite size. The difference in crystallite size may have occurred from varying concentrations of sodium in the bulk of the mixed metal oxide. The presence of sodium may stabilise the size of the manganese oxide crystallite. With increased washing leading to less sodium, this will lead to less sodium stabilisation of the manganese causing the increase in crystallite size.

The d-spacing and unit cell volume was calculated using the ceria (200) lattice plane, Table 4-9. The $Ce_{0.25}Mn_{0.75}O_x$ washed with 0 l of water had the smallest unit cell volume and this value increased as the amount of water used for washing the sample increased. This suggests when no washing occurred, the manganese incorporates into the ceria lattice causing significant shrinkage of the lattice. This may also occur due to the sodium present in the bulk which will cause higher amounts of lattice contraction due to the smaller atomic radius of the sodium compared to ceria. With less potential sodium present in the $Ce_{0.25}Mn_{0.75}O_x$ washed with higher amounts of water, this may cause less lattice shrinkage to occur causing the lattice to remain a similar size.

Table 4-9: Physical properties from XRD of the $Ce_{0.25}Mn_{0.75}O_x$ prepared *via* co-precipitation with sodium carbonate using different washing protocols

Sample	Phases present	Position of CeO_2 (111) reflection / °	Average crystallite size / Å		d-spacing from (200) lattice plane / Å	Unit Cell Volume / Å^3
			CeO_2	MnO_x		
0 l washing	CeO_2 MnO_2	28.6	65	90	2.51	126.506
1 l washing	CeO_2 Mn_2O_3	28.7	41	152	2.69	155.721
2 l washing	CeO_2 Mn_2O_3	28.7	32	269	2.70	157.464

4.3.2.2 Surface area

The surface areas of the $Ce_{0.25}Mn_{0.75}O_x$ washed using different volumes of water are shown in Table 4-10. The sample washed with 0 l of water had the lowest surface area and this increased upon increasing levelling of washing. This suggests that the washing removes material which may deposit on the surface of the catalysts. This deposited

149

material may block pores or change the morphology which lowers the surface area. This could be from formation of lower surface area sodium species which may block surface sites. Therefore as more of these species are removed upon washing, this will cause the exposure of the higher surface area ceria-manganese surface leading to the higher surface area observed.

Table 4-10: Surface areas of the $Ce_{0.25}Mn_{0.75}O_x$ prepared *via* co-precipitation with sodium carbonate using different washing protocols. Calculated using 5-point N_2 adsorption BET analysis

Sample	BET Surface area / $m^2 g^{-1}$	Surface area normalised rate of propane total oxidation at 300 °C (10^{-8}) / mol s^{-1} m^{-2}	Surface area normalised rate of naphthalene total oxidation at 175 °C (10^{-11}) / mol s^{-1} m^{-2}
0 l washing	32	2.10	0.94
1 l washing	41	3.38	1.93
2 l washing	59	4.41	2.16

With increasing surface area, the activity of the ceria based catalysts is expected to increase [14]. The effect of surface area on rates of propane and naphthalene total oxidation is shown in the table above. As the surface areas increase, so does the surface area normalised rate of propane and naphthalene total oxidation. This suggests other factors including surface area influence the activity of these catalysts which will be discussed later.

4.3.2.3   Temperature programmed reduction

Temperature programmed reduction profiles of the $Ce_{0.25}Mn_{0.75}O_x$ washed with different amounts of water are shown in Figure 4-20. The profile of the sample washed with 0 l of water had a large reduction region between 200-500 °C. Within this region was a set of two peaks around 400 °C and 480 °C along with a large shoulder peak leading into a doublet of peaks. The sample washed with 2 l of water had a similar reduction profile to the sample washed with 1 l. However, the peaks were of lower intensity and had shifted to lower temperature by 20 °C. Simultaneously, peaks assigned to reduction of bulk ceria had reduced in intensity and shifted by 50 °C. to a lower temperature
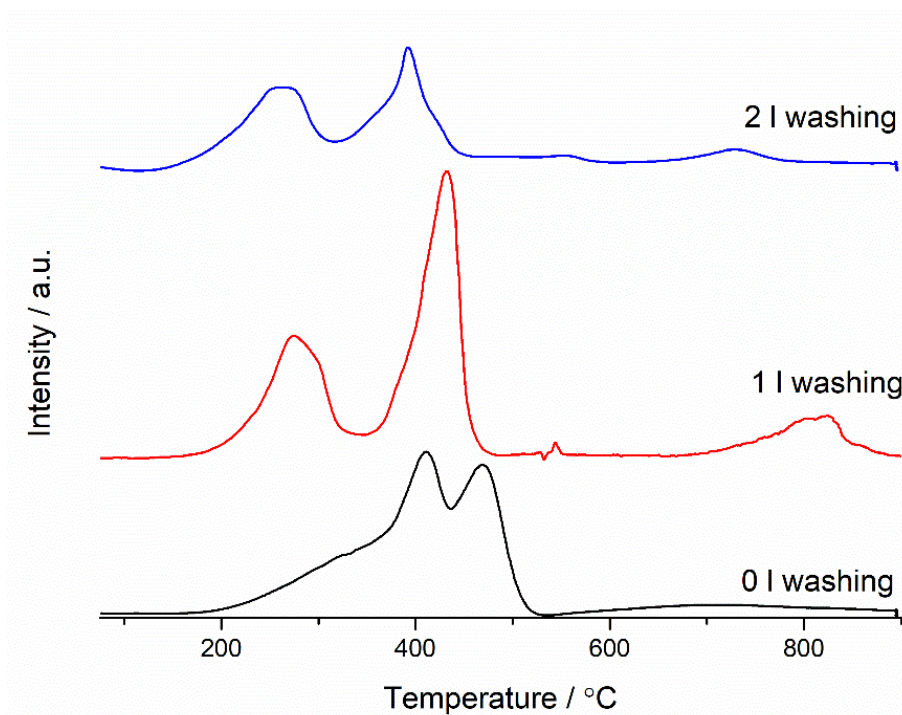
Figure 4-20: Hydrogen temperature programmed reduction profiles of the $Ce_{0.25}Mn_{0.75}O_x$ prepared *via* autotitration using different washing protocols. Reaction conditions: 30 mg sample, 30 ml min^{-1}, 10 % H_2/ Ar, temperature range: 50-850 °C

The shape of the reduction peaks of the $Ce_{0.25}Mn_{0.75}O_x$ sample washed with 0 l water indicates the manganese oxide is present in the MnO_2 phase. This is because the shoulder and first reduction peak are characteristic for MnO_2. MnO_2 reduced to Mn_3O_4 which will then reduce to MnO as seen by the peak at higher temperature in the sample. This confirms the observations from XRD, as reflections of low intensity relating to bulk MnO_2 were observed. The shapes of the peaks may have been effected by the presence of ceria, however, as mentioned previously the extent of this effect is difficult to define. The reduction profile of the sample washed with 2 l of water has reduction peaks characteristic of Mn_2O_3, therefore confirming the manganese oxide phase identification from XRD. Bulk ceria reduction was also observed on this sample. However the decrease in reduction temperature indicates the manganese is directly effected the reduction of bulk ceria. With both surface and bulk reduction temperatures decreasing upon increasing washing, this suggests the ease of reduction in both regions has increased. At lower temperatures, increased amounts of active oxygen species could be available for the total oxidation reactions compared to the samples washed with less water. This will allow the Mars van-Krevelen reactions to occur at lower temperatures, hence the decrease in reaction temperatures observed in the sample washed with 2 l of water. This will lead to an increase in VOC total oxidation activity.

4.3.2.4 Electron microscopy
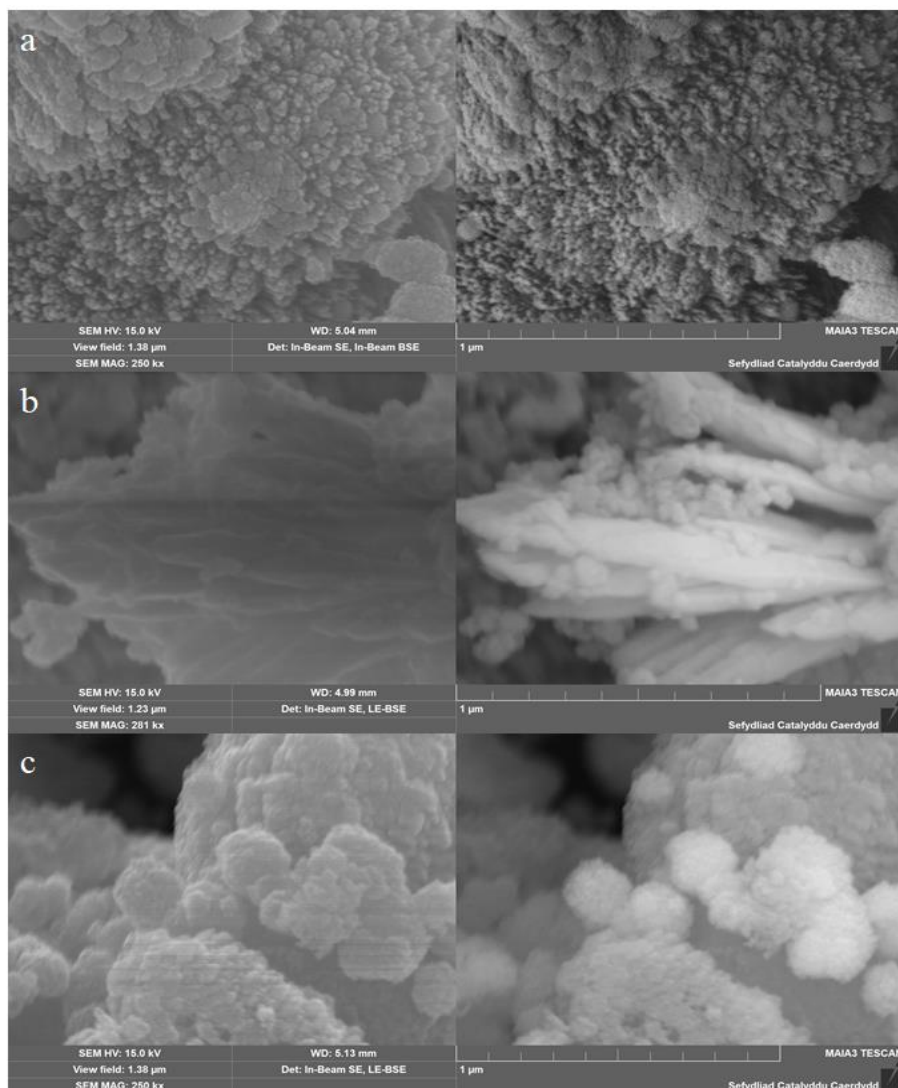
4.3.2.4.1 Scanning electron microscopy

Figure 4-21: Secondary electron (left) and back-scattered electron (right) micrographs of the $Ce_{0.25}Mn_{0.75}O_x$ prepared *via* autotitration using different washing protocols. (a) 0 l washing, (b) 1 l washing and (c) 2 l washing. Image magnification: 250 kx

The electron micrographs of the $Ce_{0.25}Mn_{0.75}O_x$ washed with different volumes of water are shown in Figure 4-21. All samples have bulbous shaped morphologies which were observed in the images of the ceria-manganese mixed metal oxides with high manganese content. There was no significant contrast in the back-scattered image of the sample washed with 0 l of water. This is in line with observations from XRD in which the ceria was the dominant phase. The back-scattered electron images of the samples washed with 1 l and 2 l of water had significant difference in contrast. This indicates phase separation has occurred, confirming the observations from XRD, in which reflections from both manganese oxides and ceria were observed.

4.3.2.4.2 Energy dispersive x-ray spectroscopy

Table 4-11: SEM-EDX derived bulk element analysis of the $Ce_{0.25}Mn_{0.75}O_x$ prepared *via* autotitration using different washing protocols.

Sample	Concentration / At.%				Relative Ce:Mn concentrations / %	
	Ce	Mn	O	Na	Ce	Mn
0 l washing	7.2	22.7	65.2	4.9	24.1	75.9
1 l washing	5.1	22.8	66.8	5.3	18.2	81.8
2 l washing	5.0	19.6	74.8	0.6	20.3	79.7

Along with scanning electron microscopy, EDX analysis was carried out with bulk elemental analysis shown in Table 4-11. The relative concentrations of each metal in each sample were close to the nominal synthesis values. All the ceria-manganese mixed metal oxides prepared *via* autotitration in the previous section had significantly high amounts of sodium present in the bulk of the samples. The 0 l washed sample had similar sodium content to the original sample washed with 1 l of water. However once the amount of water used to wash the samples increased, the amount of sodium present in the bulk decreased by ~90 %. This indicates increased volumes of water are required to more efficiently remove the sodium from the bulk of the sample.
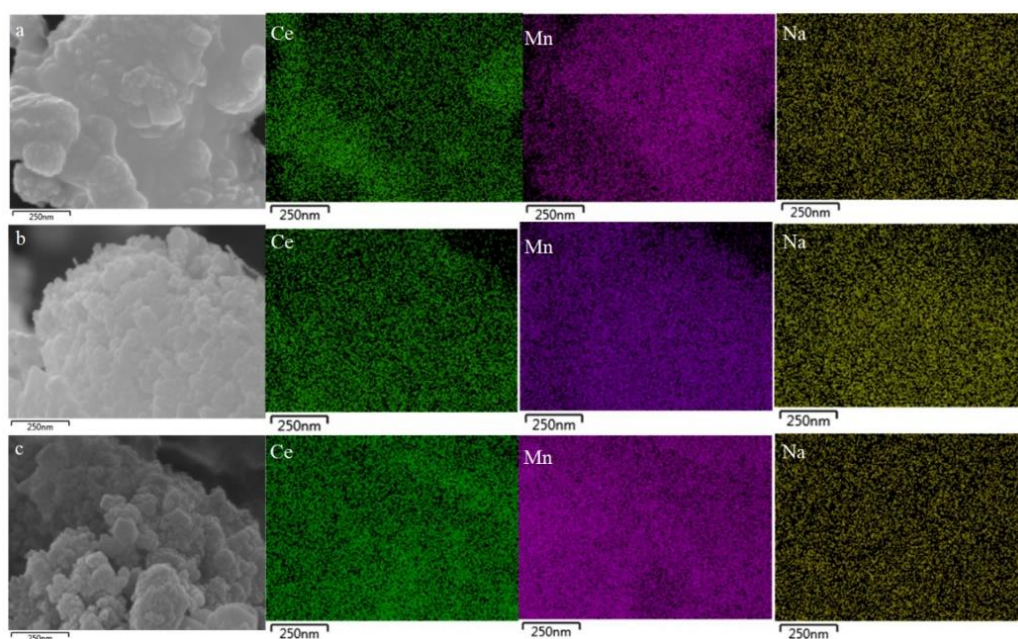

Figure 4-22: SEM-EDX mapping of the $Ce_{0.25}Mn_{0.75}O_x$ prepared *via* autotitration using different washing protocols. (a) 0 l washing, (b) 1 l washing and (c) 2 l washing. Showing cerium (green), manganese (pink) and sodium (yellow)

The SEM-EDX elemental maps of the $Ce_{0.25}Mn_{0.75}O_x$ washed with varying amounts of water are shown in Figure 4-22. As seen in the previous maps of the autotitrated ceria-

manganese mixed metal oxides, the sodium is present homogeneously across the sample. Some mixing of the cerium and manganese has occurred, however, all samples have large regions of separated cerium and manganese present. This correlates with the XRD analysis, in which reflections from both metal oxides were observed in all sample patterns. However in the XRD pattern of the $Ce_{0.25}Mn_{0.75}O_x$ sample washed with 0 l of water there were fewer reflections assigned to manganese oxides compared to the other samples. This suggests the manganese oxides present in the bulk of the sample washed with 0 l of water could be amorphous or have too small crystallite size to be observed in XRD.

4.3.2.4.3 Transmission electron microscopy
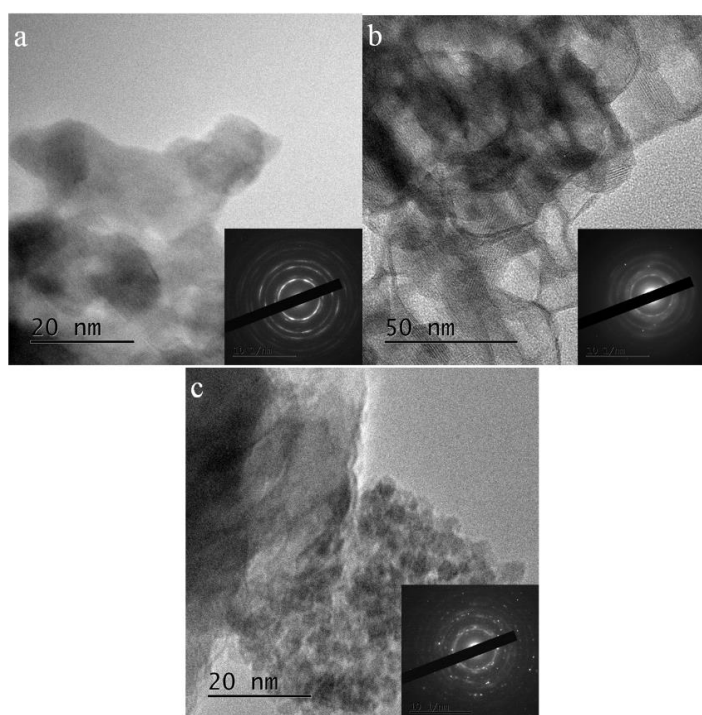
Figure 4-23: High magnification TEM images of the $Ce_{0.25}Mn_{0.75}O_x$ prepared *via* autotitration using different washing protocols. Inset: selected area electron diffraction pattern of larger 250 nm areas. (a) 0 l washing, (b) 1 l washing and (c) 2 l washing.

TEM images along with selected area electron diffraction are shown in Figure 4-23. The image of the 0 l $Ce_{0.25}Mn_{0.75}O_x$ sample is like the one observed for the sample washed with 1 l of water. It has several ceria crystallites present along with the presence of some plate-like structures, originating from manganese oxides. The plate-like structures have formed due to the presence of bulk sodium in the lattice manganese oxides [37]. The similarities may arise from the similar bulk sodium content of the 0 l and 1 l washed sample. This coincides with the XRD patterns in which crystalline ceria was the main species present, and manganese oxides were the minor phase. A difference in size of the

154

plate like crystallites is observable between the 0 l and 1 l washed samples. This coincides with the measurements of crystallites from XRD in which the 0 l had a smaller crystallite size than the 1 l catalyst.

The sampled washed with 2 l of water had a different morphology compared to the samples washed with less water. Two separate areas were observed, one containing a random array of small crystallites and the other, a layer of crystallite sheets. The plate like morphologies were not observed in this sample. This could be due to the decreased amounts of sodium present in the bulk of the sample washed with 2 l. With sodium noted to cause the formation of these manganese oxide plates. The $Ce_{0.25}Mn_{0.75}O_x$ had the most observable phase separation in XRD from the three samples analysed. The presence of the two distinct morphologies confirms the phase separation observed in the XRD and EDX mapping of the sample.

The selected area electron diffraction is shown in the inset of the images in Figure 4-23. The $Ce_{0.25}Mn_{0.75}O_x$ washed had four broken diffraction rings along with visible spots. As the volume used to wash the samples increased, these rings became more diffuse and spots became more intense in the diffraction patterns. The diffraction rings were indexed to the presence of ceria in the cubic phase. The spots are assigned to the presence of bulk manganese oxides species. As mentioned in the XRD analysis, the dominance of the ceria phase in the bulk decreases upon increasing washing. This is seen by the increase of observable reflections from manganese oxide phases in XRD. This explains the decrease in the intensity of the diffraction rings and increase in the intensity of the spots.

Table 4-12: Lattice parameters of the $Ce_{0.25}Mn_{0.75}O_x$ prepared *via* autotitration using different washing protocols determined from selected area electron diffraction

Sample	Lattice parameter calculated from selected area electron diffraction / Å
0 l washing	5.40
1 l washing	8.36
2 l washing	8.96

The lattice parameters of the $Ce_{0.25}Mn_{0.75}O_x$ washed with amounts of water were calculated and shown in Table 4-12. The lattice parameter of the 0 l washed sample was calculated from the (200) ceria lattice plane and the other two were calculated from the brightest spots. The d-spacing of the 0 l washed sample is slightly higher than the lattice parameter calculated for the ceria, suggesting the presence of manganese and sodium is influencing the ceria lattice. The $Ce_{0.25}Mn_{0.75}O_x$ washed with 2 l of water had a larger lattice parameter than the sample washed with 1 l of water. The lattice parameter Mn_2O_3

155

is 9.413 Å, and both samples have lattice parameters close to this value. This indicates Mn_2O_3 is the manganese oxide phase present in the washed $Ce_{0.25}Mn_{0.75}O_x$. The variation in lattice parameter between the literature and experimental values may have occurred to due contraction of manganese oxide from other species such as sodium. With more sodium present in the bulk of the 1 l washed $Ce_{0.25}Mn_{0.75}O_x$ compared to the 2 l, this will lead to increased contraction of the lattice.

4.3.2.5   X-ray photoelectron spectroscopy

The elemental composition of the surface of the $Ce_{0.25}Mn_{0.75}O_x$ washed with different amounts of water is shown in Table 4-13 The main observation between the different washing volumes is the reduction in the amounts of surface sodium upon increasing washing volumes. The bulk elemental analysis showed the 0 l and 1 l washed samples had similar amounts of sodium present in the bulk. The sodium concentrations on the 2 l washed sample was similar for both bulk and surface elemental analysis. This suggests that small volumes of washing (1 l) have an impact on the surface sodium species on the $Ce_{0.25}Mn_{0.75}O_x$ and higher volumes of washing lead to reduction in the presence of both surface and bulk sodium species.

Table 4-13: XPS derived surface elemental concentrations for the $Ce_{0.25}Mn_{0.75}O_x$ prepared *via* autotitration using different washing protocols.

Sample	Concentration / At.%				Relative Ce:Mn concentrations / %	
	Ce	Mn	O	Na	Ce	Mn
0 l washing	14.3	20.3	54.5	15.9	41.3	58.7
1 l washing	9.2	15.9	63.0	11.9	36.7	63.3
2 l washing	12.4	16.8	70.0	0.8	42.5	57.5

Less surface sodium present as the volume of water used to wash increased. This may lead to the increased surface areas observed as the sodium may block pores or deposit on defect sites which will increase the surface area of the samples. With less sodium present on the surface with increased washing, these sites will be exposed leading to the increase in surface area observed. With less sodium on the surface of the $Ce_{0.25}Mn_{0.75}O_x$ washed with 1 l of water compared to sample washed with 0 l water this explains the difference in total oxidation activity observed for these samples. However the sampled washed with 2 l of water has less surface and bulk sodium compared to the sample washed with 1 l of water. This will lead to even less sodium poisoning and therefore increased total oxidation activity, as seen in manganese containing mixed metal oxides for CO oxidation [46].
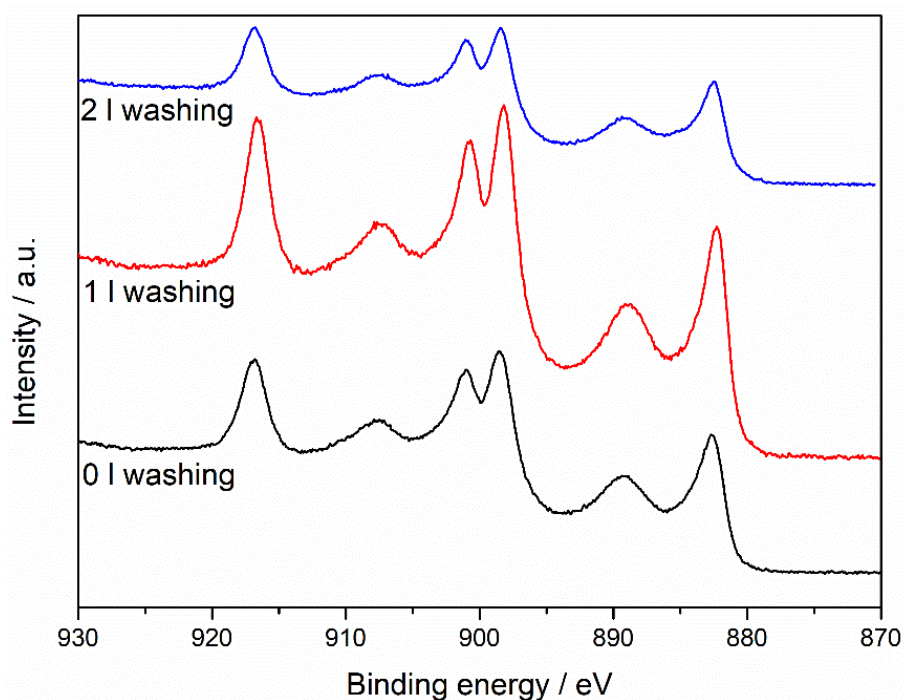
Figure 4-24: XPS spectra of the Ce 3d peaks for the $Ce_{0.25}Mn_{0.75}O_x$ prepared *via* autotitration using different washing protocols

The XPS of the Ce 3d peaks of the $Ce_{0.25}Mn_{0.75}O_x$ washed with different amounts of water is shown in Figure 4-24. There is a significant amount of Ce^{4+} present on all samples as seen by the intense peak at 917 eV. The doublet peaks between 897-903 eV are of similar symmetry indicating the extent of washing doesn't affect the concentration of Ce^{3+} in the samples. However there is a slight shift to lower binding energies upon increasing washing, suggesting the concentrations Ce^{3+} decreases upon washing. This may have occurred due to the presence of sodium on the surface of the catalysts The increased presence of sodium will negate any VOC total oxidation activity increase the Ce^{3+} will produce.

The Mn 3p XPS spectra of the $Ce_{0.25}Mn_{0.75}O_x$ washed with varying amounts of water are shown in Figure 4-25. As seen section 4.2.3.6, no satellite peak was observed at 647 eV in the spectra suggesting no MnO was observed on the ceria-manganese mixed metal oxides. Due to the intensity of the peaks, the splitting between them can be used to estimate the oxidation state [47]. Mn^{4+} is reported to have the smallest gap between peaks, with this extending upon decrease in oxidation state. The gap between the peaks extends upon increasing washing of the $Ce_{0.25}Mn_{0.75}O_x$ suggesting the oxidation state of the manganese decreases upon increased washing [48].
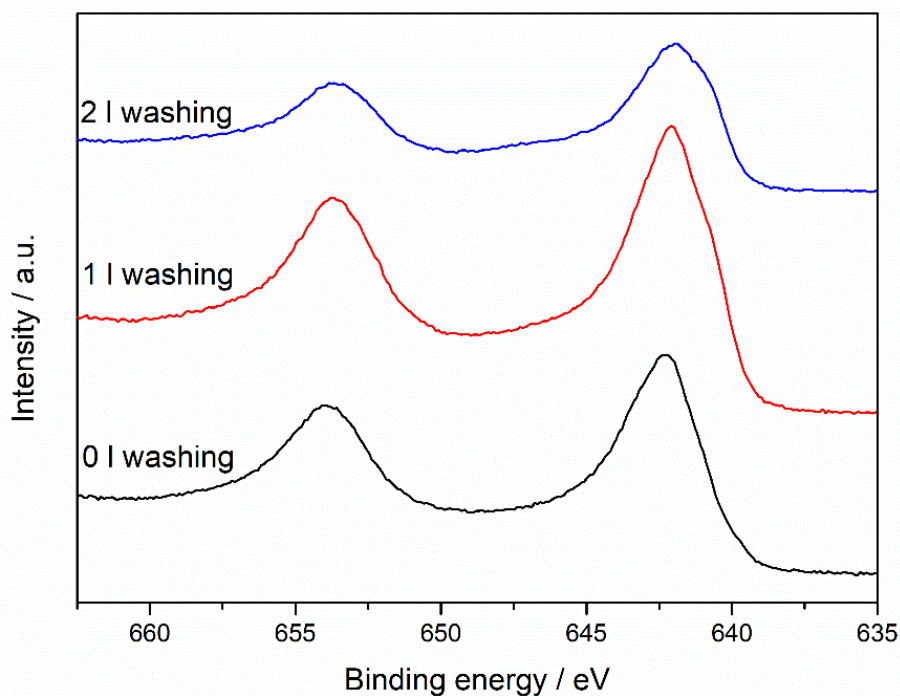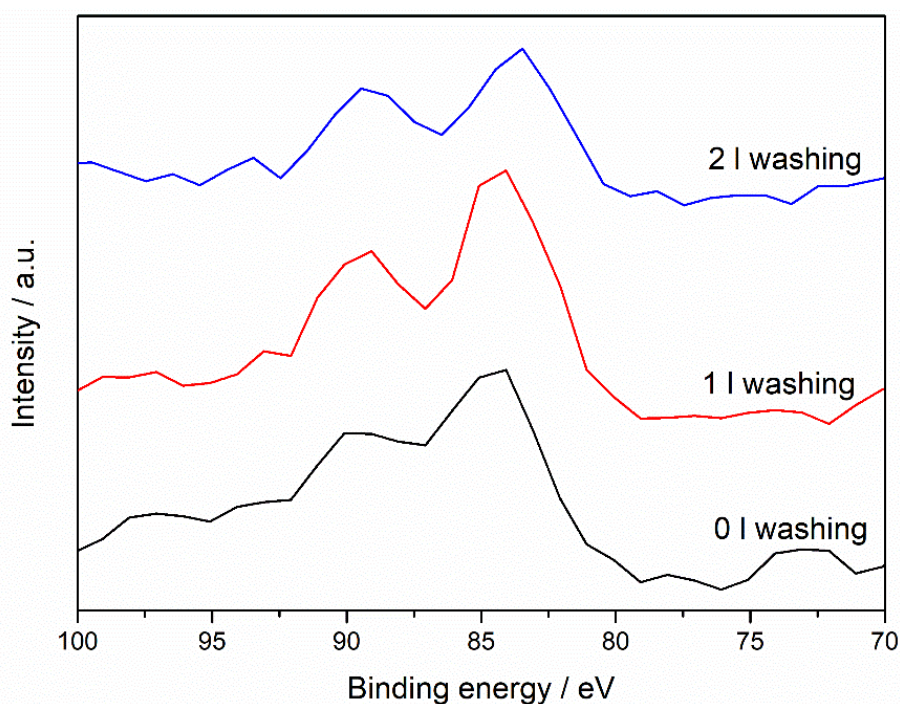
Figure 4-25: XPS spectra of the Mn 2p for the $Ce_{0.25}Mn_{0.75}O_x$ prepared *via* autotitration using different washing protocols

To gain a further understanding of the oxidation state of the manganese in the manganese oxides, the 3s spectra can be investigated, Figure 4-26. As seen in the figure above, the peaks are of high intensity and the splitting between them increases upon increased water volumes used to wash the $Ce_{0.25}Mn_{0.75}O_x$. The splitting of the Mn 3s peaks is shown in Table 4-14. All values are below 6.0 eV indicating no Mn^{2+} is present on the surface of the catalysts, as seen in the XPS 2p spectra [47]. The $Ce_{0.25}Mn_{0.75}O_x$ washed with 2 l is in the Mn^{3+} oxidation state, making the manganese oxide Mn_2O_3. However the sample which wasn't washed was in the 4+ oxidation state, so the manganese oxide is present in the MnO_2 phase. This is in line with observations from XRD, suggesting both bulk and surface oxidation states are the same.

Figure 4-26: XPS spectra of the Mn 3s for the $Ce_{0.25}Mn_{0.75}O_x$ prepared *via* autotitration using different washing protocols

With the Mn_2O_3 the more active phase for VOC total oxidation compared to MnO_2 [3]. The presence of this on both the surface and bulk of the $Ce_{0.25}Mn_{0.75}O_x$ washed samples this explains the increased activity of the samples compared to the unwashed $Ce_{0.25}Mn_{0.75}O_x$. However with increased amounts of sodium present on the surface of the $Ce_{0.25}Mn_{0.75}O_x$ washed with 1 l of water this will poison the catalyst causing the decreased activity compared to the sample washed with 2 l.

Table 4-14: Magnitude of peak splitting in the Mn 3s spectra for the $Ce_{0.25}Mn_{0.75}O_x$ prepared *via* autotitration using different washing protocols

Sample	Magnitude of Mn 3s peak splitting / eV	Surface oxidation state of Mn (all +)
0 l washing	5.2	4
1 l washing	5.5	3
2 l washing	5.9	3

The fitted O 1s spectra of the $Ce_{0.25}Mn_{0.75}O_x$ washed with various amounts of water are shown in Figure 4-27. Both lattice (O_α) and defect (O_β) oxygen species are present, between 529-31 eV and 531-3 eV respectively [14,43], on all samples. As mentioned previously the shift in binding energy indicates the extent of synergistic interaction between ceria and manganese oxide species. As the extent of washing increases, there is a noticeable shift to lower binding energies, indicating poor interaction between ceria and manganese oxides. This follows the observations from XRD, in which increased phase

159

segregation was observed upon increasing washing volumes. This indicates the surface may also have phase segregation occurring as well as the bulk. This phase separation may influence total oxidation activity, however, the extent of this is difficult to quantify.
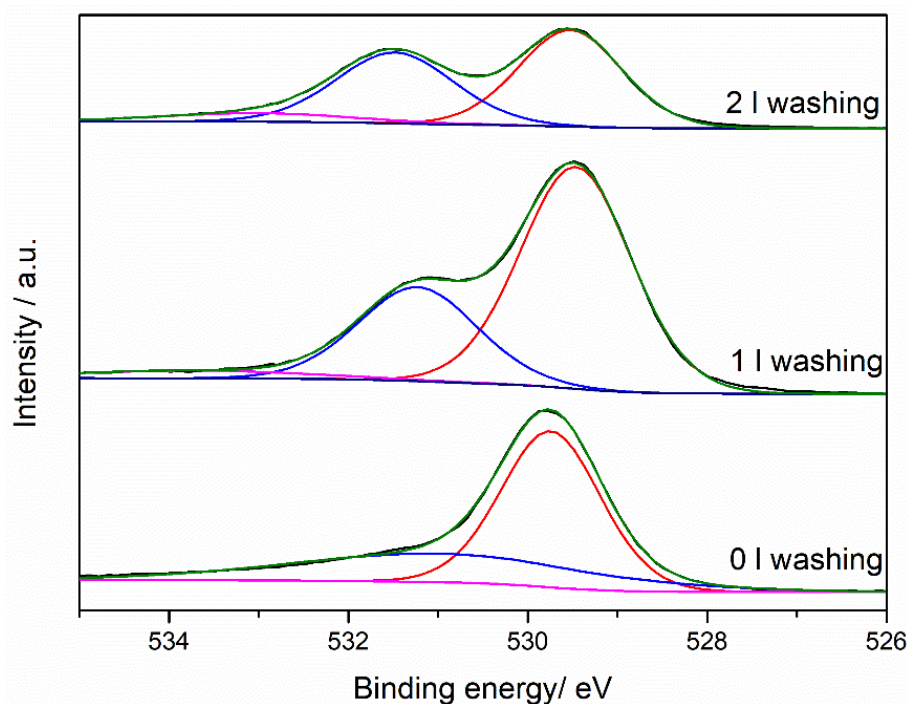

Figure 4-27: XPS spectra for the O 1s peak the $Ce_{0.25}Mn_{0.75}O_x$ prepared *via* autotitration using different washing protocols

The defect oxygen species increase upon increased volumes of washing on the $Ce_{0.25}Mn_{0.75}O_x$, shown in Table 4-15. The O_β of the $Ce_{0.25}Mn_{0.75}O_x$ washed with 1 l of water was the lowest of the 3 samples. The increased O_β of the sample washed with no water may have been caused by the presence of sodium hydroxides which are present at 531.3 eV [45]. Therefore, increased concentrations of sodium hydroxide will lead to increased concentrations of O_β compared to the other samples.

Table 4-15: XPS derived concentrations of the lattice and defect oxygen species for the $Ce_{0.25}Mn_{0.75}O_x$ prepared *via* autotitration using different washing protocols

Sample	Relative concentration of O_α / %	Relative concentration of O_β / %
0 l washing	64.6	35.4
1 l washing	68.7	31.3
2 l washing	50.2	49.8

With only small surface concentrations of sodium present on the $Ce_{0.25}Mn_{0.75}O_x$ washed with 2 l of water, the increased O_β concentration cannot be attributed to the presence of sodium species. The higher surface concentrations of sodium on the $Ce_{0.25}Mn_{0.75}O_x$ washed with 0 l and 1 l of water may adsorb onto the oxygen defect sites. Therefore once

these sodium species are removed during increased washing, more defect sites will be exposed. This will lead to an increase in in defect concentration. These are known to increased VOC total oxidation activity due to increased activation of oxygen on these sites as well as increased oxygen cycling from the lattice, allowing for the Mars van-Krevelen mechanism to be enhanced.

4.4 The effect of preparation method of the $Ce_{0.25}Mn_{0.75}O_x$ catalyst on the activity for VOC total oxidation

The effect of washing $Ce_{0.25}Mn_{0.75}O_x$ shows that the presence of sodium in the surface and bulk has a significant effect on the propane and naphthalene total oxidation activity. Therefore catalyst preparation methods which don't involve a sodium based precipitation agent were used to further optimise the $Ce_{0.25}Mn_{0.75}O_x$ catalyst. To minimise the effects of sodium, $Ce_{0.25}Mn_{0.75}O_x$ catalysts were prepared using a sodium free precipitation agent, citric acid, oxalic acid and urea, or ball milling of cerium and manganese nitrates or carbonates.

4.4.1 Catalyst performance
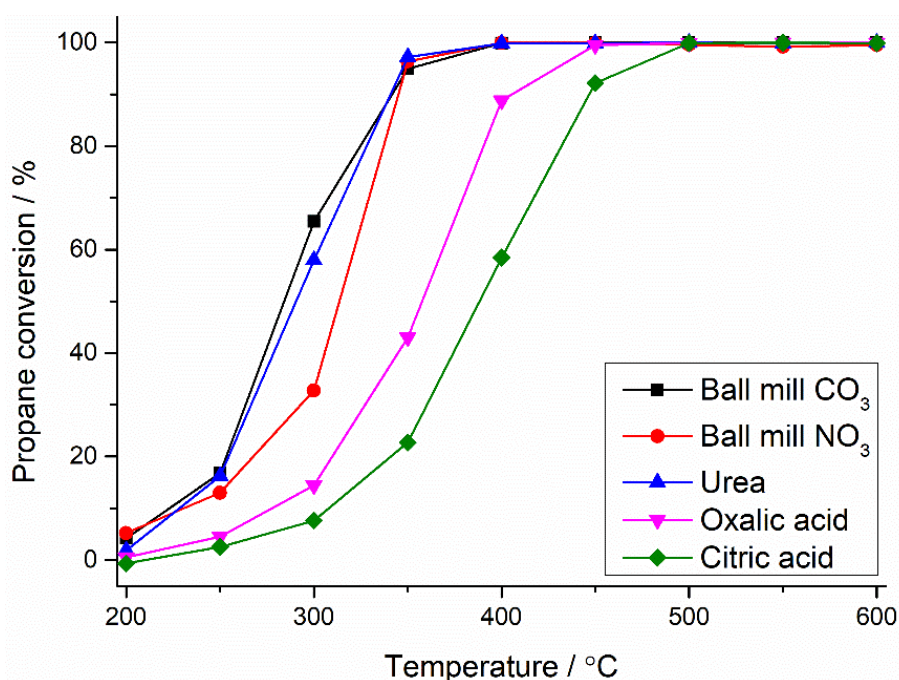
4.4.1.1 Propane total oxidation

Figure 4-28: Catalytic activities for the total oxidation of propane of the $Ce_{0.25}Mn_{0.75}O_x$ prepared *via* different preparation methods. Reaction conditions: GHSV = 45,000 h^{-1}, temperature 200-600 °C, 5000 ppm propane in air. Legend refers to the preparation method used to make the $Ce_{0.25}Mn_{0.75}O_x$ catalyst

The propane total oxidation activity of the $Ce_{0.25}Mn_{0.75}O_x$ prepared using a variety of preparation methods is shown in Figure 4-28. All catalysts showed significant performance for the total oxidation of propane with high selectivity to CO_2 (>99 %) throughout the reaction. The activity followed the trend shown below:

Ball mill- CO_3 ~ Urea > Ball mill- NO_3 > Oxalic acid > 5 % Pd/Al_2O_3 > Citric acid

The $Ce_{0.25}Mn_{0.75}O_x$ sampled prepared by ball milling of carbonate precursors had a similar propane total oxidation activity profile to the catalyst prepared by autotitration with 2 l washing. However the activity of the $Ce_{0.25}Mn_{0.75}O_x$ prepared using other methods showed activity lower than the autotitrated sample and the palladium reference catalyst. Previous studies reported the preparation method of $Ce_{0.25}Mn_{0.75}O_x$ has a profound effect on VOC total oxidation activity [49].
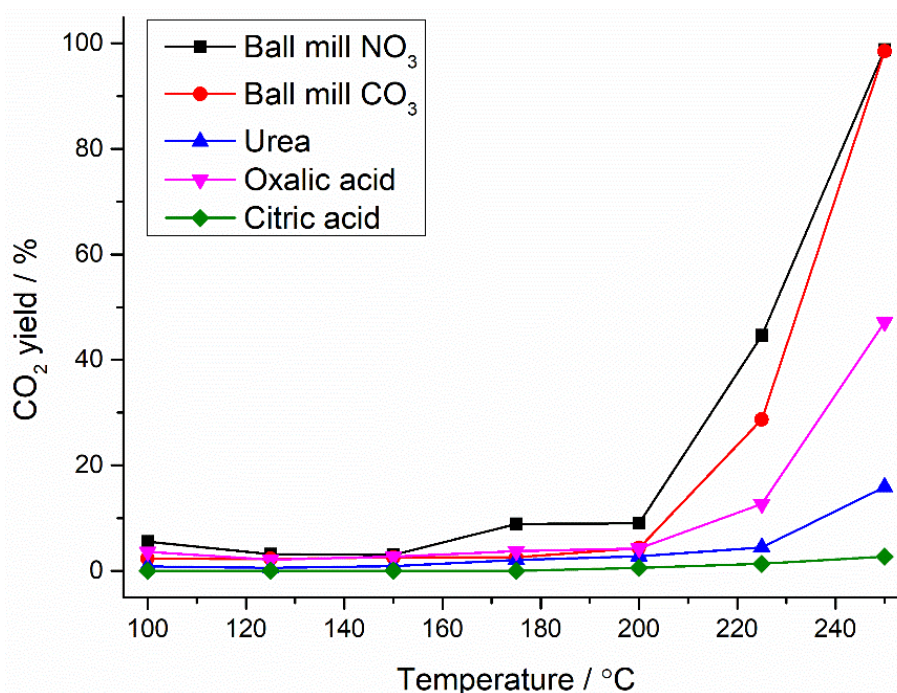
4.4.1.2 Naphthalene total oxidation

Figure 4-29: Catalytic activities for the total oxidation of naphthalene of the $Ce_{0.25}Mn_{0.75}O_x$ prepared *via* different preparation methods. Reaction conditions: GHSV = 45,000 h^{-1}, temperature 200-250 °C, 100 vppm naphthalene in 20 % O_2 balanced with He. Legend refers to the preparation method used to make the $Ce_{0.25}Mn_{0.75}O_x$ catalyst

Figure 4-29 shows the naphthalene total oxidation activity of the $Ce_{0.25}Mn_{0.75}O_x$ prepared using different methods. The sample prepared using citric acid showed no observable activity over the temperature range. Other catalysts had noticeable naphthalene total oxidation activity at temperatures above 200 °C on all samples. This is considerably different to the naphthalene activity profiles observed for the $Ce_{0.25}Mn_{0.75}O_x$ prepared *via* autotitration, which showed 100 % CO_2 yield by 200 °C. As mentioned earlier, the

preparation method has a significant effect on VOC total oxidation, especially for total oxidation of aromatic VOCs [49,50]. All $Ce_{0.25}Mn_{0.75}O_x$ prepared using the various preparation methods performed considerably poorer compared to palladium reference catalyst. Overall a trend for naphthalene total oxidation over the $Ce_{0.25}Mn_{0.75}O_x$ prepared using different methods is shown below:

5 % Pd/Al_2O_3 > Ball mill-NO_3 > Ball mill-CO_3 > Oxalic acid > Urea > Citric acid

Only carbon dioxide and naphthalene were observed in the GC analysis during all naphthalene total oxidation reactions. This indicates the total oxidation pathway occurred during the reactions. However the carbon balance varied at lower temperatures on $Ce_{0.25}Mn_{0.75}O_x$ prepared *via* ball milling and oxalic acid. This indicates naphthalene adsorption occurs at lower temperatures. No variation in the carbon balance was observed during the naphthalene total oxidation reaction over the $Ce_{0.25}Mn_{0.75}O_x$ prepared using urea and citric acid.

4.4.2 Catalyst characterisation
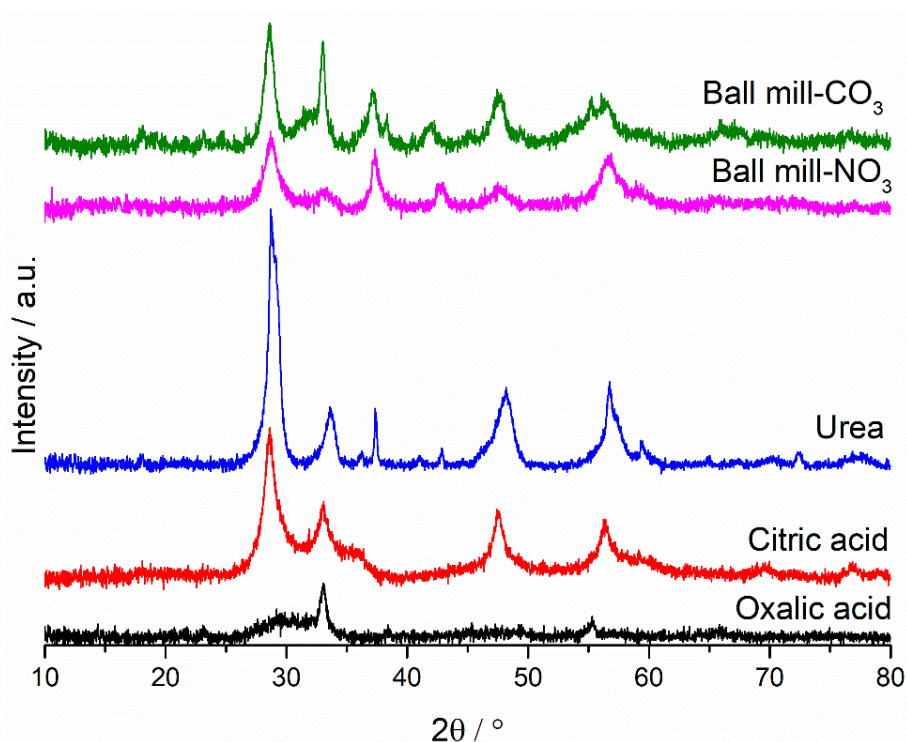
4.4.2.1 X-ray diffraction

Figure 4-30: Powder XRD patterns of the $Ce_{0.25}Mn_{0.75}O_x$ prepared using *via* different preparation methods

The XRD patterns of the $Ce_{0.25}Mn_{0.75}O_x$ prepared using various methods are shown in Figure 4-30. There is no similarity between the patterns indicating the preparation method significantly effects the crystallinity and phases present in the bulk of the catalyst. The catalyst prepared using oxalic acid was the least crystalline, which has been recorded

163

previously [51], and the sample prepared by urea the most crystalline. Both mechanochemically prepared $Ce_{0.25}Mn_{0.75}O_x$ had similar crystallinity.

The metal oxide phases present on each sample is shown in Table 4-16. Only the $Ce_{0.25}Mn_{0.75}O_x$ prepared using oxalic and citric acid showed metal oxides phases from a single metal oxide. The sampled prepared using oxalic acid had three weak reflections characteristic of the Mn_2O_3 phase. However due to the amorphous nature of the sample it was difficult to identify if any ceria phases were present. The sample prepared by citric acid only had observable phases from cubic fluorite ceria. However, a shoulder peak was observed at 35°, which could relate to a manganese oxide phase but without any other distinguishable peaks, the phase of the manganese oxide couldn't be determined. The manganese oxides may also be present as an amorphous phase, making it difficult to confirm the oxidation state of the manganese oxide.

Table 4-16: Physical properties of the $Ce_{0.25}Mn_{0.75}O_x$ catalyst prepared *via* different preparation methods

Sample	Phases present	Position of CeO$_2$ (111) reflection / °	Average crystallite size / Å		d-spacing from (200) lattice plane / Å	Unit Cell Volume / Å^3
			CeO$_2$	MnO$_x$		
Ball Mill- CO$_3$	CeO$_2$ Mn$_2$O$_3$	28.4	156	216	2.76	168.20
Ball Mill- NO$_3$	CeO$_2$ MnO$_2$	28.8	63	111	2.70	157.46
Urea	CeO$_2$ MnO$_2$	28.8	75	68	2.67	152.27
Oxalic acid	Mn$_2$O$_3$	-	-	51	-	-
Citric acid	CeO$_2$	28.7	101	89	2.70	157.46

The $Ce_{0.25}Mn_{0.75}O_x$ prepared by urea and mechanochemical grinding had both ceria and manganese oxide phases present in the bulk of the samples. All had cubic ceria present in the bulk of the sample. Along with this Mn_2O_3 was present in the sample prepared *via* mechanochemical grinding using carbonates and MnO_2 was observed on the other samples. The presence of Mn_2O_3 may explain the increased VOC total oxidation activity observed for the $Ce_{0.25}Mn_{0.75}O_x$ prepared using mechanochemical grinding of carbonate precursors, as this manganese oxide phase is noted to be more active for VOC total oxidation. Even though the $Ce_{0.25}Mn_{0.75}O_x$ prepared using oxalic acid had the Mn_2O_3 phase too, it was present in smaller crystallites. As seen from the washing investigation,

the sample washed with 2 l of water had the largest manganese oxide crystallite size and this sample also had the highest VOC total oxidation activity out of the range of catalysts. Even though the sample prepared by oxalic acid had Mn_2O_3 present, the smaller crystallite size may cause the lower activity of the sample compared to the other $Ce_{0.25}Mn_{0.75}O_x$ containing the Mn_2O_3.

The position of the ceria (111) lattice plane is shown in Table 4-16. The mechanochemically prepared sample from carbonates had the lowest peak position compared to the other samples. The increase in peak position suggests incorporation of the manganese into the ceria lattice. With the carbonate sample showing the lowest peak position, this suggests poor manganese incorporation into the ceria lattice leading to increased phase separation compared to the other samples. The phase separation is also seen in the unit cell volume, with the carbonate sample showing the largest unit cell volume. The $Ce_{0.25}Mn_{0.75}O_x$ sample prepared *via* autotitration and washed with 2 l of water also had the most phase separation in XRD, suggesting cerium and manganese oxide phase separation effects VOC total oxidation. The $Ce_{0.25}Mn_{0.75}O_x$ sampled prepared from mechanochemical grinding of carbonates also had the most observable phase separation of the $Ce_{0.25}Mn_{0.75}O_x$ prepared using different methods.

4.4.2.2 Surface area

Table 4-17: Surface area of the $Ce_{0.25}Mn_{0.75}O_x$ prepared *via* different preparation methods. Calculated using 5-point N_2 adsorption BET analysis

Sample	BET Surface area / $m^2\,g^{-1}$	Surface area normalised rate of propane total oxidation at 300 °C (10^{-8}) / $mol\,s^{-1}\,m^{-2}$	Surface area normalised rate of naphthalene total oxidation at 225 °C (10^{-11}) / $mol\,s^{-1}\,m^{-2}$
Ball mill-NO₃	44	2.72	1.09
Ball mill-CO₃	83	2.59	0.90
Urea	59	3.40	1.25
Oxalic acid	53	0.92	0.86
Citric acid	3	9.07	3.15

The surface areas of the $Ce_{0.25}Mn_{0.75}O_x$ prepared using various preparation methods are shown in Table 4-17. The catalyst prepared *via* mechanochemical grinding of carbonates a higher surface area whereas the sample prepared using citric acid had the lower surface area compared to the sample prepared by autotitration and washed with 2 l of water. Previous mixed metal oxides prepared using citric acid were reported to have very low surface areas, so this was expected [52]. All other samples had a similar surface area to the autotitrated catalyst. The catalyst preparation methods have been optimised for other

metal oxide systems. Therefore further optimisation of the $Ce_{0.25}Mn_{0.75}O_x$ preparation process, such as calcination temperature or aging times, may be required to increase the surface area of the catalysts.

The surface area normalised rates of propane and naphthalene total oxidation are shown in Table 4-17. There is no direct correlation between the surface area and propane or naphthalene total oxidation activity. The $Ce_{0.25}Mn_{0.75}O_x$ prepared using citric acid had the highest surface area normalised propane and naphthalene total oxidation. However the higher surface area normalised VOC total oxidation rates doesn't correlate with low surface area indicating other factors affect the VOC total oxidation activity.

Due to the lower naphthalene total oxidation activity of the non-autotitrated $Ce_{0.25}Mn_{0.75}O_x$ below 200 °C a direct comparison between different preparation methods $Ce_{0.25}Mn_{0.75}O_x$ could not be made. However the surface area normalised propane total oxidation show the catalyst prepared *via* autotitration and 2 l of washing showed significantly higher surface area normalised rates of propane total oxidation than the samples shown in the table above, except for the $Ce_{0.25}Mn_{0.75}O_x$ prepared using citric acid. This suggests surface area doesn't have a scalable influence on the activity of the catalysts and other factors needs to be considered.
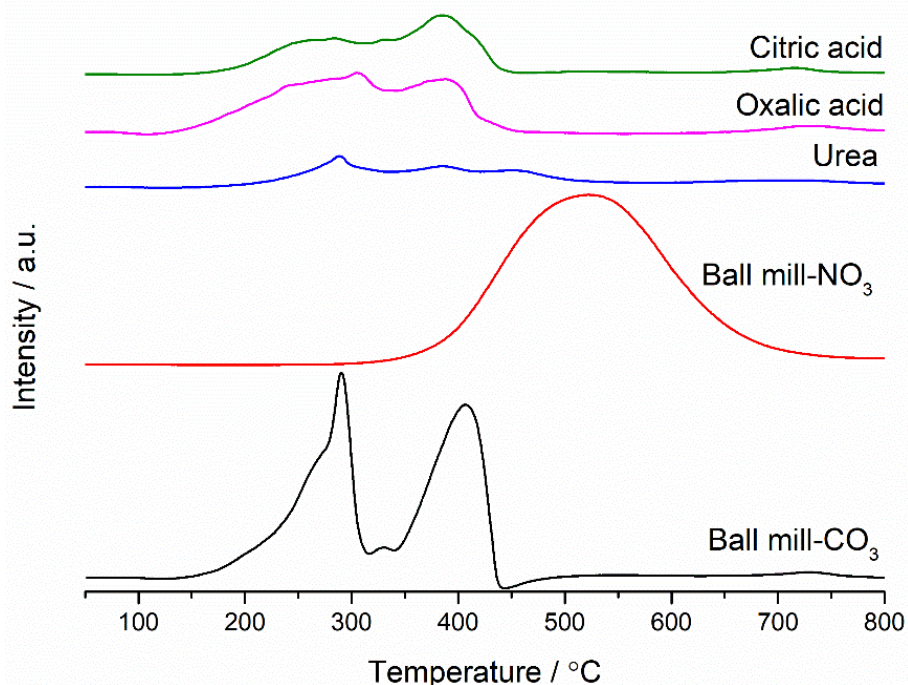
4.4.2.3 Temperature programmed reduction

Figure 4-31: Hydrogen temperature programmed reduction profiles of the $Ce_{0.25}Mn_{0.75}O_x$ prepared *via* different preparation methods. Reaction conditions: 30 mg sample, 30 ml min^{-1}, 10 % H_2/ Ar, temperature range: 50-800 °C

Hydrogen reduction profiles of the $Ce_{0.25}Mn_{0.75}O_x$ prepared *via* different preparation methods are shown in Figure 4-31. The preparation method used to make the $Ce_{0.25}Mn_{0.75}O_x$ had a significant effect on the reduction profile of the sample. The sample prepared using citric acid and oxalic acid had similar profiles, with a large reduction region observed between 200-450 °C, along with a peak with low intensity at 700 °C. The first reduction region of both samples has 2 peaks centred at 280 °C and 400 °C [30]. These peaks indicate the presence of Mn_2O_3, as seen in the XRD, on the $Ce_{0.25}Mn_{0.75}O_x$ prepared using oxalic acid. However, the reduction of surface ceria species occurs at this temperature, therefore the extent of Mn_2O_3 reduction is difficult to calculate. The peak at 700 °C arises from the reduction of bulk ceria species. As only small amounts of ceria are present in the catalysts, the intensity of the peaks is low. It is at a lower temperature than characteristic bulk ceria reduction, indicating the manganese has been incorporated into the ceria causing a decrease in the reduction temperature.

The $Ce_{0.25}Mn_{0.75}O_x$ prepared using urea had 3 low intensity peaks at 300 °C, 400 °C and 475 °C. MnO_2 was observed in the bulk of the sample and the peaks at 300 °C and 475 °C result from this phase. The peak at 400 °C comes from reduction of surface ceria. No reduction of bulk ceria is observed within the temperature range. The mechanochemically prepared $Ce_{0.25}Mn_{0.75}O_x$ from nitrates, only had one large reduction peak between 450-700 °C. This peak could arise from reduction of surface ceria and MnO_2, which has a large characteristic reduction peak at 500 °C. The mechanochemically prepared $Ce_{0.25}Mn_{0.75}O_x$ from carbonate precursors had two peaks at 290 °C and 400 °C. There was a significant shoulder peak observed on the peak at low temperatures. These peaks are characteristic of Mn_2O_3 in the sample. This phase is observed in XRD along with cubic ceria. The reduction of bulk ceria is noted by a low intensity reduction peak at 700 °C.

All $Ce_{0.25}Mn_{0.75}O_x$ catalysts, except the sampled prepared from ball milling of nitrate precursors, show low temperature reduction peaks. The temperature of the peaks are similar to the $Ce_{0.25}Mn_{0.75}O_x$ prepared from autotitration and washed with 2 l of water indicating the ease of reduction is not significantly affected by preparation method. However the extent of reduction is affected by the catalyst preparation with the $Ce_{0.25}Mn_{0.75}O_x$ sampled prepared from urea, oxalic acid and citric acid showing reduction peaks of low intensity. There is correlation between the surface areas and the reduction peak intensity. However due to difficulties identifying surface and bulk reduction regions, the correlation between surface area and reduction is difficult to determine. This suggests only small amounts of oxygen will be released from the lattice during the VOC total oxidation reactions. Therefore the Mars van-Krevelen mechanism may not occur to the

same extent on the samples prepared using organic acids and urea compared to the ball milled and autotitrated catalysts. This could explain the difference in activity observed between the various catalyst preparation methods.

4.4.2.4 Electron microscopy

4.4.2.4.1 Scanning electron microscopy

The electron micrographs of the $Ce_{0.25}Mn_{0.75}O_x$ prepared using different methods are shown in Figure 4-32. The morphology significantly changes upon differing preparation method of the $Ce_{0.25}Mn_{0.75}O_x$. The $Ce_{0.25}Mn_{0.75}O_x$ prepared using citric acid showed a smooth structure with large pores which has been observed previously in non-doped [53] and doped [54] ceria prepared using the method. There are two morphologies observed for the $Ce_{0.25}Mn_{0.75}O_x$ prepared using urea, several bulbous structures are seen deposited on a series of rod-shaped structures. The samples prepared using mechanochemical grinding had differing morphologies. Large plate like structures were observed, however, the surface of the structures differed. Finally, the sample prepared using oxalic acid had a folded plate like structure.

The extent of contrast in the back scattered images changed depending on the preparation method. There was no phase contrast observed in the $Ce_{0.25}Mn_{0.75}O_x$ prepared using citric acid, indicating good mixing between the two metal oxides has occurred. This is consistent with the XRD analysis in which only ceria phases were observed indicating no phase separation. The urea had observable phase contrast between the two morphologies in the electron micrograph. The rod-like structures were lighter indicating these had a higher cerium content and the bulbous structures were darker, suggesting these had a higher manganese content. The contrast observed in the mechanochemically prepared samples are similar, indicating the precursor used only effects the morphology of the catalysts and no the mixing of the metal oxides. The $Ce_{0.25}Mn_{0.75}O_x$ prepared using oxalic acid had areas of increased brightness indicating phase separation between ceria and manganese oxide.

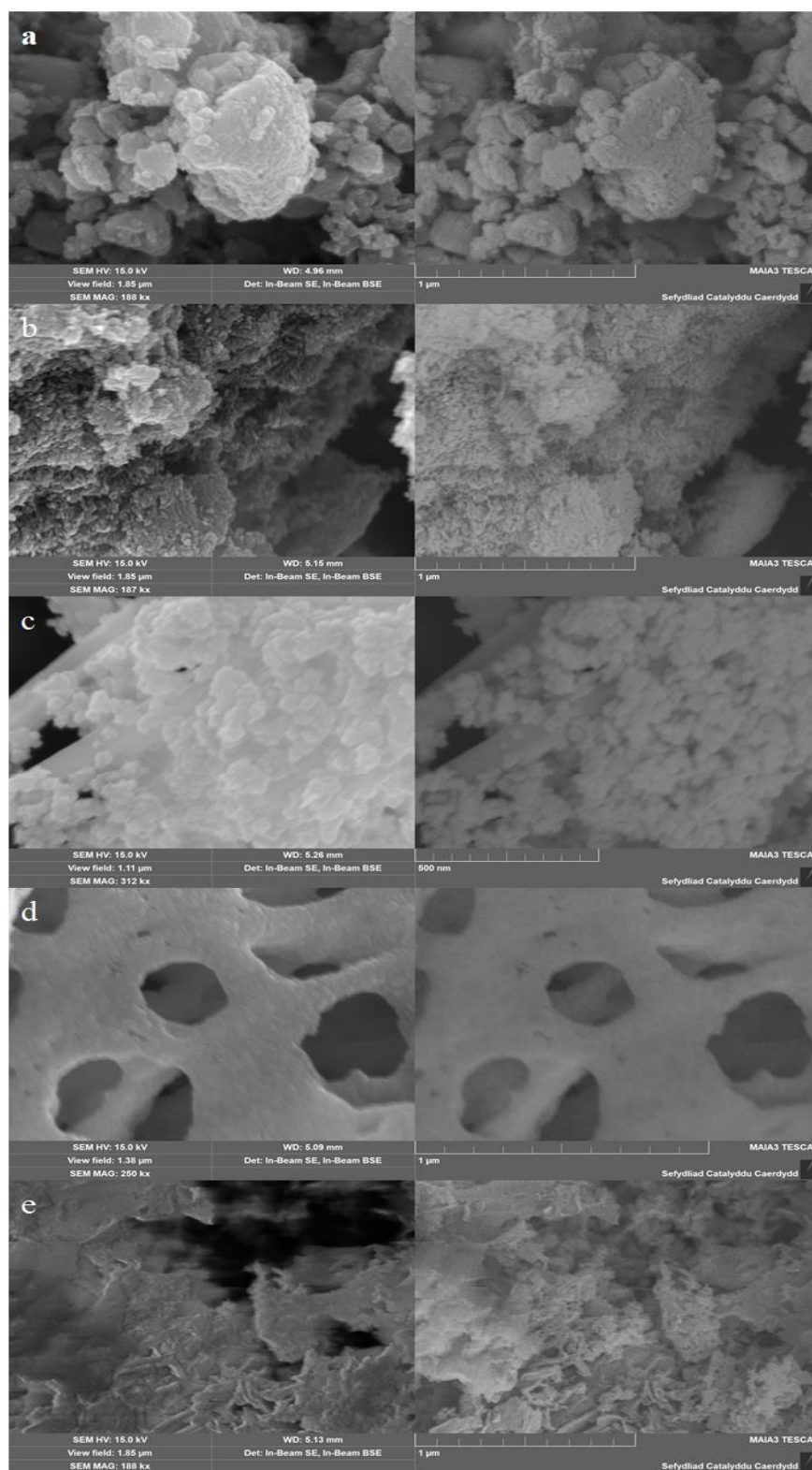Figure 4-32: The secondary electron (left) and back-scattered electron (right) micrographs of $Ce_{0.25}Mn_{0.75}O_x$ prepared *via* (a) ball mill-CO_3, (b) ball mill- NO_3, (c) urea, (d) citric acid and (e) oxalic acid. Image magnification: 200 kx

4.4.2.4.2 Energy dispersive x-ray spectroscopy

The bulk elemental analysis of $Ce_{0.25}Mn_{0.75}O_x$ prepared using a range of preparation methods, suggest the ceria and manganese ratios are close to the nominal values expected from synthesis ratios, Table 4-18. Only the sample prepared using oxalic acid had cerium content significantly higher than the nominal value. This may have occurred from the phase separation observed in the SEM image of the same leading to cerium or manganese enriched areas, causing the increased cerium observed in EDX. This may indicate the manganese oxide is present in very small or amorphous crystallites in the bulk phase and therefore can't be detected by XRD.

Table 4-18: SEM-EDX derived bulk element analysis of the $Ce_{0.25}Mn_{0.75}O_x$ prepared *via* different preparation methods

Sample	Concentration / At.%			Relative Ce:Mn concentrations / %	
	Ce	Mn	O	Ce	Mn
Ball mill-CO$_3$	8.1	26.2	65.7	23.7	76.3
Ball mill- NO$_3$	7.9	25.5	66.1	23.5	76.5
Urea	7.3	23.2	69.5	24.0	76.0
Citric acid	7.1	22.0	70.9	24.4	75.6
Oxalic acid	10.6	21.2	68.2	33.2	66.8

The phase separation observed in the backscattered electron micrographs are confirmed in the SEM-EDX maps of the $Ce_{0.25}Mn_{0.75}O_x$, Figure 4-33. The sample prepared using urea had rod-like and bulbous structures present, which correspond to manganese and cerium rich areas respectively. Some cerium and manganese phase separation was observed on the mechanochemically prepared samples and the oxalic acid sample, but not to the same extent as the urea. The sample prepared using citric acid showed intimate mixing between the cerium and manganese. The samples with some mixed phases showed higher naphthalene total oxidation activity compared to the completely homogenous or phase separated samples. This indicates high phase separation between ceria and manganese has a negative effect on naphthalene total oxidation
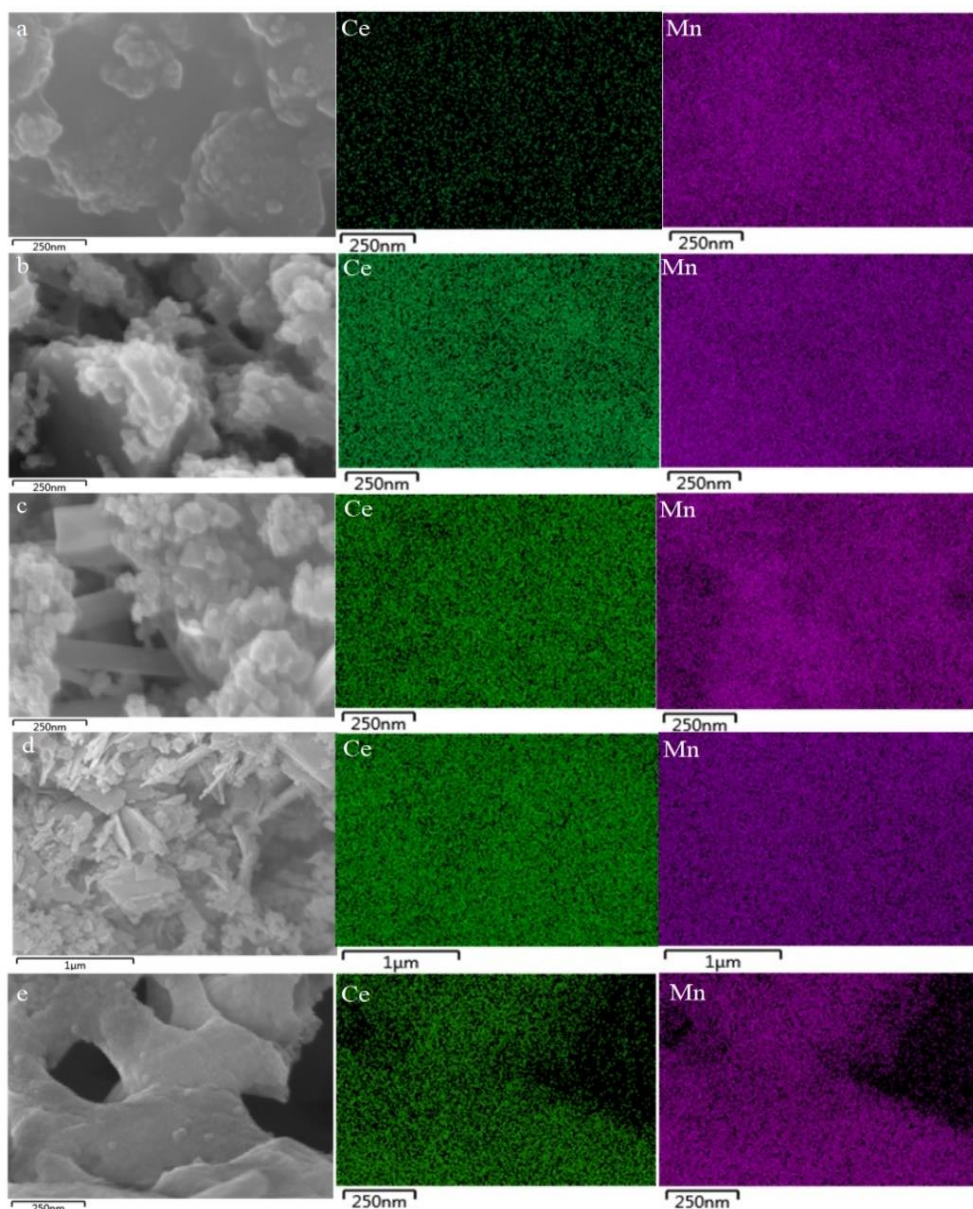
Figure 4-33: SEM-EDX mapping of $Ce_{0.25}Mn_{0.75}O_x$ prepared *via* (a) ball mill-CO_3, (b) ball mill- NO_3, (c) urea, (d) oxalic acid and (e) citric acid. Cerium (green) and manganese (pink)

4.4.2.4.3 Transmission electron microscopy

The TEM images along with selected area electron diffraction of the $Ce_{0.25}Mn_{0.75}O_x$ prepared using different methods are shown in Figure 4-34. As seen from SEM micrographs, the morphology changed upon preparation method and the same is observed in TEM. The $Ce_{0.25}Mn_{0.75}O_x$ prepared from mechanochemical grinding of carbonates and citric acid had a plate like structure whereas the other samples were an array of randomly arranged small crystallites.
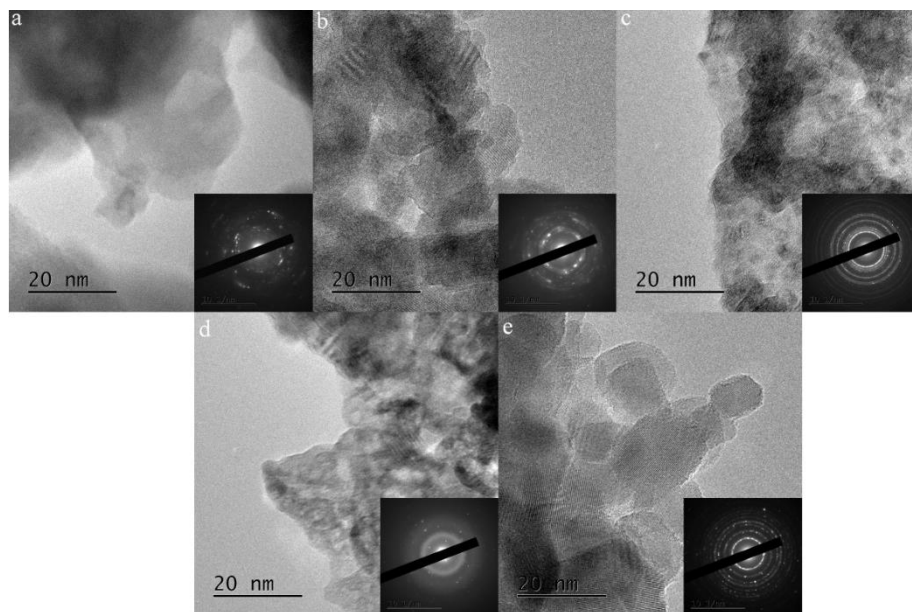
Figure 4-34: High magnification TEM images of the $Ce_{0.25}Mn_{0.75}O_x$ prepared *via* (a) ball mill-CO_3, (b) ball mill- NO_3, (c) urea, (d) oxalic acid and (e) citric acid. Inset: selected area electron diffraction pattern of larger 250 nm areas.

The selected area electron diffraction is shown in the inset of the TEM images (Figure 4-34). All the samples showed different diffraction patterns. The $Ce_{0.25}Mn_{0.75}O_x$ prepared using mechanochemical grinding of carbonates had an array of spots indicating single crystals have been formed. As seen in the TEM images, only a small number of crystallites were observed, therefore, diffuse diffraction rings won't be observed. The sample prepared from mechanochemical grinding of nitrates had diffuse rings with some intense spots present within the rings, indexed to cubic ceria. This follows the XRD in which ceria was the dominant phase. However, due to the randomly arranged crystallites, this will cause the formation of the diffuse electron diffraction rings. The diffraction patterns of the sample prepared using urea show four intense electron diffraction rings indexed for ceria. No electron diffraction spots or rings are observed from manganese oxide phases, suggesting these are amorphous or well mixed in the bulk of the sample. There are also four diffraction rings observed in the $Ce_{0.25}Mn_{0.75}O_x$ prepared using citric acid. However the diffraction rings are of low intensity and spots are observed within the rings. This indicates some of the crystallites are randomly orientated and some are present from single crystals. There were no observable rings in the $Ce_{0.25}Mn_{0.75}O_x$ prepared using oxalic acid, however some spots of low intensity were observed. This corresponds to the XRD pattern of the sample in which only low intensity reflections were observed, therefore confirming the low crystallinity of the sample [55].

The lattice parameters were calculated by using either an indexed lattice plane or from the most intense spot in the diffraction pattern (Table 4-19). The spots from diffraction on the $Ce_{0.25}Mn_{0.75}O_x$ prepared using oxalic acid were difficult to define making the lattice parameter difficult to calculate. The sample prepared using urea had the smallest lattice parameter and this is assigned to the (200) ceria lattice plane. This matches the XRD pattern indicating that cubic ceria was the dominant phase in this sample. The lattice parameter of the catalyst prepared using citric acid was slightly higher than the cubic ceria (200) phase.

Table 4-19: The lattice parameter of the $Ce_{0.25}Mn_{0.75}O_x$ prepared *via* different preparation methods determined from selected area electron diffraction

Sample	Lattice parameter calculated from selected area electron diffraction / Å
Ball mill- CO_3	9.25
Ball mill- NO_3	7.53
Urea	5.74
Citric acid	6.53
Oxalic acid	-

The mechanochemically prepared $Ce_{0.25}Mn_{0.75}O_x$ have the largest lattice parameter of the samples. The sample prepared from grinding of carbonates had the largest lattice parameter, exceeding the one observed for the $Ce_{0.25}Mn_{0.75}O_x$ prepared *via* autotitration and washed with 2 l of H_2O. Mn_2O_3 has a reported lattice parameter of 9.41 Å, suggesting the manganese oxide present in the bulk of the catalyst prepared using mechanochemical grinding of carbonates is in this phase. The smaller experimental lattice parameter can be ascribed to the presence of ceria which may cause the contraction of the lattice compared to pure manganese oxides.

4.4.2.5 X-ray photoelectron spectroscopy

Table 4-20: XPS derived surface elemental concentrations for the prepared *via* different preparation methods

Sample	Concentration / At.%			Relative Ce:Mn concentrations / %	
	Ce	Mn	O	Ce	Mn
Ball mill CO_3	5.8	34.0	60.2	14.5	85.5
Ball mill NO_3	11.2	27.1	61.7	29.2	70.8
Urea	22.5	12.5	65.0	64.4	35.6
Citric acid	9.4	31.6	59.0	23.0	77.0
Oxalic acid	14.1	23.2	62.7	37.7	62.3

The elemental composition of the surface of the $Ce_{0.25}Mn_{0.75}O_x$ prepared using different methods is shown in Table 4-20. The EDX values of $Ce_{0.25}Mn_{0.75}O_x$ prepared using various preparation methods showed all methods, except for oxalic acid, produced catalysts with bulk concentrations close to the nominal value.

In contrast to bulk concentrations, only $Ce_{0.25}Mn_{0.75}O_x$ prepared using citric acid was the only preparation method which had a surface concentration close to the nominal value. The $Ce_{0.25}Mn_{0.75}O_x$ prepared using oxalic acid had a similar surface content as the bulk. This suggests the elemental composition of the $Ce_{0.25}Mn_{0.75}O_x$ prepared using oxalic and citric acid remains consistent throughout the sample. Surface manganese enrichment occurs on the catalysts prepared from mechanochemical grinding of carbonates. Cerium enrichment occurs on the $Ce_{0.25}Mn_{0.75}O_x$ prepared from mechanochemical grinding of nitrates and urea, with urea showing the highest relative ceria concentration.
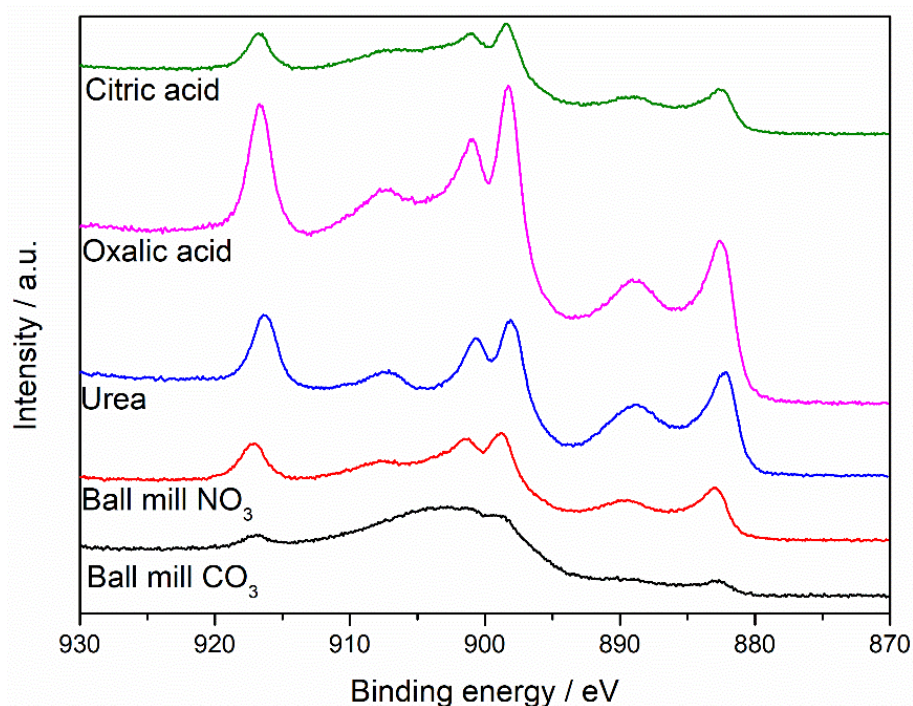
Figure 4-35: XPS spectra of the Ce 3d peaks for the $Ce_{0.25}Mn_{0.75}O_x$ prepared *via* different preparation methods

The Ce 3d XPS spectra of the $Ce_{0.25}Mn_{0.75}O_x$ prepared using different methods is shown in Figure 4-35. A significant amount of surface charging occurred on the catalyst prepared from mechanochemical grinding of carbonates, making the doublet peak around 900 eV difficult to analyse. However a characteristic peak at 917 eV indicates the presence of Ce^{4+} on the surface of the sample. All the $Ce_{0.25}Mn_{0.75}O_x$ prepared using different methods have this peak indicating Ce^{4+} is present on all samples. As mentioned in previous Ce 3d XPS analysis, the symmetry of the doublet peak around 900 eV and between 890-90 eV signifies the presence of Ce^{3+}. When comparing all the spectra of the Ce 3d peaks, it was

174

observed that all samples contained some Ce^{3+} species. However, the ratios of the two oxidation states are difficult to quantify. With the cerium and manganese species in the TPR patterns of the catalysts difficult to distinguish, the effect of Ce^{3+} on the catalysts is also hard to define.
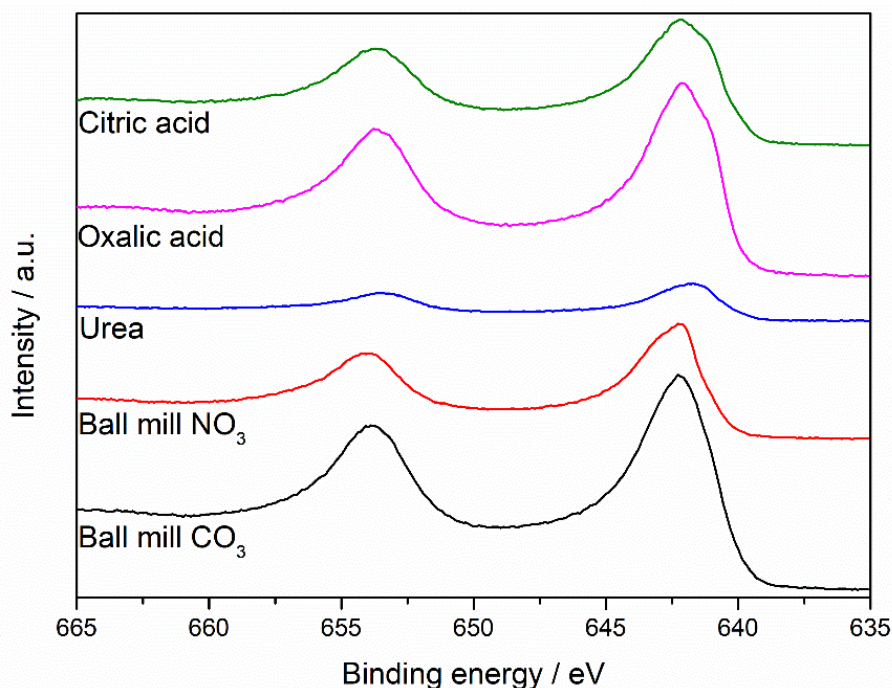

Figure 4-36: XPS spectra of the Mn 2p peaks for the $Ce_{0.25}Mn_{0.75}O_x$ prepared *via* different preparation methods

Every $Ce_{0.25}Mn_{0.75}O_{xc}$ prepared using different methods had a doublet peak present in the Mn 2p XPS spectra (Figure 4-36). No MnO satellite feature is observed in any of the 2p spectra. The position of the Mn 2p peaks remains similar and independent of the catalyst preparation method. However, the position of the Mn 2p peaks $Ce_{0.25}Mn_{0.75}O_x$ prepared using mechanochemical grinding of carbonates had moved to a slightly higher binding energy. This suggests the oxidation state of the manganese in this sample is lower than the other samples [48]. To gain further understanding of the manganese oxidation state, the 3s peaks were investigated, Figure 4-37.
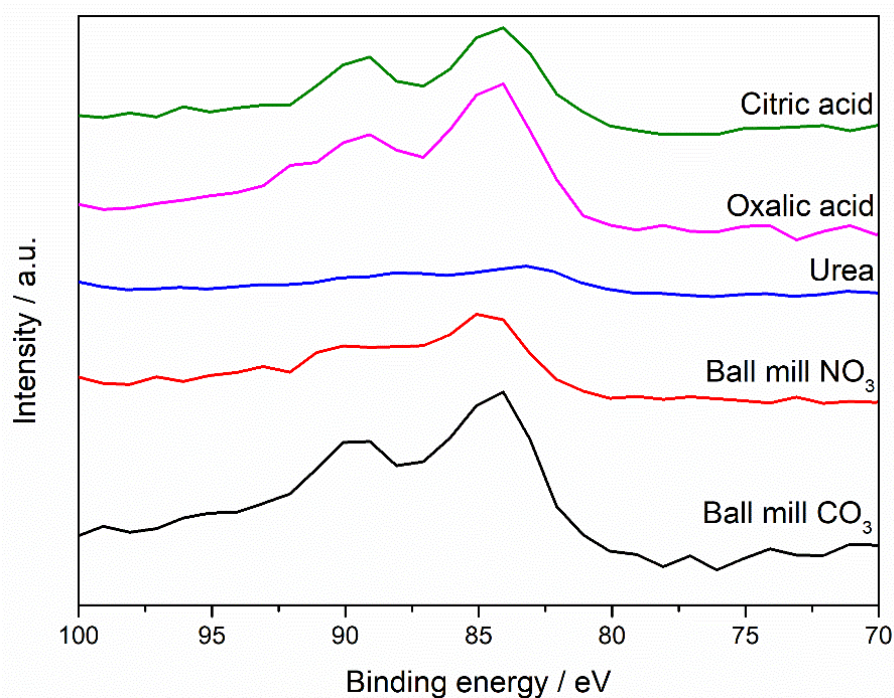
Figure 4-37: XPS spectra of the Mn 3s peaks for the $Ce_{0.25}Mn_{0.75}O_x$ prepared *via* different preparation methods

All $Ce_{0.25}Mn_{0.75}O_x$ samples, except urea, showed peaks in Mn 3s region and the splitting between the peaks is shown in Table 4-21. The manganese oxidation state of the $Ce_{0.25}Mn_{0.75}O_x$ prepared using mechanochemical grinding was 3+, whereas the samples prepared using organic acids were 4+ [42]. The bulk and surface oxidation state of the $Ce_{0.25}Mn_{0.75}O_x$ prepared by mechanochemical grinding of carbonates is the same, whereas other preparation methods have varying bulk and surface oxidation states. With Mn_2O_3 reported to have higher VOC total oxidation activity compared to MnO_2, the presence of this may explain the increased activity of the sampled prepared by mechanochemical grinding.

Table 4-21: Magnitude of peak splitting in the Mn 3s spectra for the $Ce_{0.25}Mn_{0.75}O_x$ prepared *via* different preparation methods

Sample	Magnitude of Mn 3s peak splitting / eV	Surface oxidation state of Mn (all +)
Ball mill CO₃	5.5	3
Ball mill NO₃	5.7	3
Urea	-	-
Citric acid	4.9	4
Oxalic acid	5.2	4

The fitted O 1s spectra of the $Ce_{0.25}Mn_{0.75}O_x$ prepared using different methods is shown in Figure 4-38. Lattice (O_α) and defect (O_β) oxygen species are observed at 529-31 eV and 531-3 eV respectively in all samples. Only the $Ce_{0.25}Mn_{0.75}O_x$ prepared using urea

showed a shift to lower binding energies. This indicates poor interaction between the ceria and manganese are occurring on the surface of this sample compared to the other samples. However, due to the increased relative cerium content of the $Ce_{0.25}Mn_{0.75}O_x$ prepared using urea, with ceria less active for VOC total oxidation compared to manganese, this may negate any positive effects of the phase separation on VOC total oxidation activity.
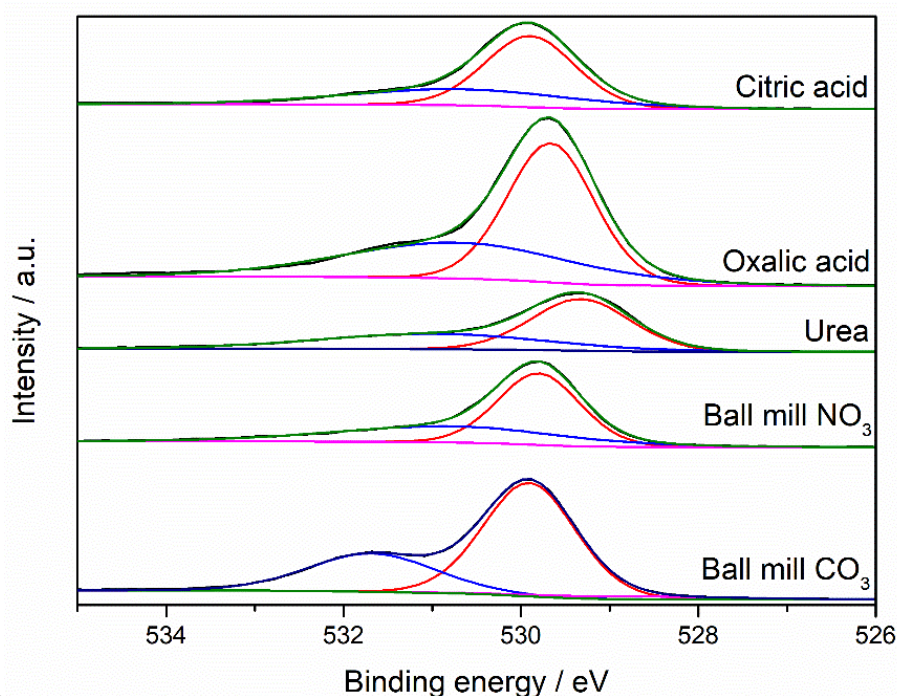

Figure 4-38: XPS spectra of the O 1s peaks for the $Ce_{0.25}Mn_{0.75}O_x$ prepared *via* different preparation methods

The relative concentrations of lattice (O_α) and defect oxygen (O_β) species on the surface of the $Ce_{0.25}Mn_{0.75}O_x$ is shown in Table 4-22. The catalyst prepared *via* mechanochemical grinding of carbonates had the lowest relative concentration of O_β, whereas the sampled prepared using urea had the highest value. However, all samples had significantly lower O_β compared to the $Ce_{0.25}Mn_{0.75}O_x$ prepared *via* autotitration and washed with 2 l of water. Although as mentioned earlier, the increased O_β could have arisen from the presence of sodium hydroxide on the surface of the catalyst.

Table 4-22: XPS derived concentration of lattice and surface O species for the $Ce_{0.25}Mn_{0.75}O_x$ prepared *via* different preparation methods.

Sample	Relative concentration of O_α / %	Relative concentration of O_β / %
Ball mill CO₃	65.7	34.3
Ball mill NO₃	61.3	38.7
Urea	59.2	40.8
Citric acid	63.5	36.5
Oxalic acid	59.3	40.7

Ce$_{.25}$Mn$_{0.75}$O$_x$ prepared using mechanochemical grinding of carbonates and autotitration using sodium carbonate with 2 l washing have similar propane total oxidation activity. This suggests concentration of O$_\beta$ doesn't have a significant impact on the propane total oxidation activity over Ce$_{0.25}$Mn$_{0.75}$O$_x$ catalysts. However, the autotitrated Ce$_{0.25}$Mn$_{0.75}$O$_x$ had superior naphthalene total oxidation activity compared to the other preparation methods. This indicates the relative concentration of O$_\beta$ has a significant effect on the naphthalene total oxidation activity.

4.5 Stability study of the Ce$_{0.25}$Mn$_{0.75}$O$_x$ sample washed with 2 l of water

4.5.1 Propane total oxidation
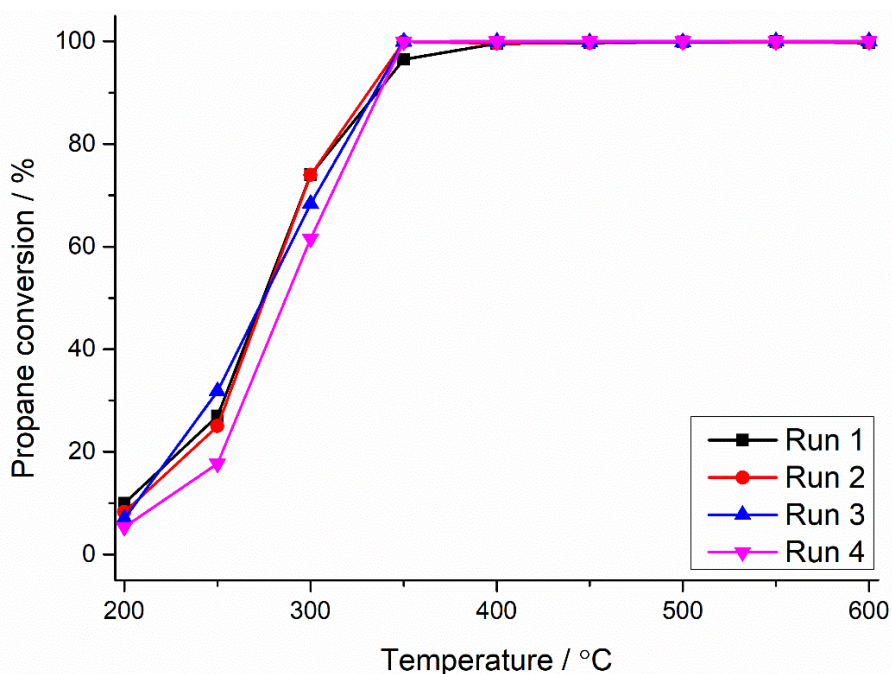
Figure 4-39: Multiple run propane total oxidation stability study of the Ce$_{0.25}$Mn$_{0.75}$O$_x$ prepared *via* autotitration and washed with 2 l of water. Reaction conditions: temperature range: 200-600 °C, GHSV: 45,000 h^{-1}, 5000 ppm in air.

The stability of the of the Ce$_{0.25}$Mn$_{0.75}$O$_x$ prepared *via* autotitration using sodium carbonate and washed with 2 l of water was investigated by undertaking four propane total oxidation reactions, Figure 4-39. All catalytic runs showed high selectivity to CO$_2$, and the carbon balance remained > 99 %. The reaction profile remained consistent upon each successive run with only the fourth propane total oxidation run showing any observable decrease in activity. The fourth run showed ~10 % decrease in propane total oxidation activity at 250 °C and 300 °C compared to the original propane total oxidation run. However, 100 % propane conversion was still observed at 350 °C indicating the

178

catalyst is active and stable. The ceria-manganese mixed metal oxide sample is significantly more stable compared to the ceria-zirconia mixed metal oxides for propane total oxidation. Only a small decrease in activity between the propane total oxidation runs is observed compared to the large drops in activity in the ceria-zirconia catalyst systems. This could be due to the higher calcination temperature used to prepare the ceria-manganese mixed metal oxide meaning the catalyst will be more stable at the higher temperatures of the propane total oxidation test.

4.5.2 Naphthalene total oxidation
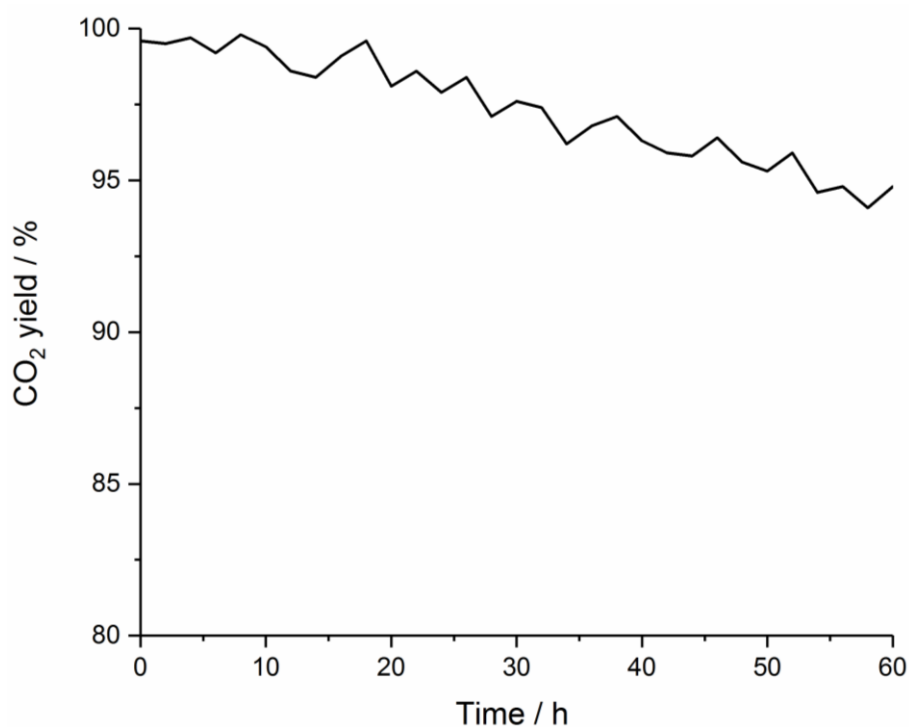
Figure 4-40: Time on line naphthalene total oxidation stability study of the $Ce_{0.25}Mn_{0.75}O_x$ prepared *via* autotitration and washed with 2 l of water. Reaction conditions: Temperature: 200 °C GHSV: 45,000 h^{-1}, 100 vppm naphthalene in 20 % O_2 balanced with He

The autotitrated $Ce_{0.25}Mn_{0.75}O_x$ prepared using sodium carbonate and washed with 2 l of water was also the most active naphthalene total oxidation catalyst. The study the stability of this catalyst, a time on line study at a constant 200 °C was undertaken over 60 hours, Figure 4-40. As seen above, the catalyst remains very stable during the time on line study with only ~5 % decrease in CO_2 yield observed over the time period. This catalyst was significantly more stable for naphthalene total oxidation compared to the ceria-zirconia mixed metal oxides prepared using mechanochemical grinding. The small decrease in activity may have arisen from changes of the catalyst surface over time leading to losses in surface area or active oxygen species.

4.6 Conclusions

Overall, this work demonstrates that cerium-manganese mixed metal oxide catalysts are active for propane and naphthalene total oxidation. The addition of manganese into the ceria lattice lead to a significant increased in total oxidation activity with $Ce_{0.25}Mn_{0.75}O_x$ showing increased activity for both reactions compared to the parent oxides. Increasing the volume of water used to wash the precipitated catalyst led to a decrease in bulk and surface sodium, which led to an observable increase in propane and naphthalene total oxidation activity. When sodium free preparation methods were used to synthesise the $Ce_{0.25}Mn_{0.75}O_x$, comparable propane total oxidation activities were observed, however, a noticeable decrease in naphthalene total oxidation activity was observed.

The increased activity of the autotitrated $Ce_{0.25}Mn_{0.75}O_x$ was assigned to phase separation of cerium and manganese oxides and the presence of Mn_2O_3 which was not observed in the other cerium-manganese mixed metal oxide catalysts. The phase separation was confirmed in SEM-EDX mapping. The crystallite sizes of the samples decreased upon increasing manganese content of the mixed metal oxide along with surface area. The $Ce_{0.25}Mn_{0.75}O_x$ had the smallest ceria crystallite size, along with the highest surface area of all the mixed metal oxide samples and this will influence the increased activity. The $Ce_{0.25}Mn_{0.75}O_x$ had the lowest reduction temperature of the ceria-manganese mixed metal oxides. This will mean the oxygen required for the Mars van-Krevelen mechanism during the total oxidation reactions will be able to become mobile at lower temperatures. This will allow for the temperature required for the total oxidation of the VOCs to reduce, leading to the increase in activity observed over the $Ce_{0.25}Mn_{0.75}O_x$. Along with the bulk, the surface manganese was present in the 3+ oxidation state in $Ce_{0.25}Mn_{0.75}O_x$. This will lead to more labile oxygen for total oxidation reactions.

However it was noted that all the samples had significantly high surface and bulk concentrations of sodium present. To investigate the effect of sodium, the $Ce_{0.25}Mn_{0.75}O_x$ was prepared using autotitration and washed with increasing amounts of water. As the amount of water used to wash the catalyst increased, so did the activity for both total oxidation reactions. This correlated with the loss of bulk and surface sodium species as the amount of water used to wash the sample increased. As the amount of water used to wash the sample increased, the phase separation seemed to increase too. Along with this, there was an increase in manganese oxide and lowering of ceria crystallites sizes as the volume of water used to wash the sample increased. This suggested that larger manganese oxide crystallites were required for active catalysts. Along with the increasing manganese

crystallite size, the surface area of the catalysts increased as the amount of water used to wash the $Ce_{0.25}Mn_{0.75}O_x$ sample increased. This in turn would lead to the increased activity observed over the samples. The reduction temperatures of the catalysts also shifted to lower temperatures as the amount of water used to wash the samples increased. This will allow the Mars van-Krevelen mechanism to activate at lower temperatures, allowing for the increase in activity observed over the samples. The manganese bulk and surface oxidation states decrease upon increasing washing of the $Ce_{0.25}Mn_{0.75}O_x$. This suggests the increased presence of sodium is causing the stabilisation of MnO_2. With this phase being of lower total oxidation activity compared to the Mn_2O_3, along with the presence of the sodium poisons, this may lead to the lower activity observed for these samples.

Five sodium-free methods were used to investigate the effect of preparation method on the synthesis of the $Ce_{0.25}Mn_{0.75}O_x$ catalyst. The different preparation methods showed similar Ce:Mn ratios are close to the expected nominal values, however, the surface was significantly different to the nominal value. The preparation method had a significant effect on the activity, with the mechanochemically prepared samples showing increased activity for both reactions compared to the other preparation methods. However, the naphthalene total oxidation activity was significantly lower than the autotitrated sample. Crystallinity and phase separation of the $Ce_{0.25}Mn_{0.75}O_x$ with mechanochemically prepared samples, showing the phase separation and the sample prepared using urea showing increased crystallinity. This suggests that increased bulk phase cerium and manganese oxide separation is required for active $Ce_{0.25}Mn_{0.75}O_x$ propane total oxidation catalysts. The manganese oxide crystallite size may effect naphthalene total oxidation activity, however, the extent of this is difficult to conclude. The surface areas of the $Ce_{0.25}Mn_{0.75}O_x$ prepared using different methods showed little effect on the total oxidation activity. Although the oxidation state of manganese on the surface of the $Ce_{0.25}Mn_{0.75}O_x$ has a significant effect on the propane total oxidation activity. All the samples with manganese in the 3+ oxidation state notable propane total oxidation activity. There was correlation between the naphthalene total oxidation and the ease and extent of reducibility of the $Ce_{0.25}Mn_{0.75}O_x$. All $Ce_{0.25}Mn_{0.75}O_x$ prepared by methods other than autotitration showed reduction peaks at higher temperatures compared to the autotitrated sampled washed with 2 l of water. Therefore, oxygen required for the total oxidation of naphthalene will require higher temperatures to release from the surface causing the activity to decrease as observed for the non-autotitrated samples.

The $Ce_{0.25}Mn_{0.75}O_x$ prepared using autotitration and washed with 2 l of water showed high stability for both propane and naphthalene reactions. The T_{100} temperature remained constant at 350 °C during a multiple run propane test. There was only minor deviations at lower temperatures suggesting the catalyst remained stable during the stability run. During the naphthalene total oxidation *time-on-line* study only a 5 % deviation over a 60 hour period in CO_2 yield was observed, confirming the stability of this sample.

4.7 References

[1]   T. García, B. Solsona, S.H. Taylor, Naphthalene total oxidation over metal oxide catalysts, Appl. Catal. B Environ. 66 (2006) 92–99. doi:10.1016/j.apcatb.2006.03.003.

[2]   Q. Feng, H. Kanoh, K. Ooi, Manganese Oxide Porous Crystal, J. Mater. Chem. 9 (1999) 319–33. doi:10.1039/a805369c.

[3]   T. Garcia, D. Sellick, F. Varela, I. Vázquez, A. Dejoz, S. Agouram, S.H. Taylor, B. Solsona, Total oxidation of naphthalene using bulk manganese oxide catalysts, Appl. Catal. A Gen. 450 (2013) 169–177. doi:10.1016/j.apcata.2012.10.029.

[4]   G. Qi, W. Li, NO oxidation to NO2over manganese-cerium mixed oxides, Catal. Today. 258 (2015) 205–213. doi:10.1016/j.cattod.2015.03.020.

[5]   Y. Liang, Y. Huang, H. Zhang, L. Lan, M. Zhao, M. Gong, Y. Chen, J. Wang, Interactional effect of cerium and manganese on NO catalytic oxidation, Environ. Sci. Pollut. Res. 24 (2017) 9314–9324. doi:10.1007/s11356-017-8645-x.

[6]   P. Venkataswamy, K.N. Rao, D. Jampaiah, B.M. Reddy, Nanostructured manganese doped ceria solid solutions for CO oxidation at lower temperatures, Appl. Catal. B Environ. 162 (2015) 122–132. doi:10.1016/j.apcatb.2014.06.038.

[7]   X. Liu, J. Lu, K. Qian, W. Huang, M. Luo, A comparative study of formaldehyde and carbon monoxide complete oxidation on MnOx-CeO2 catalysts, J. Rare Earths. 27 (2009) 418–424. doi:10.1016/S1002-0721(08)60263-X.

[8]   H. Li, G. Qi, Tana, X. Zhang, X. Huang, W. Li, W. Shen, Low-temperature oxidation of ethanol over a Mn0.6Ce0.4O2 mixed oxide, Appl. Catal. B Environ. 103 (2011) 54–61. doi:10.1016/j.apcatb.2011.01.008.

[9]   D. Delimaris, T. Ioannides, Intrinsic Activity of MnOx-CeO2 Catalysts in Ethanol Oxidation, Catalysts. 7 (2017) 339. doi:10.3390/catal7110339.

[10]   H. Chen, A. Sayari, A. Adnot, F. Larachi, Composition-activity effects of Mn-Ce-O composites on phenol catalytic wet oxidation, Appl. Catal. B Environ. 32 (2001) 195–204. doi:10.1016/S0926-3373(01)00136-9.

[11]   F. Arena, J. Negro, A. Parmaliana, L. Spadaro, G. Trunfio, Improved MnCeOx systems for the catalytic wet oxidation (CWO) of phenol in wastewater streams, Ind. Eng. Chem. Res. 46 (2007) 6724–6731. doi:10.1021/ie0701118.

[12]   J. Chen, X. Chen, X. Chen, W. Xu, Z. Xu, H. Jia, J. Chen, Homogeneous introduction of CeOyinto MnOx-based catalyst for oxidation of aromatic VOCs, Appl. Catal. B Environ. 224 (2018) 825–835. doi:10.1016/j.apcatb.2017.11.036.

[13]   L. Matějová, P. Topka, K. Jirátová, O. Šolcová, Total oxidation of model volatile organic compounds over some commercial catalysts, Appl. Catal. A Gen. 443–444 (2012) 40–49. doi:10.1016/j.apcata.2012.07.018.

[14]   E.N. Ntainjua, T.E. Davies, T. Garcia, B. Solsona, S.H. Taylor, Influence of preparation conditions of nano-crystalline ceria catalysts on the total oxidation of naphthalene, a model polycyclic aromatic hydrocarbon, Catal. Letters. 141 (2011) 1732–1738. doi:10.1007/s10562-011-0710-3.

[15]   T.J. Clarke, S.A. Kondrat, S.H. Taylor, Total oxidation of naphthalene using bulk

manganese oxide catalysts, Appl. Catal. A Gen. 450 (2013) 169–177. doi:10.1016/j.apcata.2012.10.029.

[16]	R.P. Westerdahl, P.J. Leader, thermal decomposition of manganese carbonate, Inorg. Nucl. Chem. Lett. 5 (1969) 199–201.

[17]	D.R. Sellick, A. Aranda, T. García, J.M. López, B. Solsona, A.M. Mastral, D.J. Morgan, A.F. Carley, S.H. Taylor, Influence of the preparation method on the activity of ceria zirconia mixed oxides for naphthalene total oxidation, Appl. Catal. B Environ. 132–133 (2013) 98–106. doi:10.1016/j.apcatb.2012.11.036.

[18]	T. Garcia, B. Solsona, S.H. Taylor, Nano-crystalline Ceria Catalysts for the Abatement of Polycyclic Aromatic Hydrocarbons, Catal. Letters. 105 (2005) 183–189. doi:10.1007/s10562-005-8689-2.

[19]	D. Delimaris, T. Ioannides, VOC oxidation over MnOx-CeO2 catalysts prepared by a combustion method, Appl. Catal. B Environ. 84 (2008) 303–312. doi:10.1016/j.apcatb.2008.04.006.

[20]	T.-Z. Ren, P.-B. Xu, Q.-F. Deng, Z.-Y. Yuan, Mesoporous Ce1− xMnxO2 mixed oxides with CuO loading for the catalytic total oxidation of propane, React. Kinet. Mech. Catal. 110 (2013) 405–420. doi:10.1007/s11144-013-0603-0.

[21]	T. Wada, N. Koga, Kinetics and mechanism of the thermal decomposition of sodium percarbonate: Role of the surface product layer, J. Phys. Chem. A. 117 (2013) 1880–1889. doi:10.1021/jp3123924.

[22]	S. Zhan, D. Zhu, M. Qiu, H. Yu, Y. Li, Highly efficient removal of NO with ordered mesoporous manganese oxide at low temperature, RSC Adv. 5 (2015) 29353–29361. doi:10.1039/c4ra17300g.

[23]	M. Augustin, D. Fenske, I. Bardenhagen, A. Westphal, M. Knipper, T. Plaggenborg, J. Kolny-Olesiak, J. Parisi, Manganese oxide phases and morphologies: A study on calcination temperature and atmospheric dependence, Beilstein J. Nanotechnol. 6 (2015) 47–59. doi:10.3762/bjnano.6.6.

[24]	M. Machida, M. Uto, D. Kurogi, T. Kijima, MnO x - CeO 2 Binary Oxides for Catalytic NO x Sorption at Low Temperatures . Sorptive Removal of NO x, (2000) 3158–3164. doi:10.1021/cm000207r.

[25]	G. Picasso, M. Gutierrez, M.P. Pina, J. Herguido, Preparation and characterization of Ce-Zr and Ce-Mn based oxides for n-hexane combustion: Application to catalytic membrane reactors, Chem. Eng. J. 126 (2007) 119–130. doi:10.1016/j.cej.2006.09.005.

[26]	L. Ahrens, The use of ionization potentials Part 1. Ionic radii of the elements, Geochim. Cosmochim. Acta. 2 (1952) 155–169. doi:10.1016/0016-7037(52)90004-5.

[27]	D. Jampaiah, P. Venkataswamy, K.M. Tur, S.J. Ippolito, S.K. Bhargava, B.M. Reddy, Effect of MnOx Loading on Structural, Surface, and Catalytic Properties of CeO2-MnOx Mixed Oxides Prepared by Sol-Gel Method, Zeitschrift Fur Anorg. Und Allg. Chemie. (2015) 1141–1149. doi:10.1002/zaac.201400615.

[28]	L. Liu, J. Shi, X. Zhang, J. Liu, Flower-Like Mn-Doped CeO2 Microstructures: Synthesis, Characterizations, and Catalytic Properties, J. Chem. 2015 (2015) 1–11.

[29]	J.E. Spanier, R.D. Robinson, F. Zhang, S.-W. Chan, I.P. Herman, Size-dependent properties of CeO2-y nanoparticles as studied by Raman scattering, Phys. Rev. B. 64 (2001) 245407. doi:10.1103/PhysRevB.64.245407.

[30]	E.R. Stobbe, B.A. de Boer, J.W. Geus, The reduction and oxidation behaviour of manganese oxides, Catal. Today. 47 (1999) 161–167. doi:10.1016/S0920-5861(98)00296-X.

[31]	S.C. Kim, W.G. Shim, Catalytic combustion of VOCs over a series of manganese oxide catalysts, Appl. Catal. B Environ. 98 (2010) 180–185. doi:10.1016/j.apcatb.2010.05.027.

[32] F. Arena, G. Trunfio, J. Negro, B. Fazio, L. Spadaro, Basic evidence of the molecular dispersion of MnCeOx catalysts synthesized via a novel "redox-precipitation" route, Chem. Mater. 19 (2007) 2269–2276. doi:10.1021/cm070198n.

[33] H. Huang, J. Liu, P. Sun, S. Ye, B. Liu, Effects of Mn-doped ceria oxygen-storage material on oxidation activity of diesel soot, RSC Adv. 7 (2017) 7406–7412. doi:10.1039/c6ra27007g.

[34] H. Wang, X. Chen, S. Gao, Z. Wu, Y. Liu, X. Weng, Deactivation mechanism of Ce/TiO2 selective catalytic reduction catalysts by the loading of sodium and calcium salts, Catal. Sci. Technol. (2013) 715–722. doi:10.1039/c2cy20568h.

[35] A.A. Mirzaei, H.R. Shaterian, R.W. Joyner, M. Stockenhuber, S.H. Taylor, G.J. Hutchings, Ambient temperature carbon monoxide oxidation using copper manganese oxide catalysts: Effect of residual Na+ acting as catalyst poison, Catal. Commun. 4 (2003) 17–20. doi:10.1016/S1566-7367(02)00231-5.

[36] J.A. Ṕerez-Omil, J.J. Delgado, W. Ouahbi, A.B. Hungría, N. Browning, M.A. Cauqui, J.M. Rodŕiguez-Izquierdo, J.J. Calvino, Electron microscopy investigations of nanostructured ce/mn oxides for catalytic wet oxidation, J. Phys. Chem. C. 114 (2010) 8981–8991. doi:10.1021/jp100635e.

[37] P. Strobel, C. Darie, F. Thiéry, M. Bacia, O. Proux, A. Ibarra-Palos, J.B. Soupart, New nanocrystalline manganese oxides as cathode materials for lithium batteries: Electron microscopy, electrochemical and X-ray absorption studies, Solid State Ionics. 177 (2006) 523–533. doi:10.1016/j.ssi.2005.11.025.

[38] L. Pauling, Atomic Radii and Interatomic Distances in Metals, J. Am. Chem. Soc. 69 (1947) 542–553. doi:10.1021/ja01195a024.

[39] D.B. Rogers, R.D. Shannon, A.W. Sleight, J.L. Gillson, Crystal chemistry of metal dioxides with rutile-related structures, Inorg. Chem. 8 (1969) 841–849. doi:10.1021/ic50074a029.

[40] O. Madelung, U. Rossler, M. Schulz, Non-Tretahedrally Bonded Binary Compounds II, Springer, 2000.

[41] W. Xingyi, K. Qian, L. Dao, Catalytic combustion of chlorobenzene over MnOx-CeO2 mixed oxide catalysts, Appl. Catal. B Environ. 86 (2009) 166–175. doi:10.1016/j.apcatb.2008.08.009.

[42] J.L. Junta, M.F. Hochella, Manganese (II) oxidation at mineral surfaces: A microscopic and spectroscopic study, Geochim. Cosmochim. Acta. 58 (1994) 4985–4999. doi:10.1016/0016-7037(94)90226-7.

[43] V.P. Santos, M.F.R. Pereira, J.J.M. Órfão, J.L. Figueiredo, The role of lattice oxygen on the activity of manganese oxides towards the oxidation of volatile organic compounds, Appl. Catal. B Environ. 99 (2010) 353–363. doi:10.1016/j.apcatb.2010.07.007.

[44] Y. Liu, M. Luo, Z. Wei, Q. Xin, P. Ying, C. Li, Catalytic oxidation of chlorobenzene on supported manganese oxide catalysts, Appl. Catal. B Environ. 29 (2001) 61–67. doi:10.1016/S0926-3373(00)00193-4.

[45] J. Dupin, D. Gonbeau, P. Vinatier, A. Levasseur, Systematic XPS Studies of Metal Oxides , Hydroxides and Peroxides Systematic XPS studies of metal oxides , hydroxides and peroxides, Phys. Chem. Chem. Phys. 2 (2000) 1319–1324. doi:10.1039/a908800h.

[46] G.J. Hutchings, A.A. Mirzaei, R.W. Joyner, M.R.H. Siddiqui, S.H. Taylor, Effect of preparation conditions on the catalytic performance of copper manganese oxide catalysts for CO oxidation, Appl. Catal. A Gen. 166 (1998) 143–152. doi:10.1016/S0926-860X(97)00248-2.

[47] M.C. Biesinger, B.P. Payne, A.P. Grosvenor, L.W.M. Lau, A.R. Gerson, R.S.C. Smart, Resolving surface chemical states in XPS analysis of first row transition

metals, oxides and hydroxides: Cr, Mn, Fe, Co and Ni, Appl. Surf. Sci. 257 (2011) 2717–2730. doi:10.1016/j.apsusc.2010.10.051.

[48] K. Ramesh, L. Chen, F. Chen, Y. Liu, Z. Wang, Y.F. Han, Re-investigating the CO oxidation mechanism over unsupported MnO, Mn2O3and MnO2catalysts, Catal. Today. 131 (2008) 477–482. doi:10.1016/j.cattod.2007.10.061.

[49] W. Tang, X. Wu, G. Liu, S. Li, D. Li, W. Li, Y. Chen, Preparation of hierarchical layer-stacking Mn-Ce composite oxide for catalytic total oxidation of VOCs, J. Rare Earths. 33 (2015) 62–69. doi:10.1016/S1002-0721(14)60384-7.

[50] J. Du, Z. Qu, C. Dong, L. Song, Y. Qin, N. Huang, Low-temperature abatement of toluene over Mn-Ce oxides catalysts synthesized by a modified hydrothermal approach, Appl. Surf. Sci. 433 (2018) 1025–1035. doi:10.1016/j.apsusc.2017.10.116.

[51] W. Li, H. Liu, X. Ma, S. Mo, S. Li, Y. Chen, Fabrication of silica supported mn-ce benzene oxidation catalyst by a simple and environment-friendly oxalate approach, J. Porous Mater. 25 (2018) 107–117. doi:10.1007/s10934-017-0424-z.

[52] P.N. Trikalitis, P.J. Pomonis, Catalytic activity and selectivity of perovskites LaSrV3+V4+O3 for the transformation of isopropanol, Appl. Catal. A Gen. 131 (1995) 309–322.

[53] S.G. Rudisill, N.M. Hein, D. Terzic, A. Stein, Controlling microstructural evolution in pechini gels through the interplay between precursor complexation, step-growth polymerization, and template confinement, Chem. Mater. 25 (2013) 745–753. doi:10.1021/cm303761z.

[54] L.B. Winck, J.L. de Almeida Ferreira, J.M.G. Martinez, J.A. Araujo, A.C.M. Rodrigues, C.R.M. da Silva, Synthesis, sintering and characterization of ceria-based solid electrolytes codoped with samaria and gadolinium using the Pechini method, Ceram. Int. 43 (2017) 16408–16415. doi:10.1016/j.ceramint.2017.09.017.

[55] D.B. Williams, B. Carter, Transmission Electron Microscopy A Textbook for Materials Science, 1st ed., Springer US, 2009.

5 Investigation of iron-manganese mixed metal oxide catalysts for the total oxidation of propane.

5.1 Introduction

As shown in the previous chapter metal oxides containing manganese are extremely active for VOC total oxidation reactions. Manganese oxides have been modified with a variety of elements leading to synergy and increased total oxidation activity. Adding silver into the manganese oxide lattice led to an increase in carbon monoxide oxidation activity [1]. Along with lanthanides and precious metals, manganese has been doped with a range of top row transition metals. Synergy between copper and manganese oxides have been reported for total oxidation of naphthalene [2], benzene [3,4] and carbon monoxide [5]. The increased activity of the mixed metal oxides have been attributed to increased migration of copper into the manganese oxide lattice leading to formation of solid solutions [5].

To further reduce the cost of VOC total oxidation catalysts, cheaper and abundant materials such as iron oxides have been suggested. Currently iron oxides are used as catalysts for large scale processes such as ammonia synthesis and high temperature water gas shift [6]. Iron oxides are rarely studied for VOC total oxidation reactions however have shown appreciable naphthalene total oxidation activity [7]. Also high surface area iron oxide, produced using a mesoporous silica structure, is reported to be active for propane and toluene total oxidation [8]. Gold and platinum nanoparticles have been supported on iron oxides for CO oxidation [9,10]. Iron has regularly been used as a dopant in metal oxide lattices. Addition of 5 % iron into titania showed significant increase in toluene total oxidation activity [11] and incorporation of 1 % and 2 % iron oxide into ceria showed noticeable increase for soot oxidation [12].

Solid solutions have also been reported in iron-manganese mixed metal oxides, with smaller iron ions incorporating into the manganese oxide lattice [13]. The surface of the iron-manganese oxide solid solution will contain many defect sites leading to oxygen vacancies on the surface, compared to the metal oxides components alone. This has led to synergy between iron and manganese mixed metal oxides for the total oxidation of toluene [14,15], ethanol and ethyl acetate [15]. Iron-manganese mixed metal oxides have also shown synergy for the partial oxidation of propane and propene [16]. Therefore, it is hoped synergistic propane and naphthalene total oxidation activity between iron and manganese mixed metal oxides can be observed.

Against this background, iron-manganese mixed metal oxides were prepared using co-precipitation. The effect of precipitating base will be investigated, along with calcination temperature. All catalysts with be characterised using a range of bulk and surface methods and tested for VOC total oxidation.

5.2 Results on the effects of Fe:Mn ratios on iron-manganese mixed metal oxides

For the study of iron and manganese ratios, iron-manganese mixed metal oxides were precipitated from 0.25 M premixed solutions of iron and manganese nitrates. A 1 M solution of sodium carbonate was used as the precipitating agent and the pH was kept constant at 9. The solution was aged for 2 hours at 60 °C and then filtered and washed with 1 l of warm water. The following precipitate was dried for 16 hours at 110 °C and calcined at 500 °C for 3 hours.

5.2.1 Precursor characterisation

5.2.1.1 Thermal gravimetric analysis
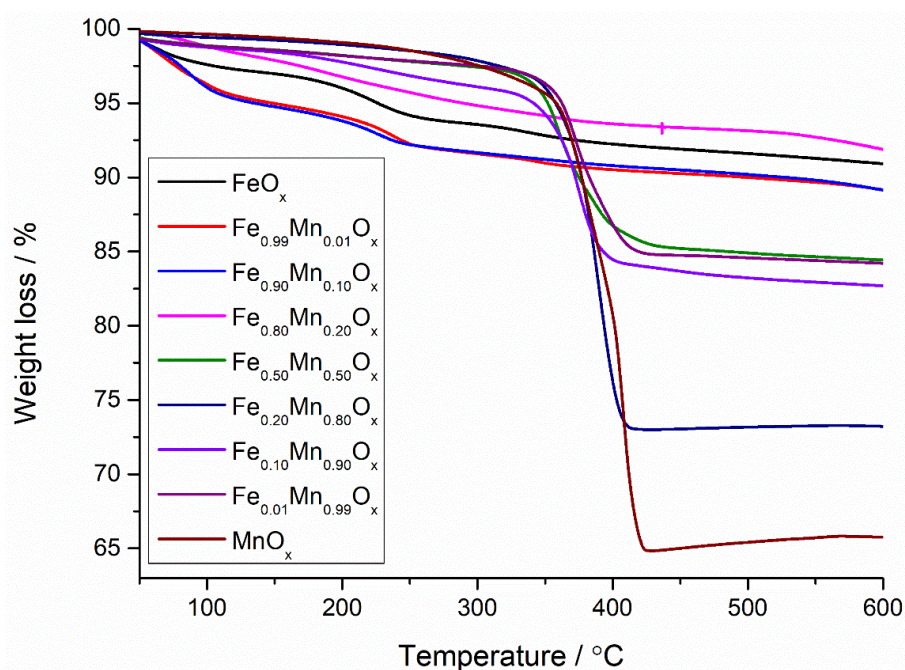
Figure 5-1: Thermogravimetric analysis of all the pre-calcined iron-manganese mixed metal oxides prepared *via* co-precipitation using sodium carbonate. Samples heated in a flowing N_2 atmosphere from 50 to 600 °C with a ramp rate of 5 °C min^{-1}

The thermal decomposition profiles of the iron-manganese mixed metal oxides are shown in Figure 5-1. The decomposition profile of the iron oxide had two weight loss events. A prolonged loss from 100-250 °C, accounting for a 7 % weight loss, and another minor weight loss is seen between 300-375 °C, accounting for 2 % weight loss. Iron nitrates

decomposed at 150 °C [17] and iron carbonates decompose at 190 °C [18] with both accounting for a 40 % weight loss. As the weight loss in this region is smaller compared to the literature values, and most of it occurring around 190 °C. This suggests only a small amounts of iron nitrate has been converted into iron carbonate. The decomposition profile of the manganese oxide occurs within a very short temperature range starting at 400 °C and accounts for 35 % weight loss.

The decomposition profiles of the iron-manganese mixed metal oxides vary depending on the iron content of the mixed metal oxide. Mixed metal oxides with high iron content (above 80 %) had similar decomposition profiles to the iron oxide, with one small decomposition regime observed between 100-250 °C. This region consists of two small weight loss events, suggesting the decomposition of both nitrates and carbonates has occurred. This suggests that only small amounts of iron nitrate and manganese nitrate species were converted into carbonates during preparation of the iron-manganese mixed metal oxides. However, as the iron content of the iron-manganese mixed metal oxide decreases below 50 %, the decomposition profile resembles manganese oxide. Only one large weight loss was observed around 400 °C, accounting for 15-23 % weight loss depending on the iron-manganese mixed metal oxide. With no separate iron nitrate/ carbonate and manganese carbonate decompositions observed in the iron-manganese mixed metal oxides, this suggests both species are well mixed in the mixed metal catalyst precursors.

Unlike in the other results chapters, no *in situ* XRD analysis was undertaken for the iron-manganese mixed metal oxides. Therefore a 500 °C calcination temperature was selected using the TGA decomposition profiles of the iron-manganese metal oxides. No further decomposition events were observed after this temperature suggesting all precursor species had been converted into the mixed metal oxide.

5.2.2 Catalyst performance

5.2.2.1 Propane total oxidation

All iron-manganese mixed metal oxides showed appreciable propane total oxidation activity, Figure 5-2. All samples showed high CO_2 selectivity (>99 %) throughout the reaction runs. The iron oxide showed the lowest propane total oxidation activity of all the samples tested throughout the investigation. Only 30 % propane conversion was achieved within the temperature range. Manganese oxide showed significantly better propane total oxidation activity compared to the iron oxide with 100 % propane conversion occurring at 500 °C.

Addition of 1 % manganese oxide into the iron oxide led to a significant increase in propane total oxidation activity compared to the iron oxide. All the other iron-manganese mixed metal oxides showed propane total oxidation higher than the manganese oxide. Addition of higher concentrations of manganese into the iron lead to higher propane total oxidation activity compared to the palladium reference catalyst and followed the general trend:
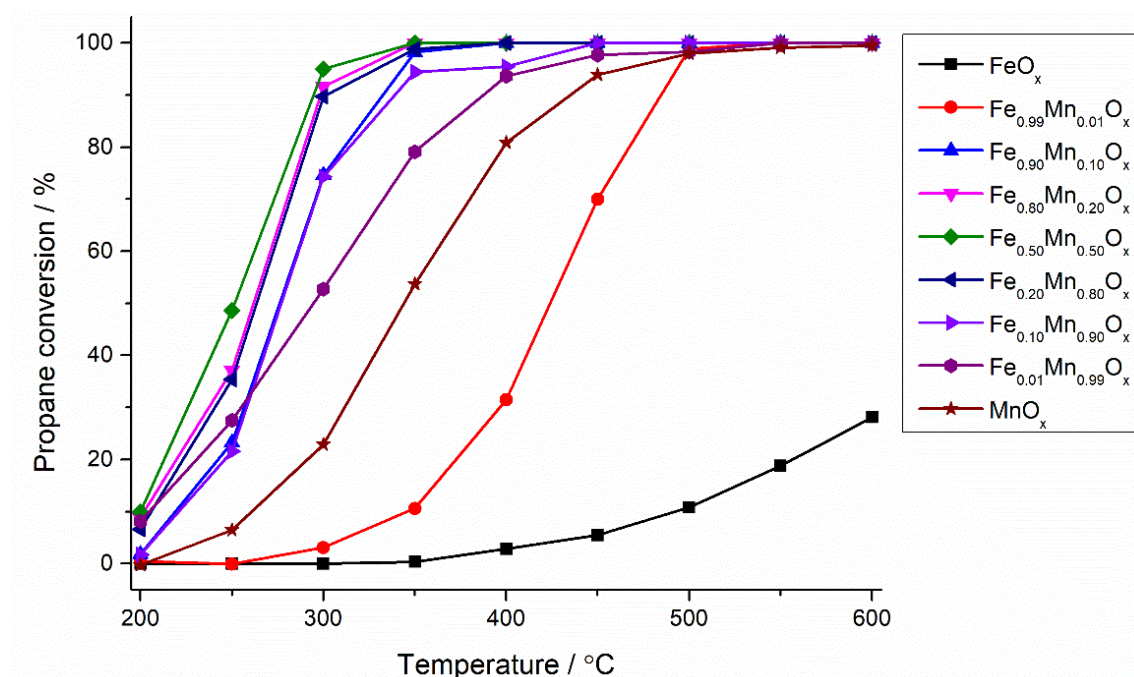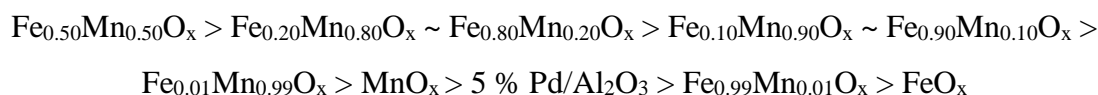
$$Fe_{0.50}Mn_{0.50}O_x > Fe_{0.20}Mn_{0.80}O_x \sim Fe_{0.80}Mn_{0.20}O_x > Fe_{0.10}Mn_{0.90}O_x \sim Fe_{0.90}Mn_{0.10}O_x >$$

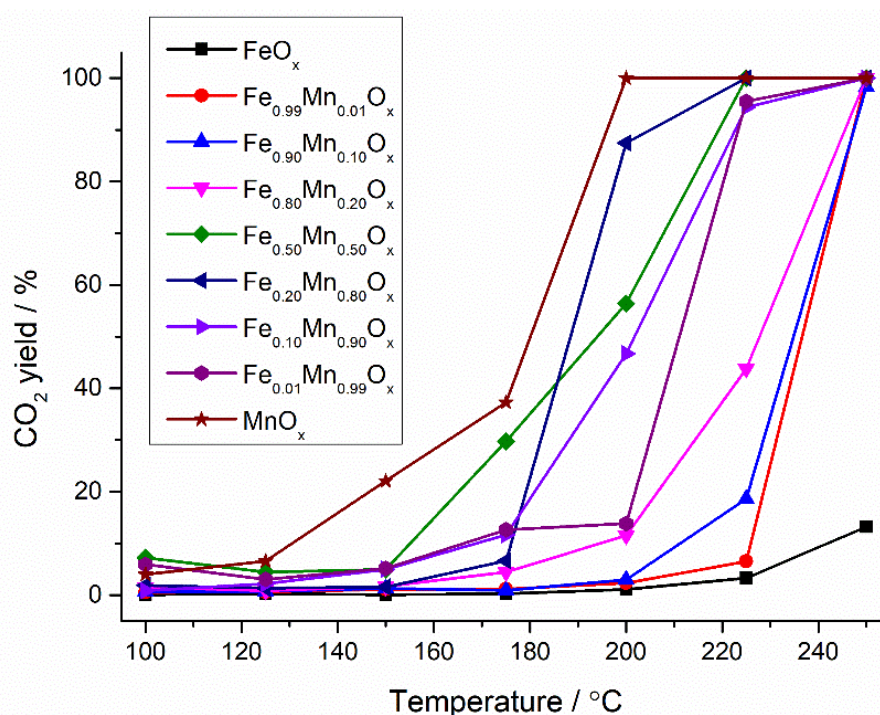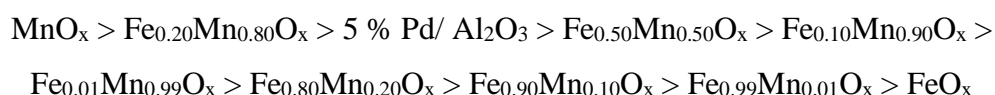$$Fe_{0.01}Mn_{0.99}O_x > MnO_x > 5 \% \ Pd/Al_2O_3 > Fe_{0.99}Mn_{0.01}O_x > FeO_x$$

Figure 5-2: Catalytic activities for the total oxidation of propane of the iron-manganese mixed metal oxide catalysts prepared *via* co-precipitation using sodium carbonate. Reaction conditions: GHSV: 45,000 h^{-1}, temperature range 200-600 °C, 5000 ppm propane in air. Legend refers to the different Fe:Mn ratios

5.2.2.2 Naphthalene total oxidation

All iron-manganese mixed metal oxides showed appreciable activity for naphthalene total oxidation, Figure 5-3. Unlike the naphthalene total oxidation over ceria containing catalysts in the previous chapters, the carbon balance did not vary during the reaction run. All reaction runs showed carbon balance above 90 % throughout the reaction runs. This indicates minimal naphthalene adsorption has occurred on the surface of the catalysts. Only naphthalene and carbon dioxide were observed in the GC suggesting only the total oxidation pathway was occurring over the catalyst samples. The iron oxide had the lowest naphthalene total oxidation activity out of the samples tested throughout the thesis. This is observed in previous studies with both manganese oxide and ceria showing higher

naphthalene total oxidation activity compared to iron oxide over the temperature range studied [7]. Manganese oxide showed significantly higher naphthalene total oxidation activity compared to the iron oxide. Addition of manganese into the iron oxide produced catalysts more active than the iron oxide however no synergy between the two metals was observed. Only one iron-manganese mixed metal oxide showed increased naphthalene total oxidation activity compared to the palladium reference. A general trend in naphthalene total oxidation over iron manganese mixed metal oxides is:

$$MnO_x > Fe_{0.20}Mn_{0.80}O_x > 5 \% \ Pd/ \ Al_2O_3 > Fe_{0.50}Mn_{0.50}O_x > Fe_{0.10}Mn_{0.90}O_x >$$

$$Fe_{0.01}Mn_{0.99}O_x > Fe_{0.80}Mn_{0.20}O_x > Fe_{0.90}Mn_{0.10}O_x > Fe_{0.99}Mn_{0.01}O_x > FeO_x$$

Figure 5-3: Catalytic activities for the total oxidation of naphthalene over iron-manganese mixed metal oxide catalysts prepared *via* co-precipitation using sodium carbonate. Reaction conditions: GHSV: 45,000 h^{-1}, temperature range: 100-250 °C, 100 vppm naphthalene in 20 % O_2 balanced with He. Legend refers to different Fe:Mn ratios

5.2.3 Catalyst characterisation

5.2.3.1 X-ray diffraction

XRD patterns of the iron-manganese mixed metal oxides are shown in Figure 5-4 along with derived data in Table 5-1. As mentioned in the previous chapter, a majority of bulk manganese oxide is present in the MnO_2 phase with Mn_2O_3 also present. Like manganese oxides, iron oxide can be present in a variety of oxidation states. XRD reflections at 24 °, 33 °, 35 °, 40 °, 49 °, 54 ° and 57 ° are attributed to Fe_2O_3 [19] and reflections at 30 °, 36

°, 43 °, 53 °, 57 ° and 62 ° indicate the presence of Fe_3O_4 [20]. The XRD reflections of the iron oxide indicate it is present in a Fe_2O_3 phase of low crystallinity.

Assessment of the XRD patterns of the iron-manganese mixed oxides show that the crystallinity increase upon increasing manganese content of the mixed metal oxide compared to the iron oxide sample. Iron-manganese mixed metal oxides with manganese content below 50 % only show XRD reflections ascribed to iron oxide present in the Fe_2O_3 phase. Combinations of Fe_2O_3 and MnO_2 mixed metal oxides have been reported in the presence of lithium precipitating agent [21]. Therefore the presence of a potential small cation, such a sodium, in the lattice of iron-manganese mixed metal oxide may stabilise the two metal oxides in a solid solution. As the manganese content of the mixed metal oxide increased above 50 %, additional reflections appear. These additional reflections were attributed to the presence of manganese oxide present in the MnO_2 phase alongside the iron oxide. With two separate metal oxides observed in the bulk of the mixed metal oxide, this indicates phase separation has occurred. Phase separation has been reported in iron-manganese mixed metal oxides calcined below 1000 °C [13].
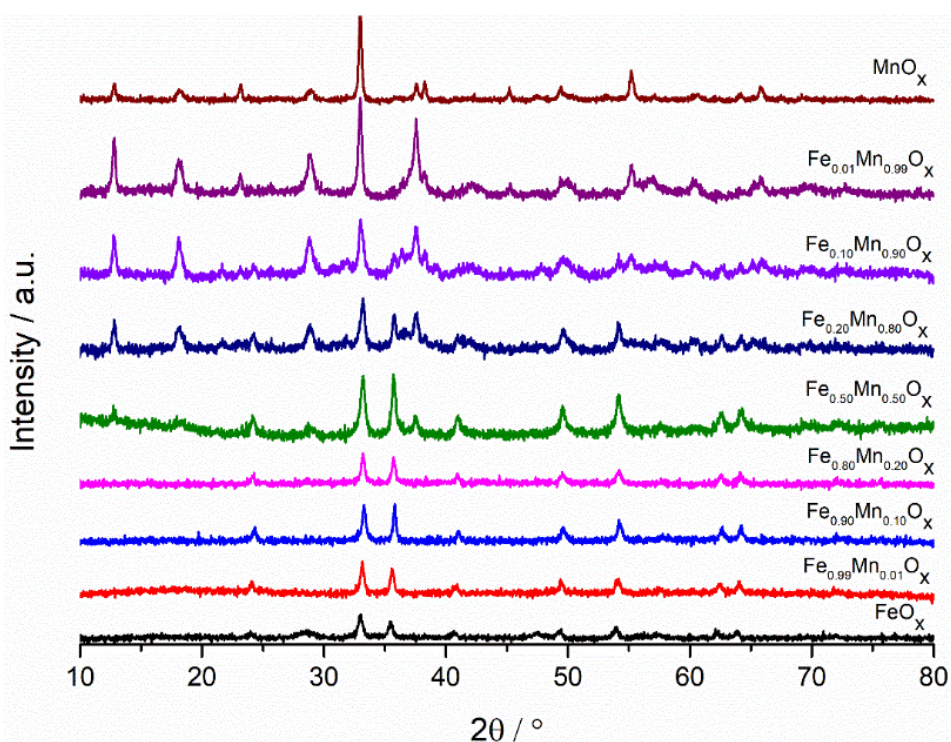
Figure 5-4: Powder XRD of the iron-manganese mixed metal oxide catalysts prepared *via* co-precipitation using sodium carbonate

MnO_2 is reported to have lower naphthalene total oxidation activity compared to Mn_2O_3 [22]. With minor phases of Mn_2O_3 present along with the MnO_2 in the manganese oxide, whereas the mixed metal oxides only contained MnO_2 in the bulk. This could be a factor

191

for the lower naphthalene total oxidation activity observed over high manganese containing iron-manganese mixed metal oxides.

The iron oxide had a relatively small crystallite size and this increased significantly as manganese oxide was introduced into the lattice, Table 5-1. This follows the increase in crystallinity observed in the mixed metal oxides. As the manganese oxide content of the iron-manganese mixed metal oxide increased, the crystallite size of the manganese oxide phase increased. However the manganese oxide still had the largest crystallite size of the manganese containing catalysts. As seen in the previous results chapter, the phase of manganese oxide along with manganese oxide crystallite size had a significant impact on the naphthalene total oxidation activity. With the large crystallite size of the manganese oxide, this may lead to the increased naphthalene total oxidation activity observed for this sample compared to the other iron-manganese mixed metal oxides. However, this trend isn't linear, as the sample with the activity of the manganese oxide with the 2nd largest crystallite size, $Fe_{0.01}Mn_{0.99}O_x$, having lower naphthalene total oxidation activity. This suggests other factors will affect the VOC total oxidation activity of the iron-manganese oxides.

Table 5-1: Physical properties of the iron-manganese mixed metal oxides derived from XRD

Sample	Phases present	Crystallite size / Å	
		FeO_x	MnO_x
FeO_x	Fe_2O_3	190	-
$Fe_{0.99}Mn_{0.01}O_x$	Fe_2O_3	387	-
$Fe_{0.90}Mn_{0.10}O_x$	Fe_2O_3	322	-
$Fe_{0.80}Mn_{0.20}O_x$	Fe_2O_3	280	-
$Fe_{0.50}Mn_{0.50}O_x$	Fe_2O_3	291	-
$Fe_{0.20}Mn_{0.80}O_x$	Fe_2O_3, MnO_2	366	188
$Fe_{0.10}Mn_{0.90}O_x$	Fe_2O_3, MnO_2	225	160
$Fe_{0.01}Mn_{0.99}O_x$	MnO_2	-	317
MnO_x	Mn_2O_3, MnO_2	-	361

5.2.3.2 Surface area

The surface areas of the iron-manganese mixed metal oxides are shown below, Table 5-2, with the iron oxide showing the highest surface area and manganese oxide the lowest of the iron-manganese mixed metal oxides analysed. Addition of manganese into the iron oxide led to a decrease in the surface area, with the iron-manganese mixed metal oxides showing surface areas lower than the iron oxide. However, as reported previously, the iron-manganese mixed metal oxides all have surface areas higher than that of the

manganese oxide [23,24]. There is a noticeable trend between surface area and crystallite size of the iron-manganese mixed metal oxide, however the trend isn't linear.

Surface area is noted to effect the activity of toluene and ethanol total oxidation over iron-manganese oxides [15]. Surface area normalised propane and naphthalene total oxidation rates are also shown in Table 5-2. An appreciable positive relationship is noted between the surface area and the rate of propane total oxidation for all the iron-manganese mixed metal oxides which showed activity at 250 °C. The same relationship between surface area and naphthalene total oxidation is noted for iron-manganese mixed metal oxides. However, due to the significantly higher activity of the manganese oxide, this trend wasn't universal for all the samples tested. This suggests that surface area of the iron-manganese mixed metal oxide effects the activity for propane and naphthalene total oxidation.

Table 5-2: Surface area of the iron-manganese mixed metal oxide catalysts prepared *via* co-precipitation using sodium carbonate. Calculated using the 5-point N_2 adsorption BET analysis

Sample	BET Surface area / $m^2 g^{-1}$	Surface area normalised rate of propane total oxidation at 250 °C (10^{-7}) / $mol\ s^{-1}\ m^{-2}$	Surface area normalised rate of naphthalene total oxidation at 175 °C (10^{-11}) / $mol\ s^{-1}\ m^{-2}$
FeO_x	62	0	0
$Fe_{0.99}Mn_{0.01}O_x$	23	0	0.01
$Fe_{0.90}Mn_{0.10}O_x$	25	0.33	0.01
$Fe_{0.80}Mn_{0.20}O_x$	31	0.41	0.24
$Fe_{0.50}Mn_{0.50}O_x$	42	0.40	1.19
$Fe_{0.20}Mn_{0.80}O_x$	33	0.37	0.33
$Fe_{0.10}Mn_{0.90}O_x$	31	0.24	0.57
$Fe_{0.01}Mn_{0.99}O_x$	35	0.27	0.59
MnO_x	18	0.14	1.70

5.2.3.3 Temperature programmed reduction

Temperature programmed reduction profiles of the iron-manganese mixed metal oxides are shown in Figure 5-5. As mentioned in the previous results chapter, the manganese oxide is present in the MnO_2 phase. Iron oxides can be present in a range of oxidation states, which have similar reduction profiles. Only one peak for reduction at 550 °C is noted during the reduction of Fe_3O_4 [25]. The reduction of Fe_2O_3 contains the peak at 550 °C, along with a minor peak 400 °C [25,26]. Depending on the temperature ramp rate, a second minor peak is also noted after the peak at 550 °C, which was assigned to reduction

of residual FeO to Fe [26]. With a clear minor reduction peak at 400 °C along with the peak at 550 °C, this suggests the iron oxide is present in the Fe_2O_3, confirming the bulk phase identification from XRD.
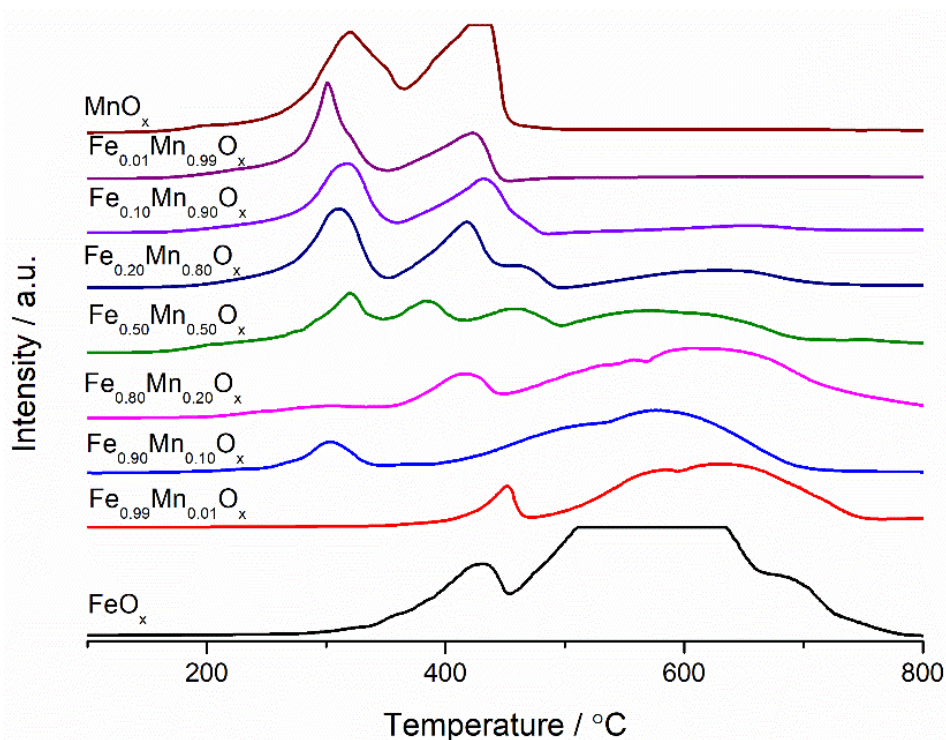

Figure 5-5: Hydrogen temperature programmed reduction profiles of the iron-manganese mixed metal oxide catalysts prepared *via* co-precipitation using sodium carbonate. Reaction conditions: 30 mg sample, 30 ml min^{-1} 10 % H_2/ Ar, temperature range: 100-800 °C

The reduction profiles of the iron-manganese mixed metal oxides vary upon the ratio of iron and manganese present in the sample. One observation noted for all reduction profiles, is the decrease in magnitude of the peak at 550 °C upon increasing manganese content of the mixed metal oxide. This confirms the presence of Fe_2O_3 in all the mixed metal oxides as seen in the bulk phase identification. Mixed metal oxides containing below 50 % iron had reduction profiles which resemble the profile of the iron oxide. However, there were some shifts in temperature of the reduction peaks which may have arisen from the manganese in the lattice effecting the ease of iron oxide reduction. The minor reduction peak of the γ-Fe_2O_3 is noted to have a lower reduction temperature compared to the α-Fe_2O_3 [25]. The $Fe_{0.50}Mn_{0.50}O_x$ had four low intensity peaks at 320 °C, 380 °C, 480 °C and 550 °C. These peaks arise from addition of reduction profiles of iron oxide and manganese oxide. Due to the overlapping of manganese oxide and iron oxide reduction temperatures, it is difficult to accurately identify the phases present. However with the large low intensity reduction regime present at 550 °C, this suggests the presence

of Fe_2O_3 as observed in XRD. The presence of a reduction peak at 380 °C also indicates the presence of Fe_2O_3.

The reduction profiles of the iron-manganese mixed metal oxides containing higher ratios of manganese follow a similar profile to the manganese oxide. The reduction profiles consist of two peaks at 300 °C and 420 °C, with an observable shoulder peak noted on the second reduction peak of $Fe_{0.20}Mn_{0.80}O_x$ and $Fe_{0.10}Mn_{0.90}O_x$. The two major reduction peaks on these samples are similar to those for reduction of MnO_2 [27], therefore confirming the phase identification from XRD. The shoulder peaks arise from the presence of Fe_2O_3, as observed in XRD.

Overall the decrease in peak intensity of the iron-manganese mixed metal oxides, compared to the parent oxides, indicates the extent of reduction significantly decreases upon mixing of iron and manganese mixed metal oxides. Only small decreases in reduction temperature observed in the mixed metal oxides compared to the parent oxides. The ease of reduction is only slightly affected upon mixing of iron and manganese mixed metal oxides. One observation from analysis of TPR is the presence of mixed iron oxide and manganese oxide phases in the $Fe_{0.50}Mn_{0.50}O_x$ and $Fe_{0.20}Mn_{0.80}O_x$ samples. With these two samples showing high propane total oxidation activity, this suggests the presence of mixed phases or potential dilution of iron or manganese oxide with the other metal oxide component may cause an increase in active sites for propane total oxidation.

5.2.3.4 Microwave-plasma atomic emission spectroscopy

Table 5-3: Elemental analysis of the iron-manganese mixed metal oxides prepared *via* co-precipitation using sodium carbonate derived from MP-AES

| Sample	Concentration / ppm			Relative Fe / %	Relative Mn / %
	Fe	Mn	Na		
FeO_x	53.8	-	4.0	100	0
$Fe_{0.99}Mn_{0.01}O_x$	45.7	0.4	5.5	99.2	0.8
$Fe_{0.90}Mn_{0.10}O_x$	53.9	3.2	3.7	94.4	5.6
$Fe_{0.80}Mn_{0.20}O_x$	43.3	8.0	5.2	84.4	15.6
$Fe_{0.50}Mn_{0.50}O_x$	33.0	26.1	4.0	55.8	44.2
$Fe_{0.20}Mn_{0.80}O_x$	16.9	48.1	3.7	26.0	74.0
$Fe_{0.10}Mn_{0.90}O_x$	7.8	52.2	3.7	13.0	87.0
$Fe_{0.01}Mn_{0.99}O_x$	2.0	60.9	4.0	3.2	96.8
MnO_x	-	60.8	4.0	0	100

Elemental analysis of the iron-manganese mixed metal oxides, Table 5-3, show the iron content of all iron-manganese mixed metal oxides to be marginally higher than the nominal value. This could arise from the different solubilities of the manganese and iron carbonate species at pH 9 [28]. This will lead to increased amounts of iron carbonate

195

precipitation compared to manganese carbonate. Also the hydroscopic nature of the iron and manganese nitrate precursors, may lead to discrepancies during weighing out of the samples. However even with the discrepancies, the table above shows that co-precipitation produces iron-manganese oxides with values consistently close to the expected nominal values.

As seen in the ceria-manganese mixed metal oxides prepared *via* co-precipitation using sodium carbonate, sodium is also present in the iron-manganese mixed metal oxides. The sodium content of the iron-manganese mixed metal oxides range between 5-10 %, which is similar to the previously mentioned ceria-manganese mixed metal oxides. The effects of sodium poisoning in manganese containing mixed metal oxides for CO oxidation have been previously reported [29]. So the presence of this sodium on the surface or bulk of the iron-manganese mixed metal oxides may lead to hinderance of VOC total oxidation activity. This is noted for the differences in naphthalene total oxidation activity of the co-precipitated iron oxides and manganese oxides compared to the literature values [7].

5.2.3.5 Electron microscopy

5.2.3.5.1 Scanning electron microscopy
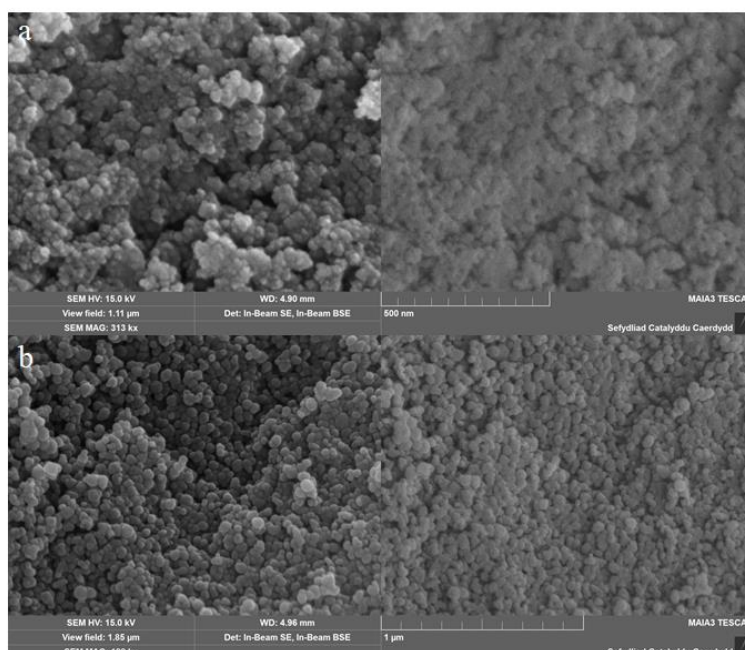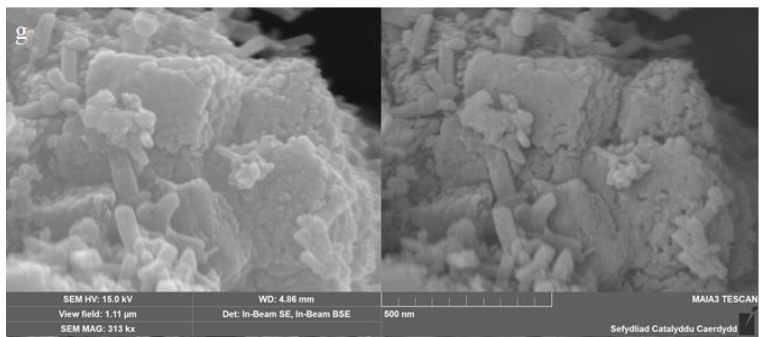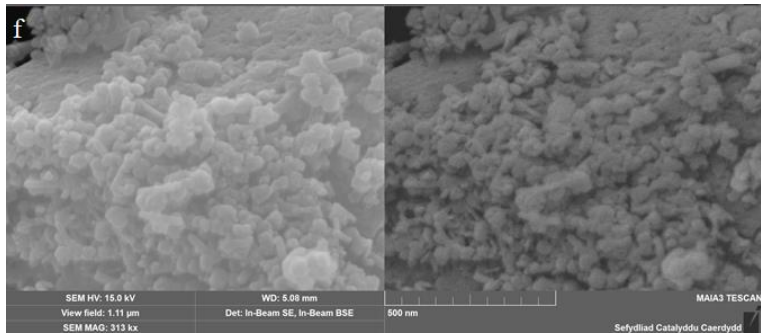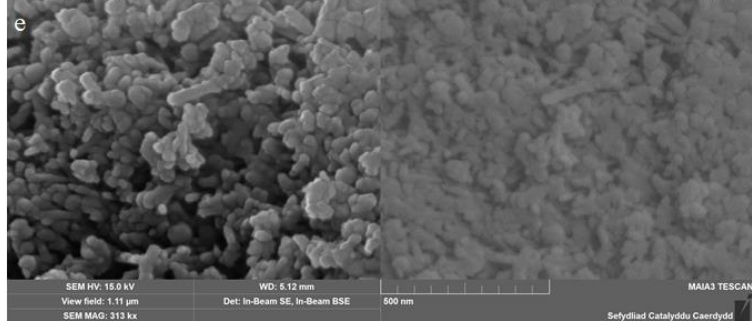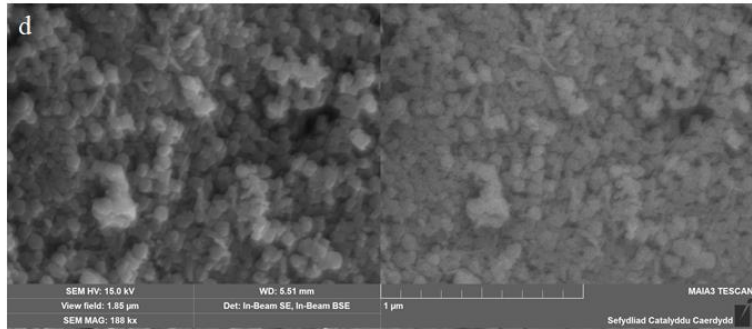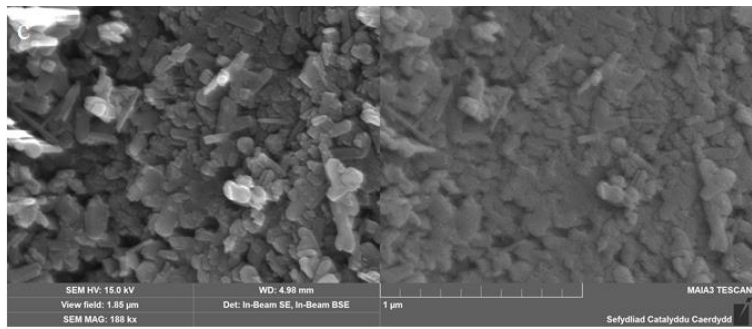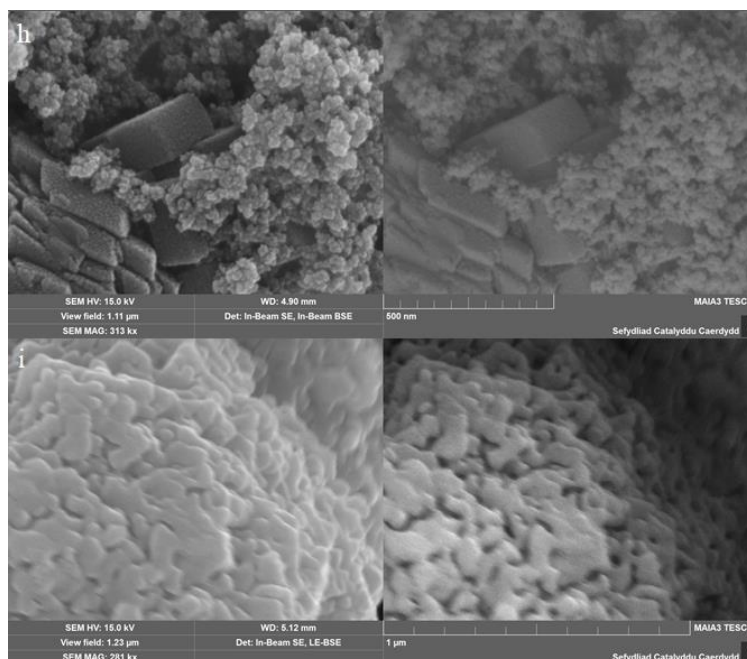
Figure 5-6: The secondary electron (left) and backscattered electron (right) micrographs of (a) FeO_x, (b) $Fe_{0.99}Mn_{0.01}O_x$, (c) $Fe_{0.90}Mn_{0.10}O_x$, (d) $Fe_{0.80}Mn_{0.20}O_x$, (e) $Fe_{0.50}Mn_{0.50}O_x$, (f) $Fe_{0.20}Mn_{0.80}O_x$, (g) $Fe_{0.10}Mn_{0.90}O_x$, (h) $Fe_{0.01}Mn_{0.99}O_x$ and (g) MnO_x. Image magnification: 313 kx

Scanning electron micrographs of the iron-manganese mixed metal oxides are shown in Figure 5-6. The iron oxide forms a spherical sponge morphology and as mentioned previously, the morphology of the manganese oxide resembles crystallites layered on top of each other. Addition of manganese into the iron oxides did not cause a significant change in the morphology of the sample. The morphology remained consistent until the $Fe_{0.50}Mn_{0.50}O_x$. However, as the manganese became the dominant component of the mixed metal oxide, the plate-like morphology became dominant. Some areas of the spherical particles were observed in the manganese dominant iron-manganese samples. This suggests the iron hasn't fully incorporated into the manganese oxide lattice as seen in the phase separation in XRD. However due to the similarity of the phase contrast between the iron and manganese, identifying the phase separation from the back-scattered image was unable to be undertaken.

5.2.3.5.2 Electron dispersive x-ray spectroscopy

In addition to the MP-AES elemental analysis, EDX analysis was undertaken to determine the elemental composition in the bulk of the iron-manganese mixed metal oxides. The MP-AES analysis of the iron-manganese mixed metal oxides show the ratios were close to the nominal values, however, they were in slight excess in iron content. The iron: manganese ratios calculated from EDX analysis show the ratios to be close to

expected nominal values. However, it is noted the samples at the extreme ends of the iron:manganese ratios showed iron content higher than the nominal ratio. As mentioned previously this may have occurred due to errors during preparation of the sample or due to the differing precipitation rates of the iron and manganese carbonates during the catalyst preparation.

Table 5-4: SEM-EDX derived bulk elemental analysis of the iron-manganese mixed metal oxides prepared using co-precipitation using sodium carbonate

Sample	Concentration / %				Relative Fe / %	Relative Mn / %
	Fe	Mn	O	Na		
FeO_x	36.6	0	60.1	3.4	100	0
$Fe_{0.99}Mn_{0.01}O_x$	33.0	0.3	63.1	3.7	99.19	0.81
$Fe_{0.90}Mn_{0.10}O_x$	28.7	2.2	66.2	2.9	93.00	7.00
$Fe_{0.80}Mn_{0.20}O_x$	22.6	5.8	66.8	4.8	79.58	20.42
$Fe_{0.50}Mn_{0.50}O_x$	15.3	16.3	64.2	4.2	48.31	51.69
$Fe_{0.20}Mn_{0.80}O_x$	6.8	23.9	66.4	2.9	22.15	77.85
$Fe_{0.10}Mn_{0.90}O_x$	3.6	24.1	68.0	4.4	12.95	87.05
$Fe_{0.01}Mn_{0.99}O_x$	0.6	26.7	69.9	2.8	2.27	97.73
MnO_x	0	36.1	59.9	4.1	0	100

As seen in the MP-AES analysis of the iron-manganese mixed metal oxides, sodium is prevalent throughout all the mixed metal oxides. The values of sodium in EDX are significantly lower than the values derived from MP-AES. This discrepency may have occurred due to the area examined under EDX, which may not have observed sodium enriched areas. As the MP-AES analysis doesn't contain oxygen in the elemental analysis, the values will also be different when compared to the EDX values. Also there maybe differences in the bulk and surface sodium content leading to potentially increased sodium on the surface rather than the bulk of the iron-manganese mixed metal oxides.

The elemental EDX maps of the single and mixed metal oxides are shown in Figure 5-7 and Figure 5-8 respectively. Sodium is regularly distributed across the iron-manganese mixed metal oxides.
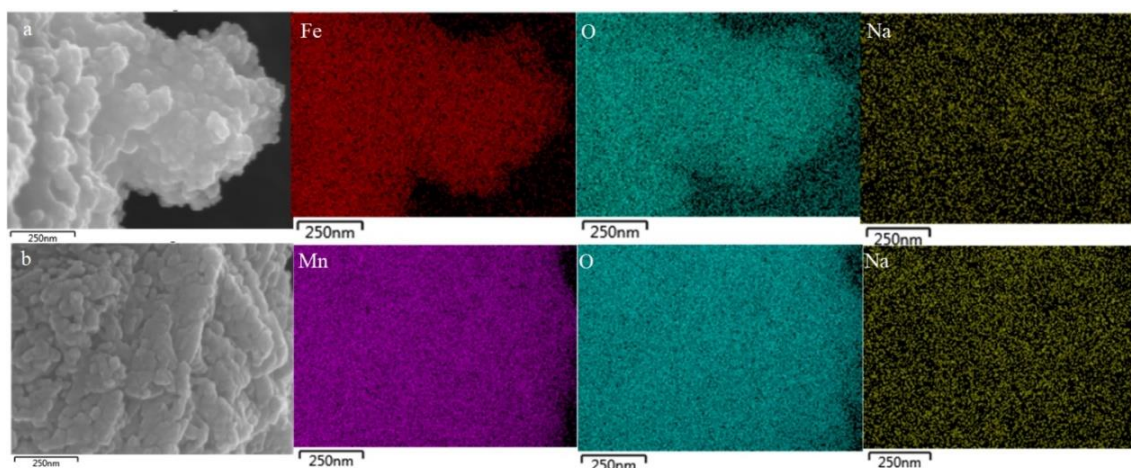
Figure 5-7: SEM-EDX mapping of (a) FeO$_x$ and (b) MnO$_x$. Showing iron (red), manganese (pink), oxygen (blue) and sodium (yellow)

The EDX maps of the iron-manganese mixed metal oxides show the iron and manganese to be very well mixed together, with very little phase segregation of each metal observed. Some iron-rich areas are observed in the EDX maps of the Fe$_{0.20}$Mn$_{0.80}$O$_x$ and Fe$_{0.10}$Mn$_{0.90}$O$_x$ which is consistent with the XRD phase analysis of these samples. These iron species may also provide the extra reduction peaks observed in the TPR of these samples. In the previous chapter, the phase segregation of the Ce$_{0.25}$Mn$_{0.75}$O$_x$ was one of the factors for its high naphthalene total oxidation activity. Therefore with very little phase segregation observed in this samples, this may lead to the poor naphthalene total oxidation activity in the iron-manganese mixed metal oxides. Another factor could be the poor activity of the iron oxide. Even if phase segregation had occurred in the iron-manganese mixed metal oxides, due to the low activity of the secondary metal the effect may not be as pronounced.
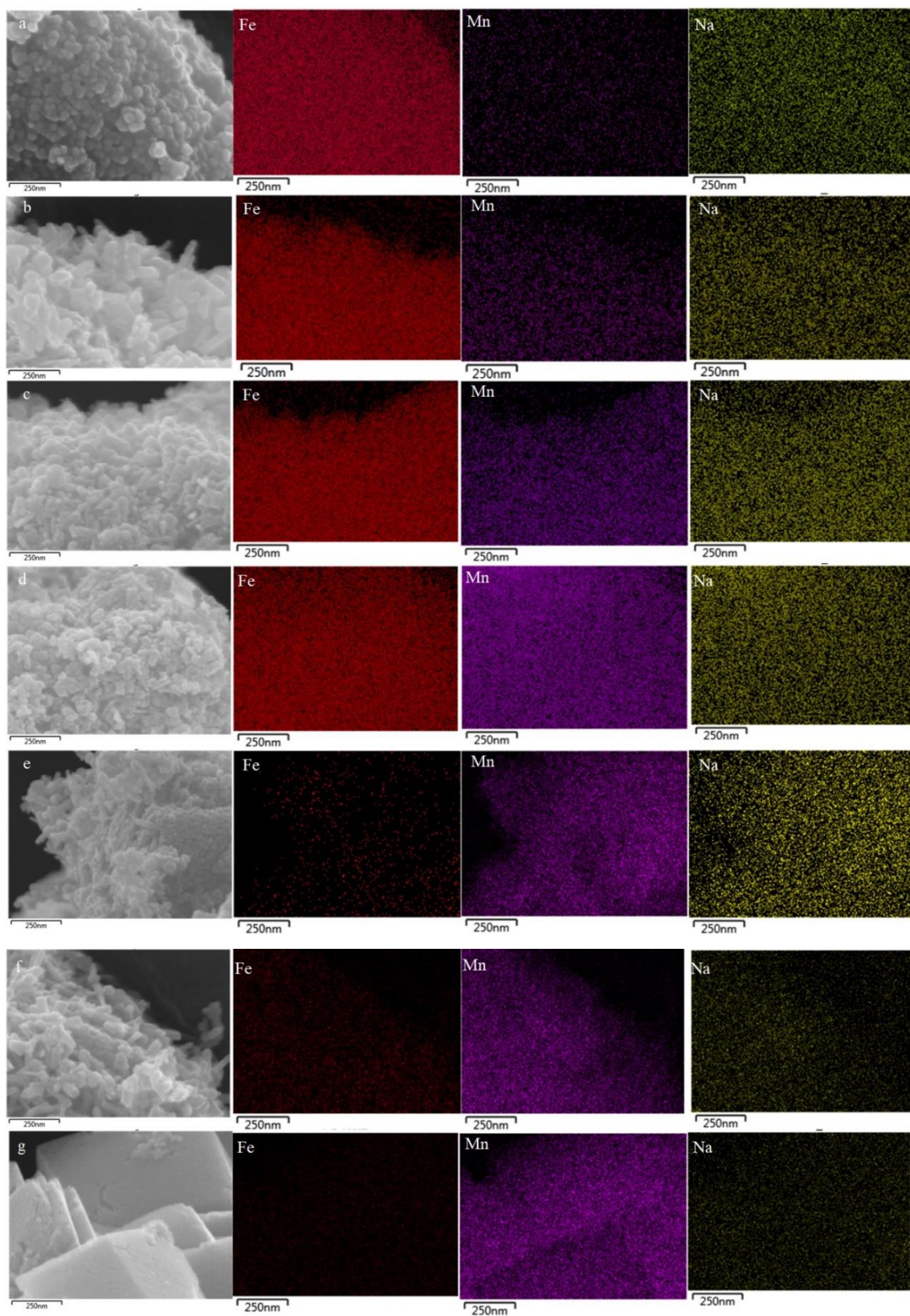
Figure 5-8: SEM-EDX mapping of (a) $Fe_{0.99}Mn_{0.01}O_x$, (b) $Fe_{0.90}Mn_{0.10}O_x$, (c) $Fe_{0.80}Mn_{0.20}O_x$, (d) $Fe_{0.50}Mn_{0.50}O_x$, (e) $Fe_{0.20}Mn_{0.80}O_x$, (f) $Fe_{0.10}Mn_{0.90}O_x$, (g) $Fe_{0.01}Mn_{0.99}O_x$. Iron (red), manganese (pink) and sodium (yellow)

5.2.3.6 X-ray photoelectron spectroscopy

Table 5-5: XPS derived surface elemental concentrations for the iron-manganese mixed metal oxides prepared *via* co-precipitation using sodium carbonate

Sample	Concentration / at. %				Relative Fe / %	Relative Mn / %
	Fe	Mn	O	Na		
FeO_x	15.6	-	81.0	3.4	100	0
$Fe_{0.99}Mn_{0.01}O_x$	21.9	0.5	65.3	12.4	97.9	2.1
$Fe_{0.90}Mn_{0.10}O_x$	19.7	3.6	69.5	7.4	84.8	15.2
$Fe_{0.80}Mn_{0.20}O_x$	15.4	6.1	67.8	10.8	71.2	28.8
$Fe_{0.50}Mn_{0.50}O_x$	13.6	13.9	67.6	4.9	49.6	50.4
$Fe_{0.20}Mn_{0.80}O_x$	10.6	18.8	68.9	1.8	36.0	64.0
$Fe_{0.10}Mn_{0.90}O_x$	6.1	22.8	69.3	1.9	21.1	78.9
$Fe_{0.01}Mn_{0.99}O_x$	3.9	24.9	70.0	1.2	13.5	86.5
MnO_x	0	31.5	61.8	6.7	0	100

To complement the EDX and MP-AES elemental analysis, XPS was used to calculate the near surface elemental composition of the iron-manganese mixed metal oxides, Table 5-5. The iron and manganese ratios are significantly different to those observed in MP-AES and EDX. Variations between bulk and surface ratios have been noted in other mixed metal oxides containing manganese prepared at pH 9 [30]. This suggests the effect maybe universal for manganese containing mixed metal oxides. The relative iron and manganese ratios indicate the metal with the minor concentration seem to segregate more on the surface. This is seen when the iron content is above 50 %, the manganese ratio is higher than the nominal value, and the reverse is noted when the iron content of the mixed metal oxide is below 50 %. When the iron and manganese ratios are the same, the relative ratio remains consistent with the nominal ratio. This suggests minor metal oxide may not form solid solutions on the surface of the mixed metal oxides and segregates to the surface of the mixed metal oxide. Manganese surface enrichment has been observed previously on iron-manganese metal oxides containing large iron particles [31].

There is also a noticeable difference between the observed bulk and surface sodium content in the iron-manganese mixed metal oxides. The iron oxide had around half the surface sodium content of the manganese oxide, even though the sodium content calculated from MP-AES showed both metal oxides had similar amounts of sodium. Variations between the EDX and MP-AES analysis are also seen in the mixed metal oxides. The sodium content of the iron-manganese mixed metal oxides varied between 5-10 % in MP-AES and 3-5 % in EDX. However the sodium content of the iron-manganese mixed metal oxides varied between 1-12 %. The iron-manganese mixed metal oxides

containing lower concentrations of manganese (below 50 %) all had surface sodium content significantly higher than the iron oxide and manganese oxide, whereas the iron-manganese mixed metal oxides with higher concentrations of manganese (above 50 %) had significantly lower sodium content compared to the mono-metallic oxides. This observation is the reverse of observations for the iron oxide and manganese oxide. This suggests the surface enrichment of the minor metal in the mixed metal oxide may reverse the sodium binding properties of the surface. However the extent of this is difficult to estimate.
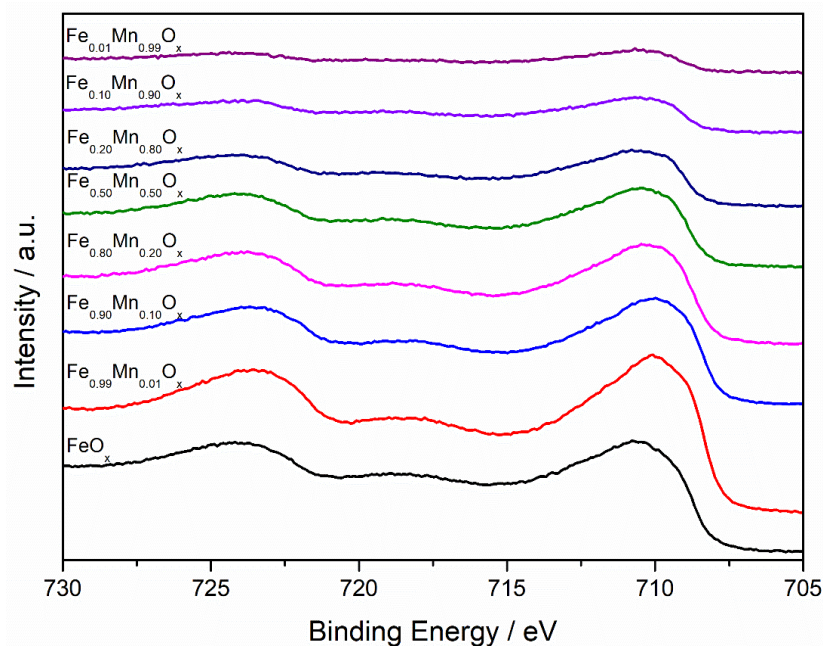
Figure 5-9: XPS spectra of the Fe 2p peaks for the iron-manganese mixed metal oxides prepared using co-precipitation using sodium carbonate

Fe 2p XPS spectra of the iron-manganese mixed metal oxides are shown in Figure 5-9. All spectra contain peaks at 710 eV and 724 eV, along with a satellite peak at 718 eV, which decrease in intensity as the iron content of the iron-manganese mixed metal oxide decreases. These peaks are characteristic of iron present in the 3+ oxidation state [32,33]. This suggests the iron species in both bulk and surface are both present in the Fe_2O_3 phase. There is a small shift to lower binding energy upon addition of manganese into the iron oxide lattice. This may arise from the increased particle size of the iron-manganese mixed metal oxides and increased electron density from the manganese, which is acting as an electron donor [31].
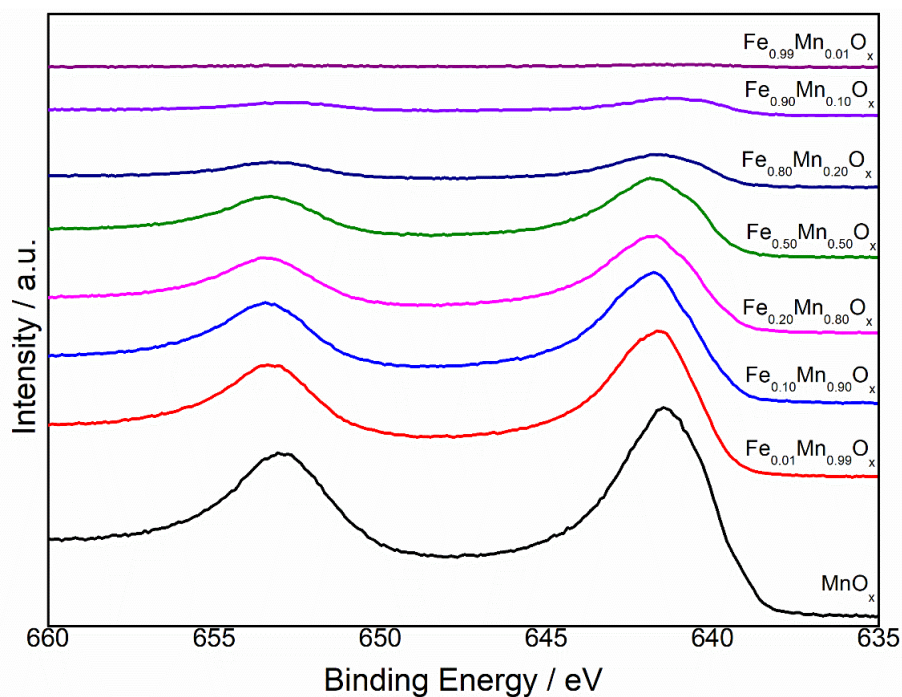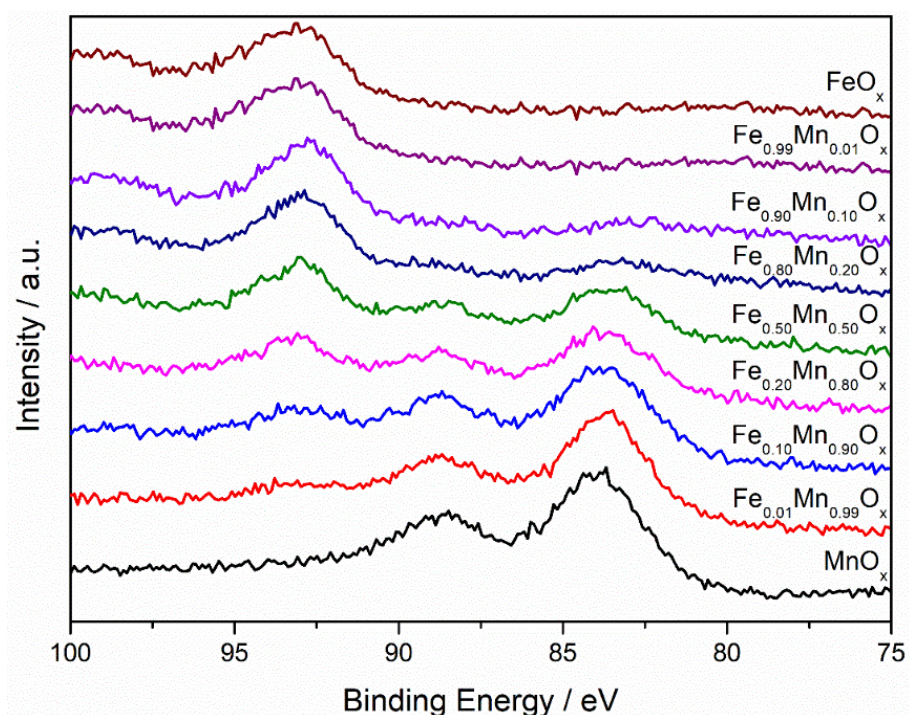
Figure 5-10: XPS spectra of the Mn 2p peaks for the iron-manganese mixed metal oxides prepared *via* co-precipitation using sodium carbonate

The Mn 2p spectra from XPS of the iron-manganese mixed metal oxides are shown in Figure 5-10. With no satellite peak observed at 647 eV on any of the Mn 2p spectra, this indicates no MnO is present on the surface of the iron-manganese mixed metal oxides [34]. As mentioned previously it is difficult to distinguish the oxidation state of the manganese oxides from the 2p spectra. However a broader peak at 640 eV is noted on the $Fe_{0.10}Mn_{0.90}O_x$, $Fe_{0.20}Mn_{0.80}O_x$ and $Fe_{0.50}Mn_{0.50}O_x$ compared to the manganese oxide. This suggests the presence of manganese in multiple oxidation states. Along with a broadening of the lower energy peak, there is a shift to higher binding energy on the minor peak upon increasing iron content of the mixed metal oxide. This is also an indication of multiple manganese oxidation states. As mentioned above, potential electron donation between the two metals may have occurred, which may also induce the shift in electron binding energy.

Figure 5-11: XPS spectra of the Mn 3s peaks for the iron-manganese mixed metal oxides prepared *via* co-precipitation using sodium carbonate

With the difficulty in determining manganese oxidation states from the 2p spectra, it can be determined by comparing the energy difference between the doublet peaks in the manganese 3s spectra, Figure 5-11. Along with the doublet peaks between 80-90 eV, assigned to manganese oxides, a peak is observed ~93 eV. The intensity of this peak increases upon increasing iron content of the iron-manganese mixed metal oxide, suggesting it arises from iron species. Previous studies noted small peaks from iron oxides at low binding energies arising from Fe 3s electron emission [35].

Table 5-6: Magnitude of peak splitting in the Mn 3s spectra for the iron-manganese mixed metal oxides prepared *via* co-precipitation using sodium carbonate

Sample	Magnitude of Mn 3s peak splitting / eV	Surface oxidation state of Mn (all +)
$Fe_{0.01}Mn_{0.99}O_x$	-	-
$Fe_{0.10}Mn_{0.90}O_x$	-	-
$Fe_{0.20}Mn_{0.80}O_x$	-	-
$Fe_{0.50}Mn_{0.50}O_x$	5.4	3
$Fe_{0.20}Mn_{0.80}O_x$	5.1	4
$Fe_{0.10}Mn_{0.90}O_x$	4.9	4
$Fe_{0.01}Mn_{0.99}O_x$	4.8	4
MnO_x	4.8	4

The peak splitting energies of the two manganese 3s peaks are shown in Table 5-6. Manganese is present in the 4+ oxidation state if the splitting is below 5.3 eV, 3+ if the

split is between 5.3-6.0 eV and 2+ if the difference is above 6.0 eV [34]. There were no peaks arising from Mn 3s in the iron-manganese mixed metal oxides containing less than 50 % manganese. However in the iron-manganese mixed metal oxides containing a majority of manganese, Mn 3s peaks were observed. The manganese oxide had the lowest peak splitting, and this increased upon increasing iron content. The increased splitting suggests potential surface defect formation from mixing of manganese oxidation states. This may lead to increased propane total oxidation activity observed in the iron-manganese mixed metal oxides. Manganese was present in the 4+ oxidation state in the manganese oxide, $Fe_{0.01}Mn_{0.99}O_x$, $Fe_{0.10}Mn_{0.90}O_x$ and $Fe_{0.20}Mn_{0.80}O_x$. This is consistent with the XRD bulk analysis of these materials, suggesting the bulk and surface species are similar in structure. However the $Fe_{0.50}Mn_{0.50}O_x$ had a splitting indicating the manganese is present in the 3+ oxidation state. Manganese oxide present in as Mn_2O_3 is known have increased VOC total oxidation activity compared to MnO_2 [22]. As seen in the previous chapter, the ceria-manganese mixed metal oxides catalysts containing Mn_2O_3 showed increased naphthalene and propane. However in the iron-manganese mixed metal oxides only synergy between iron and manganese was observed for propane total oxidation. This suggests other factors along with surface oxidation state effect VOC total oxidation in iron-manganese mixed metal oxides.

Lattice and defect oxygen species are noted for both iron and manganese oxide, and are present between 529-31 eV and 531-3 eV respectively [36,37]. The iron oxide had a high relative ratio of oxygen species compared to the manganese, which has been noted previously [38]. However when compared to the ceria-manganese mixed metal oxides, no change in the oxygen species ratios was observed, once iron and manganese oxides had been mixed together. There is a slight shift in oxygen binding energy upon increasing iron content of the iron-manganese mixed metal oxide compared to the manganese oxide. The shift had been noted in other manganese containing mixed metal oxides and arises from synergistic interactions between the two metal oxide species [39]. This synergistic interaction may cause the increased activity in propane total oxidation in the iron-manganese mixed metal oxide, however, the extent of this is difficult to analyse.
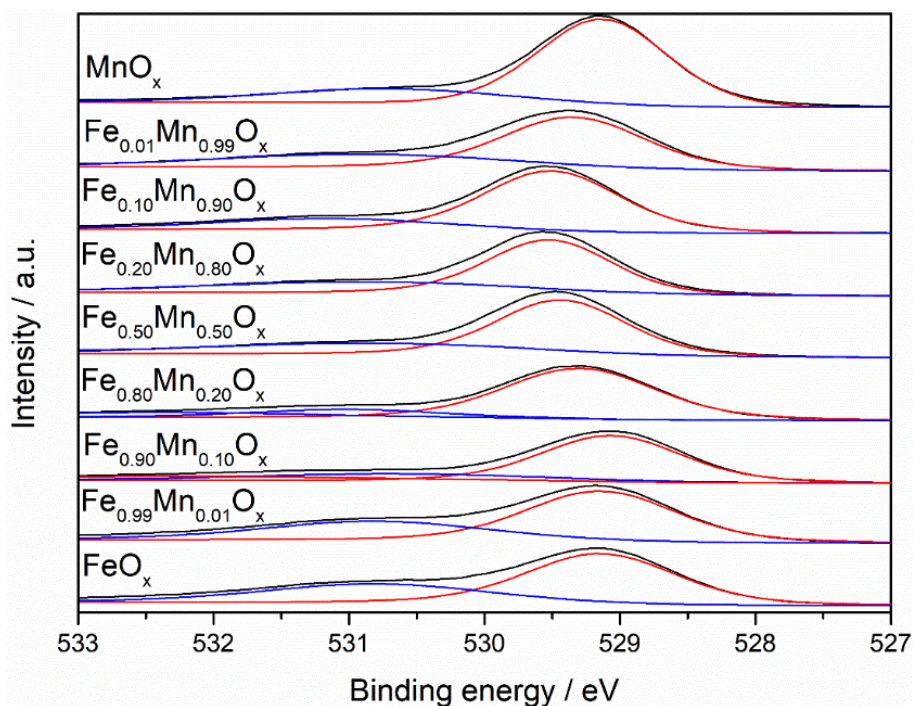
Figure 5-12: XPS spectra of the O 1s peaks of the iron-manganese mixed metal oxides prepared *via* co-precipitation using sodium carbonate

5.3 The effect of precipitating agent on the $Fe_{0.50}Mn_{0.50}O_x$ for VOC total oxidation activity

None of the iron-manganese mixed metal oxides showed synergy between the metal oxides or showed greater performance compared to the palladium reference for naphthalene total oxidation. However, synergy for propane total oxidation in iron-manganese mixed metal oxides was observed and $Fe_{0.50}Mn_{0.50}O_x$, and it was the most active iron-manganese mixed metal oxide. Therefore, for the rest of this chapter, the optimisation of $Fe_{0.50}Mn_{0.50}O_x$ for propane total oxidation was undertaken.

As seen from the previous chapter, the presence of sodium had a significant impact on the VOC total oxidation activity and effected the bulk and surface structures of the mixed metal oxides. There were difficulties in synthesising the $Fe_{0.50}Mn_{0.50}O_x$ from oxalic acid, citric acid, urea and mechanochemical grinding methods from the ceria-manganese mixed metal oxide chapter. Therefore, $Fe_{0.50}Mn_{0.50}O_x$ was prepared using co-precipitation using non-sodium precipitating agents. The same preparation method was used to prepare the $Fe_{0.50}Mn_{0.50}O_x$ however the precipitating agent was changed. Along with sodium carbonate, other carbonates: potassium carbonate and ammonium carbonate, and hydroxides, sodium hydroxide, potassium hydroxide and ammonium hydroxide solution were used to prepare the $Fe_{0.50}Mn_{0.50}O_x$.

5.3.1 Precursor characterisation

5.3.1.1 Thermal gravimetric analysis

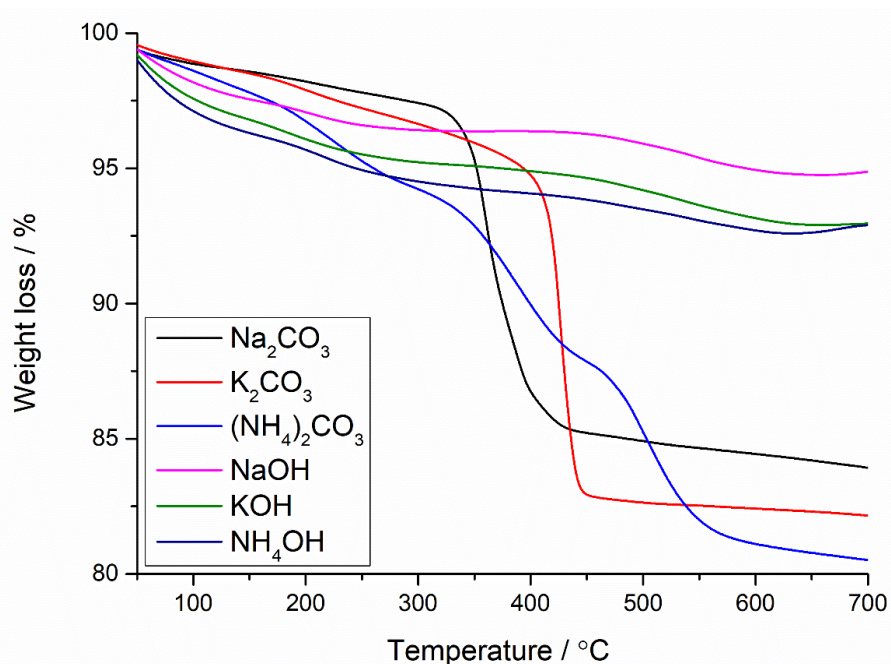Figure 5-13: Thermogravimetric analysis of the dried $Fe_{0.50}Mn_{0.50}O_x$ prepared *via* co-precipitation using different precipitating agents. Samples heated in a flowing N_2 atmosphere from 100-700 °C at a ramp rate of 5 °C min^{-1}

The decomposition profiles of the $Fe_{0.50}Mn_{0.50}O_x$ vary significantly and depend on the precipitation agent, Figure 5-13. All $Fe_{0.50}Mn_{0.50}O_x$ prepared from hydroxide based precipitating agents followed a similar decomposition profile, with two small features at 100 °C and 600 °C accounting for 4-7 % accumulative weight loss. The initial loss accounts for loss of surface or physiosorbed water and the second for hydroxide groups. This decomposition profile is characteristic of manganese hydroxide [40], suggesting all the nitrates have been substituted with hydroxide groups in the dried $Fe_{0.50}Mn_{0.50}O_x$ prepared using hydroxides. The $Fe_{0.50}Mn_{0.50}O_x$ prepared using potassium carbonate follows a similar decomposition profile to the sodium carbonate with one large observable decomposition region between 400-50 °C. This suggests the nitrates had been substituted for carbonates, as this weight loss region characteristic for carbonate decomposition. The $Fe_{0.50}Mn_{0.50}O_x$ prepared using ammonium carbonate had a different decomposition profile compared to the other two carbonate precipitating agents. Three weight loss regions centring at 200 °C, 350 °C and 500 °C were observed. The first weight loss region accounts for loss of water species and the temperature of the third region indicates the decomposition of carbonates. However, the addition region at 350 °C suggests not all the nitrate groups had been substituted by carbonates and this feature may show this. This

region could represent decomposition of ammonium groups present from the precipitating agent, which may interact with the $Fe_{0.50}Mn_{0.50}O_x$ precursor.

To keep the investigation consistent with the previous section, a calcination temperature of 500 °C was used. Also at this temperature, all the precursor species have been decomposed, or are in the region of decomposition, suggesting the $Fe_{0.50}Mn_{0.50}O_x$ is fully formed.

5.3.2 Catalyst performance

5.3.2.1 Propane total oxidation
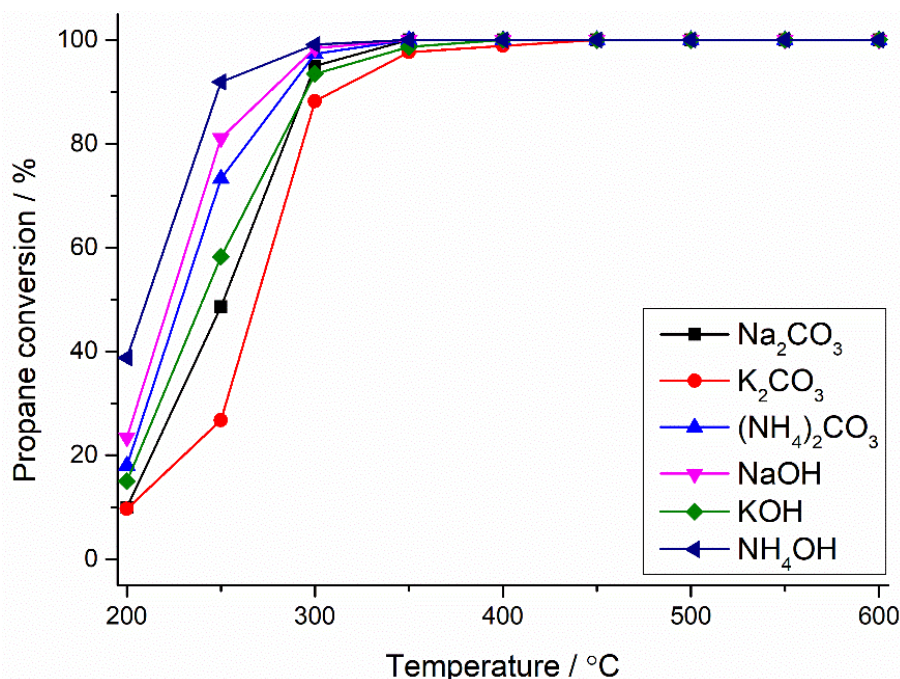
Figure 5-14: Catalytic activities for propane total oxidation over $Fe_{0.50}Mn_{0.50}O_x$ prepared *via* co-precipitation using different precipitating agents. Reaction conditions: 45,000 h⁻¹, temperature range 200-600 °C, 5000 ppm propane in air. Legend refers to the different precipitating agent used to prepare $Fe_{0.50}Mn_{0.50}O_x$

All $Fe_{0.50}Mn_{0.50}O_x$ catalysts showed high propane total oxidation and CO_2 selectivity (>99 %). Only the $Fe_{0.50}Mn_{0.50}O_x$ prepared using potassium carbonate showed propane total oxidation activity lower than the catalyst prepared using sodium carbonate, Figure 5-14. However this lower propane total oxidation activity was only observed at temperatures below 350 °C, with all samples showing 100 % propane conversion at this temperature. All $Fe_{0.50}Mn_{0.50}O_x$ prepared using hydroxide precipitating agents showed activity higher than their carbonate counterparts. The propane total oxidation activity over the $Fe_{0.50}Mn_{0.50}O_x$ samples followed the general trend:

$$NH_4OH > NaOH > (NH_4)_2CO_3 > KOH > Na_2CO_3 > K_2CO_3$$

Following the observations from the ceria-manganese mixed metal oxide chapter, this suggests that the presence of a potential surface poison may inhibit propane total oxidation activity. The ammonium-based precipitating agents will decompose during the calcination of the catalyst, therefore leaving no potential surface poisons. Whereas the sodium and potassium containing precipitating agents may leave a surface or bulk poison leading to the lower activity observed above.

5.3.3 Catalyst characterisation

5.3.3.1 X-ray diffraction
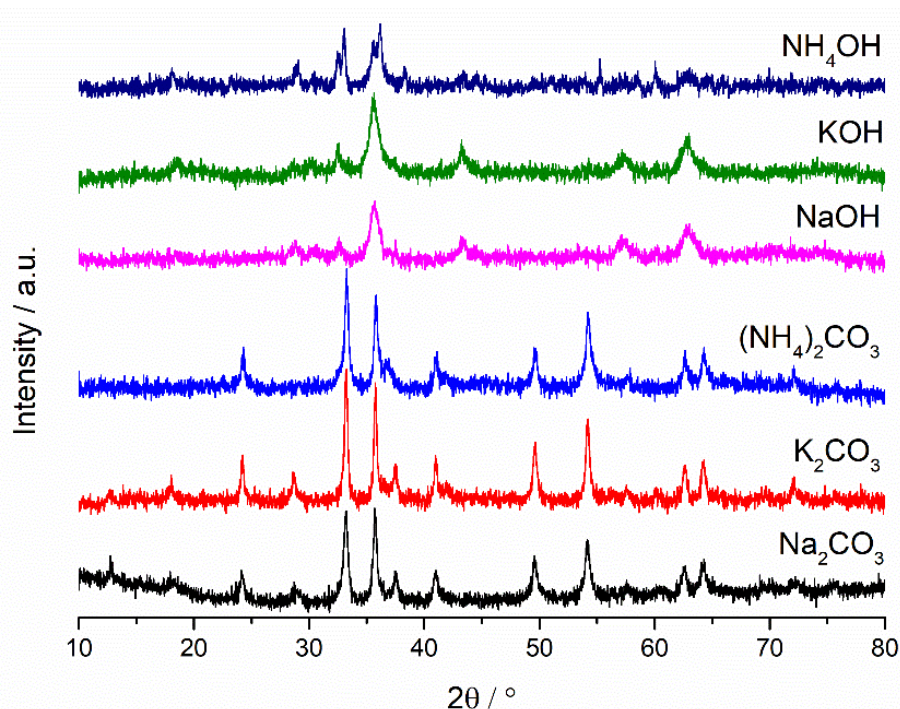
Figure 5-15: Powder XRD patterns of the $Fe_{0.50}Mn_{0.50}O_x$ prepared *via* co-precipitation using different precipitating agents.

There are similarities in the XRD patterns of the $Fe_{0.50}Mn_{0.50}O_x$ prepared using either carbonate or hydroxide bases, Figure 5-15. $Fe_{0.50}Mn_{0.50}O_x$ prepared using carbonate-based precipitating agents form samples with a higher crystallinity than the samples prepared using hydroxides. The samples prepared using carbonates formed Fe_2O_3 phases, as seen by reflections at 24 °, 33 °, 35 °, 40 °, 49 ° and 54 ° [19], whereas samples prepared from hydroxides formed Fe_3O_4 phases, represented by reflections at 30 °, 36 °, 43 °, 57 ° and 62 ° [20]. The $Fe_{0.50}Mn_{0.50}O_x$ prepared using hydroxide precipitation agents showing higher propane total oxidation activity than the samples prepared from carbonate. This suggests the phase of the metal oxide plays a role in the propane total oxidation activity, with M_3O_4 more active than the M_2O_3 phase.

Table 5-7: Physical properties of the $Fe_{0.50}Mn_{0.50}O_x$ prepared *via* co-precipitation different using precipitation agents derived from XRD

Sample	Phases present	Crystallite size / Å	
		FeO$_x$	MnO$_x$
Na$_2$CO$_3$	Fe$_2$O$_3$	291	-
K$_2$CO$_3$	Fe$_2$O$_3$	443	-
(NH$_4$)$_2$CO$_3$	Fe$_2$O$_3$	274	-
NaOH	Fe$_3$O$_4$	88	-
KOH	Fe$_3$O$_4$	100	-
NH$_4$OH	Fe$_3$O$_4$, Mn$_3$O$_4$	91	240

Alongside the affect on the metal oxide phase, there is also an observable trend in the effect of crystallite size and propane total oxidation activity. The smaller the iron oxide crystallite size lead to more active propane total oxidation catalysts. The $Fe_{0.50}Mn_{0.50}O_x$ prepared using potassium carbonate had the largest iron oxide crystallite size and performed the worst of all the bases used to prepare the $Fe_{0.50}Mn_{0.50}O_x$. The $Fe_{0.50}Mn_{0.50}O_x$ prepared from ammonium hydroxide and sodium hydroxide had similar iron oxide crystallite sizes and had the highest activity out of the samples tested. The $Fe_{0.50}Mn_{0.50}O_x$ prepared using ammonium hydroxide showed reflections from manganese oxide phases, Table 5-7, alongside iron oxide reflections. The presence of large bulk manganese oxide crystallites may have increased the propane total oxidation leading to the $Fe_{0.50}Mn_{0.50}O_x$ prepared using ammonium hydroxide solution showing the highest propane total oxidation activity.

5.3.3.2 Surface area

Table 5-8: Surface area of the $Fe_{0.50}Mn_{0.50}O_x$ prepared *via* co-precipitation using different precipitating agents. Calculated from 5-point N_2 adsorption BET analysis

Sample	BET Surface area / $m^2\,g^{-1}$	Surface area normalised rate of propane total oxidation at 250 °C (10^{-7}) / mol s^{-1} m^{-2}
Na$_2$CO$_3$	42	0.40
K$_2$CO$_3$	49	0.19
(NH$_4$)$_2$CO$_3$	88	0.29
NaOH	63	0.45
KOH	68	0.29
NH$_4$OH	98	0.32

The surface areas of the $Fe_{0.50}Mn_{0.50}O_x$ were significantly affected by the precipitating agent used to prepare the sample, Table 5-8. $Fe_{0.50}Mn_{0.50}O_x$ prepared using hydroxides

had a higher surface area compared to their carbonate counterparts. $Fe_{0.50}Mn_{0.50}O_x$ produced from potassium and sodium carbonate had ~2/3 of the surface area of their hydroxide counterpart. However, the $Fe_{0.50}Mn_{0.50}O_x$ prepared from ammonium precipitating agents had similar surface areas. Another trend observed was the $Fe_{0.50}Mn_{0.50}O_x$ prepared using ammonium precipitating agents produced the catalyst with the highest surface area, followed by potassium and then sodium salts. There was a slight correlation between iron oxide crystallite size and surface area, as noted in the iron-manganese oxides prepared *via* co-precipitation with sodium carbonate. Discrepancies between crystallite size and surface area may have arisen from small or amorphous crystallites which were undetectable in XRD, leading to increased or decreased surface area. As seen by the surface area normalised propane total oxidation rates, there isn't a trend between higher surface area and propane total oxidation activity. This suggests other factors may affect the propane total oxidation activity of the $Fe_{0.50}Mn_{0.50}O_x$.
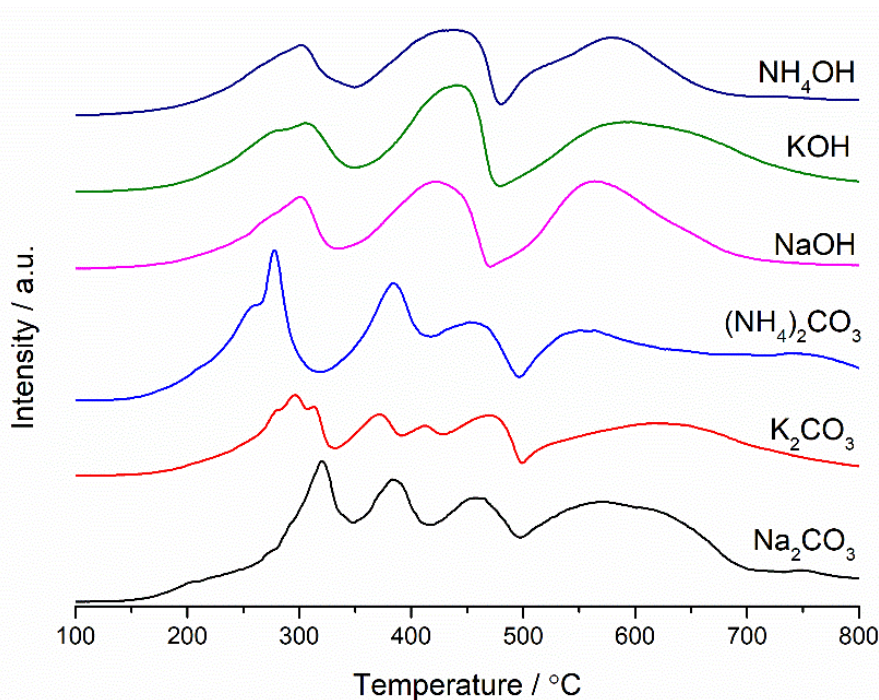
5.3.3.3 Temperature programmed reduction

Figure 5-16: Hydrogen temperature-programmed reduction profiles of the $Fe_{0.50}Mn_{0.50}O_x$ prepared *via* co-precipitation using different precipitation agents. Reaction conditions: 30 mg sample, 30 ml min^{-1} 10 % H_2/ Ar, temperature range 100-800 °C

The reduction profiles of $Fe_{0.50}Mn_{0.50}O_x$ prepared using hydroxides have three major peaks, and catalysts prepared using carbonates have four major peaks, Figure 5-16. The three peaks arising from $Fe_{0.50}Mn_{0.50}O_x$ precipitated using hydroxides, are centred at 300

°C, 460 °C and a broad reduction area from 500-650 °C. The first two reduction peaks may arise from reduction of MnO_2 phases, with reduction of this manganese oxide phase occurring at 300 °C and 500 °C [41]. The presence of iron and other cations may cause the shifting of peaks from the reduction of the pure manganese oxide phases. The last reduction peak is characteristic of Fe_3O_4 reduction [25]. With no discrete peak observed at 400 °C, indicating the presence of Fe_2O_3, this suggests the iron oxide is in the Fe_3O_4 phase. This confirms the iron oxide phase identification from XRD for all $Fe_{0.50}Mn_{0.50}O_x$ produced from hydroxide precipitating agents. Due to the potential amorphous nature or small crystallite size of the manganese oxide, could not be detected using XRD analysis. However from TPR we can indicate the manganese oxide is present in the MnO_2 phase. All the reduction peaks in the $Fe_{0.50}Mn_{0.50}O_x$ produced by hydroxide precipitating agents had a similar peak height. This suggests the extent of reduction is similar regardless of the cation used to precipitate the $Fe_{0.50}Mn_{0.50}O_x$ from hydroxide bases. However, the $Fe_{0.50}Mn_{0.50}O_x$ prepared from ammonium hydroxide had a slightly lower reduction temperature compared to the catalyst prepared by potassium and sodium hydroxide. This suggests the it is easier to reduce the $Fe_{0.50}Mn_{0.50}O_x$ prepared from ammonium hydroxide compared to the other hydroxide prepared catalysts. This in turn will mean there is potentially increased surface oxygen available at lower temperatures. This could also lower the temperature for propane total oxidation as seen in the testing data. However, with only small shifts in temperature, this may have an effect on propane total oxidation activity.

The four reduction peaks arising from $Fe_{0.50}Mn_{0.50}O_x$ prepared from carbonate precipitating agents are at similar temperatures to those observed from the catalyst prepared using sodium carbonate. Slight shifts to lower temperatures are observed when compared the potassium and ammonium to the sodium. Reduction peaks centred at 380 °C and 500 °C in all reduction profiles $Fe_{0.50}Mn_{0.50}O_x$ prepared from carbonate confirm the presence of Fe_2O_3 as identified from XRD [26]. The peaks at 280 °C and 480 °C suggest the manganese oxide is present in the MnO_2 phase [41]. However, due to overlapping of the iron oxide and manganese oxide phases, the exact phase is difficult to identify.

Unlike the $Fe_{0.50}Mn_{0.50}O_x$ prepared from hydroxide precipitating agents, the intensity of the reduction peaks of the $Fe_{0.50}Mn_{0.50}O_x$ prepared by carbonates varied depending on the precipitating agent. The $Fe_{0.50}Mn_{0.50}O_x$ prepared using ammonium carbonate had the largest peaks, followed by sodium carbonate and then potassium carbonate. This suggests the extent of reduction is significantly greater in the catalyst prepared from ammonium

carbonate. This correlates with the surface area of the $Fe_{0.50}Mn_{0.50}O_x$ prepared from the three carbonate precipitation agents. This will mean increased concentrations of oxygen will be present for oxidation reactions leading to the increase in propane total oxidation reactivity observed on this sample. The $Fe_{0.50}Mn_{0.50}O_x$ prepared from ammonium carbonate also had the lowest initial reduction temperature compared to the other catalysts prepared using carbonates. This suggests it will be easier to reduce this catalyst compared to the other samples. This will also increase surface oxygen present at lower temperatures, allowing for the catalyst to be more active at lower temperatures.

5.3.3.4 Microwave-plasma atomic emission spectroscopy

Table 5-9: Elemental analysis of the $Fe_{0.50}Mn_{0.50}O_x$ prepared using different precipitating agents derived from MP-AES

Sample	Concentration / ppm				Relative Fe / %	Relative Mn / %
	Fe	Mn	K	Na		
Na_2CO_3	33.0	26.1	-	4.0	55.77	44.23
K_2CO_3	28.6	28.3	5.9	-	50.23	49.77
$(NH_4)_2CO_3$	31.7	28.8	-	-	52.38	47.62
NaOH	40.7	36.9	-	1.6	52.49	47.51
KOH	39.9	36.6	2.1	-	52.14	47.86
NH_4OH	45.7	38.2	-	-	54.42	45.58

Elemental analysis of the $Fe_{0.50}Mn_{0.50}O_x$ prepared using different precipitating agents show the iron and manganese ratios of each catalyst are close to the nominal 50:50 ratio, regardless of the precipitating agent used to prepare the sample, Table 5-9. As mentioned previously, a discrepancy in the iron and manganese ratios may have occurred during the preparation of the precursors, due to the hydroscopic nature of the iron and manganese nitrate salts.
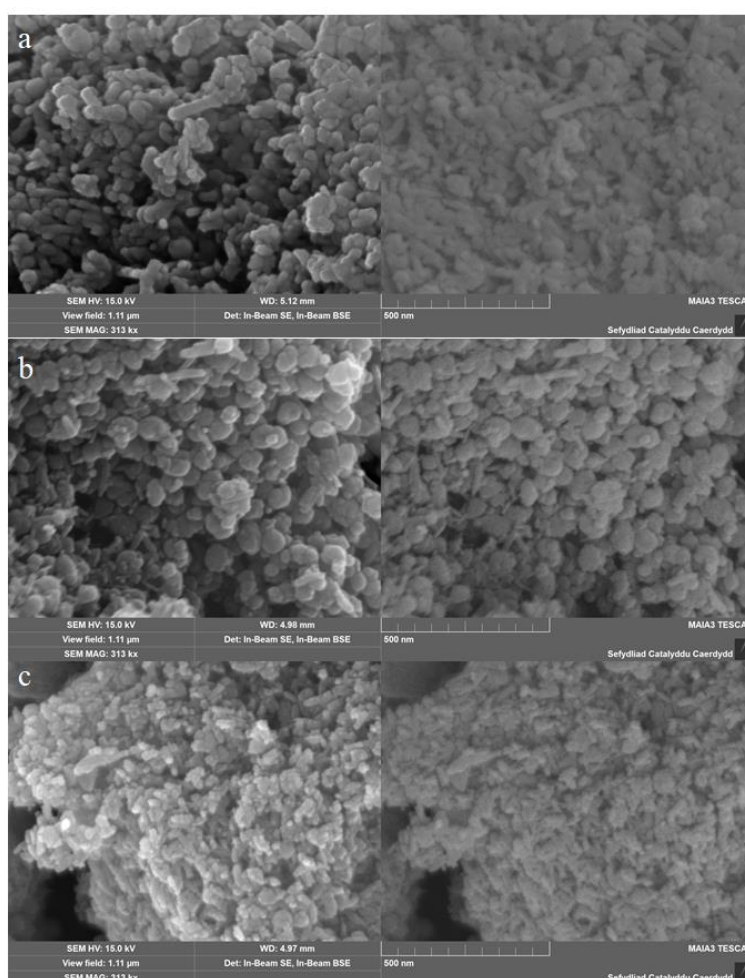
The $Fe_{0.50}Mn_{0.50}O_x$ prepared using alkali metal precipitating agents all had residual metals present in the final catalyst. The $Fe_{0.50}Mn_{0.50}O_x$ precipitated from sodium carbonate and potassium carbonate contained 6.3 % and 9.4 % respectively of the corresponding alkali metal. Whereas the $Fe_{0.50}Mn_{0.50}O_x$ prepared from sodium hydroxide and potassium hydroxide contained 2 % and 2.6 % respectively of the corresponding alkali metal. Potassium has a lower solubility in water compared to sodium, therefore increased volumes of water will be required to remove the potassium from the $Fe_{0.50}Mn_{0.50}O_x$. The hydroxides had significantly lower concentrations of sodium and potassium compared to their carbonate counterparts. Due to the increased basicity of the hydroxides compared to the carbonates, lower volumes of the hydroxides will be used to reach the precipitating

pH of 9. Therefore there will be less potassium and sodium present in the precipitation vessel when hydroxides are used, leading to lower concentrations present in the final catalyst.

A trend between percentage of alkali metal present in the elemental analysis and propane total oxidation activity is observed. The $Fe_{0.50}Mn_{0.50}O_x$ prepared using potassium carbonate had the highest concentration of alkali metal present and the lowest propane total oxidation activity. The lowering in concentration of the alkali metal leads to an increase in propane total oxidation activity. As seen in the ceria-manganese mixed metal oxide chapter, the presence of an alkali can hinder the total oxidation activity of a catalyst and this effect is also noted in iron-manganese mixed metal oxide catalysts.

5.3.3.5 Electron microscopy
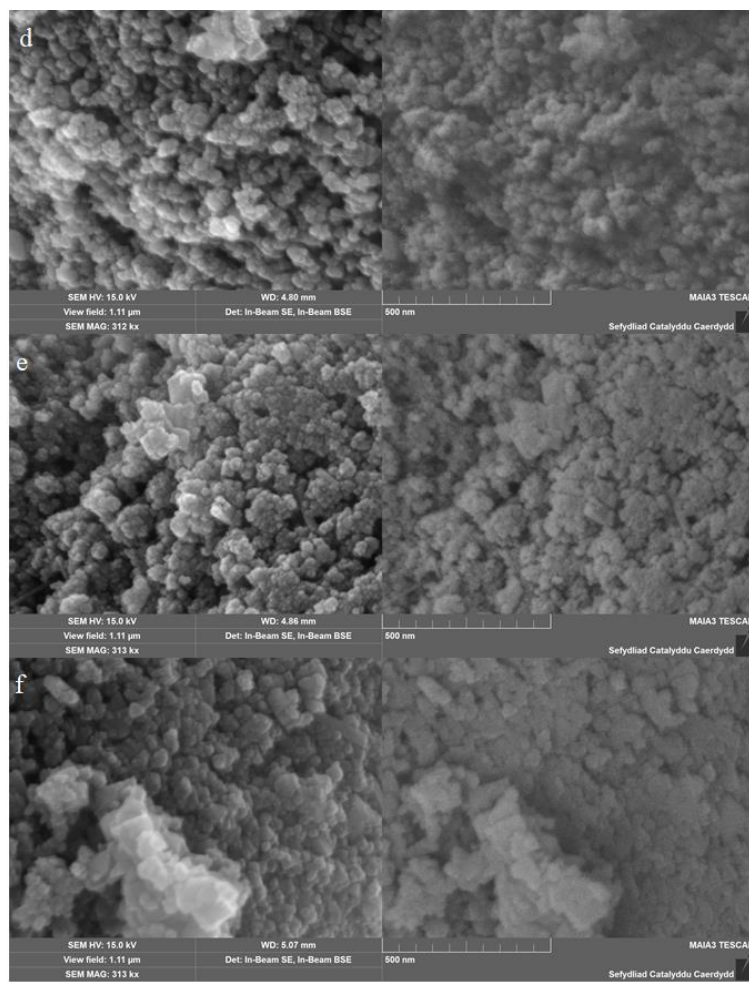
5.3.3.5.1 Scanning electron microscopy

Figure 5-17: Secondary (left) and backscattered (right) electron micrographs of the $Fe_{0.50}Mn_{0.50}O_x$ prepared *via* co-precipitation using different precipitating agents: (a) Na_2CO_3, (b) K_2CO_3, (c) $(NH_4)_2CO_3$, (d) NaOH, (e) KOH and (f) NH_4OH. Image magnification: 313 kx

The precipitating agent didn't have a significant effect on the morphology of the $Fe_{0.50}Mn_{0.50}O_x$, Figure 5-17. The spherical sponge morphology was seen in all samples and no plate-like structures were observed. This suggests the bulk structure of the $Fe_{0.50}Mn_{0.50}O_x$ is the iron oxide, as observed in XRD. However, there was a noticeable roughness observed on the samples prepared using ammonium containing precipitating agents. This may lead to the increased surface area observed on the $Fe_{0.50}Mn_{0.50}O_x$ prepared using these bases. As mentioned earlier, phase contrast is difficult to observe between manganese and iron, therefore, any potential phase separation could not be seen.

5.3.3.5.2 Energy dispersive x-ray spectroscopy

Table 5-10: SEM-EDX derived bulk elemental analysis of the $Fe_{0.50}Mn_{0.50}O_x$ prepared *via* co-precipitation using different precipitating agents

Sample	Concentration / %					Relative Fe / %	Relative Mn / %
	Fe	Mn	O	K	Na		
Na_2CO_3	15.3	16.3	64.2	-	4.2	48.3	51.7
K_2CO_3	20.4	14.8	64.0	0.7	-	57.9	42.1
$(NH_4)_2CO_3$	15.4	16.6	68.0	-	-	48.1	51.9
NaOH	17.9	12.3	66.8	-	3.6	58.5	41.5
KOH	19.9	18.4	61.4	0.3	-	52.0	48.0
NH_4OH	16.0	19.7	64.3	-	-	44.9	55.1

Further elemental analysis was undertaken using EDX on the $Fe_{0.50}Mn_{0.50}O_x$ prepared using a range of precipitating agents, Table 5-10. The relative iron and manganese ratios calculated from MP-AES showed the values were close to the nominal values, however, they had some increased iron content. The iron and manganese ratios calculated using EDX vary from the nominal values from those determined from MP-AES. However, with most of the EDX ratios close to the nominal values, we can assume the iron and manganese ratio of all $Fe_{0.50}Mn_{0.50}O_x$ is close to nominal values. Variation between the MP-AES analysis and EDX due to the errors observed from the EDX analysis.

The trends of potassium and sodium present in the $Fe_{0.50}Mn_{0.50}O_x$ observed from MP-AES are also observed in EDX analysis. $Fe_{0.50}Mn_{0.50}O_x$ produced from potassium and sodium carbonate had 1.89 % and 11.74 % respectively of the relative alkali metal present in the bulk. Whereas the $Fe_{0.50}Mn_{0.50}O_x$ produced from potassium hydroxide and sodium contain 0.8 % and 10.95 % respectively of the relative alkali metal present in the bulk. The $Fe_{0.50}Mn_{0.50}O_x$ produced using sodium precipitating agents, had significantly higher amount than the value obtained from MP-AES.

Only the SEM-EDX map, Figure 5-18, of the $Fe_{0.50}Mn_{0.50}O_x$ prepared using ammonium carbonate show clear phase separation between iron and manganese. All other $Fe_{0.50}Mn_{0.50}O_x$ show iron and manganese to be well mixed within the EDX map of the sample. As seen from the EDX elemental analysis, sodium and potassium are ever present across the $Fe_{0.50}Mn_{0.50}O_x$ precipitated using alkali precipitating agents. Both metals are spread evenly across the $Fe_{0.50}Mn_{0.50}O_x$.

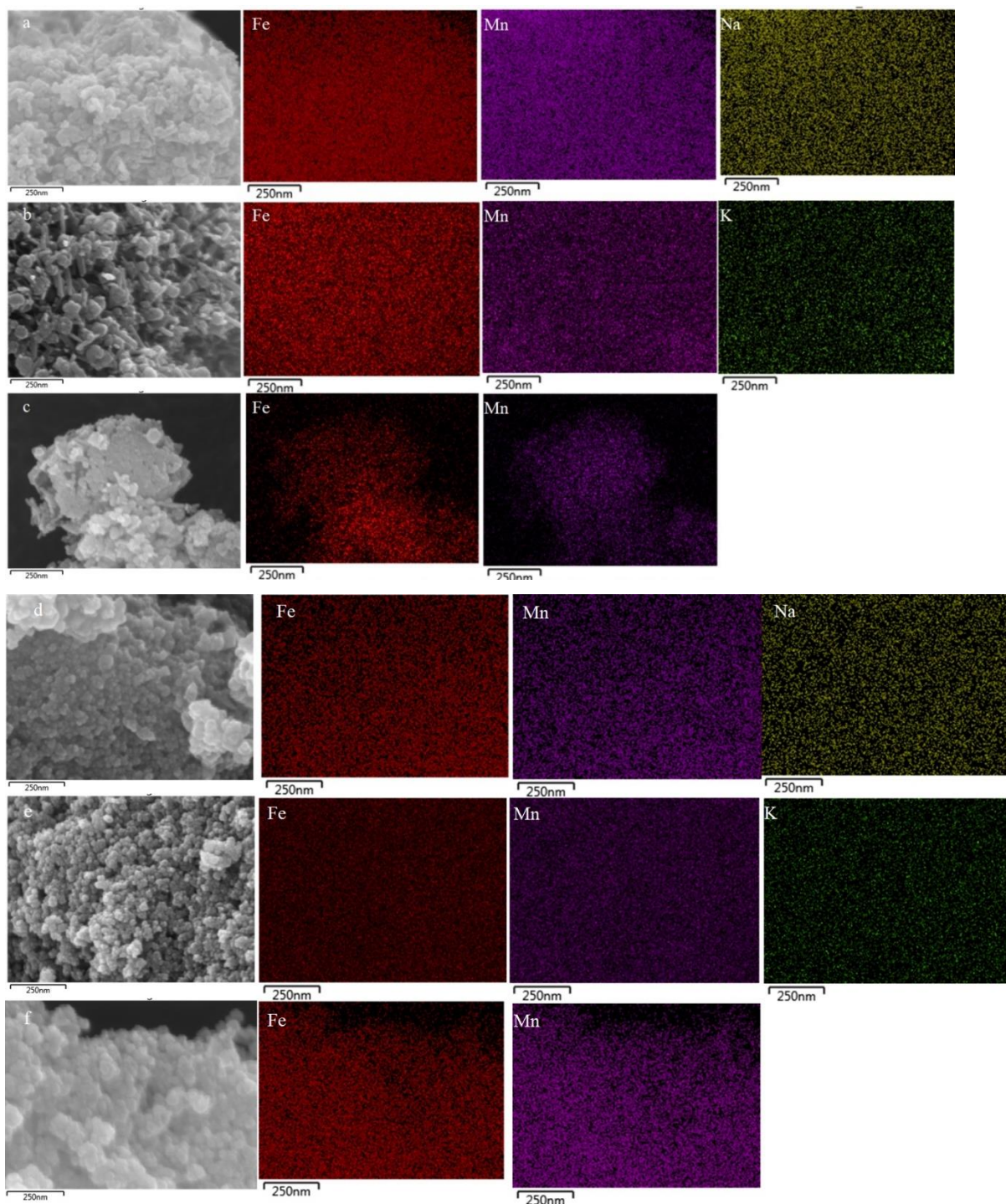Figure 5-18: SEM-EDX mapping of $Fe_{0.50}Mn_{0.50}O_x$ prepared *via* co-precipitation using different precipitating agents : (a) Na_2CO_3, (b) K_2CO_3, (c) $(NH_4)_2CO_3$, (d) NaOH, (e) KOH and (f) NH_4OH. Iron (red), manganese (pink), sodium (yellow) and potassium (green)

5.3.3.6 X-ray photoelectron spectroscopy

Table 5-11: XPS derived surface elemental concentrations of the $Fe_{0.50}Mn_{0.50}O_x$ prepared *via* co-precipitation using different precipitating agents.

Sample	Concentration / %					Relative Fe / %	Relative Mn / %
	Fe	Mn	O	K	Na		
Na_2CO_3	13.6	18.9	62.6	-	4.9	42.0	58.0
K_2CO_3	21.4	18.6	60.1	4.9	-	53.5	46.5
$(NH_4)_2CO_3$	21.5	19.1	59.5	-	-	53.0	47.0
NaOH	21.4	19.0	59.3	-	0.4	53.0	47.0
KOH	20.1	14.2	64.7	1.1	-	58.6	41.4
NH_4OH	20.3	20.3	59.4	-	-	50.1	49.9

The surface compositions of the $Fe_{0.50}Mn_{0.50}O_x$ prepared using different precipitating agents, Table 5-11, show the precipitating agent has a significant effect on the surface iron and manganese ratio. Only when ammonium hydroxide was used to the prepare the $Fe_{0.50}Mn_{0.50}O_x$ was the relative iron and manganese ratio close to the nominal value. When sodium carbonate was used the surface was enriched with manganese whereas all other bases shows surface enrichment of iron, with potassium hydroxide showing the highest relative surface iron content. As mentioned previously, the bulk and surface ratio in mixed metal oxides containing manganese don't match and this is seen here. There is no observable correlation between surface iron and manganese ratio and propane total oxidation.

The elemental analysis of sodium and potassium in the $Fe_{0.50}Mn_{0.50}O_x$ precipitated from alkali metals showed differing metal contents depending on the analysis used. MP-AES showed a lower sodium concentration compared to the potassium in both carbonate and hydroxide precipitated $Fe_{0.50}Mn_{0.50}O_x$. However, EDX analysis showed the reverse in which high concentrations of sodium were noted from both carbonate and hydroxide precipitated $Fe_{0.50}Mn_{0.50}O_x$. This arises from potential limitation in the analysis method leading to disparities between elemental concentrations between the techniques. The surface ratios calculated from XPS, show $Fe_{0.50}Mn_{0.50}O_x$ prepared from both carbonate precipitating agents show similar concentrations of alkali metal. However surface alkali metal concentrations of $Fe_{0.50}Mn_{0.50}O_x$ prepared from hydroxides differ. Surface concentrations of potassium are higher than sodium in these catalysts. There is a correlation between surface concentrations of alkali metals and propane total oxidation activity. Increasing surface concentrations of the alkali metal leads to a decrease in propane total oxidation activity. This was seen in the ceria-manganese results chapter and

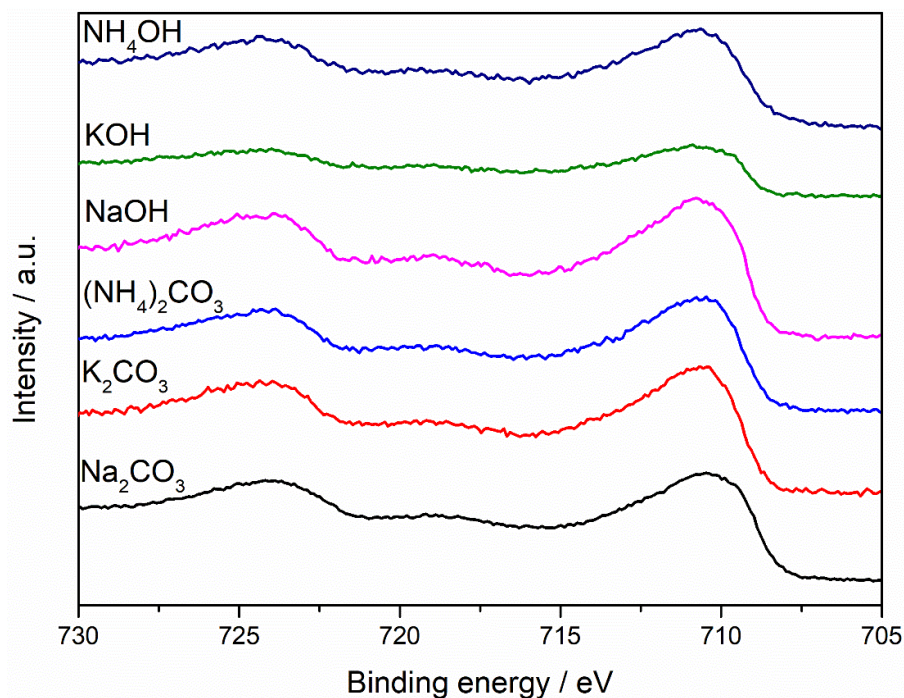suggests the presence of any surface poison can effect the VOC total oxidation behaviour of the catalyst.

Figure 5-19: XPS spectra of the Fe 2p peaks for the $Fe_{0.50}Mn_{0.50}O_x$ prepared *via* co-precipitation using different precipitating agents

All the spectra of the $Fe_{0.50}Mn_{0.50}O_x$ prepared from different precipitating agents contain two major peaks centred at 710 eV and 724 eV, Figure 5-9. Along with this a minor satellite peak is observed on all $Fe_{0.50}Mn_{0.50}O_x$ spectra, except the sample prepared using potassium hydroxide, centred at 718 eV. The presence of these three peaks suggest the iron is present in the 3+ oxidation state [32,33] and suggests the iron oxide is present in the Fe_2O_3 phase. However, the peaks centred at 710 eV in $Fe_{0.50}Mn_{0.50}O_x$ prepared using hydroxide based precipitating agents are wider compared to the carbonate based precipitating agents. This indicates Fe is present in the 2+ oxidation alongside the 3+ oxidation state suggesting the iron oxide is in the Fe_3O_4 phase [42]. This suggests the iron oxide phase is consistent throughout the surface and bulk of the $Fe_{0.50}Mn_{0.50}O_x$ precipitated using hydroxides. The $Fe_{0.50}Mn_{0.50}O_x$ containing the Fe_3O_4 phase preforming significantly better than catalysts which exclusively have the Fe_2O_3 phase. This indicates the phase of the iron oxide plays a role in the propane total oxidation activity of the catalyst with Fe_3O_4 the phase with higher activity.
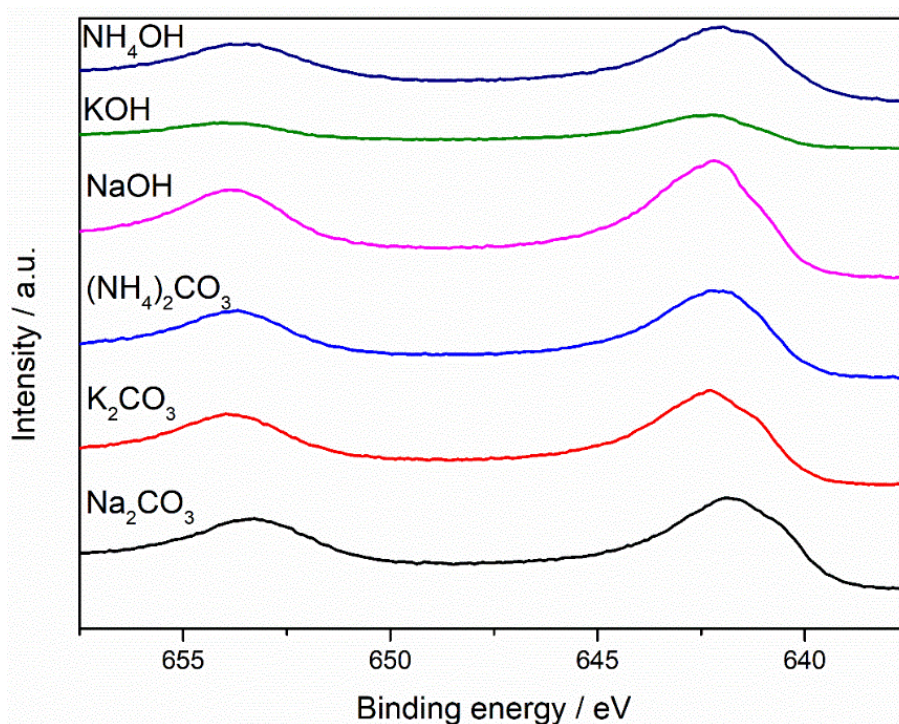
Figure 5-20: XPS spectra of the Mn 2p peaks for the $Fe_{0.50}Mn_{0.50}O_x$ prepared *via* co-precipitation using different precipitating agents

All the Mn 2p spectra of the $Fe_{0.50}Mn_{0.50}O_x$ prepared using different precipitating agents show two peaks centred at 642 eV and 653 eV, Figure 5-20. Due to the absence of a satellite peak at 647 eV, no MnO phases are present on the surface of any $Fe_{0.50}Mn_{0.50}O_x$ [34]. With the iron oxide present as Fe_3O_4 in the $Fe_{0.50}Mn_{0.50}O_x$ prepared using hydroxide precipitating agents, we could assume the manganese oxide may have also formed Mn_3O_4 phases. However with no MnO phase, alongside the manganese in the 3+ oxidation state, observed on the surface of these catalysts. However a shoulder peak is observed at 642 eV in $Fe_{0.50}Mn_{0.50}O_x$ prepared from hydroxides. This peak may have arisen from manganese present in the 2+ or 3+ oxidation state [34]. Therefore, the manganese could be present in a phase containing multiple oxidation states indicating the presence of Mn_3O_4.

The oxidation state of the $Fe_{0.50}Mn_{0.50}O_x$ prepared using a range of precipitating agents was calculated from the manganese 3s XPS spectra, Figure 5-21. The two peaks arising from manganese 3s are present between 80-90 eV and peaks from iron 3s emission occur at 93 eV [34,35]. The magnitude of the manganese 3s peak splitting for the $Fe_{0.50}Mn_{0.50}O_x$ catalysts is shown in Table 5-12.
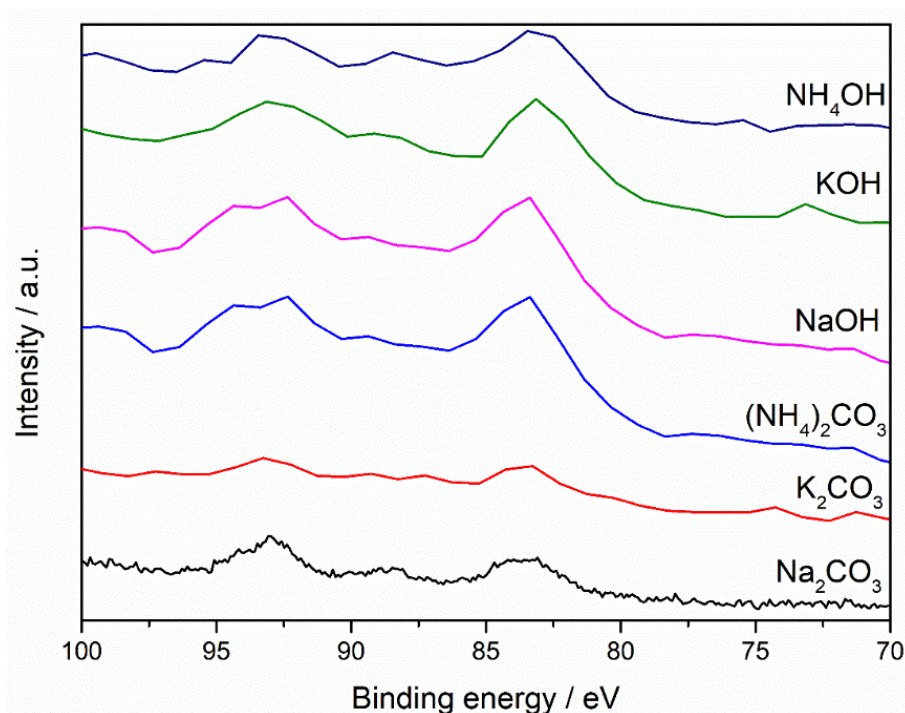
Figure 5-21: XPS spectra of the Mn 3s peaks for the $Fe_{0.50}Mn_{0.50}O_x$ prepared *via* co-precipitation using different precipitating agents

Only the catalyst prepared using potassium carbonate had a peak splitting below 5.3 eV, indicating the manganese oxide was in the MnO_2 phase. All the other $Fe_{0.50}Mn_{0.50}O_x$ catalysts had a splitting above 5.3 eV and below 6.0 eV suggesting the manganese oxide was in the Mn_2O_3 phase [34]. As seen previously, mixed metal oxide catalysts with manganese oxide present in the Mn_2O_3 had significantly increased VOC total oxidation activity. The same trend is observed in the $Fe_{0.50}Mn_{0.50}O_x$, with the sample prepared using potassium carbonate, the catalyst with the poorest propane total oxidation activity and the only catalyst with manganese present in the MnO_2 phase. This suggests the manganese oxide phase is an important factor in determining the VOC total oxidation behaviour of a catalyst.

Table 5-12: Magnitude of peak splitting in the Mn 3s spectra for the $Fe_{0.50}Mn_{0.50}O_x$ prepared *via* co-precipitation using different precipitating agents

Sample	Magnitude of Mn 3s peak splitting / eV	Surface oxidation state of Mn (all +)
Na_2CO_3	5.4	3
K_2CO_3	4.7	4
$(NH_4)_2CO_3$	5.7	3
NaOH	5.9	3
KOH	5.7	3
NH_4OH	5.5	3

Two oxygen species, lattice and surface defect, are observed in the XPS spectra of the oxygen 1s of the $Fe_{0.50}Mn_{0.50}O_x$,

Figure 5-22. A majority of the oxygen present in all $Fe_{0.50}Mn_{0.50}O_x$ samples is within the lattice, as seen by relatively large peak at 529-31 eV [36]. Synergisitc interactions between the secondary metal and manganese are noted by shifting of the lattice oxygen peaks to higher binding energies [39]. The $Fe_{0.50}Mn_{0.50}O_x$ prepared using both ammonium carbonate and hydroxide had the largest relative shift compared to the other samples. Both samples had high propane total oxidation activity, suggesting this synergistic effect may influence propane total oxidation activity. However, the extent of this effect is difficult to examine.
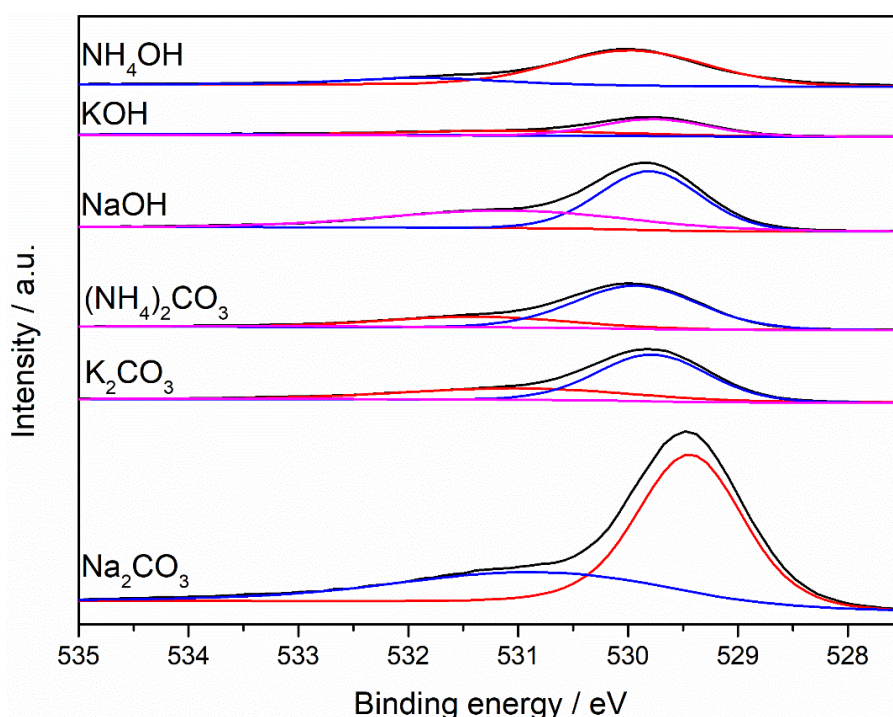

Figure 5-22: XPS spectra of the O 1s peaks for the $Fe_{0.50}Mn_{0.50}O_x$ prepared *via* co-precipitation using different precipitating agents

5.4 The effect of calcination temperature on $Fe_{0.50}Mn_{0.50}O_x$ for VOC total oxidation activity

The optimal precipitating agent used to prepare $Fe_{0.50}Mn_{0.50}O_x$ for propane total oxidation was ammonium hydroxide so this will be the base of choice for the calcination temperature study. The effect of calcination has a significant effect on manganese oxide for naphthalene [22], benzene, toluene and xylene total oxidation [43]. Calcination temperature used to prepare manganese containing mixed metal oxides has been reported to affect its activity for total oxidation reactions. With the activity of formaldehyde total oxidation over ceria-manganese mixed metal oxides [44] and CO oxidation over copper-

manganese mixed metal oxides [45] effected by calcination temperature. Therefore, against this background it can be assumed the calcination temperature may have a significant effect on the iron-manganese mixed metal oxide. The TGA profile of the $Fe_{0.50}Mn_{0.50}O_x$ prepared using ammonium hydroxide remained stable after 400 °C, indicating most of the precursor species had decomposed. Higher calcination temperature can have a significant effect on the bulk and surface properties of the catalyst. The same preparation method was used to prepare the catalyst. However the $Fe_{0.50}Mn_{0.50}O_x$ catalyst was calcined at 400 °C, 450 °C and 500 .
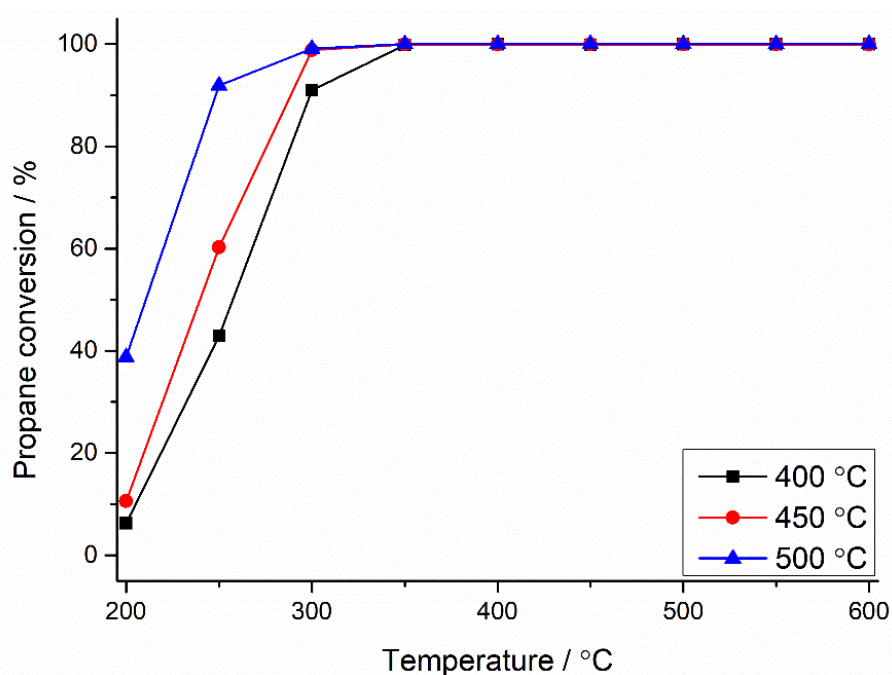
5.4.1 Catalyst performance

5.4.1.1 Propane total oxidation

Figure 5-23: Catalytic activities for propane total oxidation over $Fe_{0.50}Mn_{0.50}O_x$ prepared *via* co-precipitation using NH_4OH and calcined at various temperatures. Reaction conditions: 45,000 h^{-1}, temperature range 200-600 °C, 5000 ppm propane in air. Legend refers to the different calcination temperatures used to prepare $Fe_{0.50}Mn_{0.50}O_x$

All $Fe_{0.50}Mn_{0.50}O_x$ calcined at different temperatures had high propane total oxidation and high CO_2 selectivity (>99 %). Increasing the temperature used to calcine the $Fe_{0.50}Mn_{0.50}O_x$ led to an increase in the propane total oxidation activity, Figure 5-23, following the general trend:

$$500 °C > 450 °C > 400 °C$$

The decrease in calcination temperature by 100 °C led to a increase in T_{100} by 50 °C. The $Fe_{0.50}Mn_{0.50}O_x$ calcined at 450 °C had the same T_{100} temperature as the sample calcined

at 500 °C, however, it had lower propane total oxidation activity at lower temperatures. Increasing the calcination temperature in ceria-manganese mixed metal oxides for formaldehyde total oxidation also led to an increase in activity [44]. The same effect was noted for copper-manganese catalysts for CO oxidation [45]. In both cases, catalysts calcined at 500 °C produced the most active catalysts.

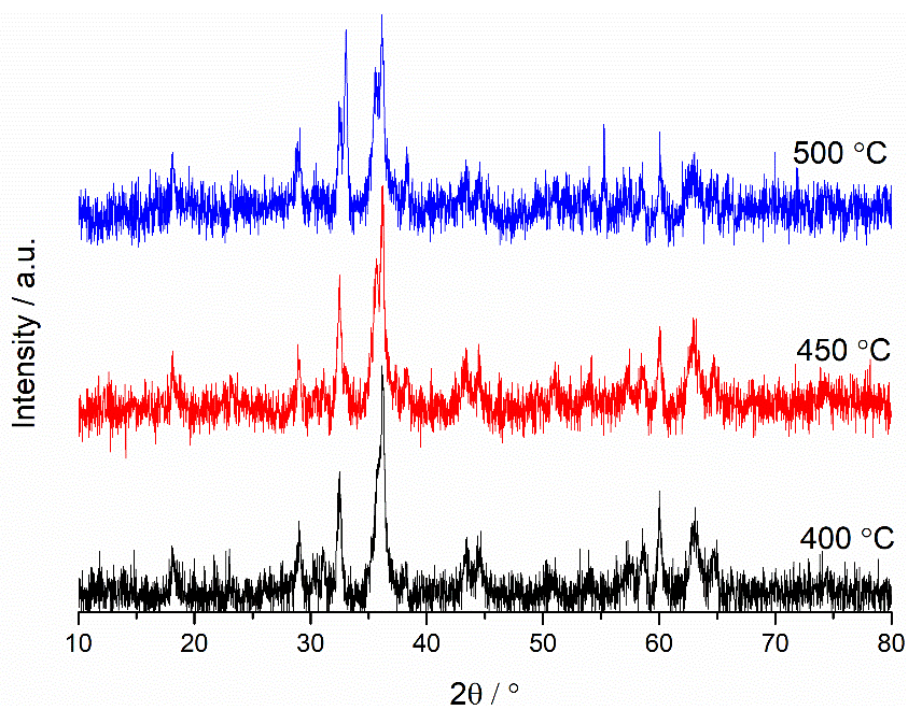## 5.4.2 Catalyst characterisation

5.4.2.1 X-ray diffraction

Figure 5-24: Powder XRD patterns of the $Fe_{0.50}Mn_{0.50}O_{x\ 50}O_x$ prepared *via* co-precipitation using NH_4OH and calcined at various temperatures.

All the XRD patterns of $Fe_{0.50}Mn_{0.50}O_x$ calcined at various temperatures show reflections characteristic of Mn_3O_4, with reflections present at 33 °, 38 °, 44 ° and 52 ° [46], and Fe_3O_4, with reflections present at 30 °, 36 °, 43 °, 57 ° and 62 ° [20]. Some overlap between Mn_3O_4 and Fe_3O_4 reflections are noted. However with discrete peaks from each metal oxide observed, this suggests mixed metal oxide solid solutions haven't been formed between the manganese oxide and iron oxides. It has been reported that calcination temperatures above 1000 °C are required to form iron-manganese solid solutions [13]. Therefore the solid solution structure wasn't able to be formed. Metal oxides in the M_3O_4 phase had increased propane total oxidation compared to metal oxides in the M_2O_3 phase. This may explain the high propane total oxidation activity observed over these samples.

The XRD patterns of the $Fe_{0.50}Mn_{0.50}O_x$ indicate phases that are low in crystallinity and slightly increase in crystallinity upon increasing calcination temperature, Figure 5-24. The increasing calcination temperature will lead to sintering and increasing crystallinity and crystallite size as observed in Table 5-13. The iron oxide crystallite size decreases upon increasing calcination temperature of the $Fe_{0.50}Mn_{0.50}O_x$. However, the reverse is observed for crystallite size of the manganese oxide. This is an interesting observation as the expectation would be both manganese and iron crystallite sizes will increase upon increasing calcination temperature. However, with the size of the iron oxide crystallite shrinking upon increasing calcination temperature, we can assume the iron oxide is either forming amorphous crystallites or becoming incorporated into the manganese oxide.

Table 5-13: Physical properties of the $Fe_{0.50}Mn_{0.50}O_x$ $_{50}O_x$ prepared *via* co-precipitation using NH_4OH and calcined at various temperatures derived from XRD

Sample	Phases present	Crystallite size / Å	
		FeO_x	MnO_x
400 °C	Fe_3O_4, Mn_3O_4	283	138
450 °C	Fe_3O_4, Mn_3O_4	163	228
500 °C	Fe_3O_4, Mn_3O_4	91	240

During this investigation, it was found that the manganese oxide crystallite size has a significant effect on VOC total oxidation. The $Fe_{0.50}Mn_{0.50}O_x$ calcined at 500 °C had the largest manganese oxide crystallites, so we can assume this factor, alongside the metal oxide phase, has impacted the propane total oxidation activity of this catalyst. Also the presence of small iron oxide crystallites may also lead to increased propane total oxidation activity. The $Fe_{0.50}Mn_{0.50}O_x$ prepared from co-precipitation using sodium carbonate had one of the smallest iron crystallite sizes of the iron-manganese mixed metal oxides investigated. It was also one of the most active catalysts from the range of catalysts investigated. Therefore we can assume that the iron crystallite size alongside the manganese oxide crystallite size can influence the propane total oxidation activity.

5.4.2.2   Surface area

The surface areas of the $Fe_{0.50}Mn_{0.50}O_x$ prepared from ammonium hydroxide, increased as the calcination temperature increased, Table 5-14. This is in line with the decreasing iron oxide crystallite size. However with the manganese crystallite size increasing, it may be assumed that this will lead to a decrease in surface area. The average manganese oxide and iron oxide crystallite size decreases upon increasing calcination temperature of the $Fe_{0.50}Mn_{0.50}O_x$. This will lead to smaller crystallites which in turn will lead to increased surface area observed over these catalysts.

Table 5-14: Surface area analysis of the $Fe_{0.50}Mn_{0.50}O_x$ $_{50}O_x$ prepared *via* co-precipitation using NH_4OH and calcined at various temperatures. Calculated from, 5-point N_2 adsorption BET analysis

Sample	BET Surface area / $m^2 g^{-1}$	Surface area normalised rate of propane total oxidation at 250 °C (10^{-7}) / mol s^{-1} m^{-2}
400 °C	60	0.25
450 °C	87	0.24
500 °C	98	0.32

The surface area normalised rate of propane total oxidation remains stable as the temperature used to calcine the $Fe_{0.50}Mn_{0.50}O_x$ increases from 400 to 450 °C. This suggests surface area controls the activity of the $Fe_{0.50}Mn_{0.50}O_x$ for propane total oxidation. However the higher surface normalised rate of propane total oxidation arising from the $Fe_{0.50}Mn_{0.50}O_x$ calcined at 500 °C suggests other factors also influence propane total oxidation activity.

5.4.2.3 Temperature programmed reduction

The reduction profiles of the $Fe_{0.50}Mn_{0.50}O_x$ calcined at various temperatures all feature three major peaks, Figure 5-25. The sample calcined at 400 °C had a completely different reduction profile to the other samples. It contained peaks at 400 °C, 520 °C and 650 °C, which successively increased in intensity. Due to the overlap in manganese oxide and iron oxide reduction peaks, it is difficult to clearly identify the exact phase of each metal oxide present in the sample. The peak at 520 °C, may represent the manganese oxide in the Mn_3O_4 phase [41]. A shift from the literature temperature to higher temperatures may have occurred due to possible interactions between the iron oxide and the Mn_3O_4 phase. The presence of this peak suggests the manganese oxide is uniform in the bulk with Mn_3O_4 also observed in the XRD patterns of this sample. The reduction peaks at 400 °C and 650 °C indicate the presence of both Fe_2O_3 and Fe_3O_4 in the catalyst. Due to the decreased intensity of the 400 °C, we can assume not all the iron oxide had been converted into Fe_3O_4 during the lower calcination temperature used for this sample [47]. The presence of this may lead to the decreased propane total oxidation activity observed on this sample. As seen previously in this chapter, iron oxide present in the Fe_2O_3 phase produced catalysts with lower propane total oxidation activity than those in the Fe_3O_4 phase. Along with this the sample calcined at 400 °C has some of the highest temperatures at which reduction occurs. This suggests the ease of reduction is lower in this sample

which can also hinder the propane total oxidation activity of the sample, as the lability of lattice oxygen was reduced.
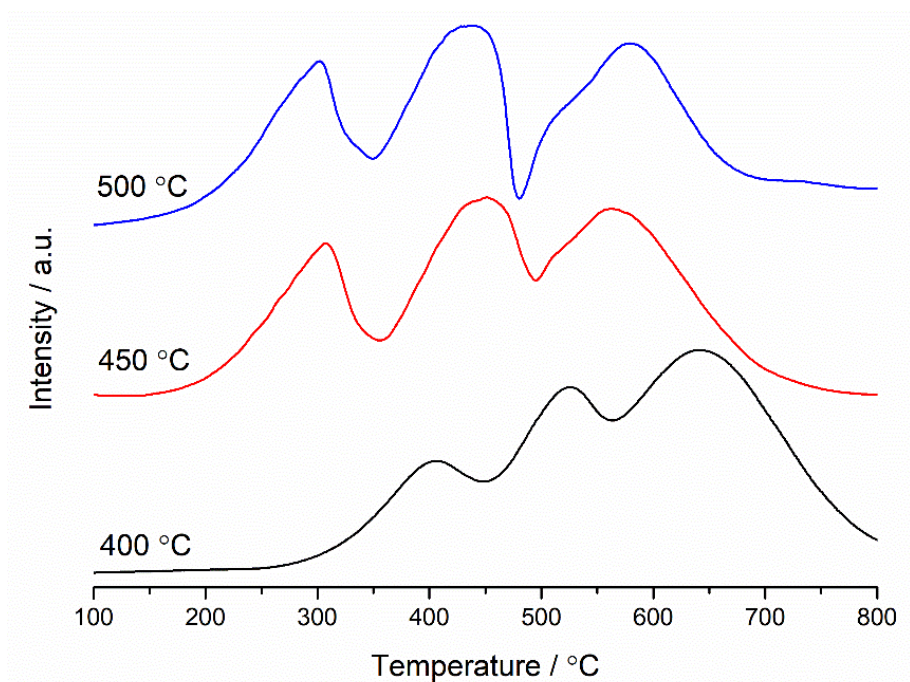

Figure 5-25: Hydrogen temperature-programmed reduction profiles of the Fe$_{0.50}$Mn$_{0.50}$O$_x$ prepared *via* co-precipitation using NH$_4$OH and calcined at various temperatures. Reaction conditions: 30 mg sample, 30 ml min^{-1} 10 % H$_2$/ Ar, temperature range 100-800 °C

The Fe$_{0.50}$Mn$_{0.50}$O$_x$ sample calcined at 450 °C has a similar reduction profile of the catalyst calcined at 500 °C. However, all three peaks have shifted by ~15 °C to higher temperatures. This suggests the sample calcined at 450 °C has similar manganese oxide, MnO$_2$, and iron oxide, Fe$_3$O$_4$, phases to the sample calcined at 500 °C. However the ease of reduction is decreased in the Fe$_{0.50}$Mn$_{0.50}$O$_x$ calcined at 450 °C compared to the sample calcined at 500 °C. This ease in reduction of the Fe$_{0.50}$Mn$_{0.50}$O$_x$ calcined at higher temperature may have arisen from the larger crystallite size and surface area compared to the samples calcined at lower temperatures. This ease in reduction, along with the increased surface area may lead to the increased propane total oxidation activity observed in the Fe$_{0.50}$Mn$_{0.50}$O$_x$ calcined at 500 °C compared to the other temperatures.

5.4.2.4 Electron microscopy

5.4.2.4.1 Scanning electron microscopy

The temperature used to calcine the Fe$_{0.50}$Mn$_{0.50}$O$_x$ prepared from ammonium hydroxide, didn't have a significant impact on the morphology of the sample, Figure 5-26. The coarse sponge-like morphology is maintained throughout the Fe$_{0.50}$Mn$_{0.50}$O$_x$ catalysts. XRD patterns of the catalysts showed phase separation between the iron oxide and manganese

oxide. However, due to the similarities in contrast between both metal oxides in the back scattered electron images, this wasn't observed.
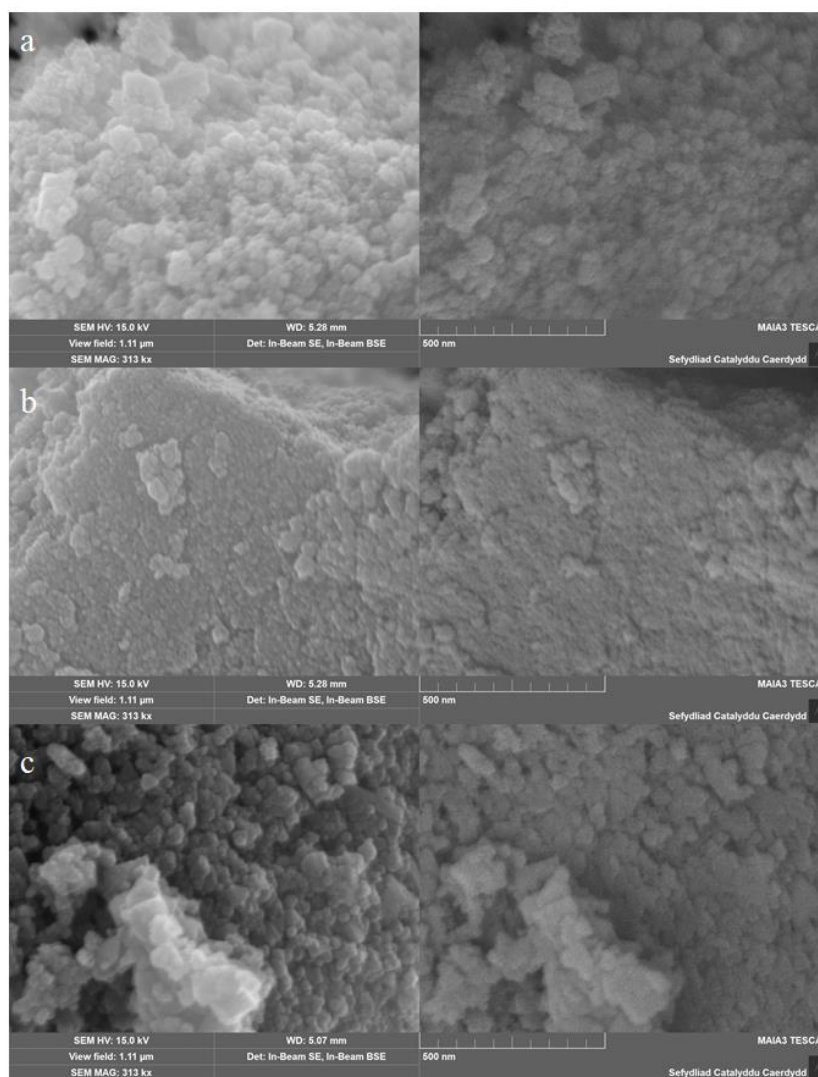

Figure 5-26: Secondary (left) and backscattered (right) electron micrographs of the $Fe_{0.50}Mn_{0.50}O_x$ prepared *via* co-precipitation using NH_4OH and calcined at various temperatures. (a) 400 °C, (b) 450 °C and 500 °C. Image magnification: 313 kx

5.4.2.4.2 Energy dispersive x-ray spectroscopy

The MP-AES analysis of the $Fe_{0.50}Mn_{0.50}O_x$ prepared using ammonium hydroxide showed the relative iron and manganese concentrations to be 54.4 % and 45.6 % respectively. EDX was undertaken to investigate the effect of calcination temperature on bulk elemental concentration of iron and manganese in $Fe_{0.50}Mn_{0.50}O_x$, Table 5-15. The relative bulk iron concentration decreased upon increasing calcination temperature on the $Fe_{0.50}Mn_{0.50}O_x$. The concentrations deviate significantly from the MP-AES values. This suggests the increasing calcination temperature may cause phase separation of iron oxides and manganese oxides. Potential surface changes may also impact the relative iron concentration.

Table 5-15: SEM-EDX derived bulk element analysis of the $Fe_{0.50}Mn_{0.50}O_x$ prepared *via* co-precipitation using NH_4OH and calcined at various temperatures.

Sample	Concentration / %			Relative Fe / %	Relative Mn / %
	Fe	**Mn**	**O**		
400 °C	17.3	17.5	65.2	49.8	50.2
450 °C	22.8	29.0	48.2	44.1	55.9
500 °C	16.0	19.7	64.3	44.9	55.1

However, the SEM-EDX maps of the $Fe_{0.50}Mn_{0.50}O_x$ calcined at various temperatures, Figure 5-27, show both metals to be homogenously distributed at the level of magnification employed. This suggests no significant phase separation between iron and manganese species has occurred. Therefore variations between the MP-AES and EDX iron and manganese ratios may have occurred during the EDX analysis of the samples [48].
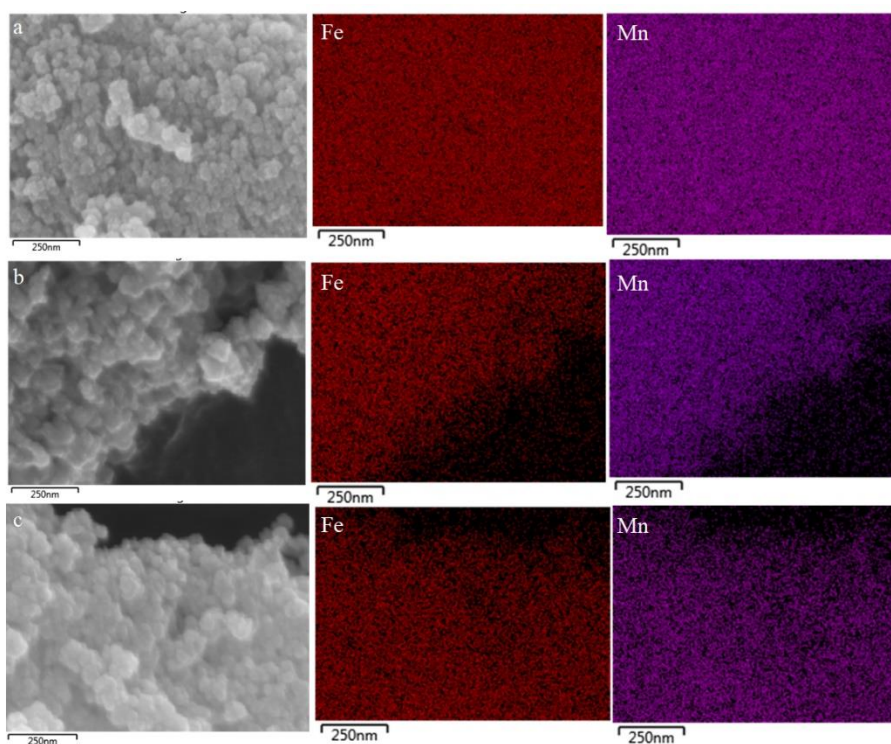

Figure 5-27: SEM-EDX mapping of $Fe_{0.50}Mn_{0.50}O_x$ prepared *via* co-precipitation using NH_4OH and calcined at various temperatures, (a) 400 °C, (b) 450 °C and 500 °C. Iron (red) and manganese (pink)

5.4.2.5 X-ray photoelectron spectroscopy

Table 5-16: XPS derived surface elemental concentrations for the $Fe_{0.50}Mn_{0.50}O_x$ prepared *via* co-precipitation using NH_4OH and calcined at various temperatures.

Sample	Concentration / %			Relative Fe / %	Relative Mn / %
	Fe	**Mn**	**O**		
400 °C	17.3	16.6	66.1	51.1	48.9
450 °C	17.1	16.7	66.2	50.6	49.4
500 °C	20.3	20.3	59.4	50.1	49.9

The relative concentration of surface iron decreases upon increasing temperature used to calcine the $Fe_{0.50}Mn_{0.50}O_x$, Table 5-16. This suggests the surface is restructuring as the calcination temperature increases. This follows the decreasing relative iron concentration as observed in EDX, however the decreases observed in XPS are significantly lower than those observed in EDX. With increased concentrations of manganese oxide present on the surface of the $Fe_{0.50}Mn_{0.50}O_x$ calcined at 500 °C, this may lead to the higher propane total oxidation activity observed of this catalyst.
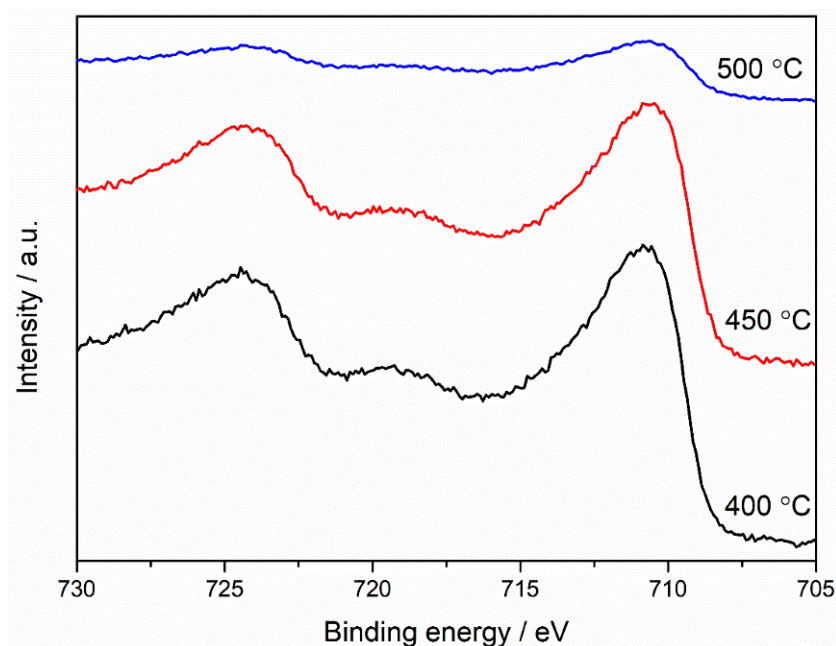

Figure 5-28: XPS spectra of the Fe 2p peaks for the $Fe_{0.50}Mn_{0.50}O_x$ prepared *via* co-precipitation using NH_4OH and calcined at various temperatures.

The Fe 2p XPS spectra of the $Fe_{0.50}Mn_{0.50}O_x$ were all similar with two major observable peaks, centred at 710 eV and 724 eV, present in all spectra, Figure 5-28. Along with this a satellite peak was observed at 718 eV in the samples calcined at 400 °C and 450 °C. As the temperature used to calcine the $Fe_{0.50}Mn_{0.50}O_x$ increases, the intensity of the peaks slightly decreases and broadens. This is in line with the decreasing concentration of iron observed on the surface of the $Fe_{0.50}Mn_{0.50}O_x$ as the calcination temperature increases.

Along with this, the satellite peak at 718 eV becomes less observable. As mentioned previously, the two major peaks signify iron oxide present in the 3+ oxidation state. However, the broadening of peak width as the calcination temperature increases, suggests the presence of iron in the 2+ oxidation state [42].

This suggests, as the temperature used to calcine the $Fe_{0.50}Mn_{0.50}O_x$ increases, the oxidation state of the iron becomes a mixture of 2+ and 3+ indicating the presence of Fe_3O_4. This is also noted with the decreasing intensity of the satellite peak at 718 eV upon increasing calcination temperature. This peak arises from iron in the 3+ oxidation state and the decrease in intensity of the peak indicates less 3+ is present, reinforcing the suggestion of formation of Fe_3O_4. This will mean the phase of the surface and bulk become more similar as the calcination temperature of the $Fe_{0.50}Mn_{0.50}O_x$ increases. As seen previously in this chapter, when iron oxide is present in the Fe_3O_4 phase in iron-manganese mixed metal oxide samples, it has increased propane total oxidation performance. Therefore the increased presence of the Fe_3O_4 phase throughout the $Fe_{0.50}$-$Mn_{0.50}O_x$ as the calcination temperature increases may lead to the higher propane total oxidation activity noted for these samples.

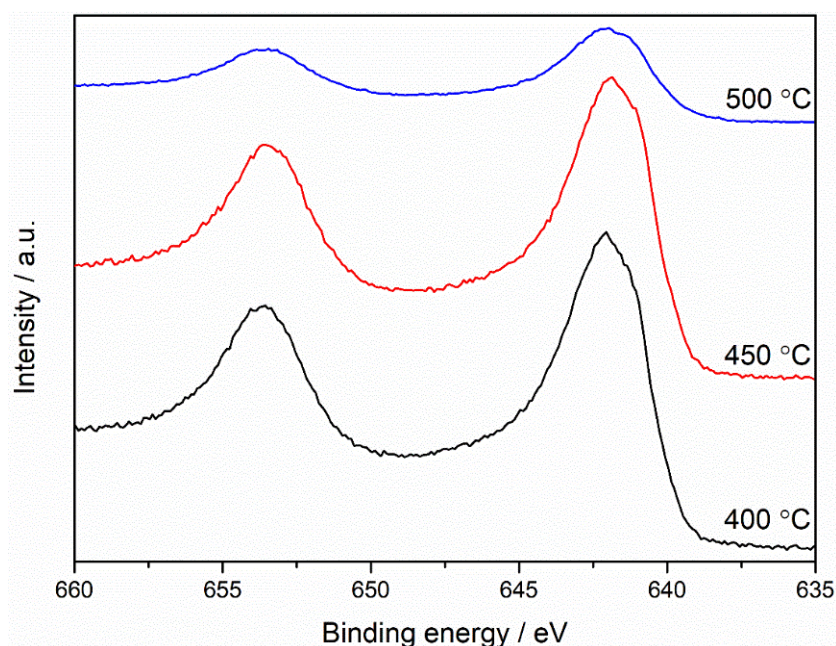Figure 5-29: XPS spectra of the Mn 2p peaks for the $Fe_{0.50}Mn_{0.50}O_x$ prepared *via* co-precipitation using NH_4OH and calcined at various temperatures.

There were two peaks centred at 642 eV and 653 eV in the $Fe_{0.50}Mn_{0.50}O_x$ calcined at various temperatures, Figure 5-29. The peaks centred at 642 eV seem to be formed of two separate peaks, due to the presence of a large shoulder peak present at the lower binding energy side of the peak. This may suggest the presence of manganese present in multiple oxidation states [34]. However, with no satellite peak at 647 eV, this suggests the

232

majority of the manganese is not present in the 2+ oxidation state. This means most of the manganese will be present in the 3+ oxidation state. This suggests that Mn_3O_4 may be present on the surface of $Fe_{0.50}Mn_{0.50}O_x$ calcined at the three different temperatures.
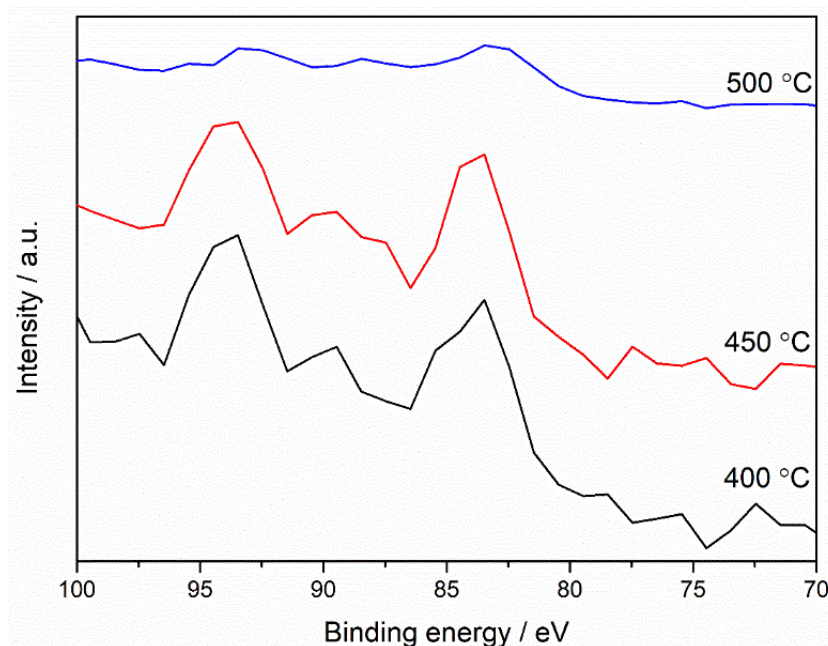

Figure 5-30: XPS spectra of the Mn 3s peaks for the $Fe_{0.50}Mn_{0.50}O_x$ prepared *via* co-precipitation using NH_4OH and calcined at various temperatures.

To investigate the oxidation state of the manganese in the $Fe_{0.50}Mn_{0.50}O_x$ samples, the Mn 3s peaks were used, Figure 5-30. The splitting between the Mn 3s peaks increased slightly upon increasing temperature used to calcine the $Fe_{0.50}Mn_{0.50}O_x$, Table 5-17. Only the sample calcined at 500 °C had manganese present in the 3+ oxidation state. It also shows the manganese phases in the surface and bulk are similar in the $Fe_{0.50}Mn_{0.50}O_x$.

Table 5-17: Magnitude of the peak splitting in the Mn 3s spectra for the $Fe_{0.50}Mn_{0.50}O_x$ prepared *via* co-precipitation using NH_4OH and calcined at various temperatures.

Sample	Magnitude of Mn 3s peak splitting / eV	Surface oxidation state of Mn (all +)
400 °C	5.2	4
450 °C	5.3	4
500 °C	5.5	3

Two oxygen species are observed in the XPS spectra of the all the $Fe_{0.50}Mn_{0.50}O_x$ calcined at different temperatures, Figure 5-31, representing defect and lattice oxygen. However, the intensity of both species decrease upon increasing temperature used to calcine the $Fe_{0.50}Mn_{0.50}O_x$. There is also a shift in both peaks to lower binding energies upon increasing calcination temperature. This shift suggests synergistic interactions between

iron and manganese decrease upon increasing calcination temperature of the $Fe_{0.50}Mn_{0.50}O_x$. This may lead to increased phase separation between the iron and manganese which was shown to increase the propane total oxidation activity of the ceria-manganese mixed metal oxides in the previous chapter.
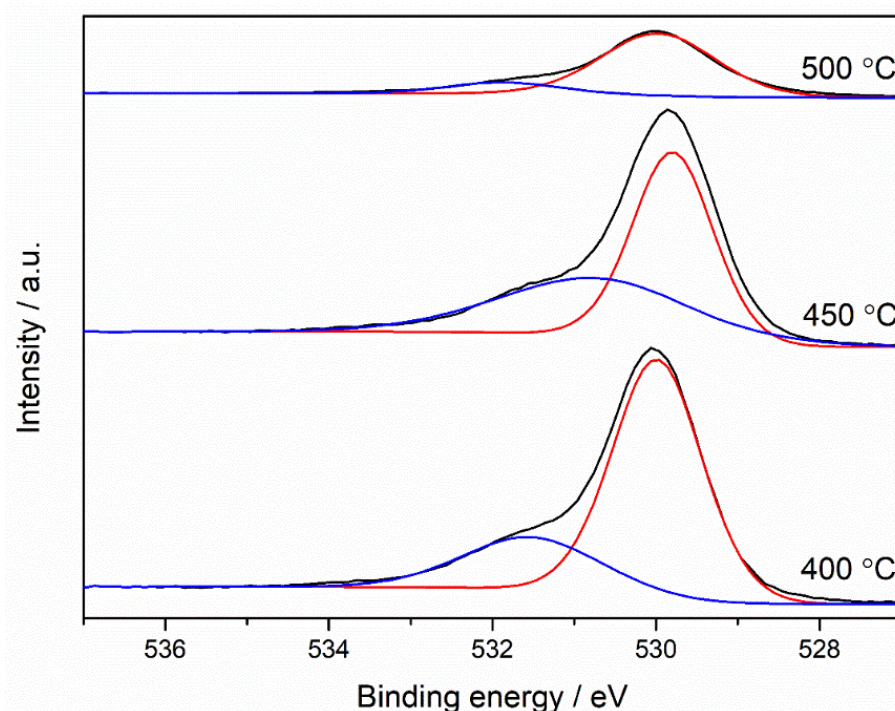

Figure 5-31: XPS spectra of the O 1s peaks of the $Fe_{0.50}Mn_{0.50}O_x$ prepared *via* co-precipitation using NH_4OH and calcined at various temperatures.

5.5 Conclusions

This work shows the iron-manganese mixed metal oxides are very active for propane total oxidation. The ratios of iron and manganese within the mixed metal oxide were investigated, along with precipitating agents and calcination temperatures used to prepare the final catalyst. $Fe_{0.50}Mn_{0.50}O_x$ catalyst prepared by co-precipitation using ammonium hydroxide and calcined at 500 °C showed the highest propane total oxidation activity out of the samples tested throughout the investigation. However no synergy was observed for the naphthalene total oxidation between iron oxides and manganese oxides. Co-precipitation produced iron-manganese mixed metal oxides with ratios close to the nominal values, no matter which precipitating agent, or iron/manganese ratio, was used. The iron-manganese mixed metal oxides were initially prepared using sodium carbonate as a precipitating agent. Most of the iron-manganese mixed metal oxides prepared using this method had higher propane total oxidation activity compared to the base iron oxides and manganese oxide, with the $Fe_{0.50}Mn_{0.50}O_x$ the most active out of all the samples tested. The $Fe_{0.50}Mn_{0.50}O_x$ was the iron-manganese mixed metal oxide with the highest

manganese content that showed no iron oxide and manganese oxide phase separation. It also had one of the smallest iron oxide crystallite size of the iron-manganese mixed metal oxides. The higher activity of the mixed metal oxides compared to the parent oxides were assigned to higher surface areas of the mixed metal oxides when compared to the manganese oxide, which may have arisen from the small iron oxide crystallites. The presence of manganese in the iron oxide, lead to easier reduction of the iron oxide as seen by the reduction in TPR peak temperatures upon increasing manganese content of the iron-manganese mixed metal oxide. However, the extent of reduction in the iron-manganese mixed metal oxides significantly decreased compared to the parent oxides. This will allow for increased concentration of surface oxygen species at lower temperatures therefore allowing for oxidation reactions to become enhanced at these temperatures giving increased activity. The surface oxidation states of the iron and manganese in the mixed metal oxides also changed compared to the parent metal oxides. Addition of iron oxide into the manganese led to an increase in the Mn 3s XPS peak splitting suggesting a change in oxidation state was occurring, The $Fe_{0.50}Mn_{0.50}O_x$ had the largest peak splitting and manganese present in the 3+ oxidation state. With the 3+ oxidation state noted to have higher VOC total oxidation activity, the increased propane total oxidation activity of this sample may have influenced this. However, due to the dilution of those manganese species and higher surface concentrations of iron, which has significantly lower naphthalene oxidation activity. This may have led to the poor synergy between the metal oxides observed in this catalyst for naphthalene total oxidation. Also with low phase separation between the iron oxide and manganese oxide, this may have led to lower naphthalene total oxidation.

As seen in the previous chapter, the presence of surface sodium had a significant impact on the VOC total oxidation activity of the mixed metal oxide catalyst. To investigate the effect of sodium on the $Fe_{0.50}Mn_{0.50}O_x$ a range of sodium, potassium and ammonium containing precipitating agents were investigated. The $Fe_{0.50}Mn_{0.50}O_x$ prepared from potassium containing precipitating agents had lower propane total oxidation activity than the $Fe_{0.50}Mn_{0.50}O_x$ prepared from sodium. However the samples prepared from ammonium containing precipitating agents performed significantly better than the sodium containing samples. This suggests that any alkali containing precipitating agent leads to poor total oxidation activity. Along with this trend, all $Fe_{0.50}Mn_{0.50}O_x$ prepared from hydroxides performed better for propane total oxidation than their carbonate counterparts. This trend was seen in surface and bulk elemental analysis of the $Fe_{0.50}Mn_{0.50}O_x$ catalysts. The catalysts prepared by carbonates had higher concentrations of sodium or potassium

compared to the hydroxides. The higher propane total oxidation activity from the hydroxides were ascribed to the smaller iron oxide crystallites observed in XRD, Also the bulk iron oxide was present as Fe_3O_4 in $Fe_{0.50}Mn_{0.50}O_x$ prepared from hydroxides whereas it formed Fe_2O_3 in the catalyst prepared from carbonates. Along with the smaller iron oxide crystallites phase separation in the $Fe_{0.50}Mn_{0.50}O_x$ prepared from ammonium hydroxide occurred. The manganese oxide formed large crystallites, in the form of Mn_3O_4. As seen in the previous chapter, the presence of phase separation led to an increase in VOC total oxidation and this effect is noted in the $Fe_{0.50}Mn_{0.50}O_x$. These bulk iron oxide and manganese oxides were also observed in the TPR of the $Fe_{0.50}Mn_{0.50}O_x$ prepared from hydroxides. All $Fe_{0.50}Mn_{0.50}O_x$ had similar ease and extent of reduction suggesting this doesn't effect the catalyst as much as other factors. The catalyst prepared from ammonium hydroxide had the highest surface area out of all the $Fe_{0.50}Mn_{0.50}O_x$ prepared. All catalysts which had a higher propane total oxidation activity than the $Fe_{0.50}Mn_{0.50}O_x$ prepared by sodium carbonate had manganese present in the 3+ oxidation state. The $Fe_{0.50}Mn_{0.50}O_x$ prepared from hydroxides also had manganese present in the 2+ oxidation state indicating it was in the Mn_3O_4 phase. This may have led to higher propane total oxidation activity of the $Fe_{0;50}Mn_{0.50}O_x$ prepared from hydroxides compared to the carbonates.

Finally to investigate the influence of calcination temperature on propane total oxidation activity, the $Fe_{0.50}Mn_{0.50}O_x$ prepared using ammonium hydroxide was calcined at 400 °C, 450 °C and 500 °C. The highest calcination temperature produced the most active propane total oxidation catalyst. This was ascribed to the increased iron oxide and manganese oxide phase, both in M_3O_4. Along with this, the large manganese oxide crystallites observed in the sample also correlated with increase propane total oxidation activity. It also had the highest surface area and the was the easiest to reduce. Along with this the surface manganese was present in the 3+ oxidation state. This suggests that these factors have the greatest influence on the propane total oxidation activity of the $Fe_{0.50}Mn_{0.50}O_x$.

5.6 References

[1]   R. Lin, W.P. Liu, Y.J. Zhong, M.F. Luo, Catalyst characterization and activity of Ag-Mn complex oxides, Appl. Catal. A Gen. 220 (2001) 165–171. doi:10.1016/S0926-860X(01)00718-9.

[2]   T.J. Clarke, S.A. Kondrat, S.H. Taylor, Total oxidation of naphthalene using bulk manganese oxide catalysts, Appl. Catal. A Gen. 450 (2013) 169–177. doi:10.1016/j.apcata.2012.10.029.

[3]   H. Cao, X. Li, Y. Chen, M. Gong, J. Wang, Effect of loading content of copper oxides on performance of Mn-Cu mixed oxide catalysts for catalytic combustion of benzene, J. Rare Earths. 30 (2012) 871–877. doi:10.1016/S1002-

0721(12)60148-3.

[4]   W. Tang, X. Wu, S. Li, X. Shan, G. Liu, Y. Chen, Co-nanocasting synthesis of mesoporous Cu-Mn composite oxides and their promoted catalytic activities for gaseous benzene removal, Appl. Catal. B Environ. 162 (2015) 110–121. doi:10.1016/j.apcatb.2014.06.030.

[5]   T.J. Clarke, T.E. Davies, S.A. Kondrat, S.H. Taylor, Mechanochemical synthesis of copper manganese oxide for the ambient temperature oxidation of carbon monoxide, Appl. Catal. B Environ. 165 (2015) 222–231. doi:10.1016/j.apcatb.2014.09.070.

[6]   L.C.A. Oliveira, J.D. Fabris, M.C. Pereira, Iron Oxides and their applications in catalytic processes: a review, Quim. Nova. 36 (2013) 123–130. doi:10.1590/S0100-40422013000100022.

[7]   T. García, B. Solsona, S.H. Taylor, Naphthalene total oxidation over metal oxide catalysts, Appl. Catal. B Environ. 66 (2006) 92–99. doi:10.1016/j.apcatb.2006.03.003.

[8]   B. Solsona, T. García, R. Sanchis, M.D. Soriano, M. Moreno, E. Rodríguez-Castellón, S. Agouram, A. Dejoz, J.M. López Nieto, Total oxidation of VOCs on mesoporous iron oxide catalysts: Soft chemistry route versus hard template method, Chem. Eng. J. 290 (2016) 273–281. doi:10.1016/j.cej.2015.12.109.

[9]   A.A. Herzing, C.J. Kiely, A.F. Carley, P. Landon, G.J. Hutchings, Identification of Active Gold Nanoclusters on Iron Oxide Supports for CO Oxidation, Science (80-.). 321 (2008) 1331–1335. doi:10.1126/science.1159639.

[10]   T.A. Yamamoto, T. Nakagawa, S. Seino, H. Nitani, Bimetallic nanoparticles of PtM (M = Au, Cu, Ni) supported on iron oxide: Radiolytic synthesis and CO oxidation catalysis, Appl. Catal. A Gen. 387 (2010) 195–202. doi:10.1016/j.apcata.2010.08.020.

[11]   T. Barakat, V. Idakiev, R. Cousin, G.S. Shao, Z.Y. Yuan, T. Tabakova, S. Siffert, Total oxidation of toluene over noble metal based Ce, Fe and Ni doped titanium oxides, Appl. Catal. B Environ. 146 (2014) 138–146. doi:10.1016/j.apcatb.2013.05.064.

[12]   Q. Shen, G. Lu, C. Du, Y. Guo, Y. Wang, Y. Guo, X. Gong, Role and reduction of NOx in the catalytic combustion of soot over iron-ceria mixed oxide catalyst, Chem. Eng. J. 218 (2013) 164–172. doi:10.1016/j.cej.2012.12.010.

[13]   H.H. Kedesey, A. Tauber, Formation of Manganese Ferrite by Solid-State Reaction, J. Am. Ceram. Soc. 39 (1956) 425–431. doi:10.1111/j.1151-2916.1956.tb15616.x.

[14]   T. Garcia, B. Solsona, S.H. Taylor, Handbook of Advanced Methods and Processes in Oxidation Catalysis: From Laboratory to Industry, 1st ed., Imperial College Press, 2014.

[15]   F.G. Durán, B.P. Barbero, L.E. Cadús, C. Rojas, M.A. Centeno, J.A. Odriozola, Manganese and iron oxides as combustion catalysts of volatile organic compounds, Appl. Catal. B Environ. 92 (2009) 194–201. doi:10.1016/j.apcatb.2009.07.010.

[16]   M. Baldi, V.S. Escribano, J.M.G. Amores, F. Milella, G. Busca, Characterization of manganese and iron oxides as combustion catalysts for propane and propene, Appl. Catal. B Environ. 17 (1998) 175–182. doi:10.1016/S0926-3373(98)00013-7.

[17]   A.J. Kozak, The thermal decomposition of Fe(NO3)3.9H2O, J. Therm. Anal. Calorim. 58 (1999) 647–651. doi:10.1023/A:1010112814013.

[18]   L. Markov, V. Blaskov, D. Klissurski, S. Nikolov, The thermal decomposition mechanism of iron(III) hydroxide carbonate to α-Fe2O3, J. Mater. Sci. 25 (1990) 3096–3100. doi:10.1007/BF00587656.

[19]   A. Lassoued, B. Dkhil, A. Gadri, S. Ammar, Control of the shape and size of iron

oxide (α-Fe2O3) nanoparticles synthesized through the chemical precipitation method, Results Phys. 7 (2017) 3007–3015. doi:10.1016/j.rinp.2017.07.066.

[20]   L. Zhuang, W. Zhang, Y. Zhao, H. Shen, H. Lin, J. Liang, Preparation and characterization of Fe3O4particles with novel nanosheets morphology and magnetochromatic property by a modified solvothermal method, Sci. Rep. 5 (2015) 1–6. doi:10.1038/srep09320.

[21]   Y. Huang, S. Hao, J. Pan, M. Srinivasan, B. Zhang, Y. Liu, J. Feng, S. Ball, Nanoscale ion intermixing induced activation of Fe 2 O 3 /MnO 2 composites for application in lithium ion batteries , J. Mater. Chem. A. 5 (2017) 8510–8518. doi:10.1039/c7ta00172j.

[22]   T. Garcia, D. Sellick, F. Varela, I. Vázquez, A. Dejoz, S. Agouram, S.H. Taylor, B. Solsona, Total oxidation of naphthalene using bulk manganese oxide catalysts, Appl. Catal. A Gen. 450 (2013) 169–177. doi:10.1016/j.apcata.2012.10.029.

[23]   M.R. Morales, B.P. Barbero, L.E. Cadús, Combustion of volatile organic compounds on manganese iron or nickel mixed oxide catalysts, Appl. Catal. B Environ. 74 (2007) 1–10. doi:10.1016/j.apcatb.2007.01.008.

[24]   S.D. Neelapala, A. Shetty, G. Gaggar, R. Mall, H. Dasari, Development of Iron Doped Manganese oxide (Mn 2-x Fe x O 3) Catalysts for Soot Oxidation Applications, 13 (2018) 245–251.

[25]   X. Wei, Y. Zhou, Y. Li, W. Shen, Polymorphous transformation of rod-shaped iron oxides and their catalytic properties in selective reduction of NO by NH3, RSC Adv. 5 (2015) 66141–66146. doi:10.1039/c5ra08254d.

[26]   M. Liang, W. Kang, K. Xie, Comparison of reduction behavior of Fe2O3, ZnO and ZnFe2O4 by TPR technique, J. Nat. Gas Chem. 18 (2009) 110–113. doi:10.1016/S1003-9953(08)60073-0.

[27]   S.C. Kim, W.G. Shim, Catalytic combustion of VOCs over a series of manganese oxide catalysts, Appl. Catal. B Environ. 98 (2010) 180–185. doi:10.1016/j.apcatb.2010.05.027.

[28]   B. Khonsari, M. Hoppert, N. Schäfer, C. Wickbold, J. Reitner, B. Rincón-Tomás, D. Mühlen, D. Hause-Reitner, Manganese carbonates as possible biogenic relics in Archean settings, Int. J. Astrobiol. 15 (2016) 219–229. doi:10.1017/s1473550416000264.

[29]   A.A. Mirzaei, H.R. Shaterian, R.W. Joyner, M. Stockenhuber, S.H. Taylor, G.J. Hutchings, Ambient temperature carbon monoxide oxidation using copper manganese oxide catalysts: Effect of residual Na+ acting as catalyst poison, Catal. Commun. 4 (2003) 17–20. doi:10.1016/S1566-7367(02)00231-5.

[30]   A.A. Mirzaei, H.R. Shaterian, M. Kaykhaii, The X-ray photoelectron spectroscopy of surface composition of aged mixed copper manganese oxide catalysts, Appl. Surf. Sci. 239 (2005) 246–254. doi:10.1016/j.apsusc.2004.05.274.

[31]   Y. Liu, J.-F. Chen, Y. Zhang, The effect of pore size or iron particle size on the formation of light olefins in Fischer–Tropsch synthesis, RSC Adv. 5 (2015) 29002–29007. doi:10.1039/C5RA02319J.

[32]   A.P. Grosvenor, B.A. Kobe, M.C. Biesinger, N.S. McIntyre, Investigation of multiplet splitting of Fe 2p XPS spectra and bonding in iron compounds, Surf. Interface Anal. 36 (2004) 1564–1574. doi:10.1002/sia.1984.

[33]   T. Yamashita, P. Hayes, Analysis of XPS spectra of Fe2+ and Fe3+ ions in oxide materials, Appl. Surf. Sci. 254 (2008) 2441–2449. doi:10.1016/j.apsusc.2007.09.063.

[34]   M.C. Biesinger, B.P. Payne, A.P. Grosvenor, L.W.M. Lau, A.R. Gerson, R.S.C. Smart, Resolving surface chemical states in XPS analysis of first row transition metals, oxides and hydroxides: Cr, Mn, Fe, Co and Ni, Appl. Surf. Sci. 257 (2011) 2717–2730. doi:10.1016/j.apsusc.2010.10.051.

[35] Y. Feng, M. V. Dobrotvorska, J.W. Anderegg, C.G. Olson, D.W. Lynch, Fe−3s core-level splitting and local magnetism in Fe2VAl, Phys. Rev. B. 63 (2001) 054419. doi:10.1103/PhysRevB.63.054419.

[36] T.L. Barr, An ESCA study of the termination of the passivation of elemental metals, J. Phys. Chem. 82 (1978) 1801–1810. doi:10.1021/j100505a006.

[37] J.L. Junta, M.F. Hochella, Manganese (II) oxidation at mineral surfaces: A microscopic and spectroscopic study, Geochim. Cosmochim. Acta. 58 (1994) 4985–4999. doi:10.1016/0016-7037(94)90226-7.

[38] A. Miyakoshi, A. Ueno, M. Ichikawa, XPS and TPD characterization of manganese-substituted iron-potassium oxide catalysts which are selective for dehydrogenation of ethylbenzene into styrene, Appl. Catal. A Gen. 219 (2001) 249–258. doi:10.1016/S0926-860X(01)00697-4.

[39] Y. Liu, M. Luo, Z. Wei, Q. Xin, P. Ying, C. Li, Catalytic oxidation of chlorobenzene on supported manganese oxide catalysts, Appl. Catal. B Environ. 29 (2001) 61–67. doi:10.1016/S0926-3373(00)00193-4.

[40] A. Keshavaraja, N.E. Jacob, A.V. Ramaswamy, Thermal decomposition of co-precipitated oxide hydrates of zirconium and manganese, Thermochim. Acta. 254 (1995) 267–275.

[41] E.R. Stobbe, B.A. de Boer, J.W. Geus, The reduction and oxidation behaviour of manganese oxides, Catal. Today. 47 (1999) 161–167. doi:10.1016/S0920-5861(98)00296-X.

[42] S.A. Chambers, Y.J. Kim, Y. Gao, Fe 2p Core-level spectra for pure, epitaxial α-Fe2O3(0001), γ-Fe2O3(001), and Fe3O4(001), Surf. Sci. Spectra. 5 (1998) 219. doi:http://dx.doi.org/10.1116/1.1247873.

[43] W. Tang, X. Wu, D. Li, Z. Wang, G. Liu, H. Liu, Y. Chen, Oxalate route for promoting activity of manganese oxide catalysts in total VOCs' oxidation: Effect of calcination temperature and preparation method, J. Mater. Chem. A. 2 (2014) 2544–2554. doi:10.1039/c3ta13847j.

[44] H. Zhu, Y. Xu, X. Tang, Y. Li, W. Shen, J. Wang, X. Huang, MnOx–CeO2 mixed oxide catalysts for complete oxidation of formaldehyde: Effect of preparation method and calcination temperature, Appl. Catal. B Environ. 62 (2005) 265–273. doi:10.1016/j.apcatb.2005.08.004.

[45] G.J. Hutchings, A. a. Mirzaei, R.W. Joyner, M.R.H. Siddiqui, S.H. Taylor, Effect of preparation conditions on the catalytic performance of copper manganese oxide catalysts for CO oxidation, Appl. Catal. A Gen. 166 (1998) 143–152. http://www.scopus.com/inward/record.url?eid=2-s2.0-0012474326&partnerID=40&md5=68d9269adad50570f9186cf0282e3eb0.

[46] M. Augustin, D. Fenske, I. Bardenhagen, A. Westphal, M. Knipper, T. Plaggenborg, J. Kolny-Olesiak, J. Parisi, Manganese oxide phases and morphologies: A study on calcination temperature and atmospheric dependence, Beilstein J. Nanotechnol. 6 (2015) 47–59. doi:10.3762/bjnano.6.6.

[47] G. Ketteler, W. Weiss, W. Ranke, R. Schlo, F. Haber, I. Der Max, P. Gesellschaft, Bulk and surface phases of iron oxides in an oxygen and water atmosphere at low pressure Ž, Phys. Chem. Chem. Phys. 3 (2001) 1114–1122.

[48] P.J. Van Espen, H.A. Nultens, F.C. Adams, Possible errors in energy dispersive X-ray spectrometry due to Raman scattering, Anal. Chem. 51 (1979) 1580–1583. doi:10.1021/ac50045a054.

6 Conclusions and Future Work

6.1 Conclusions

This work presented a range of mixed metal oxide catalysts for total oxidation of propane and naphthalene, along with bulk and surface characterisation of the catalysts. The optimum ratio for each catalysts system is shown in Table 6-1. Along with this, both ceria-zirconia and ceria-manganese mixed metal oxide catalysts showed appreciable stability for both total oxidation reactions.

Table 6-1: The optimum metal ratios for ceria-zirconia, ceria-manganese and iron-manganese mixed metal oxide catalysts for propane and naphthalene total oxidation

Catalyst	Optimum metal ratio	Preparation method	Propane T_{50} / °C	Naphthalene T_{50} / °C
Ce-Zr	$Ce_{0.90}Zr_{0.10}O_x$	Mechanochemical grinding of nitrates	400	160
	$Ce_{0.95}Zr_{0.05}O_x$	Mechanochemical grinding of carbonates	375	180
Ce-Mn	$Ce_{0.25}Mn_{0.75}O_x$	Co-precipitation using sodium carbonate and 2 l washing	270	160
Fe-Mn	$Fe_{0.50}Mn_{0.50}O_x$	Co-precipitation using ammonium hydroxide	220	-

6.1.1 Ceria-zirconia mixed metal oxides

Preparation of ceria-zirconia mixed metal oxides were undertaken using mechanochemical grinding of two types of precursors, nitrates and carbonates. In both cases, lower concentrations of zirconia provided the most active catalysts for propane and naphthalene total oxidation. Ceria-zirconia mixed metal oxides prepared from nitrates were slightly more active for naphthalene total oxidation, whereas mixed metal oxides prepared from carbonates showed increased propane total oxidation activity. The stability of propane and naphthalene total oxidation was also significantly different between both precursors. The ceria-zirconia mixed metal oxides prepared from nitrate showed minor deactivation upon repeated propane total oxidation runs and extended naphthalene total oxidation. However the sample prepared from carbonates, showed significant deactivation for both total oxidation reactions.

Incorporation of zirconia into the ceria lattice led to an increase in the surface area and a decrease in the crystallite size compared to ceria. The reduction temperature of surface ceria species also decreased upon addition of zirconia into the ceria lattice. The hydrogen

consumption of the surface also increased indicating both ease and extent of reduction of the ceria was positively effected upon addition of zirconia. All these factors will lead to the increase in propane and naphthalene total oxidation activity observed over the ceria-zirconia mixed metal oxides compared to the parent oxides. Surface area affects naphthalene total oxidation activity over ceria catalysts [1]. The ceria-zirconia mixed metal oxides prepared from nitrates had a slightly higher surface area compared to the mixed metal oxides prepared from carbonates. Therefore, the increased naphthalene total oxidation activity of the ceria-zirconia mixed metal oxides prepared from nitrates can be ascribed to the higher surface area.

Elemental analysis of the ceria-zirconia mixed metal oxides showed zirconia enrichment occurred on the surface of all of the mixed metal oxide catalysts. With the surface concentrations of zirconia increasing upon increasing zirconia content of the ceria-zirconia mixed metal oxide. This led to a decrease in propane and naphthalene total oxidation, due to the poor activity of zirconia for the reactions. The higher surface zirconia concentrations were ascribed to poor incorporation of zirconia into the ceria lattice and not from contamination from the milling surface. The relative surface oxygen species increased upon addition of low concentrations of zirconia into the ceria. The higher relative concentrations of surface oxygen defects correlated with increased VOC total oxidation over the mixed metal oxides catalysts.

Differences in stability between the ceria-zirconia mixed metal oxide samples was ascribed to the stability of the catalysts under the reaction conditions. The higher reaction temperatures used during propane total oxidation led to loss of surface area and formation of phase separated ceria and zirconia, as observed from *in situ* XRD analysis of the samples. The loss of naphthalene total oxidation over extended periods of time was ascribed to potential loss of surface area and potential adsorption of naphthalene on the surface of the catalysts, causing blockage of active sites. However further investigation of these factors has to be carried out.

6.1.2 Ceria-manganese mixed metal oxides

Unlike the ceria-zirconia mixed metal oxides, ceria-manganese containing high concentrations of ceria were less active for propane and naphthalene total oxidation compared to the low ceria content mixed metal oxides. Only the $Ce_{0.25}Mn_{0.75}O_x$ samples showed higher propane and naphthalene total oxidation compared to the manganese oxide. This was ascribed to a range of factors. The manganese in the $Ce_{0.25}Mn_{0.75}O_x$ was in the 3+ oxidation state whereas the majority of the manganese in the manganese oxide

was in the 4+ oxidation state. Lower oxidation states of manganese oxide were noted to have increased naphthalene total oxidation activity, which led to the higher activity observed for the mixed metal oxide [2]. Along with the difference in manganese oxide phases, the $Ce_{0.25}Mn_{0.75}O_x$ had a significantly higher surface area compared to the parent oxides, and the lowest reduction temperature of the ceria-manganese mixed metal oxides prepared from co-precipitation.

However, the $Ce_{0.25}Mn_{0.75}O_x$ prepared by co-precipitation using sodium carbonate and washed with 1 l of water had high surface and bulk concentrations of sodium. To investigate the effect of the sodium, the $Ce_{0.25}Mn_{0.75}O_x$ was washed with increasing amounts of water and prepared using non-sodium containing methods. Increased washing of the $Ce_{0.25}Mn_{0.75}O_x$ led to a significant decrease in bulk and surface sodium content compared to the original sample. Increased phase separation and manganese oxide crystallite sizes were observed upon increased washing of the sample. Along with this, the surface area increased. The reduction temperature of the mixed metal oxide also decreased and the 3+ manganese oxidation state was maintained.

The $Ce_{0.25}Mn_{0.75}O_x$ prepared using the range of sodium-free methods all showed appreciable propane total oxidation activity. However, all the catalysts had poor naphthalene total oxidation activity. The $Ce_{0.25}Mn_{0.75}O_x$ prepared mechanochemically from carbonate and nitrate precursors had the highest propane total oxidation activity and had phase separation between ceria and manganese oxides. This indicated phase separation along with large manganese oxide crystallites were required for high VOC total oxidation activity over the ceria-manganese mixed metal oxides. The preparation method also affected the reducibility of the mixed metal oxide. The $Ce_{0.25}Mn_{0.75}O_x$ prepared using co-precipitation with high washing had the lowest reduction temperature compared to the other samples. With this sample having the highest total oxidation activity of the different methods, this indicates the reducibility of the catalyst significantly effects the total oxidation activity.

Unlike the ceria-zirconia mixed metal oxides, the $Ce_{0.25}Mn_{0.75}O_x$ was extremely stable for both propane and naphthalene total oxidation reactions.

6.1.3 Iron-manganese mixed metal oxides

The iron-manganese mixed metal oxides produced the most active propane total oxidation catalysts during this project. Synergy was observed for propane total oxidation however, no synergy between the two metal oxides were observed for naphthalene total oxidation. $Fe_{0.50}Mn_{0.50}O_x$ was noted to the be the most active ratio for propane total oxidation. It had

the smallest iron crystallite size and the highest surface area of the iron-manganese mixed metal oxides prepared using co-precipitation. The surface reduction temperature of the $Fe_{0.50}Mn_{0.50}O_x$ was the lowest of the iron-manganese mixed metal oxides, suggesting ease of reduction accounts for the activity of VOC total oxidation for iron-manganese mixed metal oxide catalysts. The other main factor for the $Fe_{0.50}Mn_{0.50}O_x$ high activity is ascribed to the increased reducibility of surface manganese in the 3+ oxidation state, which was only observed on this sample.

To further optimise the iron-manganese mixed metal oxide catalyst for propane total oxidation, the precipitating agent and calcination temperature were investigated. $Fe_{0.50}Mn_{0.50}O_x$ prepared from hydroxides out performed their carbonate counterparts with the catalyst prepared using ammonium hydroxide solution performing the best. This sample had no bulk or surface sodium contamination, which as seen from the ceria-manganese mixed metal oxides can effect the VOC total oxidation activity of the sample. This sample had the largest manganese oxide crystallites, indicating this is a key factor for high propane total oxidation activity. The manganese was present in the Mn_3O_4 phase in the $Fe_{0.50}Mn_{0.50}O_x$ prepared from ammonium hydroxide and this phase was also noted on the surface. The presence of the Mn_3O_4 was noted to be active for propane total oxidation. When the calcination temperature used to prepare the $Fe_{0.50}Mn_{0.50}O_x$ was decreased, this phase wasn't formed and the propane total oxidation activity decreased as a result.

6.2 Future Work

For all the catalysts, the reaction pathway for both propane and naphthalene total oxidation will be interesting to study. Previous studies have used DRIFTS and IR methods to monitor naphthalene [3] and propane [4] total oxidation reactions respectively. Along with this, the stability of the catalysts should be more thoroughly investigated. By using large scale reactors, larger amounts of catalyst can be used and post reaction analysis of the sample can be done. 'Industrial' mixtures contain a range of VOCs from their exhausts or emissions [5]. Therefore to further investigate the catalyst in 'industrial' conditions, mixtures of VOCS should be used to investigate performance of the most active catalysts from this investigation.

The effect of milling material on ceria-zirconia mixed metal oxide will be an interesting investigation. By using a harder material such as silicon carbide, this may lead to higher incorporation of zirconia into the ceria lattice. This may lead to less surface segregation of zirconia and form more active VOC total oxidation catalysts. To increase incorporation

of zirconia into ceria, organic solvents or water, could be added to the preparation vessel [6]. Addition of a solvent was noted to increase the incorporation of mixed metal oxides, so this can be used to future optimise the ceria-zirconia catalyst.

Optimisation of the preparation methods can be used to provide a more comparable study on the effect of preparation method of $Ce_{0.25}Mn_{0.75}O_x$ on propane and naphthalene total oxidation. The preparation methods were optimised for preparation of various metal oxides. Therefore factors such as calcination temperature, aging time and aging temperature will need to be further optimised. With some of the methods, especially mechanochemical, showing high activity for propane total oxidation, these methods could be optimised to produce extremely active catalysts for both propane and naphthalene total oxidation.

The TEM analysis and stability of the iron-manganese mixed metal oxides need to be fully investigated to provide the complete examination of the materials. Along with this the $Fe_{0.50}Mn_{0.50}O_x$ can be further optimised by changing a range of factors such as aging time, rate of addition of nitrates and aging temperature. This may lead to an increase in the naphthalene total oxidation activity of the catalysts, as it may create synergy between the two metal oxides.

6.3 References

[1]   T. Garcia, B. Solsona, S.H. Taylor, Nano-crystalline Ceria Catalysts for the Abatement of Polycyclic Aromatic Hydrocarbons, Catal. Letters. 105 (2005) 183–189. doi:10.1007/s10562-005-8689-2.

[2]   T. Garcia, D. Sellick, F. Varela, I. Vázquez, A. Dejoz, S. Agouram, S.H. Taylor, B. Solsona, Total oxidation of naphthalene using bulk manganese oxide catalysts, Appl. Catal. A Gen. 450 (2013) 169–177. doi:10.1016/j.apcata.2012.10.029.

[3]   D.R. Sellick, A. Aranda, T. García, J.M. López, B. Solsona, A.M. Mastral, D.J. Morgan, A.F. Carley, S.H. Taylor, Influence of the preparation method on the activity of ceria zirconia mixed oxides for naphthalene total oxidation, Appl. Catal. B Environ. 132–133 (2013) 98–106. doi:10.1016/j.apcatb.2012.11.036.

[4]   M.A. Hasan, M.I. Zaki, L. Pasupulety, IR investigation of the oxidation of propane and likely C3 and C2 products over group IVB metal oxide catalysts, J. Phys. Chem. B. 106 (2002) 12747–12756. doi:10.1021/jp0214413.

[5]   H.L. Wang, L. Nie, J. Li, Y.F. Wang, G. Wang, J.H. Wang, Z.P. Hao, Characterization and assessment of volatile organic compounds (VOCs) emissions from typical industries, Chinese Sci. Bull. 58 (2013) 724–730. doi:10.1007/s11434-012-5345-2.

[6]   K. Ralphs, C. Hardacre, S.L. James, Application of heterogeneous catalysts prepared by mechanochemical synthesis., Chem. Soc. Rev. 42 (2013) 7701–18. doi:10.1039/c3cs60066a.